Thesis report

Optimization framework for design of a hybrid electric vertical takeoff and landing multirotor - Application to the GoAERO competition

Master Thesis Aerospace Engineering

Bas van Leeuwen

Delft University of Technology

Thesis report

Optimization framework for design of a hybrid electric vertical takeoff and landing multirotor - Application to the GoAERO competition

by

Bas van Leeuwen

To obtain the degree of Master of Science at the Delft University of Technology

Student number:	4834925
Assessment Committee:	Marilena Pavel, Responsible thesis supervisor
	Gianfranco la Rocca, Chair
	Alessandro Bombelli, Examiner
Institution:	Delft University of Technology
Place:	Faculty of Aerospace Engineering, Delft
Date of submission:	02-02-2025
Defense date:	17-02-2025

Abstract

Since the 1970s, helicopters have been vital in disaster response but face limitations in cost, infrastructure, and maneuverability. This thesis presents the design and optimization of an emergency response flyer tailored for the GoAERO competition. Multirotor configurations with hybrid-electric propulsion are investigated to overcome the limitations of existing fully electric VTOL technologies.

A Multidisciplinary Design Optimization (MDO) framework is applied to hybrid-electric quadrotor, hexarotor, and octorotor configurations, optimizing the balance between rotor count, mass, and performance. The objective is to minimize Maximum Takeoff Mass (MTOM) while enhancing dynamic performance and maximizing the payload-to-system mass ratio. This study addresses a key research gap by integrating early-stage handling qualities (HQ) evaluation and exploring trade-offs between optimized rotor count configurations. Aerodynamic forces and energy consumption are estimated using momentum theory, while system dynamics are analyzed through Newton-Euler equations and eigenvalue assessments.

Results show that the hexarotor configuration achieves the fastest convergence, balancing design complexity and design space exploring. Configurations maintain a disk loading between 43–$63 [kg/m^2]$ with hover efficiency between 5 and 5.8. A higher rotor count improves hover efficiency and disk loading, making performance comparable to eHang and Vahana while achieving nearly twice the cruise speed, rivaling helicopters.

At a hybridization factor (HF) of 0.1, MTOM is reduced by 75%, with only a 3% mass variation between configurations. However, at higher HF, mass increases by 20% due to relatively low energy density of batteries further impacting structural support demands, underscoring the need for a more detailed support structure model. Stability analysis confirms neutral hover stability, while a real, negative eigenvalue at cruise identifies the surge subsidence mode, governed by system mass.

Rotor count significantly impacts design flexibility. Hexacopters and octocopters offer better disk loading homogeneity, whereas quadrotors face constrained rotor sizing and elevated blade and disk loading, limiting efficiency. Quadrotors excel in payload-to-mass ratio and simplicity, making them ideal for productivity missions but less suited for maneuvering-intensive tasks with lower disk loading and control authority, highlighting the importance of early HQ considerations.

This thesis makes a valuable contribution to the advancement of eVTOL research by addressing early-stage HQ assessments where on the basis of other literature and configuration optimization, the hexacopter emerges as the most viable for the GoAERO competition, striking the best balance between mass, handling qualities, and mission performance.

Contents

Nomenclature

Abbreviations

Abbreviation	Definition
3D	Three-Dimensional
AAM	Advanced Air Mobility
ADS	Aeronautical Design Standard
AFDD	Army Flight Dynamics Directorate
AI	Artificial Intelligence
AGL	Above Ground Level
AR	Aspect Ratio
bat	Battery
BSFC	Brake-Specific Fuel Consumption
CFRP	Carbon Fiber Reinforced Polymer
CFD	Computational Fluid Dynamics
CoG	Center of Gravity
COM	Center of Mass
CR	Cruise
DRB	Disturbance Rejection Bandwidth
DRP	Disturbance Rejection Peak
DEP	Distributed Electric Propulsion
DSCT	Descent
eVTOL	Electric Vertical Take-Off and Landing
eg	Electric Generator
ELEC	Electrical
EMS	Emergency Medical Services
em	Electric Motor
ENV	Environmental
ER	Emergency Response
ES	Emergency Scenarios
EASA	European Union Aviation Safety Agency
FoM	Figure of Merit
FUS	Fuselage
f	Fuel
GNSS	Global Navigation Satellite System
gt	Gas Turbine
HF	Hybridization Factor
HEMS	Helicopter Emergency Medical Services
HQ	Handling Qualities
HOV	Hover
ICE	Internal Combustion Engine
LG	Landing Gear
LND	Landing
MDA	Minimum Descent Altitude
MDF	Multi-Disciplinary Feasibility
MDO	Multidisciplinary Optimization
MRKT	Market
MTOW	Maximum Takeoff Weight
MTOM	Maximum Takeoff Mass

Abbreviation	Definition
NED	North-East-Down
OEW	Operating Empty Weight
OEM	Operating Empty Mass
OPS	Operational
OZ	Operation Zone
OTS	Off-The-Shelf
PERF	Performance
PM	Power Margin
PRE	Pre-Flight
PROP	Propulsion
PSS	Propulsion Support Structure
RF	Radio Frequency
RVLT	Revolutionary Vertical Lift Technology
SH	Series Hybrid
SLSQP	Sequential Least Squares Programming
SoC	State of Charge
STRCT	Structural
TLAR	Top-Level Aircraft Requirements
TO	Take-Off
UAM	Urban Air Mobility
USD	United States Dollar
VTOL	Vertical Take-Off and Landing
XDSM	eXtended Design Structure Matrix

Symbols

Symbol	Definition	Unit
A	Rotor disk area	[m²]
AR	Aspect Ratio	[-]
BED	Battery Energy Density	[Wh/kg]
$BSFC$	Brake-Specific Fuel Consumption	[g/kWh]
C_D	Drag coefficient	[-]
$C_{D,profile}$	Profile drag coefficient	[-]
C_Q	Torque coefficient	[-]
C_T	Thrust coefficient	[-]
$C_{T_{gl}}$	Glauert thrust coefficient	[-]
C_x, C_y, C_z	Aerodynamic force coefficients in x, y and z	[-]
CoG_x, CoG_y, CoG_z	Center of Gravity coordinates in x, y and z	[m]
D	Drag	[N]
$D_{propeller}$	Propeller diameter	[m]
E	Modulus of elasticity	[Pa]
$E_{battery}$	Battery energy capacity	[Wh]
F_g	Gravitational force	[N]
F_g^b	Gravitational force in body frame	[N]
F_x, F_y, F_z	Forces in body frame x, y and z	[N]
FoM	Figure of Merit	[-]
g	Gravitational acceleration	[m/s²]
H_x, H_y, H_z	Angular momenta	[kg·m²/s]
HF_{SH}	Hybridization Factor for Series Hybrid	[-]
I	Moment of inertia	[kg·m²]
I_x, I_y, I_z	Principal moments of inertia around x, y and z	[kg·m²]
I_{xy}, I_{yz}, I_{xz}	Products of inertia around xy, yz and xz	[kg·m²]
k	Induced power factor	[-]

Symbol	Definition	Unit
M	Moment	[N·m]
$M_{T_{adv}}$	Tip Mach number of advancing blade	[-]
$m_{battery}$	Battery mass	[kg]
$m_{fuselage}$	Fuselage mass	[kg]
m_i	Mass of component i	[kg]
m_{mto}	Maximum takeoff mass	[kg]
m_{pipe}	Pipe mass	[kg]
$m_{propeller}$	Propeller mass	[kg]
m_{rotor}	Rotor mass	[kg]
m	Mass	[kg]
m_e	Empty mass	[kg]
m_{Useful}	Useful mass	[kg]
N_{blades}	Number of blades	[-]
p, q, r	angular rates	[rad/s]
p_0, q_0, r_0	Initial angular rates	[rad/s]
Δp, Δq, Δr	Perturbation in angular rates	[rad/s]
P	Power	[W]
P_{actual}	Actual power	[W]
$P_{battery}$	Power from battery	[W]
P_{cruise}	Power during cruise	[W]
$P_{descent}$	Power during descent	[W]
P_f	Fuel power	[W]
P_{hover}	Power during hover	[W]
P_{ideal}	Ideal power	[W]
$P_{induced}$	Induced power	[W]
$P_{parasitic}$	Parasitic power	[W]
$P_{profile}$	Profile power	[W]
$P_{rotor_{max}}$	Maximum rotor power	[W]
$P_{\text{EM, max}}$	Maximum power of electric motor	[W]
$P_{\text{ICE, max}}$	Maximum power of ICE	[W]
$P_{req_{h_{batt}}}$	Required power for battery	[W]
$P_{req_{h_{EM}}}$	Required power Electric Motor	[W]
$P_{req_{h_{ICE}}}$	Required power Internal Combustion Engine	[W]
PM	Power Margin	[-]
R	Rotor radius	[m]
SoC	State of Charge	[-]
T	Thrust	[N]
T_{hover}	Hover thrust	[N]
t, dt	Time and time step	[s]
u, v, w	Body translational velocities	[m/s]
u_0, v_0, w_0	Initial body translational velocities	[m/s]
Δu, Δv, Δw	Perturbation in velocities	[m/s]
v_{hover}	Hover induced velocity	[m/s]
V_{axial}	Axial velocity	[m/s]
V_{climb}	Climb velocity	[m/s]
V_{cruise}	Cruise speed	[m/s]
V_∞	Free stream velocity	[m/s]
W	weight	[N]
W_e	Empty weight	[N]
W_{Useful}	Useful weight	[N]
x, y, z	Position coordinates	[m]
α_{disk}	Rotor disk angle of attack	[deg]
λ	Eigenvalue	[-]
μ	Advance ratio	[-]

Symbol	Definition	Unit
ρ	Air density	[kg/m³]
σ	Solidity ratio	[-]
ω	Angular rate	[rad/s]
Ω	Rotor angular velocity	[rad/s]
ϕ, θ, ψ	Roll, Pitch and yaw angles	[rad]
ϕ_0, θ_0, ψ_0	Initial Roll, Pitch and yaw angles	[rad]
$\Delta\phi$, $\Delta\theta$, $\Delta\psi$	Perturbation in Euler angles	[rad]

List of Figures

List of Tables

1 Introduction

Since the 1970s, VTOL (Vertical Take-Off and Landing) aircraft, specifically helicopters, have played a critical role in disaster and emergency response, providing quick and independent access to remote or inaccessible areas. In such emergencies, where conventional infrastructure is either absent or severely compromised, there is a need for vehicles that can operate with minimal space requirements and deliver aid as efficiently as possible. The increasing frequency and severity of emergencies, from ambulance deserts to natural disasters, underscore the growing demand for VTOL solutions.

In the United States alone, approximately 4.5 million people live in "ambulance deserts," regions where emergency medical services are more than 25 minutes away. Meanwhile, in 2022, the world witnessed approximately 380 natural disasters, with flooding alone affecting over 55 million people. These global natural disasters in 2022 affected 185 million people and claimed over 30,000 lives, emphasizing the urgent need for effective response mechanisms. These challenges are further exacerbated by climate change, which increases the unpredictability and severity of such events.

As mentioned above, helicopters have traditionally served in disaster and emergency response roles. However, helicopters face significant limitations due to high operational and acquisition costs, complex facility requirements, extensive pilot training, and limited maneuverability in confined spaces. As a result, there is a growing need for more cost-effective, versatile, and user-friendly alternatives that can overcome these limitations, driven by modern technological advancements.

At the heart of the GoAERO competition [1] is the development of an emergency response flyer designed to carry a single person and operate safely in both urban and rural environments. This flyer must outperform current alternatives by addressing the unique challenges posed by natural disasters, humanitarian crises, medical emergencies, and other urgent situations. As further defined in the GoAERO competition [1], the aircraft must be reliable, efficient, and adaptable to a wide range of flight conditions and environments, from adverse weather to unfamiliar terrain. The system must also ensure resilience, precision control, and minimal pilot training requirements, all while maintaining tight maneuverability in confined spaces.

However, such an innovative solution does not materialize without careful planning. In accordance with standard practices in aerospace engineering, a preliminary design must be developed to lay the foundation for further advancements. This initial design phase serves as the backbone for future refinements, ensuring that the final solution meets all operational and performance requirements. The proposed flyer must perform across diverse scenarios, from delivering first responders to evacuating flood victims, requiring the eVTOL to be versatile in both hovering performance and overall endurance to complete these missions effectively and on time. This research addresses the need of new and innovative eVTOL development with offering insights into achieving an optimal design in application to the GoAERO competition.

Thesis overview

Before consolidating the preliminary design, Chapter 2 provides an overview of the GoAERO competition, describing the three defined missions along with their requirements and objectives. Chapter 3 presents a comprehensive literature review, detailing the history, recent advancements, and limitations of VTOL technology. It examines relevant configurations, propulsion systems, and defines handling qualities critical for the GoAERO competition.

Chapter 4 outlines the research objectives and central research question, addressing the design challenges and gaps identified in existing research. It also introduces the research methodology employed to achieve the study's goals. Chapter 5 focuses on the requirements and functional analysis of the emergency response flyer, defining the top-level aircraft requirements (TLARs) based on the GoAERO competition and mapping out the flyer's critical mission profiles.

Chapter 6 elaborates on the conceptual design process, including the fuselage layout, system mass modeling, and propulsion system integration. It also focuses on the aerodynamic and power modeling of the rotors, as well as the dynamics of the flyer. Chapter 7 defines the optimization framework, detailing the constraints, bounds, and overall setup implemented in the study.

Chapter 8 processes and discusses the outcomes of the design and optimization process, while Chapter 9 highlights the key findings related to the flyer's performance, stability, configuration, evaluation of configuration specific handling qualities and overall feasibility for the GoAERO missions.

2
GoAERO Competition

The GoAERO competition focuses on developing and operating a single-occupant, affordable, robust, and effective emergency response aircraft designed around three primary missions. Recent technological advancements, along with the emergence of new eVTOL aircraft, have made it possible to create simpler, more reliable, and more versatile aircraft configurations [1].

The competition encourages revolutionary designs that can safely operate in both densely populated urban environments and remote or rural areas. For such versatility, the flyer must be roadable and trailerable, allowing for easy deployment on-site, ensuring both reliability and efficiency. In comparison to current solutions, the proposed aircraft must require less pilot training, have lower acquisition and maintenance costs, and face fewer facility constraints. Current Helicopter Emergency Medical Services (HEMS), for example, are not only expensive in terms of acquisition and operational costs but also require specialized facilities and extensive pilot training, all while being limited in maneuverability within confined spaces.

2.1. Missions

The flyer's capabilities are evaluated through three distinct missions, each highlighting a critical aspect of its performance:

1. Productive: Demonstrate the ability to deploy on-site efficiently and operate consistently, reliably, and effectively.
2. Versatile: Showcase robustness and adaptability to perform critical tasks across diverse environments and challenging conditions.
3. Capable: Exhibit precision and agility, enabling responsive operation in unpredictable and dynamic scenarios.

These qualities are assessed through three mission types: the Productivity mission, the Adversity mission, and the Maneuvering mission. Each mission is evaluated during the final fly-off event, which includes simulations using manikins to represent human occupants. These simulations are designed to replicate a range of real-world emergency scenarios, testing the flyer's performance under realistic conditions as listed below [1].

1. 'Deliver a first responder to the scene in a dense urban environment (building, signs, wires, tight spaces)'
2. 'Deliver (or retrieve) a firefighter on a burning hillside'
3. 'Get water and rations to communities cut off by natural disaster'
4. 'Retrieve an injured person from under a forest canopy'
5. 'Rescue victims from car accidents when traffic at a stand-still'
6. 'Evacuate flood victims'
7. 'Land in earthquake rubble and uneven terrain'
8. 'Move a patient to urgent care'

9. ’Retrieve a drowning victim at the beach or rescue a swimmer pulled out by a riptide’
10. ’Douse a nascent wildfire’
11. ’Rescue from highrise rooftops’
12. ’Transport a patient from urgent care to a hospital or blood/organ delivery from a nearby hospital’
13. ’Rescue in urban tunnels or remote caves’
14. ’Rescue someone who has fallen through the ice on a frozen lake’
15. ’Locate / identify / observe an emergency situation’
16. ’Act as a fire truck “ladder extension”’

2.1.1. Productivity Mission

The objective of the Productivity mission is to demonstrate the flyer’s capability for rapid deployment and efficient, continuous payload transport. The mission begins with the flyer transported via a ground vehicle with specified width and height limitations (maximum $4.1\,[\mathrm{m}]$). Upon arrival, the aircraft is unloaded and prepared for operation within the designated Operation Zone (OZ) as outlined in Table 2.1 [1] indicating the surface type, shape and dimensions.

The mission profile and OZ is visualized in Figure 2.1 where the mission profile involves flying a series of segments beyond the ground effect. Each segment consists of three laps, defined as flying from behind the baseline, crossing the end line approximately one-quarter mile away, and returning across the baseline. This sequence is repeated, alternating between flights with and without payload, until the maximum payload is transported within the 90-minute time limit [1].

Mission requirements, such as course length and number of crossings, are designed to replicate real-world scenarios. The mission mandates a minimum payload weight of $567\,[\mathrm{kg}]$ to be ferried, with performance ranked based on the ratio of total payload weight transported to the system’s total weight [1]. The payload may include combinations of the following items:

1. Up to one Alex manikin ($57\,[\mathrm{kg}]$)
2. Up to twelve $1.8\,[\mathrm{m}]$ lengths of #5 rebar ($2.8\,[\mathrm{kg}]$ per piece)
3. Up to three $18\,[\mathrm{kg}]$ sandbags (note: sandbags lack handles).

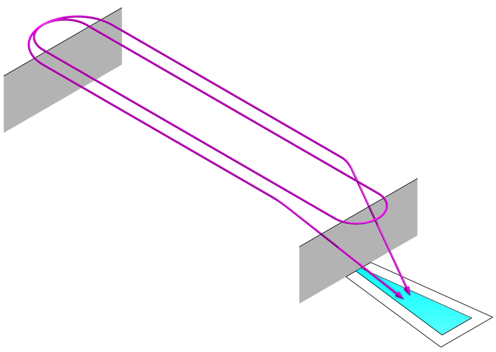

Figure 2.1: Flight profile of the Productivity mission and OZ (gray projections represent the end line and baseline)[1]

Table 2.1: Operation zone ’The Depot’ characteristics

Operation Zone ’The Depot’	
Surface type	Hard
Surface shape	Trapezoid
Surface dimensions	$30\,[\mathrm{m}] \times (1.5\,[\mathrm{m}] - 9\,[\mathrm{m}])$

2.1.2. Adversity Mission

The Adversity mission evaluates the flyer's capability to take off and land under challenging conditions. This mission requires the flyer to navigate through five distinct Operation Zones, each with specific requirements and constraints detailed in Table 2.2. The primary objective is to complete the course in the shortest possible time, with a maximum allowable duration of 30 minutes [1].

Table 2.2: Operational zones of the Adversity mission characteristics

Operation Zone 'The Base'	
Surface type	Hard
Surface shape	Rectangle
Surface dimensions	7.6 [m] $\times$ 15 [m]
Operation Zone 'The Pit'	
Surface type	Loose dry sand
Surface shape	Rectangle
Surface dimensions	3.7 [m] $\times$ 3.7 [m]
Condition	Low visibility
Operation Zone 'The Hill'	
Surface type	Elevated inclined carpeted platform
Surface shape	Square
Surface dimensions	3.4 [m] $\times$ 3.4 [m] at 12° incline
Operation Zone 'The Flood'	
Surface type	Wet floor
Surface shape	Circle
Surface dimensions	7.3 m diameter, 0.5 m deep pool
Conditions	4 mm/hr rainfall
Goal	Touch or pop balloon floating on the pool surface with 1.8 m moving radius
Operation Zone 'The Tornado'	
Surface type	Hard surface
Surface shape	Square
Surface dimensions	4.6 [m] $\times$ 4.6 [m]
Conditions	Strong, non-uniform wind currents, no closer than 5.5 [m] from the center of the zone
Operation Zone 'The Unknown'	
Surface type	Hard surface
Surface shape	Rectangle
Surface dimensions	18 [m] $\times$ 7.6 [m]
Conditions	Obstacles up to 0.9 [m] tall, not in direct view of the operating crew

2.1.3. Maneuvering Mission

The Maneuvering mission assesses the flyer's capability to navigate through confined spaces and avoid obstacles, as illustrated in Figure 2.2. This figure outlines the Operation Zones (OZ) and the associated flight profile, emphasizing the sequence of tasks the flyer must complete. The mission begins with navigating around obstacle 1, a vertical pylon, while maintaining an altitude of at least 15 m above ground level (AGL) as the flyer passes. Next, the flyer must maneuver around obstacle 2, another vertical pylon, keeping below 11 m AGL while passing between obstacles 2 and 4.

The mission continues with the flyer negotiating obstacle 3, a 15 m high virtual wall, either by flying around or over it, before maneuvering around obstacle 4 in a manner similar to obstacle 2. This challenging obstacle course spans a distance of 69 to 99 meters, requiring precise control and agile handling. Furthermore, the mission is divided into two distinct Operation Zones, as detailed in Table 2.3, with performance evaluated based on the fastest completion time [1].

Table 2.3: Operational zones of the Maneuvering mission characteristics

Operation Zone 'The Base'	
Surface type	Hard
Surface shape	Rectangle
Surface dimensions	7.6 [m] $\times$ 15 [m]
Operation Zone 'The Spot'	
Surface type	Hard
Surface shape	Rectangle
Surface dimensions	2.4 [m] $\times$ 2.4 [m]
Entrance	8.5 [m] wide by 9 [m] high gate with threshold 1.2 m from one edge
Condition	May be shielded by structures designed to degrade GNSS quality

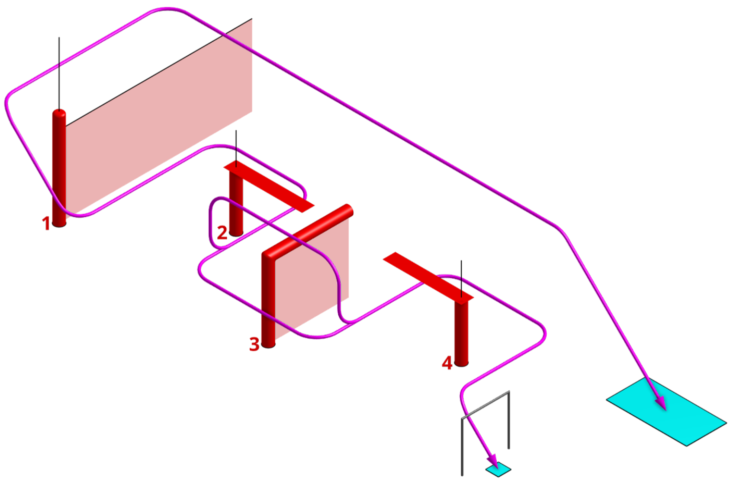

Figure 2.2: Flight profile of the Maneuvering mission including obstacles and operation zones[1]

2.2. Primary and Secondary Requirments

This section outlines the primary and secondary requirements, as presented in Table 2.4, derived from the competition's mission profiles, operational guidelines, and additional rules as presented in the GoAER competition [1]. The primary requirements represent the essential criteria that the aircraft and team must fulfill to successfully achieve the competition's objectives. These are directly tied to mission success and scoring metrics, including payload ferrying, maneuverability, and adaptability to adverse conditions.

The secondary requirements serve as supplementary criteria that enhance overall performance, safety, and compliance. These include operational constraints, deployment capabilities, and design considerations that improve mission feasibility and efficiency. Together, the primary and secondary requirements provide a structured framework for guiding system design, operational planning, and performance evaluation throughout the competition.

Although the GoAERO competition rulebook [1] defines key elements such as payload requirements, mission descriptions, ranking methodology, and implied dimensional constraints, no explicit performance or operational requirements are provided. To address this gap, key parameters are systematically identified and analyzed in Chapter 5, including overall performance constraints. This approach ensures that the necessary functions and requirements are defined to meet both operational needs and competitive objectives as implied by the rulebook.

Table 2.4: Primary and Secondary Requirements

Category	**Requirement**
Primary Requirements	
Missions	Perform three missions: Productivity, Adversity, and Maneuvering, each with specific goals and rankings.
Payload	Include a 57 kg manikin ”Alex” as the primary mission payload.
Deployment	Deploy system quickly, adhering to the competition's transport and staging requirements with moving the system at a minimum of 4 km/h on a hard surface.
System Weight	Total system weight includes aircraft, tools, and consumables but excludes transport vehicles and payloads.
Competition Spirit	Adapt to changing conditions, as event parameters may not match pre-event practice scenarios.
Secondary Requirements	
Productivity Mission	Ferry at least 567 kg of payload within 90 minutes; minimize the total system weight.
Adversity Mission	Land and take off from five challenging zones within 30 minutes, ranked by the fastest time.
Maneuvering Mission	Navigate an obstacle course and complete multiple flight legs, ranked by the fastest time.
Payload Handling	Use up to four handlers for Productivity, and up to three for Maneuvering; maintain safe distances from moving systems.
Staging	Prepare for missions within 15 minutes; clear the course within 10 minutes post-mission.
Bonus Points	Earn points for minimal operator inputs, quick deployment, and single-crew operations.
Penalties	Avoid penalties for going out of bounds, unsafe staging, or damaging payloads.
Rank Points	Earn rank points by performance in missions, including completion and bonus points, highest ranked team per mission earns 10 points.
Completion points	Achieve at least 30 points to win the top prize.

3

Literature Review

3.1. History of VTOL

Vertical takeoff and landing (VTOL) aircraft are designed to ascend and descend vertically, requiring minimal space and infrastructure compared to conventional airplanes. This unique capability makes VTOLs highly appealing for military, civilian, and emergency applications, as they can operate in environments where runways are unavailable or prohibitively expensive to construct. Their versatility enables them to land and take off from almost any location, proving invaluable in challenging or remote settings [2].

While VTOL technology has gained significant attention in recent years, the concept itself dates back centuries. The origins of VTOL can be traced to the 15th century, when Leonardo da Vinci conceptualized the ”Aerial Screw,” widely regarded as one of the earliest VTOL designs [3]. However, it would take more than five centuries before the first manned helicopter successfully achieved flight. Since then, technological advancements have revolutionized VTOL capabilities, facilitating a wide array of applications across various domains [4].

Notably, many modern VTOL designs draw upon historical concepts. As Filipenko [5] highlights, so-called ”super-disruptive” innovations often have roots in earlier research, including mid-20th-century NASA studies and World War II-era German prototypes. This historical progression is reflected in the work of Anderson [6], who reported in 1967 that McDonnell Aircraft had tested or proposed over 60 distinct V/STOL (Vertical/Short Takeoff and Landing) configurations, as illustrated in Figure 3.1 by the wheel of “*V/STOL Aircraft and Propulsion Concepts*” [7]. Anderson [6] observed that, for over 25 years, there was a dedicated effort to combine the vertical takeoff and landing capabilities of helicopters with the high-speed cruising performance of conventional aircraft.

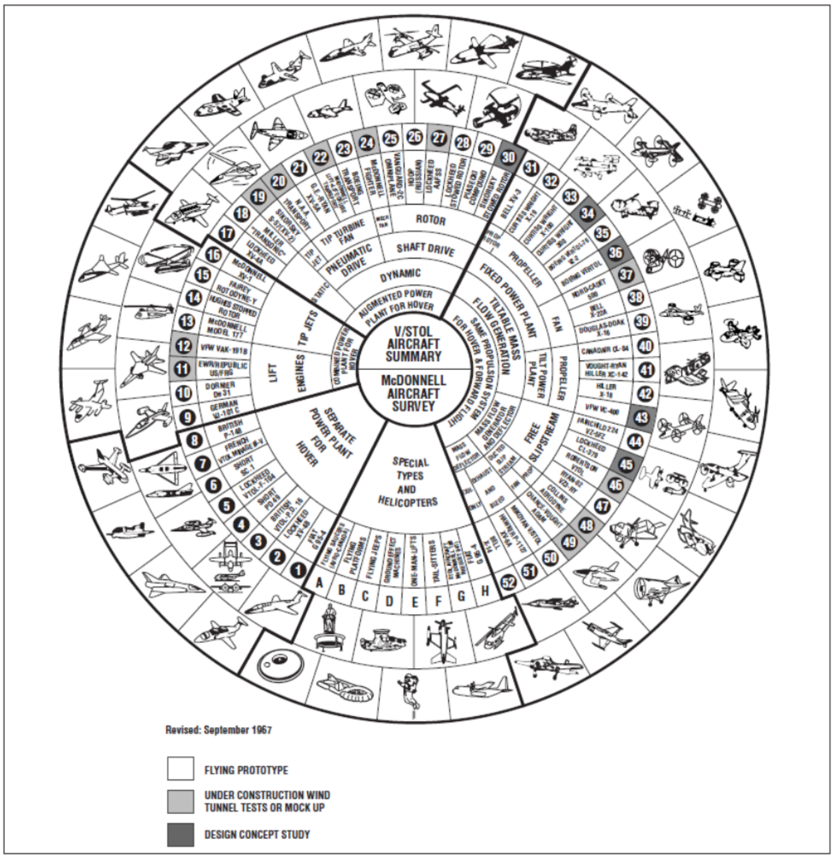

Figure 3.1: Overview of STOL/VTOL concepts compiled in 1967 by McDonnell Aircraft in the wheel of V/STOL Aircraft and Propulsion Concepts [6]

3.2. Modern Day VTOL Architecture

The fundamental principle of flight lies in generating lift to counteract the weight of an aircraft. Traditional Vertical Take-Off and Landing (VTOL) technologies fall into two primary categories: rotorcraft and powered-lift vehicles [2]. Rotorcraft, such as helicopters, rely entirely on their rotor systems for lift generation, distinguishing them from other VTOL configurations. In contrast, powered-lift vehicles utilize fixed wings for lift during horizontal flight while employing alternative mechanisms, such as tilting or vectored thrust, for vertical operations [2].

Recent advancements in the electrification of VTOL solutions have enabled innovative concepts around distributed electric propulsion and introduced a clear distinction from traditional VTOL aircraft. According to the European Union Aviation Safety Agency (EASA) [8], a defining feature of modern eVTOL aircraft is their use of multiple propulsion units to generate lift, unlike conventional rotorcraft. This distinction underscores a critical evolution in the field: while all helicopters are VTOLs, not all VTOLs are helicopters. This differentiation is particularly relevant in the context of the GoAERO competition, which emphasizes the development of an emergency response flyer that surpasses traditional helicopters in cost-effectiveness, facility requirements, and maneuverability in confined spaces [1]. Furthermore, minimizing pilot training requirements is a key priority in GoAERO, making handling qualities and precision essential considerations in the design process.

As shown in Figure 3.1, various VTOL concepts adopt different approaches to achieving vertical take-off and landing. With the growing emphasis on designs based on electric propulsion technology, five prominent VTOL configurations are frequently discussed in the literature and depicted in Figure 3.9. These include rotorcraft and four key eVTOL architectures: multicopter, Lift + Cruise, tilt rotor/wing, and combined thrust. Each configuration has distinct strengths and limitations, making them suitable for specific operational scenarios. It is also important to note that performance factors such as speed and range are inherently interrelated, meaning that improvements in one domain often come at the expense of the other [9].

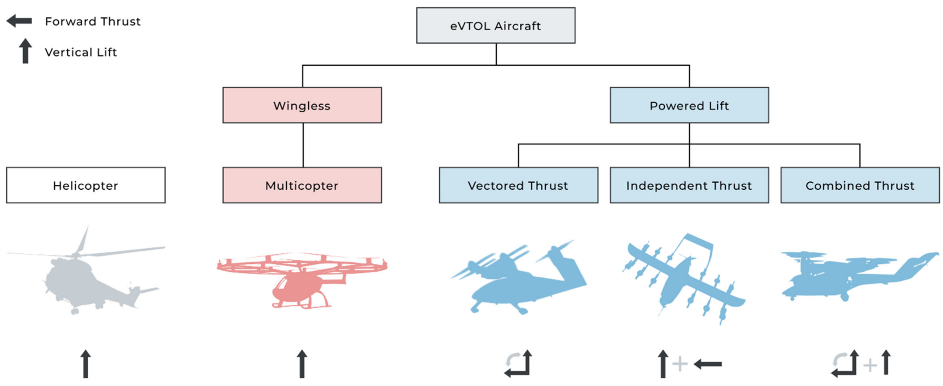

Figure 3.2: Classification of conventional modern VTOL aircraft [10]

3.2.1. Conventional Rotorcraft

As Pavel and Padfield [11] stated, "*Rotorcraft are nowadays reliable flying machines capable of conducting missions impossible to achieve with fixed-wing aircraft.*" Indeed, as discussed in the introduction, VTOL aircraft, such as rotorcraft, already play a key role in emergency response missions. However, this utility comes with significant drawbacks, including high operational and acquisition costs, facility requirements, and extensive pilot training [1]. Moreover, their large rotor sizes hinder their ability to operate effectively in tight quarters, which presents a major limitation in the context of the GoAERO competition requirements.

One of the core challenges posed by GoAERO is the need for a compact aircraft capable of navigating restricted spaces. Specifically, GoAERO requires the aircraft to pass through an 8.5-meter-wide gate, with a 1.2-meter threshold from the edge, as specified for the Maneuvering Mission (Section 2.1.3). This requirement restricts the usable design span to just 7.3 meters.

To illustrate the challenging sizing demands of the GoAERO competition, the Bell 505 Jet Ranger serves as a useful reference aircraft concerned with dimensional sizing as this is promoted by Bell Helicopter as "the only HEMS-capable short light single aircraft with the speed and range to aid global communities and save lives" [12]. However, as depicted in Figure 6.3, the rotor span of the Bell 505 exceeds the GoAERO size limit by nearly four meters, rendering it unsuitable for the competition's spatial restrictions.

Even the CFX-XE, a single-seat light helicopter known as the Mosquito and often regarded as a benchmark in its class, has a rotor span of 7.12 meters. While it narrowly complies with GoAERO's size requirements, this comparison underscores the inherent limitations of conventional rotorcraft in achieving a compact design without sacrificing performance. These constraints highlight the need for innovative approaches to eVTOL design to meet the competition's strict spatial and performance criteria.

Reducing rotor size to meet these constraints poses a significant challenge. Rotor size is directly related to lift efficiency, stability, and handling qualities. Larger rotors offer better lift and are crucial for effective hover and maneuvering, but they also increase the aircraft's footprint, making them unsuitable for confined environments. Thus, the performance trade-offs inherent in conventional rotorcraft design make it difficult for these aircraft to satisfy the GoAERO competition's requirements, necessitating the exploration of alternative VTOL configurations.

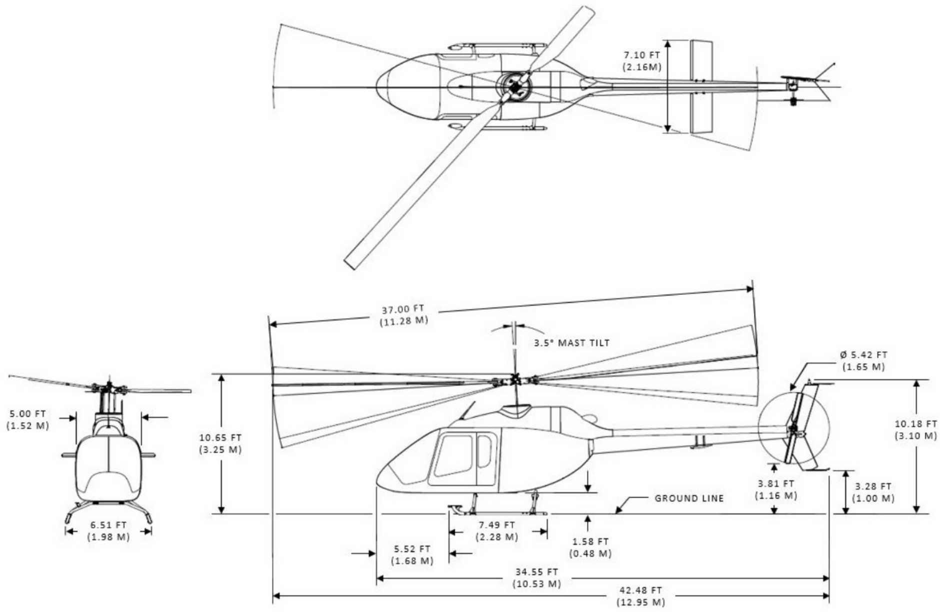

Figure 3.3: Bell 505 dimensional schematic drawing [12]

3.2.2. Wingless eVTOL

Wingless eVTOL designs generate both vertical lift and forward thrust exclusively through their propulsion systems, eliminating the need for wings or lifting surfaces. These configurations, particularly multirotor designs, are distinguished by their simplicity and versatility. However, a significant challenge lies in their high energy consumption. Because vertical lift must be sustained by the propulsion system throughout all phases of flight, wingless eVTOLs require considerable power, making battery energy density a critical determinant of performance and range [10].

The multirotor is one of the most common wingless eVTOL configurations. It employs multiple propulsion units to provide the degrees of freedom needed for precise maneuvering. Multirotors excel in vertical operations such as takeoff, landing, and hovering due to their low disc loading, which enhances efficiency during hover and low-speed maneuvers [9]. This makes them ideal for scenarios requiring precise control, such as urban operations or emergency response. However, the absence of lifting surfaces significantly compromises cruise efficiency, leading to higher energy consumption during forward flight compared to VTOL designs incorporating wings.

The simplicity of the multirotor design lies in its reliance solely on electric motor control for thrust generation and maneuvering. Unlike other VTOL configurations, multirotors do not require control surfaces, wings, or tractor/pusher propellers to maintain flight. Instead, they achieve stability and control in all flight phases by modulating the differential thrust of their multiple rotors [13].

Table 3.1 presents the relative performance of multirotor and tilt-wing/tilt-rotor designs, using the performance of the Lift + Cruise configuration as the baseline for comparison. The table indicates that multirotors generally consume more power during cruise than Lift + Cruise configurations but require less power during hover. This trade-off often leads to a reduced overall range and speed, making multirotors less suitable for long-distance or high-speed operations.

Table 3.1: Main advantages and drawbacks of different e-VTOL aircraft types [13]

Aircraft Type	Power Consumption in Cruise	Power Consumption in Hover	Complexity	Noise in Hover	Range and Speed	Internal Comfort
Lift+Cruise	Baseline	Baseline	Baseline	Baseline	Baseline	Baseline
Multi-rotor	Higher	Lower	Lower	Lower	Lower	Lower
Tilt-wing/rotor	Lower	Higher	Higher	Higher	Higher	Higher

3.2.3. Powered Lift eVTOL

As previously mentioned, powered-lift VTOLs incorporate additional lifting surfaces, such as wings, which allow them to perform similarly to conventional fixed-wing aircraft during horizontal flight. This makes powered-lift configurations significantly more efficient for extended-range missions compared to wingless eVTOLs [10]. The added lifting surfaces reduce the reliance on propulsion systems for generating lift during cruise, thereby improving energy efficiency and increasing range.

However, these benefits come with trade-offs. The incorporation of wings and other aerodynamic structures results in a more complex design, which introduces additional weight, structural challenges, and aerodynamic considerations. This complexity, along with the associated design and maintenance costs, makes powered-lift VTOLs more suitable for medium- to long-range missions, where their superior energy efficiency can be fully leveraged [10]. In short-range operations, the increased complexity may not justify the performance gains over simpler, wingless VTOL designs.

Lift + Cruise eVTOL

The Lift + Cruise concept integrates a multicopter for vertical takeoff and landing (VTOL) with a conventional fixed-wing aircraft for efficient cruising. This configuration employs dedicated propulsion systems for both cruise flight and vertical operations, enabling each system to operate in its most effective state. As Finger et al. [14] notes, "*it is the easiest way to give a fixed-wing aircraft VTOL capabilities since each system is decoupled and used in its most effective state*". This design leverages the cruise efficiency of fixed-wing flight while maintaining the simplicity and effectiveness of a multicopter for vertical operations.

Despite these advantages, the Lift + Cruise design has notable drawbacks. The propulsion units responsible for vertical flight become "dead weight" during horizontal flight, increasing overall mass and aerodynamic drag, as highlighted by Ugwueze et al. [10]. To minimize these inefficiencies, vertical lift propellers are typically designed with fewer blades and shorter chords, reducing drag during cruise. Additionally, the propellers are often locked parallel to the slipstream during horizontal flight to further enhance aerodynamic efficiency.

However, these smaller propellers for vertical lift introduce challenges, particularly related to noise generation. Higher disc loading and increased blade tip velocities exacerbate noise issues, making noise reduction a critical design focus for Lift + Cruise configurations. Hover performance can also be impacted, emphasizing the need for careful optimization to balance efficiency, noise, and performance during takeoff and landing [9].

Vectored Thrust eVTOL

Vectored thrust concepts address the limitations of other VTOL designs by employing a single propulsion system capable of supporting both vertical and horizontal flight. This is achieved by vectoring the thrust or repositioning the propulsion system to transition seamlessly between flight modes. The tilt concept, a prominent variation, manifests in several forms: rotating only the propulsion units, tilting the entire wing, or redirecting the thrust flow.

While vectored thrust systems offer exceptional versatility by integrating vertical and horizontal flight capabilities into a single propulsion mechanism, they are not without significant challenges. The transition phase between vertical and horizontal flight is particularly demanding, as it requires precise control to achieve smooth and efficient dynamics. Moreover, the mechanical and control systems necessary for thrust vectoring introduce added complexity, which has been an enduring engineering hurdle since the 1960s [10].

Combined Thrust eVTOL

A solution to mitigate the 'dead weight' problem in Lift + Cruise configurations and reduce the complexity of the vectored thrust transition phase is the combined thrust concept. This approach combines elements of both configurations by allowing some propulsion units to be vectored while others remain stationary during vertical flight. This ensures that all propulsion units are utilized during vertical take-off and landing, while reducing the number of unused units during horizontal flight, thus improving overall efficiency [10].

3.2.4. Current VTOL Concepts

Beyond the conventional rotorcraft and powered-lift aircraft currently in use, there has been growing interest in newly developed and innovative VTOL concepts. Given the wide range of VTOL designs emerging today, it would be highly time-consuming to manually evaluate each concept. As a result, a thought experiment was conducted using artificial intelligence (AI), a key trend in modern technology. Specifically, ChatGPT 3.0 [15] was utilized to generate a list of VTOLs and rotorcraft with a total width not exceeding the 7.3 meters specified by the GoAERO competition. The AI provided the following response: "*Sure, here's a list of eVTOLs (Electric Vertical Takeoff and Landing aircraft) or rotorcraft with a total width not exceeding 7.3 meters:*"

ChatGPT 3.0 response

1. Lilium Jet
2. Joby Aviation
3. Volocopter 2X
4. EHang 216
5. Bell Nexus
6. Airbus CityAirbus
7. AeroMobil
8. Jaunt Air Mobility
9. Hyundai S-A1
10. Kitty Hawk Heaviside
11. Overair
12. Vahana by A³ by Airbus
13. Opener BlackFly
14. Vertical Aerospace Seraph
15. Archer Aviation
16. EmbraerX

Table 3.2: Actual width parameters of the proposed eVTOLS

Width constraint complient eVTOLS	Width
EHang 216	5.61 [m]
Kitty Hawk Heaviside	6 [m]
Vahana A³ by Airbus	6.25 [m]
Vertical Aerospace Seraph	6 [m]
Opener BlackFly	4.1 [m]
Non width constraint complient eVTOLS	Width
Lilium Jet	13.9 [m]
Joby Aviation	11.89 [m]
Volocopter 2X	9.15 [m]
Bell Nexus	15.24 [m]
Airbus CityAirbus	12 [m]
AeroMobil	8.8 [m]
Jaunt Air Mobility	15.24 [m]
Hyundai S-A1	15 [m]
Archer Aviation	14.6 [m]
EmbraerX	11 [m]

Upon verifying the AI's output, it was found that only six of the suggestions actually met the width requirement of 7.3 meters. These six VTOL options are listed in Table 3.2, alongside others that do not meet the competition's specifications. This experiment revealed two interesting insights with at first AI is not to be trusted yet and second, many of the most promising current VTOL concepts are not designed with a small enough planform to meet GoAERO's specific needs. This can be attributed, in part, to the primary missions of these VTOLs, which are often focused on passenger transport, as seen in the case of Urban Air Mobility solutions. Additionally, it is important to note that AI, in its current form, is limited in its ability to produce novel solutions, as the models are trained on existing information.

However, a valuable insight emerged from examining VTOL concepts with smaller planforms: these designs often prioritize configurations such as Lift + Cruise or multirotor setups to achieve the necessary compact size. This design focus aligns closely with the GoAERO competition's requirement for a VTOL aircraft capable of operating effectively in tight quarters.

For instance, Figure 3.4 depicts the Vahana Alpha Two concept by Airbus, designed for short-range advanced air mobility with seating for one person. Similarly, the Kittyhawk concept, shown in Figure 3.6, is a single-seat eVTOL; however, it differs from the Vahana by employing a tiltrotor configuration instead of a tilt-wing design. In contrast, the Pivotal concept, shown in Figure 3.5, combines fixed wings with rotors, rotating the entire aircraft's attitude to generate lift during cruise via its wings.

To illustrate multirotor platforms, the Vertical Aerospace VA-X2 (Figure 3.7) and Ehang's eVTOL (Figure 3.8) provide examples of human transport concepts. The VA-X2 is larger, with a higher payload capacity, while both concepts demonstrate variations in rotor count and positioning, showcasing different approaches to achieving multirotor functionality.

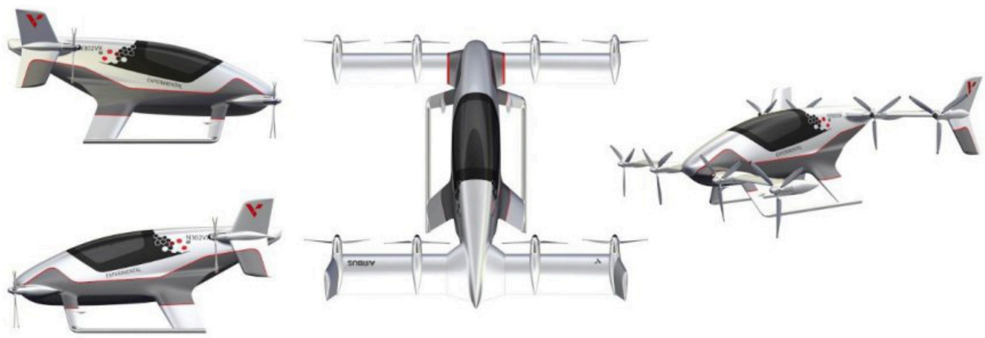

Figure 3.4: Vahana Alpha Two concept by Airbus [16]

Figure 3.5: Pivotal Helix concept [17]

Figure 3.6: Kittyhawk concept [18]

Figure 3.7: Vertical Aerospace VA-X2 concept [19]

Figure 3.8: Ehang's eVTOL concept [20]

3.3. VTOL Propulsion Systems

While traditional VTOL configurations utilize fully fossil fuel based propulsion systems most current VTOL concepts utilize fully electric propulsion, largely due to its relative simplicity and the innovative possibilities enabled by distributed electric propulsion (DEP). According to Shamiyeh [21], DEP expands the design space for VTOL aircraft by reducing the complexity and effort required for vertical take-off and landing operations. This simplicity has positioned fully electric systems as a preferred choice for many eVTOL developers. It is important to note that while innovations are being explored using hydrogen as a potential solution in the ongoing energy transition, the GoAERO competition explicitly prohibits the use of hydrogen as a fuel source [1].

However, the limitations of fully electric propulsion, particularly for mid-range applications, have brought hybrid solutions into focus. A study on a hybrid-electric tilt-wing aircraft for Emergency Medical Services (EMS) highlights the constraints of current battery technology in achieving the required energy density for fully electric systems [22]. Hepperle [23] further argues that the low energy density of current batteries makes fully electric propulsion impractical for applications demanding extended range or high payload capacity. Similarly, Barra et al. [22] emphasize that hybrid-electric configurations provide a more viable alternative, combining the benefits of electric propulsion with the extended range and flexibility of conventional power sources.

NASA's research into Advanced Air Mobility (AAM) aircraft, as part of the Revolutionary Vertical Lift Technology project, supports the viability of hybridized systems over fully electric alternatives. This project explores VTOL concepts for emerging aviation markets, with several designs illustrated in Figure 3.12 [24]. A key takeaway from NASA's research is that high battery energy density is critical for developing competitive electric VTOL aircraft. However, even with cutting-edge battery technology, all-electric systems are significantly heavier than hybrid or turbo-electric alternatives, as shown in Figure 3.9. This weight disparity makes hybrid-electric and turbo-electric propulsion more practical options for Advanced Air Mobility applications [21].

Hybrid-electric systems offer a promising pathway toward greater electrification in aviation. These systems pair the efficiency and reduced emissions of electric propulsion with the extended operational capabilities of conventional propulsion systems. However, the literature does not address the areas like hovering performance, disk loading, and system complexity for hybrid-electric VTOL configurations. The lack of detailed comparative data on these factors leaves gaps in the understanding of their overall performance impact.

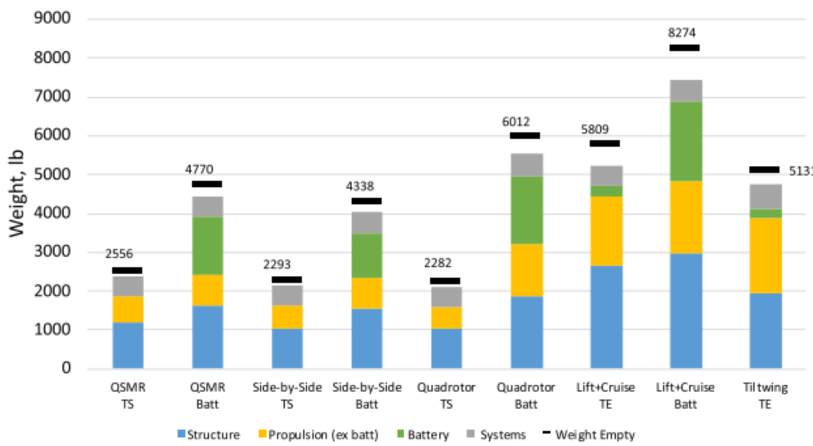

Figure 3.9: Structure, propulsion and systems components of the empty weight; (TS = turboshaft, TE = turbo-electric, QSMR = Quiet Single Main Rotor Helicopter) [24]

Hybrid Propulsion Configurations

Several hybrid propulsion configurations have been explored, each with distinct advantages and trade-offs. For a series configuration, the turbine powers a generator, which then provides electrical power to the propulsion system, eliminating the need for a mechanical link. This simplifies propulsion control but reduces overall efficiency due to energy conversion losses [25].

Concerned with the Side-by-Side Configuration, both the turbine and generator supply power directly to the propulsion system via a mechanical link. This configuration offers redundancy and improved efficiency but increases design complexity and weight due to the mechanical coupling [25].

Combining the systems, resulting in the Combined Series-Parallel Configuration, this hybrid approach uses a planetary gear system to distribute power between the combustion engine and electric motor, optimizing performance while adding mechanical and control-system complexity [25].

3.4. VTOL Cost Analysis

As outlined by the GoAERO competition, the solution for emergency response (ER) situations must offer a more competitive alternative to conventional helicopters in terms of both acquisition and operational costs. Concerned with the acquisition cost within the aircraft industry, Cakin and Aydogan [25] make the overall notion of lower aircraft weight generally leading to reduced costs. However, this assumption is further nuanced in the research on Advanced Air Mobility (AAM) aircraft by Johnson and Silva [24], who emphasize that the purchase cost of an aircraft is largely determined by its empty weight, installed power, complexity, and the costs associated with electronic systems.

A significant portion of operating costs comes from fuel or energy consumption. For missions with short enough ranges to make electric propulsion viable, energy costs are typically lower for all-electric configurations, even though these aircraft may be heavier. However, it is important to consider that electric propulsion systems often bring along higher costs due to the need for battery replacement, which can be a major driver of overall expenses.

A study by Mihara et al. [26] compared multicopter, tilt-wing, and vectored thrust VTOL configurations in a cost analysis for Japan's Air Ambulance System. The study projected that, overall, eVTOL concepts could reduce the total operating cost per seat mile by 26% compared to conventional helicopters. However, battery replacement costs accounted for approximately 50% of the direct operating costs for all configurations, underscoring the significant impact of battery technology on total expenses. Given the prominence of battery replacement costs, hybrid systems could offer a more cost-effective alternative by reducing the reliance on batteries.

The study also provides insights into the costs of different configurations, including fixed-wing designs like the Lilium Jet and Vahana, as well as a multirotor configuration represented by the Volocopter. Among these, only the Volocopter demonstrated a lower cost than the R22 Robinson helicopter, referenced to be around 200.000 USD, though it came at the expense of reduced range compared to the other configurations. While the study is based on a highly assumption-driven cost model, the comparisons between these configurations offer valuable insights into overall cost differences across VTOL platforms.

Another critical factor in cost-effectiveness is the development cost of the aircraft. As will be discussed in more detail in Section 3.7, addressing handling qualities (HQ) early in the design phase is crucial for ensuring a cost-effective solution. If the HQ levels are not adequately addressed, additional flight tests, control systems, and equipment modifications may be required, leading to higher project costs, delays, and increased manpower requirements [27].

3.5. VTOL Performance Analysis

To evaluate the performance of various VTOL configurations, key metrics such as disc loading and cruise speed are commonly used. As pointed out in a guide to Vertical Take-off and Landing [2], disc loading, defined as the aircraft's weight divided by the total rotor disc area, is a significant indicator of hover lift efficiency. Typically, a higher disc loading results in reduced hovering efficiency, and higher downwash speeds, which describe the airspeed experienced around the aircraft. This factor is particularly relevant for urban operations, where landing sites might be near people or in rescue missions involving loose debris or water. Although noise is not a concern in the GoAERO competition, downwash remains a critical factor to consider.

When examining conventional VTOL designs from the 1970s, helicopters generally have the lowest disc loading due to their large main rotors, as shown in Figure 3.10. However, the figure also highlights the relationship between conventional designs and newer VTOL models. It is important to note that these figures assume the propulsion systems are providing maximum power output, although the actual power required for hovering is often much lower [5]. A performance comparison, visualized by normalized estimates of disc loading and cruise speed in Figure 6.22, shows that fixed-wing VTOL designs tend to have higher cruise speeds at the cost of higher disc loading.

Despite the rough estimation of performance metrics, using a consistent method across different VTOL concepts still provides valuable insights into their relative performance. As demonstrated in Figure 3.10 and Figure 6.22, multirotor configurations exhibit the most favorable disc loading and hover efficiency, while VTOL designs focused more on cruise phase rather than vertical lift generally perform worse than both multirotor configurations and conventional helicopters. Specifically, as cruise speed increases, disc loading tends to decrease, reflecting a trade-off between hover efficiency and cruise performance.

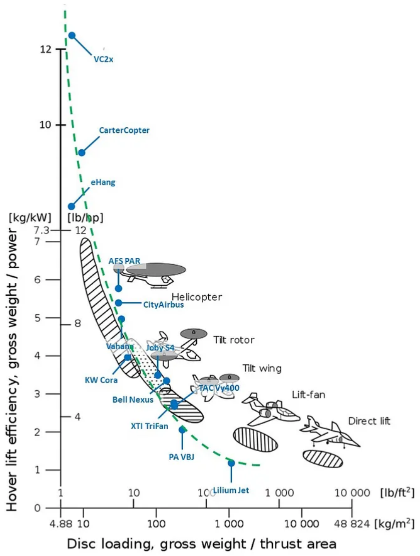

Figure 3.10: Disc loadings and hover lift efficiencies of VTOL concepts [5]

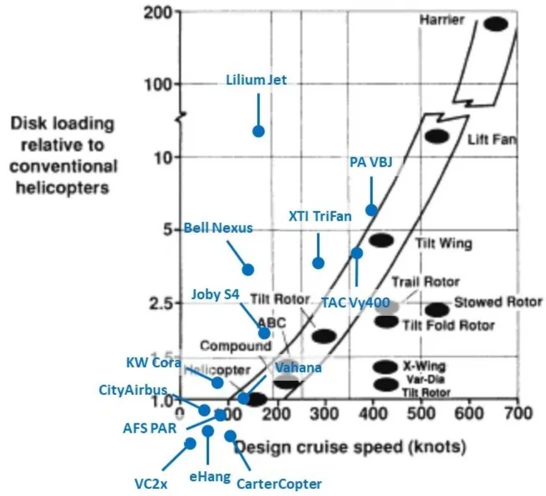

Figure 3.11: Disc loading vs speed of VTOL concepts [5]

Further insights into the performance of various VTOL configurations are provided by Johnson and Silva's study on UAM concepts [24] as shown in Figure 3.12. Their research shows that multirotor configurations consistently outperform other designs in terms of disc loading, as summarized in Table 3.3. Notably, Lift + Cruise and tilt-wing configurations exhibit worse disc loading, partly due to their higher gross weight. On the other hand, the quadrotor configuration demonstrates superior disc loading compared to conventional rotorcraft, with the lowest installed power requirements and competitive design gross weight.

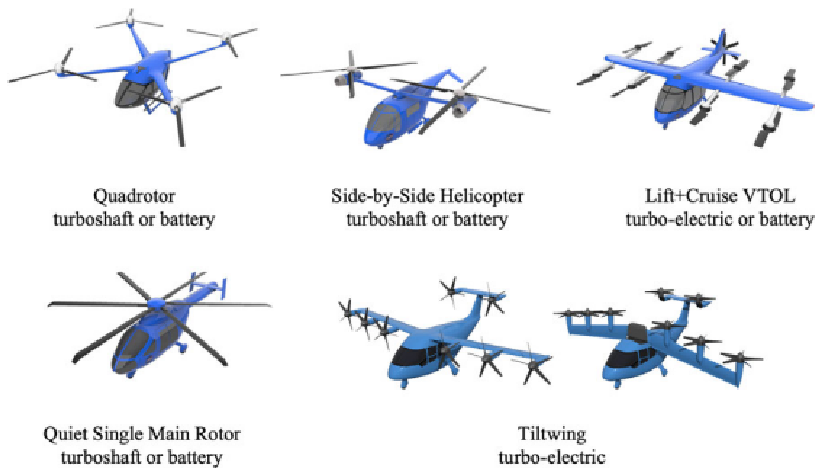

Figure 3.12: NASA UAM aircraft concept [24]

As discussed in Section 3.2 and Section 3.3, Lift + Cruise aircraft typically result in the heaviest configurations for the same mission when compared to other eVTOL designs. This is primarily due to increased structural and propulsion system weight, making all-electric Lift + Cruise aircraft the heaviest option.

While Lift + Cruise configurations offer higher cruise efficiency, this advantage does not fully compensate for the weight penalty. Additionally, the extra weight and drag from the rotor-supporting structures further reduce the potential efficiency gains, shifting the optimal solution away from pure cruise performance. This observation is consistent with findings on the empty weight of concept vehicles, where the Lift + Cruise configuration, with its eight lifting rotors, exhibits higher structural weight despite its superior cruise efficiency [24].

Table 3.3: Characteristics of NASA UAM concept vehicles [24]

Aircraft	QSMR		Side-by-Side		Quadrotor		Lift+Cruise		Tiltwing
Propulsion	TS	E	TS	E	TS	E	TE	E	TE
Payload [lb]	1,200	1,200	1200	1,200	1,200	1,200	1,200	1,200	1,200
Range [nm]	75	75	75	75	75	75	75	75	75
Rotor radius [ft]	17.7	23.3	10.8	15.9	9.1	13.8	5.0	5.0	3.6
Disk loading lb/ft^2	4	3.5	5	4	3.5	3	11.6	15.1	20
Tip speed [ft/sec]	450	500	450	450	450	450	450	550	550
L/D_e = WV/P [-]	5.4	6.0	5.9	7.2	4.9	5.8	8.5	7.9	8.6
V_{br} [kt]	100	84	103	89	112	91	81	83	148
Power [hp]	2x241	2x272	2x234	2x234	2x294	4x181	8x126	8x189	8x244
DGW [lb]	3,951	5,980	3,665	5,547	3,678	7,221	7,271	9,482	6,584
Empty weight [lb]	2,556	4,770	2,294	4,338	2,282	6,012	5,809	8,274	5,130
Structure [lb]	1,190	1,616	1,054	1,533	1,033	1853	2,670	2,973	1954
Propulsion [lb]	685	804	558	813	567	1,375	1,772	1866	1918
Battery [lb]	0	1,502	0	1,150	0	1,742	254	2058	244

In another study on performance trade-offs between VTOL and cruise efficiency, the effects of range and vertical climb requirements were explored [21]. For a design mission with a required vertical climb altitude of 300 [m], the multicopter configurations designed for a range of 25.7 [km] showed higher transport energy efficiency for shorter distances compared to Lift + Cruise VTOLs. However, Lift + Cruise configurations only demonstrated comparable or better efficiency at cruise distances beyond 26 [km]. The required vertical climb height has a more significant impact on the sizing of Lift + Cruise configurations, though these designs excel in longer-distance flights due to their higher cruise speeds.

As a result, performance trade-offs between hover efficiency and cruise capability remain a defining characteristic of VTOL design optimization. Lift + Cruise configurations for example are better suited for longer distances, achieving higher cruise efficiency and speed despite their structural weight penalties, while multicopters excel in hover performance and shorter-range missions, offering superior transport energy efficiency for vertical maneuvers.

3.6. Multirotor Configuration

Multirotor aircraft are most commonly associated with small-scale UAVs, such as drones used for cinematography, surveillance, hobbies, and package delivery. In these applications, any configuration can achieve flight with sufficiently capable controllers. However, as noted by Kotarski et al. [28], multirotor systems are inherently unstable, nonlinear, and multivariable from a control perspective, necessitating the use of robust flight controllers to maintain stability.

Conventional multirotor designs typically feature an even number of rotors arranged in a single plane. These designs are underactuated and exhibit strong coupling between translational and rotational dynamics, posing challenges for missions requiring precise or complex movements, particularly those involving changes in orientation. Despite these challenges, multirotors are often favored for their mechanical simplicity, as they rely on fewer moving parts compared to other VTOL configurations.

One of the simplest configurations is the quadrotor, which uses four rotors to provide both lift and control moments. Its mechanical simplicity is complemented by relatively straightforward system dynamics compared to more complex designs, such as those employing thrust vectoring [29]. However, this simplicity does not extend to all designs with fewer rotors. For example, tri-rotor systems introduce greater dynamic complexity, despite having fewer rotors, due to the need for more intricate control mechanisms to stabilize flight.

While increasing the number of rotors may intuitively seem to enhance lift for a given platform size, this approach is not without trade-offs. Adding rotors can increase static performance, such as total lift capacity, but often at the expense of dynamic performance due to the added weight and increased inertia. Studies comparing multirotor UAVs have demonstrated that while additional rotors improve static performance, the benefits diminish when dynamic performance is considered [30]. As a result, increased rotor count can negatively impact agility and energy efficiency if the system is not properly optimized.

Rotor Count and Control Effort

Determining the optimal number of rotors for a multirotor configuration involves balancing lift, stability, energy efficiency, and control effort. A study on control effort during accurate trajectory tracking [29] compared various multirotor configurations, examining how well each could follow a trajectory with minimal error. Despite differences in geometry and behavior, the trajectory outputs across configurations were similar as long as actuator limits were not exceeded.

The study assessed control effort both instantaneously and over the entire maneuver, revealing that systems remained continuous and linear in closed-loop control under comparable conditions. Interestingly, while the magnitudes of control signals were similar for quadrotor and octorotor configurations, the octorotor consumed significantly more power [29]. This indicates that energy consumption increases almost linearly with the number of rotors, underscoring the importance of design optimization to mitigate weight and power penalties.

Yaw control, however, is a notable challenge in multirotors, as the yawing moment is typically smaller than the moments responsible for roll and pitch. Yaw is controlled by the net torque differential between counter-rotating rotors, making it particularly susceptible to rotor limitations during large yaw commands.

Examining yaw performance across different configurations during the same maneuver highlighted these challenges. For both the quadrotor and hexrotor, yaw commands remained within input limits throughout the maneuver. In contrast, the octocopter exhibited dynamic discontinuities due to input saturation. This behavior arose from the larger moment of inertia in the octocopter, which requires a greater yawing moment for equivalent commands. Despite having more rotors to generate torque, the higher inertia proved to be a limiting factor, especially during demanding yaw maneuvers [29].

3.7. Handling Qualities

The definition of Handling Qualities, as given by Cooper and Harper [31], refers to ”*those qualities or characteristics of an aircraft that govern the ease and precision with which a pilot can perform the tasks required in support of an aircraft role*.”. As suggested by their definition, which emphasizes the pilot’s role, handling qualities incorporate a degree of subjectivity. Therefore, to quantify handling qualities (HQ), the focus extends to key attributes such as the aircraft’s maneuverability and agility. Maneuverability is defined as ”*the ability to change the flight path of a vehicle through the application of acceleration*”, while agility is ”*the rate of change of maneuverability, or the quickness with which different maneuver states can be entered or exited*” [32]. HQ thus encompasses a range of aircraft characteristics, influenced by the following key factors:

1. **Flight dynamics**: This refers to how the aircraft responds to control inputs and external disturbances [33].
2. **Control system design**: The design of control systems, including control laws that govern the system’s behavior, plays a critical role in HQ [34].
3. **Pilot-vehicle interface**: This concerns how information is presented and communicated to the pilot [33].
4. **Vehicle design**: Factors such as size, weight, shape, and configuration influence HQ [33].
5. **Environmental conditions**: External factors such as wind and turbulence also affect HQ [33].

HQ Evaluation

As noted by Gibson [35], handling qualities (HQ) are primarily influenced by aerodynamic stability and control. However, with the advent of fly-by-wire systems, control augmentation has become increasingly significant, often introducing inherent challenges to achieving optimal handling qualities. This shift aligns with the earlier observation that controllers play a central role in multirotor designs, where control system design frequently takes precedence over vehicle design considerations.

Traditionally, HQ evaluations were conducted during the flight testing phase, as they were often considered secondary objectives in the design process. Yilmaz et al. [27] highlights this with noting that HQ assessments typically occurred post-design, making them reactive rather than proactive. Similarly, Pavel [11] points out that in earlier helicopter designs, HQ considerations were often neglected during the design phase, reflecting a broader industry trend at the time.

Despite their critical role in overall mission success, HQ has frequently been overlooked during the early stages of design. Typically, HQ assessments are conducted only after preliminary designs have been finalized, once the majority of specifications and configurations are locked in. If deficiencies in handling qualities are identified at this stage, costly and time-intensive interventions such as additional flight tests, controller refinements, and structural modifications become necessary [27].

To mitigate these challenges, recent research advocates for the integration of HQ evaluations early in the design process, facilitated by multidisciplinary design approaches. Yilmaz et al. [27] and Pavel [11] emphasize that incorporating HQ assessments during the initial design phase significantly increases the likelihood of producing aircraft with superior handling qualities. Pavel, in particular, stresses the importance of a multidisciplinary approach to improving HQ throughout the development process, ensuring a balance between mission requirements, vehicle design, and control system performance.

4
Research Objective

This thesis aims to contribute to the development of an innovative emergency response flyer for the GoAERO competition. The competition demands a single-occupant, affordable, robust, and effective VTOL aircraft capable of operating in challenging environments. These environments impose unique requirements across three critical mission profiles, i.e. Productivity, Adversity, and Maneuvering, emphasizing endurance, stability, handling qualities (HQ), and overall performance. The primary research objective is to establish a preliminary design framework that meets these requirements while surpassing the performance of existing VTOL concepts through technological innovation and design optimization.

Research Platform

As identified in the literature review, current VTOL designs, particularly fully electric configurations, face notable limitations in meeting the stringent demands of the GoAERO competition. These challenges include excessive mass, large size, and suboptimal performance for emergency response scenarios. Key difficulties include achieving efficient hover performance and compactness for rapid deployment.

While Lift + Cruise and combined thrust designs enhance cruise efficiency for longer ranges, they introduce complexity and additional mass, making them unsuitable for the short-range missions prioritized in the GoAERO competition. Vectored thrust designs, while excelling in cruise efficiency, suffer from high mechanical complexity and poor hover performance, conflicting with the competition's emphasis on simplicity and robustness.

In contrast, multirotor configurations offer simplicity and superior hover efficiency, though at the cost of higher power consumption during forward flight due to the absence of lifting surfaces. However, this drawback is less critical for the short-range missions in the GoAERO competition. Furthermore, integrating hybrid propulsion systems into multirotor designs has demonstrated superior performance for short-range operations compared to Lift + Cruise configurations.

Regarding propulsion systems, fully electric designs exhibit inefficiencies during both hover and cruise phases due to battery mass. Moreover, long recharging times hinder rapid mission deployment, further reducing their feasibility for emergency response scenarios. Hybrid propulsion systems emerge as a viable alternative, offering significant reductions in Maximum Takeoff Mass (MTOM), rapid refueling capability, and enhanced mission turnaround times. Hybrid systems have the possibility to improve the payload-to-system mass ratio, a key scoring metric in the GoAERO competition.

Research Gap and Objectives

Existing studies often generalize that increasing the rotor count in multirotor designs leads to mass penalties without exploring the potential for design optimization to mitigate these effects and properly evaluate the HQ benefits of increased rotor counts. Furthermore, HQ incorporation typically occur late in the design process or focus exclusively on closed-loop stability analysis, neglecting intrinsic design characteristics that influence HQ during the early stages of development. This reactive approach frequently results in costly modifications, delays, and suboptimal performance.

To address these gaps, this thesis introduces an "*Optimization framework for design of an hybrid electric vertical takeoff and landing multirotor - Application to the GoAERO competition*". This framework systematically analyzes and optimizes quadrotor, hexarotor, and octorotor configurations to balance rotor count, rotor parameters, system mass and performance. The proposed configurations incorporate a hybrid-electric propulsion system featuring a gas turbine in a series configuration. This innovation eliminates reliance on battery recharging or swapping, enhancing mission reliability, rapid deployment, and overall mass efficiency. Furthermore, the framework emphasizes early-stage HQ assessment to ensure dynamic performance while minimizing design penalties associated with increased rotor counts. As a result, this thesis seeks to address the following primary research question:

> *What are the optimal design parameters that drive handling qualities for a hybrid multirotor emergency response eVTOL in the GoAERO competition?*

By answering this question, the research aims to address key gaps in the literature, provide actionable insights for VTOL design optimization, and contribute to the development of an aircraft that meets the stringent requirements of the GoAERO competition.

Methodology

The literature emphasizes the importance of a multidisciplinary approach in improving the development process, ensuring a balance between mission requirements and vehicle design. MDO fosters innovative solutions by integrating diverse perspectives and expertise. By considering multiple disciplines simultaneously, MDO can exploit their interactions, leading to superior design outcomes—particularly in complex aerospace systems.

As a result, this research employs a Multidisciplinary Design Optimization (MDO) framework to integrate key disciplines, related to aerodynamics, propulsion, structures, and dynamics, into a unified optimization process. The optimization is mass-driven, as minimizing aircraft mass directly correlates with improved dynamic performance and higher rankings in the GoAERO competition, which prioritizes the ferried payload-to-system mass ratio. The optimization results serve as the foundation for evaluating mass increases due to additional rotors and the trade-offs between rotor count and performance. Additionally, the framework examines the impact of hybrid propulsion on overall mass and operational efficiency.

To incorporate handling qualities (HQ) considerations in the early design stages, this thesis integrates eigenvalue analysis to assess eVTOL stability, supplemented by a review of existing literature on HQs for quadrotor, hexarotor, and octorotor configurations. This combined approach offers valuable insights into the relationship between vehicle design parameters, HQs, and overall mission performance, aligning with and expanding upon existing multirotor research.

5

Aircraft Functions and Requirements

5.1. Function and Requirement Mapping

The process of defining the aircraft's functions and requirements starts with systematically mapping key parameters, such as overall performance, payload capacity, crew specifications, and dimensional constraints. This process ensures that all necessary functions and requirements are identified to meet both operational and competitive objectives.

In cases where specific design parameters are not explicitly provided by the GoAERO competition guidelines, competitive benchmarks are established to maintain alignment with industry standards. These benchmarks are drawn from comparable rotorcraft and provide a foundation for ensuring the design's competitiveness. As a result, comparisons are made with the smallest Helicopter Emergency Medical Services (HEMS)-capable rotorcraft, such as the Bell 505 Jet Ranger, which serves as a relevant baseline, as discussed in Section 3.2.1.

5.1.1. Performance Evaluation

Mission Range

As highlighted by GoAERO [1], approximately 4.5 million people in the United States live in "ambulance deserts" i.e. regions where emergency medical services cannot reach residents within 25 minutes. For instance, in Pickens County, Alabama, a single ambulance station in Carrollton, serving 20,000 residents across 900 square miles, operates with just two ambulances [36].

To estimate the mission range, we assume the hospital is centrally located within a circular area covering 900 square miles. The maximum operating distance from the hospital corresponds to approximately 27.25 km. This value aligns with the findings of Mihara et al. [26], who identified a similar maximum operating range of 31 [km] for air ambulance systems in Japan, which is also the distance within which patients must be reached in under 25 minutes.

For the GoAERO competition, the Productivity mission imposes strict endurance requirements. The mission profile involves completing three laps per segment, each including a quarter-mile stretch, alternating between loaded and unloaded trips. The total payload of 567 kg, which is ferried in increments of 144.6 [kg] per trip, results in a total horizontal distance being covered of approximately 19.3 [km]. Although this is shorter than the ambulance desert range, it represents the primary range requirement for the competition at the preliminary design stage.

Mission Altitude

Although GoAERO does not specify mission altitude, insights from Helicopter Emergency Medical Services (HEMS) operations are valuable. According to the North West Air Ambulance Charity [37], typical HEMS cruise altitudes are around 305 meters above ground level (AGL), providing clearance from obstacles such as buildings, power lines, and trees. In more rugged areas like the southern Lake District, altitudes may reach up to 914 meters AGL. As a result, based on these operational insights and a study evaluating helicopter missions [38], a cruise altitude of 600 meters AGL is selected. This altitude strikes a balance between operational performance and safety, accommodating a wide range of terrains.

Rates of Climb and Descent Evaluation
To further define the performance requirements related to climb and cruise rates for effective HEMS missions, Mihara et al. [26] stated that the maximum operating distance of 31 [km] should be covered within 15 minutes of an emergency call. Additionally, to remain competitive with existing HEMS solutions, the climb rate of the Bell 505 Jet Ranger X, approximately 7 [m/s] [39], is adopted as the target.

In an idealized scenario where this climb rate is achieved immediately after takeoff and the descent rate matches the climb rate, the total time required to ascend and descend from a 600-meter cruise altitude is 2.8 minutes. This leaves 12.2 minutes for the cruise segment. At a cruise speed of 231 [km/h] (matching that of the Bell 505), the aircraft can cover the 31 [km] range in approximately 8.5 minutes, leaving 3.7 minutes for activation and contingencies. These calculations confirm that the selected climb, descent, and cruise speed parameters meet the operational requirements for a competitive HEMS mission.

5.1.2. Payload Evaluation

The Productivity mission requires the aircraft to accommodate a variety of payload configurations, as detailed in Table 5.1. Each trip must support a maximum payload of 144.6 [kg], with potential combinations including the ”Alex” manikin (57 [kg], 1.65 meters in length), rebar (1.8-meter lengths), and sandbags (18 [kg] each). The payload compartment must be at least 1.8 meters in length to accommodate the rebar, while still providing enough space for other cargo items. This flexibility is crucial for ensuring the aircraft can handle diverse mission requirements while maintaining operational efficiency.

Table 5.1: Payload specifications

Payload	Amount	Mass	Dimmensions
Alex manikin	1	$57[kg]$	H: $1.65[m]$
#5 Rebar	12	$2.8[kg/piece]$	L: $1.8[m]$, D: $15.875[mm]$ [40]
Sanbags	3	$18[kg/piece]$	$36[cm] \times 66[cm]$ [41]
Total payload	N.A	$144.6[kg]$	N.A

5.1.3. Operational Crew Evaluation

Although GoAERO specifies a single occupant, emergency response missions often require additional personnel, such as a caregiver or other emergency responders. As emphasized by T. Judge in his expert lecture, HEMS missions typically operate with two crew members: one pilot and one caregiver. This division of roles enhances operational efficiency by enabling clear delegation of responsibilities during critical missions.

For the purpose of this design, it is assumed that two crew members, each with a mass of 80 [kg] (including personal equipment), will be onboard. The aircraft must comfortably accommodate the pilot, caregiver, and single occupant, ensuring adequate space and mass distribution to support efficient and safe operations. This consideration is critical for maintaining functionality and ergonomic efficiency during high-stress emergency scenarios.

5.1.4. Dimensional Evaluation

Meeting GoAERO’s maneuverability challenges requires the flyer to navigate through a gate measuring 8.5 meters in width and 9 meters in height, with a 1.2-meter clearance from the edge. Assuming forward motion during navigation, the effective maximum width available for the flyer is 7.3 meters.

Additionally, constraints imposed by ground transportation requirements limit the dimensions of the transportation vehicle to a maximum width and height of 4.1 meters. These restrictions play a critical role in defining the flyer’s compactness and overall architectural design, as summarized in Table 5.2.

Furthermore, for safe and stable operation, the flyer’s landing gear must fit within a rectangular area of 2.4 [m] $\times$ 2.4 [m], as specified in the Maneuvering mission. This constraint ensures compatibility with designated landing zones while maintaining sufficient ground clearance and structural stability during takeoff and landing phases.

Table 5.2: GoAERO flyer dimensional requirements

Aircraft maximum dimensions	
Width	7.3 [m]
Length	4.1 [m]
Height	4.1 [m]
Landing gear maximum dimensions	
Width	2.4 [m]
Length	2.4 [m]
Payload compartment minimum dimensions	
Width	0.44 [m]
Length	1.8 [m]
Height	0.85 [m]

5.2. Function and Requirement Analysis

A comprehensive analysis of functions and requirements forms the cornerstone of any successful aircraft design. This process is critical for defining the operational purpose, design constraints, and performance expectations that shape and inform subsequent design decisions. Through an integrated approach combining functional and requirements analyses, the key criteria for the final design can be systematically identified, prioritized, and aligned with the mission objectives.

5.2.1. Functional Analysis

Functional analysis offers a systematic breakdown of the tasks the aircraft is designed to perform. These tasks encompass primary mission objectives, secondary capabilities, and auxiliary functions across the entire system and its subsystems. By addressing critical operational scenarios, functional analysis ensures that all mission-specific and support requirements are considered during the conceptual and preliminary design phases. This approach helps identify potential challenges early, promoting a more robust and efficient design process.

System Level

Table 5.3: Functional Analysis GoAERO flyer - System Level (PRE = Pre-flight, TO = Take-off, CR = Cruise, HOV = Hover, DSCT = Descent, LND = landing, ES = Emergency scenarios, MS = Mission-specific, OPS = Operational, MRKT = Market)

Function	Description
	Pre-flight functions
F-PRE-1.0	The aircraft should allow for easy refueling or recharging
F-PRE-2.0	The payload should be secured and safely stored inside the aircraft
F-PRE-3.0	The aircraft should comply with highway-legal transport constraints, including size and weight limits
F-PRE-4.0	The aircraft should be staged and ready to fly within 15 minutes of arriving at the operations zone
	Take-off phase
F-TO-1.0	The aircraft should accelerate from a stationary state to take-off speed
F-TO-2.0	The aircraft should climb to the cruise altitude
	Cruise phase
F-CR-1.0	The aircraft should maintain altitude, flight trajectory, and speed
F-CR-2.0	The aircraft should perform required maneuvers and course corrections
	Hover phase
F-HOV-1.0	The aircraft should maintain steady hover and hold position
	Descent and landing phases
F-DSCT-1.0	The aircraft should reduce its speed gradually and descend safely
F-LND-1.0	The aircraft should land smoothly under varying ground conditions
	Emergency scenarios
F-ES-1.0	The aircraft should deliver a first responder to dense urban environments
F-ES-2.0	The aircraft should transport or retrieve firefighters in dangerous terrains
F-ES-3.0	The aircraft should deliver critical supplies to isolated communities
F-ES-4.0	The aircraft should retrieve injured individuals from remote locations
F-ES-5.0	The aircraft should evacuate victims from areas with limited access
F-ES-6.0	The aircraft should navigate and operate in ”Adversity Mission” environments such as sand, inclines, or water
	Mission-specific functions
F-MS-1.0	The aircraft should be quickly deployable
F-MS-2.0	The aircraft should transport payload efficiently over multiple cycles
F-MS-3.0	The aircraft should operate well out of ground effect
F-MS-4.0	The aircraft should navigate tight spaces and avoid obstacles effectively
F-MS-5.0	The aircraft should operate effectively in environments with degraded GNSS or RF signals
	Operational functions
F-OPS-1.0	The aircraft should allow for loading/unloading of payload without external equipment
F-OPS-2.0	The aircraft should use technology of today’s standards
F-OPS-3.0	The aircraft should require less pilot training than a convetnional rotorcraft
F-OPS-4.0	The aircraft should be easily safed when not in operation, ensuring secure radio transmission settings
	Market
F-MRKT-1.0	The aircraft should be cheaper than a helicopter in both acquisition and operational

Subsystem Level

Table 5.4: Functional Analysis GoAERO flyer - Subsystem Level, (PROP = Propulsion, FUS = Fuselage, LG = Landing Gear, PSS = Propulsion Support Structure)

Function	Description
	Propulsion System
F-PROP-1	The propulsion system should provide thrust for vertical take-off, cruise, and landing
F-PROP-2	The propulsion system should provide electrical power for aircraft instruments
F-PROP-3	The propulsion system should ensure efficient energy consumption for long-duration missions
F-PROP-4	The propulsion system should allow for precise maneuvering and obstacle avoidance in tight spaces
F-PROP-6	The propulsion system should ensure safe and unimpeded access for users during operational tasks, such as loading and maintenance.
	Fuselage
F-FUS-1	The fuselage should protect passengers, crew, and payload from external conditions
F-FUS-2	The fuselage should maintain optimal internal temperature
F-FUS-3	The fuselage should securely store passengers, crew, and cargo
F-FUS-4	The fuselage should provide structural integrity and rigidity
F-FUS-5	The fuselage should provide visibility and situational awareness for crew members
F-FUS-6	The fuselage should integrate plausible restraint systems for Alex and other payloads as required
	Landing Gear
F-LG-1	The landing gear should support the aircraft's full weight on the ground
F-LG-2	The landing gear should absorb shock during landing on various terrains
F-LG-3	The landing gear should support operations on inclined or submerged surfaces
	Propulsion Support Structure
F-PSS-1	The propulsion support structure should provide mechanical rigidity and withstand rotor forces
F-PSS-2	The propulsion support structure should be resistant to wear and degradation from adverse environmental conditions
F-PSS-3	The propulsion support structure should allow unobstructed access to critical areas of the aircraft, including entry points and maintenance sections.

5.2.2. Requirements Analysis

Building on the functional analysis, the requirements analysis defines the essential quantitative and qualitative criteria that the aircraft must meet. These criteria are formalized as Top-Level Aircraft Requirements (TLARs), which serve as the cornerstone for the design's capabilities. The TLARs are directly aligned with the mission objectives and operational constraints specified by the GoAERO competition, ensuring the design addresses critical performance metrics such as mission range, payload capacity, and operational rates. These parameters establish clear benchmarks to evaluate the design's ability to fulfill its intended operational goals effectively and reliably.

System Requirements

Table 5.5: GoAERO flyer System Requirements, (PERF = Performance, OPS = Operational, ENV = Environmental, MRKT = Market)

Requirement	Description
	Performance Requirements
REQ-PERF-01	The aircraft shall have a maximum range of at least 19.3 [km] for the productivity mission.
REQ-PERF-02	The aircraft shall maintain a cruise altitude of at least 600 meters for safe operation during emergency response missions.
REQ-PERF-03	The aircraft shall achieve a rate of climb and descent of at least 7 [m/s], matching the Bell 505 Jet Ranger's performance.
REQ-PERF-04	The aircraft shall achieve a cruise velocity of at least 65 [m/s], matching the Bell 505 Jet Ranger's performance.
	Operational Requirements
REQ-OPS-01	The aircraft shall carry a minimum payload of 144.6 [kg], including the Alex manikin and other mission payloads.
REQ-OPS-02	The aircraft shall navigate tight spaces with a maximum span of 7.3, length of 4.1, and height of 4.1 meters.
REQ-OPS-03	The aircraft shall be staged and ready to fly within 15 minutes of arriving at the operations zone.
REQ-OPS-04	The aircraft shall be operable in crosswind conditions up to 30 knots for adverse mission scenarios.
	Environmental Requirements
REQ-ENV-01	The aircraft shall operate in loose sand, inclines, water, and other uneven terrains typical of adversity missions.
REQ-ENV-02	The aircraft shall remain functional under moderate rainfall (e.g., 4 [mm/hr]) or similar weather conditions.
	Market Requirements
REQ-MRKT-01	The aircraft shall have a unit price of no more than $1.5 million$ [USD] [42] to remain competitive.

Subsystem Requirements

Table 5.6: GoAERO flyer Subsystem Requirements, (STRCT = Structural, PROP = Propulsion, ELEC = Electrical)

Requirement	Description
	Structural Requirements
REQ-STRCT-01	The propulsion support structure shall not deflect more than 1 [mm] under maximum rotor thrust to ensure integrity.
REQ-STRCT-02	The structure shall remain resilient under varied environmental conditions such as temperature and humidity changes.
REQ-STRCT-03	The propulsion support structure shall not block access to critical areas of the aircraft, including entry points, payload bays, and maintenance sections.
	Propulsion Requirements
REQ-PROP-01	The propulsion system shall generate sufficient thrust in all phases to support the MTOW.
REQ-PROP-02	The propulsion system shall handle rapid throttle changes during tight maneuvers and obstacle avoidance.
REQ-PROP-03	The propulsion system shall resist wind disturbances in the ”Tornado” operations zone.
REQ-PROP-04	The propulsion system shall not interfere with users accessing the aircraft for loading, boarding.
	Electrical Systems
REQ-ELEC-01	The aircraft’s electrical systems shall provide redundancy for critical systems, ensuring safe operation during emergency missions.
REQ-ELEC-02	The aircraft shall maintain GNSS and RF signal robustness in degraded environments.

Driving Requirements

The following driving requirements have the largest influence on the final design decisions and are critical to meeting the objectives of the GoAERO competition for the preliminary design in this report. These requirements drive the design to balance performance, operational efficiency, and safety while meeting the technical and environmental constraints outlined in the GoAERO Fly-Off Rulebook [1]. They also ensure the aircraft is optimized for real-world emergency response scenarios, aligning with the competition’s focus on adaptability and robustness.

- **REQ-PERF-01:** The aircraft must have a minimum range of 19.3 [km] to complete the productivity mission, emphasizing energy efficiency and endurance.
- **REQ-PERF-02:** The aircraft shall maintain a cruise altitude of at least 600 meters for safe operation during emergency response missions.
- **REQ-PERF-03:** The aircraft shall achieve a rate of climb and descent of at least 7 [m/s], matching the Bell 505 Jet Ranger’s performance.
- **REQ-OPS-01:** The aircraft must carry a minimum payload of 144.6 [kg], including 1 pilot, 1 caregiver, and the ”Alex” manikin, ensuring it meets operational payload requirements.
- **REQ-OPS-02:** The aircraft shall navigate tight spaces with a maximum span of 7.3, length of 4.1, and height of 4.1 meters.
- **REQ-PROP-01:** The propulsion system must generate sufficient thrust across all flight phases to support the maximum takeoff weight (MTOW) while maintaining efficiency.
- **REQ-STRCT-01:** The propulsion support structure must limit deflection to no more than 1 [mm] to ensure rotor stability and structural integrity under maximum thrust conditions.
- **REQ-STRCT-03** The propulsion support structure shall not block access to critical areas of the aircraft, including entry points, payload bays, and maintenance sections.
- **REQ-PROP-04** The propulsion system shall not interfere with users accessing the aircraft for loading, boarding.
- **REQ-PERF-04:** The aircraft shall achieve a cruise velocity of at least 65 [m/s], matching the Bell 505 Jet Ranger’s performance.

6

Multicopter eVTOL Modelling

6.1. Fuselage conceptual model

As established in Chapter 5, the fuselage must accommodate the maximum allowable payload, including the Alex manikin in a non-restrictive position, as well as a pilot, a caregiver, and all necessary technical support equipment. The design must balance compactness with functionality, ensuring comfort and accessibility for occupants during emergency response operations.

To inform the design, the Bell 505 HEMS (Helicopter Emergency Medical Services) configuration is used as a reference. The Bell 505 is the only HEMS-capable short light single aircraft currently in operation, providing a well-tested basis for fuselage sizing and layout since it is already optimized for emergency medical operations.

As shown in Figure 6.1, the Bell 505 fuselage meets the key requirement of accommodating a pilot, an caregiver, and a single occupant (the Alex manikin), all in practical and ergonomic positions. This configuration not only demonstrates the feasibility of housing all essential personnel and equipment but also highlights an efficient cabin layout that minimizes the overall size of the eVTOL. This compact design is critical for achieving the small form factor necessary for the GoAERO competition.

Figure 6.1: Fuselage layout displaying the seating arrangement for pilot, medical personnel, and passenger [43]

Further examination of the technical specifications, as seen in Figure 6.2, confirms that the Bell 505's fuselage offers sufficient space for the pilot, emergency personnel, occupant, and any additional payload. Despite its compact form, the fuselage adheres to the dimensional requirements set by the competition, including expected space for emergency equipment.

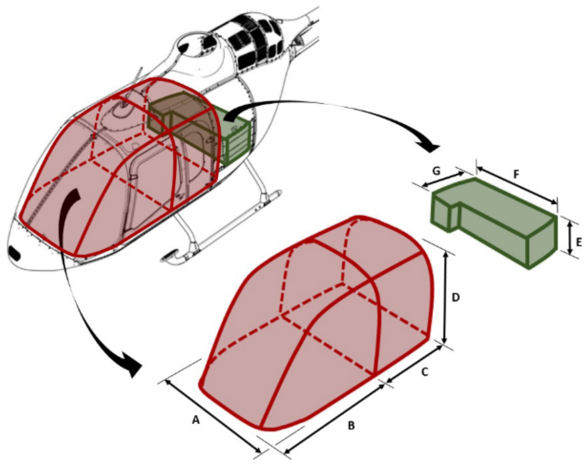

Figure 6.2: Internal dimension convention of the Bell 505 [44]

Table 6.1: Internal dimensions of the Bell 505 [44]

Dimension	Value [cm]
A	142
B	135
C	84
D	84
E	46
F	140
G	82

6.1.1. External dimensional Considerations

The Bell 505 fuselage, is further analyzed for its ability to meet the dimensional constraints specified by the GoAERO competition [1], particularly with regard to landing gear and overall size limitations where the flyer must land on a surface no larger than 2.4 [m] × 2.4 [m] (Section 5.1.4). As can be seen in Figure 6.3, the landing gear fitted on the Bell 505 already meets these specifications, making it a viable reference for the eVTOL's design. Additionally, the overall width and height of the Bell 505 fall within the design space required by the GoAERO competition.

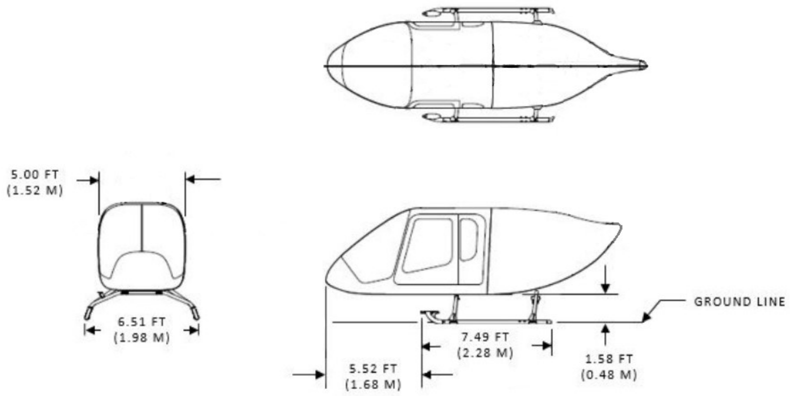

Figure 6.3: External dimensions of the Bell fuselage 505

6.1.2. Integration of Hybrid Systems

The fuselage must also house the turbine generator, fuel tank, battery, and other technical equipment required for the eVTOL's hybrid system. Since the Bell 505 is already a turbine-driven rotorcraft, its fuselage is optimized to accommodate these sub components, as depicted schematically in Figure 6.4. With the hybridized system, which includes an efficient turbine engine and eliminates the need for mechanical linkages between the engine and rotors, the design is expected to yield an even more compact form factor. This enables the fuselage to maintain a similar form while still housing all necessary components including batteries. Consequently, the Bell 505 fuselage serves as a feasible basis for the preliminary design, onto which the multirotor configuration will be integrated.

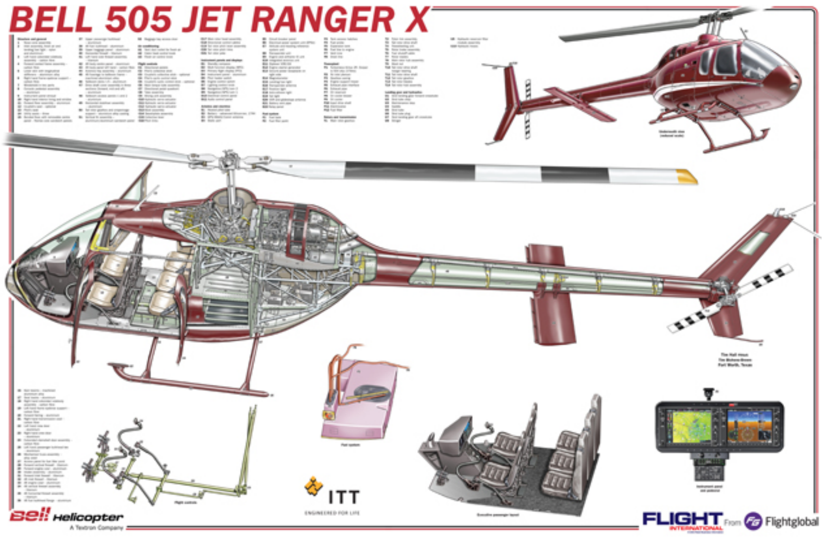

Figure 6.4: Schematic of Bell 505 internal components [45]

6.1.3. Visualization of Design Space

To provide a clear sense of the dimensional constraints and spatial allowances for the multirotor configuration, the Bell 505 fuselage model is implemented within a 3D design space. This space is constrained by the dimensions listed in Table 5.2, and the fuselage is visualized from multiple perspectives in Figure 6.5, Figure 6.6 and Figure 6.7. These visuals help demonstrate how the multirotor system can be applied to the fuselage while adhering to the size and layout requirements of the GoAERO competition where the grey box illustrates the design space for the rotors.

Figure 6.5: Dimensional design space front view

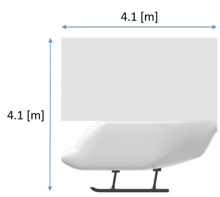

Figure 6.6: Dimensional design space side view

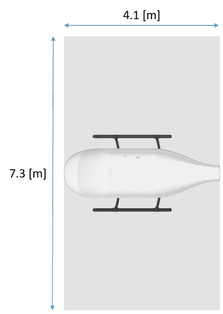

Figure 6.7: Dimensional design space top view

6.2. Fuselage Area Terms

To evaluate the aerodynamic drag during different flight phases i.e., axial climb, cruise, and axial descent, the drag forces acting on the eVTOL's fuselage are approximated for each phase. The drag coefficients are estimated based on the dominant areas interacting with the incoming airflow during each flight phase. For the axial climb and descent phases, the top and bottom areas of the eVTOL are the primary contributors to drag, whereas during cruise, the frontal area is assumed to be the key factor. The resulting drag forces for each steady flight phase are essential in balancing the total forces acting on the eVTOL.

One advantage of utilizing the fuselage from an existing rotorcraft, such as the Bell 505, is that well-established statistical rotorcraft methods can be applied more accurately to estimate the fuselage's frontal area and calculate its drag coefficient during the cruise phase. However, it is important to note that while the Bell 505 serves as a reference for the conceptual fuselage design, the helicopter differs from the intended multirotor configuration. Specifically, the presence of additional components, such as rotor-support structures and motors in the multirotor design, is likely to result in a higher overall drag coefficient. Nevertheless, at this stage of the design process, the drag characteristics are assumed to be similar to those of the Bell 505 fuselage for simplicity.

Using Figure 6.8, the equivalent flat plate area is estimated by employing statistical methods, considering the fuselage's mass of 3680 [lbs] (1669 [kg]) [12], resulting in an equivalent flat plate area of $6.2[ft^2]$ (approximately $0.576\,[m^2]$). Incorporating the obtained equivalent flat plate area in Equation 6.1 together with the assumption of the frontal area of the fuselage being approximated as a rectangular box with dimensions of 1.52 [m] $\times$ 1.42 [m], the frontal drag coefficient is calculated to be approximately 0.27.

$$C_D = \frac{\sum C_{D_i} S_i}{S} \tag{6.1}$$

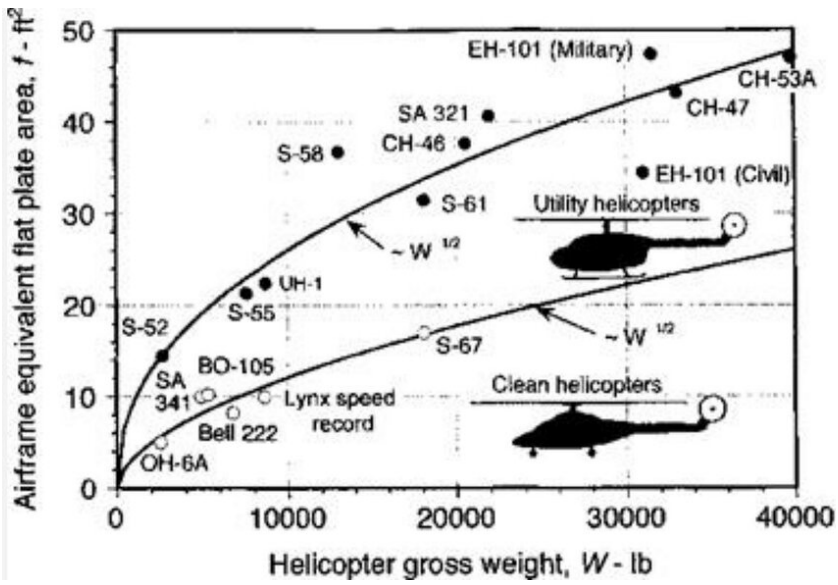

Figure 6.8: Equivalent flat plate area of helicopter fuselage [46]

For the axial climb and descent phases, the top and bottom drag coefficients are estimated separately, as the previous method only provides the frontal drag coefficient. To estimate the drag coefficient for the top and bottom surfaces, the fuselage is assumed to resemble an ellipsoid. Based on the total top and bottom area of $4.73[m^2]$ (derived from Figure 6.3), and referring to a study on drag force coefficients for ellipsoidal particles in cross flow [47], the drag coefficient for these surfaces is approximated to be 0.956.

By calculating these drag coefficients for the relevant flight phases, the total drag forces acting on the eVTOL's fuselage during axial climb, cruise, and descent can be approximated, allowing for a more accurate analysis of the forces that must be countered by propulsion. However it should be noted that for the preliminary design phase the drag forces are assumed to act through the center of gravity of the whole system so that no moments are created due to the aerodynamic forces.

6.3. Aircraft Mass Modelling

The maximum takeoff mass (MTOM) is a critical parameter in the design phase, as it directly influences many other design considerations. For instance, the MTOM determines the rotor characteristics, which must provide sufficient lift for both hovering and forward flight. In turn, the power required to operate the rotor dictates the propulsion system specifications, which subsequently determine the energy needed to complete the planned missions.

However, during the early stages of conceptual design, available data is limited. As a result, mass estimations primarily rely on statistical methods to predict the aircraft's mass breakdown. These methods allow for the development of reasonable approximations, which can guide the design process until more precise data is available.

The total aircraft mass is the sum of the useful mass and the operating empty mass (OEM), as described in Equation 6.2. The OEM refers to "*the mass of the aircraft, engines, and all items of operating equipment that are permanently installed in the aircraft, plus the crew and the equipment required for flight, but excluding fuel and payload*" [48]. This distinction is important because it separates the fixed elements of the aircraft from the variable elements, such as fuel and payload.

For a more detailed breakdown, the useful mass comprises both the payload and fuel mass. Although batteries, in a similar way to fuel, contribute to the useful mass, they differ in that their mass remains constant regardless of the energy stored. Therefore, in this hybrid setup, batteries are considered part of the OEM.

In the hybrid configuration, the generator does not contribute to propulsion via a direct mechanical link. Instead, it is permanently installed and contributes to the OEM, as detailed in Equation 6.4. This ensures that the mass of the generator is properly accounted for in the overall mass of the aircraft.

The total mass of the propulsion system includes both the motor and propeller masses, as outlined in Equation 6.6. Additionally, the airframe mass consists of the fuselage mass and the mass of the propulsion support structure, which integrates the motors onto the fuselage.

It is essential to recognize that the mass breakdown provided here is an estimation intended to support the optimization process, with the goal of minimizing the MTOM. In more detailed design phases, additional elements, such as controllers, wiring, and other system components, should be incorporated into the mass breakdown to achieve more accurate results.

$$MTOM = OEM + m_{\text{Useful}} \tag{6.2}$$

$$m_{\text{Useful}} = m_{Payload} + m_{Fuel} \tag{6.3}$$

$$OEM = m_{Battery} + m_{Airframe} + m_{Propulsion} + m_{ICE} + m_{Crew} \tag{6.4}$$

$$m_{airframe} = m_{Fuselage} + m_{\text{propulsion support structure}} \tag{6.5}$$

$$m_{Propulsion} = m_{motor} + m_{Propeller} \tag{6.6}$$

6.3.1. Payload and Crew mass

As derived from the payload requirements in Section 5.1.2 set by the GoAERO competition, the total payload mass amounts to 144.6 [kg], as shown in Table 5.1. Another essential component of the useful mass is the crew mass. As previously discussed in Section 5.1.3, T. Judge argues that HEMS missions typically require two crew members: one pilot and one caregiver, ensuring distinct roles for each discipline. For this analysis, the crew mass is estimated by assuming two members, each with a mass of 80 [kg].

6.3.2. Fuselage sizing

As shown in Equation 6.5, the mass of the airframe consists of the fuselage mass and the mass of the propulsion support structure. In Section 6.1, the use of the Bell 505 fuselage is justified for this design. One significant advantage of this approach is that rotorcraft statistical estimation methods can now be used to estimate the fuselage mass fraction. Schwinn et al. [49] provide a detailed assessment of rotorcraft fuselage mass, which includes individual components such as the fuselage tail, rear cap, and engine cowling, as shown in Figure 6.9.

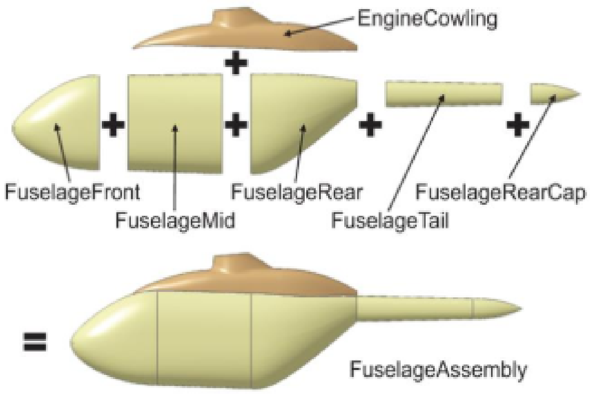

Figure 6.9: Assembly of rotorcraft fuselage components [49]

For the multicopter configuration, however, components like the fuselage tail, rear cap, and engine cowling are unnecessary, leading to a slight overestimation of the fuselage mass. Despite this, such overestimations are considered acceptable during the preliminary design phase, where precision is less critical than in later stages.

Using the mass estimation method outlined in the paper [49], the fuselage mass depends on the surface area of the aircraft body. Layton's method categorizes helicopters into three weight classes, as shown in Table 6.2, with corresponding formulas for body surface area provided in Equation 6.7, Equation 6.8 and Equation 6.9. It's important to note that in Layton's method, the empty mass (m_e) and design gross mass are in pounds (lb), and the resulting surface area is in square feet (ft^2).

Table 6.2: Weight classes according to Layton [49]

Weight class	m_{mto} range
Light [lb]	m_{mto} <1360.78
Medium [lb]	1360.78 ≤ m_{mto} ≤ 11339.82
Heavy [lb]	m_{mto} >11339.82

$$S_{b,light} = 194.274 \cdot \ln(m_e) - 1306.779 \tag{6.7}$$

$$S_{b,medium} = 636.081 \cdot e^{0.0000098 \cdot m_g} \tag{6.8}$$

$$S_{b,heavy} = 426.378 \cdot e^{0.000045 \cdot m_g} \tag{6.9}$$

Since Layton's method was developed before the widespread use of composite materials, it may overestimate the fuselage weight for modern airframes. To address this limitation, Prouty [49] developed an improved method that incorporates additional factors, such as fuselage length, to provide a more accurate weight estimate, as shown in Equation 6.10.

$$m_{fuselage} = 6.9 \cdot (\frac{m_{mto}}{1000})^{0.49} \cdot l_{fuselage}^{0.61} \cdot s_b^{0.25} \tag{6.10}$$

Using the Bell 505's maximum takeoff mass (MTOM) of 3680 [lbs] (1669 [kg]), the aircraft falls into the Medium weight class as defined by Layton. Applying the surface area formula for this class (Equation 6.8) results in a surface area of 649.82 ft^2 (61.26 m^2). Plugging this surface area and the MTOW into Prouty's method (Equation 6.10) yields a fuselage mass of 118.34 [kg].

This result can be compared to the calibrated Army Flight Dynamics Directorate (AFDD) model shown in Figure 6.10, which estimates the fuselage mass to be 14.3% of the operating empty mass (OEM). Given the Bell 505's OEM of 989 [kg] [12], this calculation results in a fuselage mass of approximately 141.43 [kg]. The close agreement between the two methods, both yielding values within the same order of magnitude, validates the estimation as reliable for this design phase.

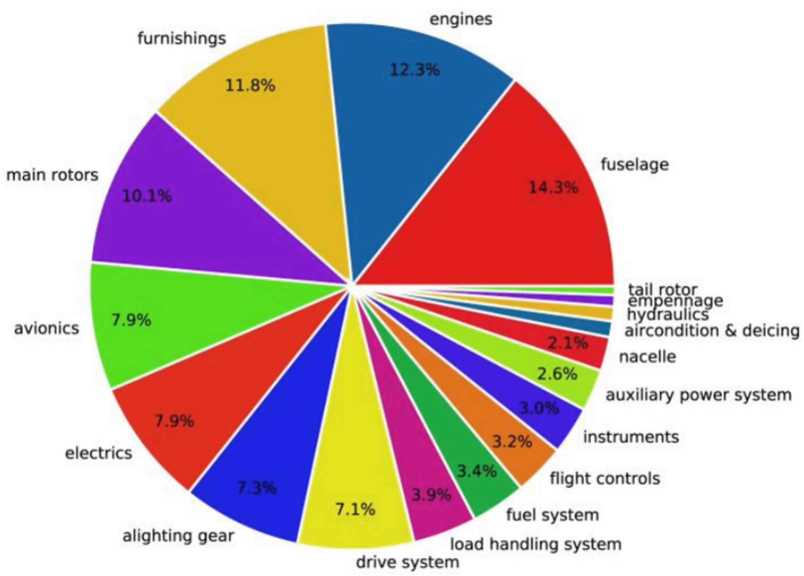

Figure 6.10: Composition of rotorcraft empty mass [49]

6.4. Propulsion and Energy System Sizing

6.4.1. Hybrid Propulsion Modelling

As discussed in Section 3.3, hybrid propulsion systems offer a promising solution for eVTOL aircraft by addressing the limitations of current battery technology, particularly in terms of energy density and weight. Among the various hybrid configurations, this study selects the series hybrid configuration due to its relative simplicity in power transmission. Unlike parallel hybrid systems, which require complex mechanical linkages to share power between energy sources, the series configuration simplifies the propulsion architecture by relying exclusively on electrical power transmission.

In the selected series hybrid configuration, a gas turbine generator serves as the primary power source for propulsion, while a battery provides supplemental energy. This configuration eliminates direct mechanical connections between the turbine generator and the propulsion system, enabling decoupled operation. This design facilitates simpler propulsion system control but at the cost of reduced redundancy compared to parallel configurations. Figure 6.11 illustrates the series hybrid configuration, emphasizing the electrical power transmission pathway from the turbine generator and battery to the propulsors [50].

The inclusion of a battery in the series hybrid system enhances operational flexibility. Acting as a buffer during transient power demands, the battery minimizes fluctuations in turbine operation, potentially improving fuel efficiency. This capability is particularly advantageous for eVTOL missions, which frequently involve rapid power changes, such as during takeoff and hover. However, achieving optimal performance requires careful consideration of the Power distribution between the battery and the gas turbine generator to balance efficiency, redundancy, and mass which are key parameters for meeting the performance objectives of the GoAERO competition.

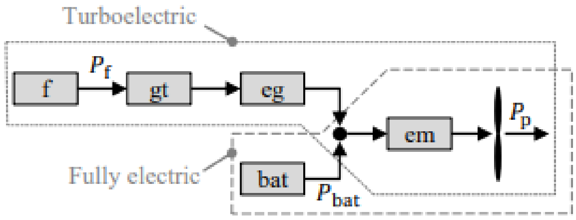

Figure 6.11: Schematic of the series hybrid-electric powerplant [51]

Power Distribution in the Hybrid System

Power distribution in a series hybrid system is governed by the hybridization factor (HF), a key metric that quantifies the proportion of power supplied by the battery relative to the total power required at the propeller shaft. Mathematically, the hybridization factor is defined as the ratio of the required power for the electric motors to the installed battery power, as described by Equation 6.11. The HF value ranges between 0 and 1, indicating the degree of reliance on battery power [25]:

- HF = 0 indicates that the turbine generator supplies all the required power, representing a purely turbine-driven system.
- HF = 1 corresponds to a fully battery-powered system, where the turbine generator is not utilized.

This power distribution is further quantified using the required power equations for the turbine generator and the battery, given in Equation 6.12 and Equation 6.13, respectively. These equations incorporate the efficiencies of the generator, combustion engine, and battery to calculate the adjusted power requirements. A summary of these technical assumptions and their associated efficiencies is provided in Table 6.3. Note that the hybridization factor not only determines the operational load on each energy source but also significantly influences the overall system efficiency and mass distribution over the overall propulsion system due to the difference in efficiencies and power densities.

$$HF_{\text{SH}} = \frac{P_{\text{EM, max}}}{P_{\text{batt, max}}} \tag{6.11}$$

$$P_{req_{h_{ICE}}} = P_{req_{h_{EM}}} \cdot \frac{(1 - HF_{\text{SH}})}{\eta_{gen} \cdot \eta_{ICE}} \tag{6.12}$$

$$P_{req_{h_{batt}}} = \frac{P_{req_{h_{EM}}} \cdot (HF_{\text{SH}})}{\eta_{batt}} \tag{6.13}$$

Table 6.3: Technology assessment of hybrid-electric systems

Parameters	
Gas Turbine Power Density	3 [kW/kg]
Battery Energy Density	260 [Wh/kg]
Battery efficiency	0.99
Electric motor efficiency	0.95
Electric generator efficiency	0.98
Gas turbine efficiency	0.35

6.4.2. Energy System Sizing

As outlined in Section 6.4.1, the degree of hybridization plays a critical role in determining the overall performance and mass of the eVTOL. Both the fuel system and battery system must be sized appropriately to align with the selected hybridization factor (HF).

The hybridization factor directly influences the distribution of energy demand between the battery and fuel systems. A higher HF prioritizes battery usage resulting in increased battery mass and volume, which can negatively impact payload capacity and overall mission performance. Conversely, a lower HF shifts the energy burden toward the fuel system, reducing battery size requirements but increasing dependence on fuel storage and internal combustion components.

Battery Sizing

From the literature, it is evident that the level of battery technology plays a crucial role in the system's performance, particularly in terms of mass. Since the GoAERO competition focuses on the development of an eVTOL solution based on current technology readiness levels, a battery energy density of 260 [Wh/kg]] and a battery efficiency of 99% are assumed [52].

To calculate the required battery mass for the mission, the Euler integration method is applied with proper time discretization for each flight phase. The total energy required for the mission is determined using Equation 6.14, where $P_{\text{battery}}(t)$ represents the time-history of power provided by the battery during the mission, and η_{battery} is the battery discharge efficiency. The power demand on the battery depends on the hybridization factor, as discussed in Section 6.4.1.

$$E_{battery} = \frac{1}{\eta_{battery}} \int_{t_{start}}^{t_{end}} P_{battery}(t)dt \tag{6.14}$$

Once the total battery energy is known, the battery mass is computed using Equation 6.15. This equation takes into account the battery's state of charge (SoC) and its energy density. To preserve battery lifespan, only 80% of the total battery capacity will be utilized during normal operations, meaning the final state of charge, SoC_{final}, is set to 20% [52].

$$m_{battery} = \frac{E_{battery}}{(\text{SoC}_{initial} - \text{SoC}_{final})BED} \tag{6.15}$$

Fuel Mass

In the preliminary design phase of conventional aircraft, the Breguet range equation is often employed to estimate fuel requirements for fuel-based missions. However, this method, tailored for traditional fixed-wing aircraft, does not adequately account for hybrid power systems or multirotor configurations. To address these limitations, a simplified approach is adopted for the hybrid configuration considered in the short-range mission requirements of the GoAERO competition.

This simplified method focuses on the energy requirements of a series hybrid powertrain, as provided in Section 6.4.1, where the turbine generator is sized to supply the total power needed for propulsion. This design choice ensures redundancy by allowing the generator to fully meet power demands even in the event of a battery system cutoff. For each flight phase, i.e. hover, climb, cruise, and descent, the energy consumed by the turbine generator is computed using the Euler integration method previously applied to calculate battery energy in Equation 6.14, but extended to encompass the total power requirements of the system.

To refine the approach, data from a study on the initial sizing of hybrid eVTOL aircraft [53] informs the fuel consumption characteristics of the turbine generator. This study simulates turbine performance and provides insights into speed and brake-specific fuel consumption (BSFC). Assuming the turbine generator operates at its optimal speed setting, a BSFC value of 280 [g/kWh] is used to estimate the fuel weight for each flight phase, as derived from Figure 6.12.

A key assumption underlying this estimation is that fuel mass does not decrease during flight. While this introduces a slight overestimation of total fuel mass, the assumption aligns with the mission's short-range nature and the absence of reserve fuel requirements in the competition guidelines. The reduction in fuel mass relative to the maximum takeoff mass (MTOM) is considered negligible for these missions. Furthermore, any excess fuel carried due to this overestimation is assumed to serve as an implicit reserve, offsetting the lack of explicitly specified reserve fuel requirements.

Despite this simplification, it is acknowledged that ignoring the reduction in aircraft mass over the mission duration leads to a theoretical over-dimensioning of the propulsion system. However, this conservative assumption ensures robustness in power system design and aligns with the redundancy and reliability criteria prioritized for the GoAERO competition and allows for reserve fuel considerations.

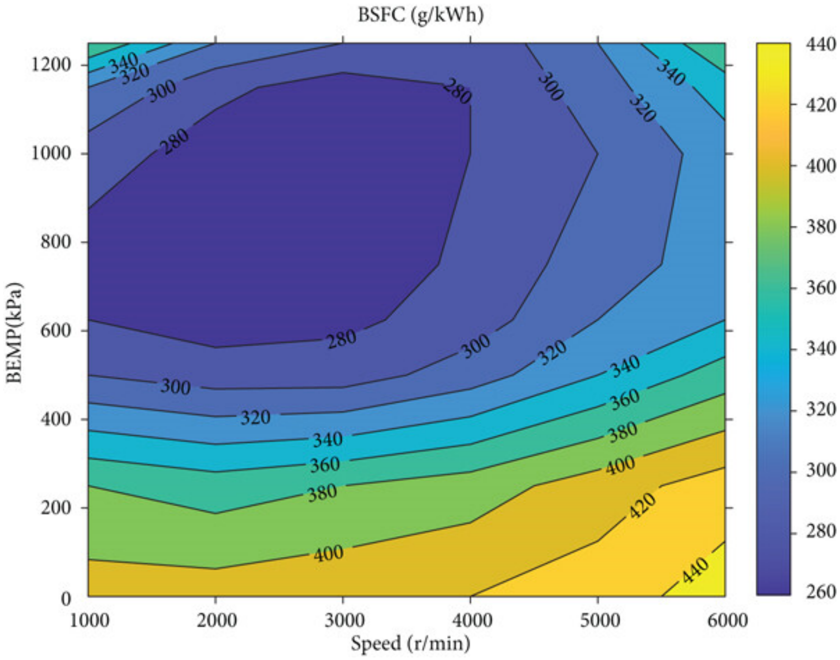

Figure 6.12: Fuel consumption characteristics related to speed and BEMP [53]

6.4.3. Electric Motor and Propeller Sizing

Electric Motor

The sizing of electric motors is critical to ensuring that the eVTOL meets the power demands of its most energy-intensive flight phase. As outlined by Ugwueze et al. [10], the power requirements for electric motors are determined using a power density relationship derived from publicly available data on aerospace DC electric motors. This relationship, summarized in Table 6.4, provides a reliable basis for estimating motor mass. The linear regression model derived from these data points is expressed in Equation 6.16, where P denotes the motor's power output. This model allows for efficient preliminary sizing while ensuring alignment with current industry trends in electric motor technology.

To enhance reliability and safety, a power margin is incorporated into the motor sizing process. Following established rotorcraft design practices, a safety margin of 30% to 50% is typically applied to accommodate unexpected power demands, such as those arising in emergency situations or adverse weather conditions. This ensures the motors can maintain operational effectiveness even under non-ideal circumstances.

Table 6.4: OTS electric motor performance data. [10]

Motor(s)	Power [kW]	Mass [kg]
Emrax 188	52	7
Emrax 208	68	9.1
Emrax 228	109	12
Emrax 268	200	20
Emrax 348	380	41
MAGicALL MAGiDRIVE 12	12	1.5
MAGicALL MAGiDRIVE 150	150	16
MAGicALL MAGiDRIVE 20	20	3
MAGicALL MAGiDRIVE 300	300	30
MAGicALL MAGiDRIVE 40	40	5
MAGicALL MAGiDRIVE 500	500	50
MAGicALL MAGiDRIVE 6	6	0.7
MAGicALL MAGiDRIVE 75	75	9
Magnix magni350 EPU	350	111.5
Magnix magni650 EPU	640	200
Siemens SP200D	204	49
Siemens SP260D	260	50
Siemens SP260D-A	260	44
Siemens SP55D	72	26
Siemens SP70D	92	26
Siemens SP90G	65	13
Yuneec Power Drive 10	10	4.5
Yuneec Power Drive 20	20	8.2
Yuneec Power Drive 40	40	19
Yuneec Power Drive 60	60	30

$$m_{mot} = 0.165P(1 + PM) \tag{6.16}$$

Propeller
During the initial stages of the design process, detailed propeller specifications are often unavailable forming and as a result form a limitation in preliminary sizing studies. To address the limitation the Torenbeek propeller mass estimation method is employed, suitable for propellers with maximum shaft power ratings of up to 1100 [kW] [10]. The Torenbeek method estimates the propeller mass using Equation 6.17 [54], where $D_{propeller}$ represents the propeller diameter, P denotes the power delivered to the propeller, and N_{blades} specifies the number of blades. This empirical relationship provides a straightforward approach to estimating the propeller mass based on readily available design parameters.

However, it is important to recognize the limitations of this method. The Torenbeek model was originally developed for propellers used in conventional fixed-wing aircraft, which generally operate with lower blade loading compared to rotorcraft. For rotorcraft and eVTOL applications, where blade loading is typically higher to meet design and performance requirements, this method may underestimate the propeller mass. As a result, the findings from the Torenbeek method [54] should be interpreted as a baseline estimate. Adjustments may be necessary in later design stages when more detailed specifications and performance data for the propellers become available.

$$m_{propeller} = 0.144(D_{propeller} P N_{blades}^{0.5})^{0.782} \tag{6.17}$$

6.4.4. Rotor Support Structure Sizing

The rotor support structure plays a critical role in ensuring the stability and effectiveness of the rotor system. To account for the mass of the rotors and propellers, as well as the maximum thrust each rotor must generate, the structural design must prioritize stiffness and strength. In this preliminary phase, a simplified approach is adopted to estimate the structural mass and establish design constraints.

To prevent unwanted deflections in the support structure that could misalign rotor thrust vectors and degrade performance, the structure must exhibit adequate stiffness. Stiffness is a measure of resistance to deflection under applied loads and is influenced by both the material properties and the geometry of the structure. The deflection of a structural element depends on its moment of inertia (I) and the modulus of elasticity (E), as described by Equation 6.18. The moment of inertia reflects how the cross-sectional area is distributed relative to the centroid; a larger I results in greater resistance to bending. For the same cross-sectional area, hollow shapes, such as tubes, thus offer higher stiffness-to-weight ratios due to their efficient distribution of material [55].

$$\delta_{max} = \frac{PL^3}{3EI} \tag{6.18}$$

6.4.5. Structural model

In this analysis, the rotor support structure is modeled as a cantilever beam subjected to a point load (see Figure 6.13) where the deflection is minimized by maximizing $E \times I$. It is important to note that for this simplified model, the self-weight of the beam is not included in the deflection calculations. Instead, only the point forces acting on the beam (e.g., thrust and rotor mass) are considered.

To further model the structure, hollow circular tubes are selected for the support structure due to their uniform stiffness in all directions and high specific stiffness. These tubes are particularly advantageous in rotorcraft applications, where lightweight yet robust components are essential. The moment of inertia for a hollow circular tube is given by Equation 6.19, and the tube's mass is calculated using Equation 6.20 using the convention as displayed in Figure 6.14. These equations provide a foundation for estimating the support structure's mass while ensuring adequate stiffness for operational loads.

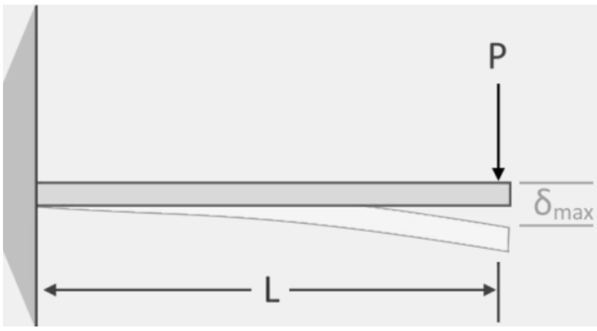

Figure 6.13: Cantilever beam deflection schematic [55]

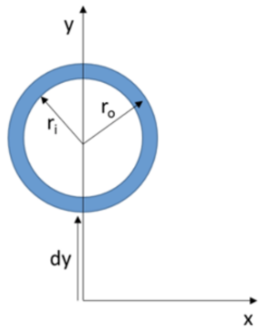

Figure 6.14: Hollow tube cross section convention [56]

$$I = \frac{\pi}{4}(r_o^4 - r_i^4) \tag{6.19}$$

$$m_{pipe} = \pi(r_o^2 - r_i^2)L\rho \tag{6.20}$$

6.4.6. Material selection

The material selection for the support structure must balance stiffness and mass. While minimizing deflection is essential, the mass of the structure must also be kept as low as possible in this mass-critical system. Therefore, it is important to maximize the material properties ratio $\frac{E^{1/3}}{\rho}$, where E is the Young's modulus and ρ is the material density, to achieve the minimum mass for a given deflection. The Young's modulus is a material constant and independent of the test-piece size, allowing for direct comparison of materials using a materials-selection map.

The materials-selection map shown in Figure 6.15 is plotted on logarithmic scales, with the optimal materials indicated by straight lines. The materials in the top-middle region of the plot represent those with the best $\frac{E^{1/3}}{\rho}$ values, making CFRP the ideal choice for this application [57]. As a result, for this analysis, Carbon Fiber Reinforced Polymer (CFRP) with a Young's modulus of 181 GPa and a density of 1600 kg/m^3 is selected.

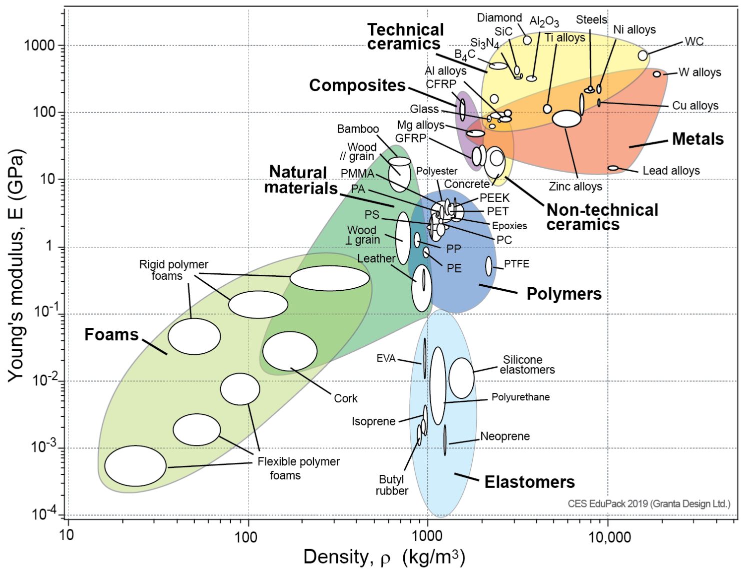

Figure 6.15: Ashby chart [58]

6.5. Rotor modelling

The rotorcraft must operate in a variety of flight regimes with hover, climb, forward flight and descent or a combination of the regimes concerned with certain manoeuvres. As pointed out by Leishman [59], even with current mathematical models, predictions of the rotor flow are difficult to accurately predict. As a solution to still analyse the rotor characteristics and performance, the momentum theorem allows for a relatively simple first-order derivative prediction of the rotor thrust and power. Note that this predicts the individual rotor thrust and power under the assumption of no aerodynamic interference between the components of the aircraft influencing the individual rotors.

The previously mentioned momentum theory, also known as the actuator disk theory, is a fundamental principle used in aerodynamics to analyse the performance of propellers and rotors. The theory provides a simplified model to understand how thrust is generated by considering the conservation of momentum and energy in the airflow through the rotor disk. The rotor or propeller is modelled as an ”actuator disk” which is infinitely thin and completely efficient allowing for a uniform pressure change to the fluid passing through it, while purely focusing on the overall effects on the flow [60]. The rotor disk and blades are assumed to be rigidly attached to the rotor shaft and to be rigid structures where the actuator disk operate on a streamtube that crosses the whole rotor area. It should be noted however that the simplified model is based on a variety of assumptions as mentioned below:

1. Inviscid Flow: Assumes no viscosity, simplifying fluid motion equations.
2. Incompressible Flow: The fluid density is constant, which is often a valid assumption for liquids and low-speed air flows.
3. Steady Flow: The flow is steady, implying that all properties (velocity, pressure, etc.) at any point in the flow field do not change over time.
4. Uniform Pressure Change: The pressure change across the disk is uniform.

While the actuator disk theory offers valuable insights, it is an idealized model. Real-world factors such as blade shape, wake rotation, and viscous effects are not accounted for. As a result, the Figure of Merit (FoM) is a crucial parameter in the context of actuator disk theory, especially when analyzing the efficiency of rotors. In essence, the Figure of Merit quantifies how effectively a rotor or propeller converts mechanical energy into useful thrust or lift compared to an ideal scenario. It is a measure of the rotor's efficiency in generating thrust while considering the induced power losses. As a result, mathematically, it is given by the ratio of the ideal power required to produce a certain thrust to the actual power consumed as described by Equation 6.21.

The Figure of Merit primarily applies to the induced power, as it is a measure of the efficiency of a rotor in generating the necessary lift relative to an ideal rotor. As a result, $FoM = 1$ implies a perfect rotor with no losses, where the actual power consumed is equal to the ideal power, while $FoM < 1$ is a more realistic scenario accounting for the presence of inefficiencies and losses in the rotor system. Typical FoM values for the rotorcraft, applied to eVTOL aircraft, are between 0.5 and 0.8 [10]. As also stated by Leishman [59], for a real rotor the FOM should always be less than one and used as a comparative measurement for two rotors with the same disk loading.

$$FoM = \frac{P_{ideal}}{P_{actual}} = \frac{P_{ideal}}{P_{induced} + P_{profile}} = \frac{\frac{C_T^{3/2}}{\sqrt{2}}}{\frac{kC_T^{3/2}}{\sqrt{2}} + \frac{\sigma C_{D_p}}{8}} \tag{6.21}$$

As can be seen from the actual power equations however, the ideal power gets multiplied with the induced power factor or inflow correction factor k which is inversely proportional to the Figure of Merit when the induced power term dominates as given by Equation 6.22 and is typically assumed to be around 1.15. The induced power correction factor encompasses a number of non-ideal physical effects like non-uniform inflow, tip losses, wake swirl, and less than ideal wake contraction for a finite number of blades [59].

$$FOM = \frac{1}{k} \tag{6.22}$$

6.5.1. Rotor power modelling

For an aircraft, the total power required at the rotor entails the profile power, the induced power, and the parasitic power as expressed in equation Equation 6.23[61]. The induced power can be related to the energy involved in the downward momentum generated by the rotor wake and exerted on the air. The profile power accounts for the pressure and viscous drag of the blades, while the parasite power is the power required to overcome the drag of the aircraft. Essentially, the induced power entails the ideal power required to generate thrust by increasing the momentum of a column of air.

$$P_{total} = P_{parasitic} + P_{induced} + P_{profile} \tag{6.23}$$

From momentum theory, it follows that the thrust generated by the rotor is equal to the rate of change of momentum of the air passing through the disk i.e. $T = \dot{m} \cdot v_{induced}$ where v_i is normal to the disk actuator. In this, the mass flow rate through the disk is defined as $\dot{m} = \rho A v_{induced}$ with the area of the disk A [60]. In accordance with Bernoulli's principle, the pressure difference across the rotor disk causes the acceleration of the air where the induced velocity far downstream, for uniform flow is $2 \cdot v_{induced}$. As a result, when considering the far downstream condition where disturbances in the flow have dissipated, the thrust from the rotor disk is described by Equation 6.90. The ideal power is then the thrust force multiplied by the speed at which it is applied as described by Equation 6.25. As follows from the FoM, the actual power is thus the ideal power times the induced power factor as described in Equation 6.26 [60].

$$T = 2\rho A v_{inudced}^2 \tag{6.24}$$

$$P_{ideal} = T \cdot v_i \tag{6.25}$$

$$P_{actual} = k \cdot P_{ideal} = k(T \cdot v_i) \tag{6.26}$$

As can be seen in the induced velocity term as described by Equation 6.31, the ratio T/A is known as the disk loading. The disk loading is a key parameter in rotorcraft aerodynamics that measures the amount of thrust generated per unit area of the rotor disk where it is an important indicator of the rotorcraft's performance characteristics. Lower disk loading generally indicates higher efficiency, particularly in hover and low-speed flight, because the rotor generates more lift with less induced drag. As a result, induced power can thus be minimised by minimising the induced velocity resulting in the mass flow through the disk being large resulting in a large disk area. Rotorcraft with lower disk loading are typically more efficient in hover since they can produce the necessary lift with lower induced velocities and hence lower induced drag. Higher disk loading on the other hand generally requires more power to produce the same amount of lift since higher disk loading results in higher downwash velocities, which increases induced drag and thus the power required to overcome it.

Another performance indicator is the power loading T/P where the ideal power loading is inversely proportional the the induced velocity at the disk where power loading decreases quickly with an increase in disk loading [59]. As a result, low disk loading will require low-power units per unit thrust and will be more efficient since less power is required to generate a certain amount of thrust.

Another term that influences the rotor characteristics is the solidity factor as described by Equation 6.27 which affects the drag of the rotor. This implies that reducing the solidity factor reduces the profile drag of the rotor by minimizing the blade area. However, minimizing solidity must be done with caution since reducing solidity means a higher blade section angle of attack is needed with a higher lift coefficient to obtain the same thrust coefficient and disk loading. This increases the blade loading, as described by Equation 6.28, and can lead to blade stall. As a result, the minimum value of solidity is constrained by the onset of blade stall [59].

$$\sigma = \frac{N_{blades}c}{\pi R} \tag{6.27}$$

$$\frac{C_T}{\sigma} = \frac{T}{\rho A(\omega R^2)}(\frac{A}{A_b}) \tag{6.28}$$

6.5.2. Power in hover

At hover, the total power is described by the sum of the induced power and profile power as described in Equation 6.29. Note that no parasitic power is present in this equation since no free stream velocity acts on the model.

$$P_{hover} = P_{induced,hover} + P_{profile,hover} \tag{6.29}$$

The induced power, $P_{induced,hover}$, is given by Equation 6.30, where the induced velocity in hover, v_{hover}, represents the change in airspeed caused by the rotor blades relative to the free-stream velocity. This induced velocity can be estimated using Equation 6.31, derived from momentum theory under the assumption of constant air density ρ. It is important to note, however, that the thrust in the power equation corresponds to the rotor-generated thrust required to maintain hover, which is equal to the aircraft's weight. This relationship is expressed as $T_{hover} = W = MTOM \cdot g$, where MTOM represents the maximum takeoff mass.

$$P_{induced,hover} = T \cdot v_{induced} = k\frac{T^{3/2}}{\sqrt{2\rho A}} \tag{6.30}$$

$$v_{hover} = v_{induced} = \sqrt{\frac{T}{2\rho A}} = \sqrt{\frac{T}{2\rho\pi R^2}} \tag{6.31}$$

The profile power is described by Equation 6.32 where the solidity factor is introduced. As described by Equation 6.27, the solidity factor defines the ratio of the area of the rotor blades to the area of the rotor disk influencing the overall profile drag of the disk.

$$P_{profile,hover} = \frac{\sigma C_{D,profile}}{8}\rho(\Omega R)^3\pi R^2 \tag{6.32}$$

6.5.3. Power in Axial flight

For axial flight, an additional velocity component comes into play when modelling the power and velocity at the rotor disk. At the plane of the rotor, the total velocity is namely described by $v_{axial} + v_{induced}$ resulting in the induced power equation now being described by Equation 6.33 here $\frac{v_{axial}}{v_{hover}}$ is the work done to change the potential energy of the rotor and $\frac{v_{induced}}{v_{hover}}$ is the work done on the air by the rotor.

$$\frac{P_{induced}}{P_{induced,hover}} = \frac{v_{axial} + v_{induced}}{v_{hover}} \tag{6.33}$$

In axial flight the axial velocity affects the total velocity experienced by the rotor blades and consequently, the profile power required. As a result, the condition changes from hover due to the additional vertical velocity component. This velocity component not only contributes to the parasitic power, as described by Equation 6.45, but also affects the effective blade tip speed in vertical flight. As a result the profile power now combines the rotational speed and the axial velocity component as approximated by $V_{eff} = \sqrt{(\Omega R)^2 + v_{axial}^2}$ resulting in the profile power equations as described by Equation 6.34 and Equation 6.35.

$$P_{profile,axial} = \frac{\sigma C_{D,profile}}{8}\rho(V_{eff})^3\pi R^2 \tag{6.34}$$

$$P_{profile,axial} = \frac{\sigma C_{D,profile}}{8}\rho((\Omega R)^2 + v_{axial}^2)^{3/2}\pi R^2 \tag{6.35}$$

Operational modes
In the extreme regions of the angle of attack of the disk, where flight is close to vertical, rotorcraft have three operational modes with the so-called normal working state, vortex ring state and windmill brake state [62]. To define the three modes, the following fractions of axial velocity v_{axial} over the induced hover velocity v_{hover} apply:

1. Normal working state: $\frac{v_{axial}}{v_{hover}} \geq 0$
2. Vortex ring state (VRS): $-2 \leq \frac{v_{axial}}{v_{hover}} < 0$
3. Windmill brake state: $\frac{v_{axial}}{v_{hover}} < -2$

During regular operation, air moves downward through the rotor, while in the windmill brake condition, air ascends through the rotor as a result of rapid descent [62]. The normal working state thus requires a higher power required to climb compared to hover while the power required for ascending flight is less than hover since the rotor is extracting power from the air by functioning as a windmill. It should be noted however that as the climb speed increases the induced power becomes a smaller fraction of the total power required to climb. An additional note has to be made for the axial descent phase where the slipstream will now be above the rotor [59].

The first two modes can be interpreted as simplified cases with Equation 6.52 as derived with the conservation of momentum where $\cos\alpha_{disk}$ is equal to zero as also depicted in Figure 6.16 [63]. The third mode concerned with the vortex ring state involves a recirculation phenomenon that greatly diminishes the rotor efficiency. In the vortex state namely, the slipstream is not well developed and the flow can take two different directions. As a result, the induced velocity varies greatly, particularly over the domain $-1.4 \geq \frac{v_{axial}}{v_{hover}} \geq -0.4$ reducing aerodynamic damping [63].

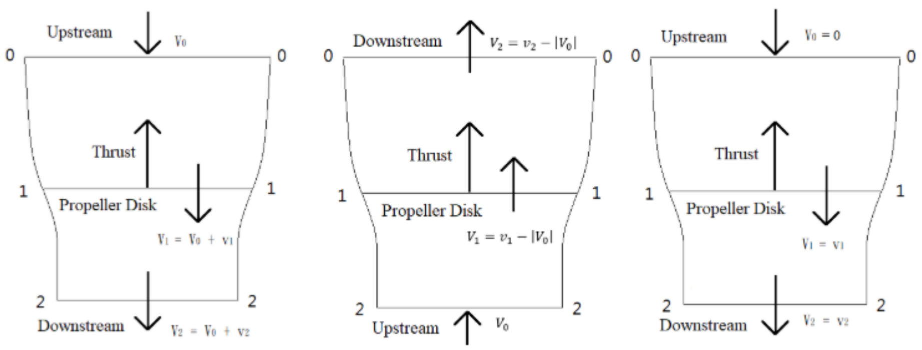

Figure 6.16: Propeller momentum theory model for climb, descent and hover condition in order[64]

Climb (normal working state): During vertical climb, the rotor must produce not only the lift to support the weight of the aircraft but also additional thrust to overcome drag forces. The power required in vertical climb includes the power to produce lift and the power to overcome drag which can be seen in the total power equation for climb Equation 6.36.

$$P_{climb} = P_{induced,climb} + P_{profile,axial} + P_{parasitic,climb} \tag{6.36}$$

$$P_{parasitic,climb} = D_s v_{climb} = \frac{1}{2}\rho v_{climb}^3 \sum (C_D S)_s \tag{6.37}$$

With the induced velocity at climb as described by Equation 6.38, the induced power needed in vertical climb can be described by Equation 6.39 which is also known as the power ratio $\frac{P_{induced,climb}}{P_{induced,hover}}$ [59]. It should be noted that this equation holds for the condition of $v_{climb}/v_{hover} \geq 0$ in accordance with the previously described normal working state.

$$\frac{v_{induced,climb}}{v_{hover}} = -(\frac{v_{climb}}{2v_{hover}}) + \sqrt{(\frac{v_{climb}}{2v_{hover}})^2 + 1} \tag{6.38}$$

$$\frac{P_{induced,climb}}{P_{induced,hover}} = \frac{v_{climb}}{2v_{hover}} + \sqrt{(\frac{v_{climb}}{2v_{hover}})^2 + 1} \tag{6.39}$$

Descent: Contrary to the climb condition, at higher descent speeds the power required to maintain the condition is significantly lower than for the hover condition [59]. This is because gravity now acts as a force acting in the same direction as the desired path. Additionally, the parasitic drag force now acts as a lifting force, further reducing the power required for descending flight. It should be noted that when talking about the descent condition and as pointed out by Leishman [59], the velocity is measured positively as pointing downward for the descent mode and thus at the plane of the rotor, the velocity is described by $|v_{axial}| - v_{induced}$.

$$P_{descent} = P_{induced,descent} + P_{profile,descent} - P_{parasitic,descent} \tag{6.40}$$

$$P_{parasitic,descent} = D_s v_{descent} = \frac{1}{2}\rho v_{descent}^3 \sum (C_D S)_s \tag{6.41}$$

As mentioned in the operational modes, for the descent phase, there are two modes present namely the Vortex Ring State and Windmill brake state. Concerned with the windmill brake state, the power ratio for the descent flight is described by Equation 6.43 valid for $v_a/v_{hov} \leq -2$. It should be noted that due to the descending motion of the aircraft, the parasitic drag force now acts in the opposite way of movement, adding to the lifting force. As a result, the parasitic power is subtracted from the overall power in descent as shown in Equation 6.40. Additionally, the induced velocity and as a result induced power equations are now described by Equation 6.42 and Equation 6.43.

$$\frac{v_{induced,descent}}{v_{hover}} = -(\frac{v_{axial}}{2v_{hover}}) - \sqrt{(\frac{v_{axial}}{2v_{hover}})^2 - 1} \tag{6.42}$$

$$\frac{P_{induced,descent}}{P_{induced,hover}} = \frac{v_{descent}}{2v_{hover}} - \sqrt{(\frac{v_{axial}}{2v_{hover}})^2 - 1}, \tag{6.43}$$

It should be noted however that for the vertical velocity ratios of $-2 \leq v_{descent}/v_{hover} \leq 0$ the actuator disk theory is not valid where in this flight regime of the Vortex Ring State, there is no analytical solution for thrust. As a result, the imperial relationship Equation 6.44 is used in combination with the power ratio as described by Equation 6.33. To still solve for the induced velocity in the Vortex Ring State, Leishman [59] provides an empirical model of induced velocity valid for $-2 \leq \frac{v_{axial}}{v_{hover}} \leq 0$ which is used in combination with Equation 6.33 to calculate the induced power.

$$v_{induced,descent} = -v_{hover}(k - 1.125(\frac{v_{descent}}{v_{hover}}) - 1.372(\frac{v_{descent}}{v_{hover}})^2 - 1.718(\frac{v_{descent}}{v_{hover}})^3 - 0.655(\frac{v_{descent}}{v_{hover}})^4) \tag{6.44}$$

6.5.4. Cruise

For a rotorcraft to achieve forward flight, both the mass and the forward thrust have to be sustained by the rotors resulting in a tilt angle between the free stream velocity and the rotor disk. As a result, the rotors move through the air with an edgewise component of velocity parallel to the rotor plane as described by Equation 6.45 [59].

$$V_{advance} = v_\infty \cos \alpha_{disk} / \Omega R \tag{6.45}$$

As for the axial power modelling, the total power in cruise also consists of the profile, induced, and parasitic term, as described by Equation 6.47 in Equation 6.46. Additionally the profile power is now described by Equation 6.48 being dependent on the advance ratio in cruise as described by Equation 6.49

$$P_{cruise} = P_{profile,cruise} + P_{induced,cruise} + P_{parasitic,cruise} \tag{6.46}$$

$$P_{parasitic,cruise} = D_s v_{cruise} = \frac{1}{2}\rho v_{cruise}^3 \sum (C_D S)_s \tag{6.47}$$

$$P_{profile,cruise} = P_{profile,hover}(1 + 4.65\mu^2) \tag{6.48}$$

$$\mu = \frac{v_{cruise}}{\Omega R} \tag{6.49}$$

Note that to achieve propulsion in the translational direction, the rotor disk must be tilted forward (positive α_{disk}) as the rotors are required to produce the total force of the aircraft. For straight and steady flight with the vertical equilibrium $T \cos \alpha_{disk} = W$ and horizontal equilibrium $T \sin \alpha_{disk} = D \cos \alpha_{disk} \approx D$, where the drag is composed of the parasitic drag of the fuselage, this means that the rotor disk angle of attack is thus related to the thrust and drag by means of Equation 6.50 [59].

$$\tan \alpha_{disk} = \frac{D}{W} = \frac{D}{L} \approx \frac{D}{T} \tag{6.50}$$

As a result, in cruise, the total thrust varies not only with the power input but also with the free stream velocity and the angle of attack of the disk. Again, the induced power is the power input required to create the induced velocity, so when the rotorcraft undergoes translational motion, or changes the angle of attack, the induced power requirement of a rotorcraft changes [63]. This is because the induced power demand for the rotorcraft varies as the angle of attack at which the thrust matches the hover value increases with higher forward speed. As a result, for level flight, the power necessary to maintain altitude increases as forward speed increases [62]. This overall relationship between free-stream speed V_0 and propeller-induced velocity v_1 is depicted in Figure 6.17.

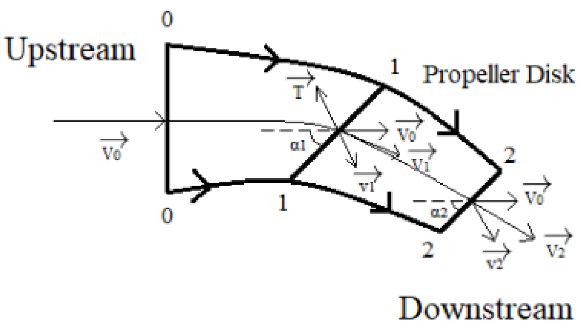

Figure 6.17: Propeller momentum theory model for cruise condition [64]

This relation of change in angle of attack and induced velocities is given by the power ratio equation in forward flight (Equation 6.51) [59]. The first term $T \cdot v_{cruise} \sin \alpha_{disk}$ corresponds to the power required to propel the rotor forward, whereas the second term $T \cdot v_{induced}$ is the term of induced power. As a result, the power required first decreases to a minimum after which it increases again, as it depends on the rotor disk angle of attack and the cruise speed. Note that the induced velocity as described in Equation 6.52 in cruise is not only dependent on the angle of attack of the rotor disk with the freestream velocity, it is also dependent on its own solution, resulting in the need to be solved iteratively [65].

$$\frac{P_{cruise}}{P_{hover}} = \frac{v_{cruise}\sin\alpha_{disk} + v_{induced}}{v_{hover}} \tag{6.51}$$

$$v_{induced,cruise} = \frac{v_{hover}^2}{\sqrt{(v_{cruise}\cos\alpha_{disk})^2 + (v_{cruise}\sin\alpha_{disk} + v_{induced,cruise})^2}} \tag{6.52}$$

6.6. Multicopter Dynamics

The kinematics and dynamics of the multicopter are evaluated using standard aerodynamic symbol notation, which decomposes the motion of a rigid body into translational and rotational components based on the Newton-Euler equations. This analysis employs two reference frames: the earth inertial frame (e-frame) and the body-fixed frame (b-frame), both defined using the North-East-Down (NED) coordinate system, as visualized in Figure 6.18. The transformation between the body and inertial frames is achieved using the rotation matrix C_b^e as described by Equation 6.53, where the relationship $C_b^{eT} = C_b^{e-1} = C_e^b$ holds [66].

$$C_b^e = C_e^{bT} = \begin{bmatrix} \cos\theta\cos\psi & -\cos\theta\sin\psi + \sin\phi\sin\theta\cos\psi & \sin\phi\sin\psi + \cos\phi\sin\theta\cos\psi \\ \cos\theta\sin\psi & \cos\theta\cos\psi + \sin\phi\sin\theta\sin\psi & -\sin\phi\cos\psi + \cos\phi\sin\theta\sin\psi \\ -\sin\theta & \sin\phi\cos\theta & \cos\phi\cos\theta \end{bmatrix} \tag{6.53}$$

The angular positions of the body frame relative to the inertial frame are described by the Euler angles: roll (ϕ), pitch (θ), and yaw (ψ) [67]. The velocity vector in the body-fixed frame consists of three components: u, v, and w, aligned with the x, y, and z axes, respectively, as depicted in Figure 6.18 and summarized in Table 6.5. Similarly, the angular velocity vector comprises the components p, q, and r, corresponding to rotations about the same axes. The moments and forces acting on the multicopter are denoted as L, M, N (moments) and F_x, F_y, F_z (forces), all expressed in the body-fixed frame. The total moments of inertia are represented by the diagonal components I_x, I_y, and I_z, with the off-diagonal products of inertia given by I_{xy}, I_{yz}, and I_{xz} [66].

Table 6.5: Multirotor Dynamics Convention

Axis	Velocity	Angular Rate	Moment	Moment of Inertia	Force
x	u	p	L	I_x	F_x
y	v	q	M	I_y	F_y
z	w	r	N	I_z	F_z

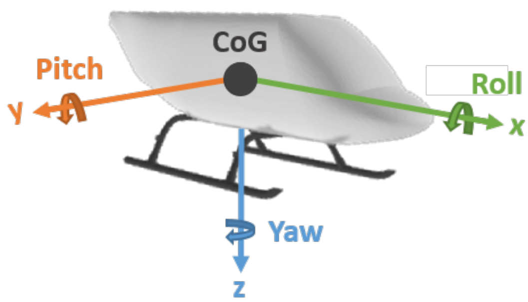

Figure 6.18: Coordinate frame for Multirotor dynamics

6.6.1. Center of Gravity

To analyze the moments acting on the multicopter, determining the center of gravity (CoG) is essential. The CoG is the point within an object at which the gravitational force can be considered to act. This point represents the object's balance center, irrespective of its orientation, and serves as the axis about which the multicopter rotates and moments are applied. The CoG of the multicopter is calculated by treating each component as a point mass located at its own center of mass (CoM). The position of the overall CoG is then determined using the following equations where x_i, y_i and z_i denote the position coordinate of the components CoM and m_i denoting the components mass:

$$CoG_x = \frac{\sum x_i \cdot m_i}{\sum m_i} \tag{6.54}$$

$$CoG_y = \frac{\sum y_i \cdot m_i}{\sum m_i} \tag{6.55}$$

$$CoG_z = \frac{\sum z_i \cdot m_i}{\sum m_i} \tag{6.56}$$

6.6.2. Inertia Frame

The moment of inertia quantifies an object's resistance to rotational motion and depends on both the object's mass and the distribution of that mass relative to the axis of rotation. Using the mass moment of inertia tensor, the mass distribution in three dimensions can be fully characterized. The components of the tensor include the moments of inertia and the products of inertia, which describe rotational properties about any given axis.

As represented in Equation 6.57, the diagonal elements I_{xx}, I_{yy}, and I_{zz} are the principal moments of inertia about the x-, y-, and z-axes, respectively, with the center of gravity (CoG) located at the origin. The off-diagonal elements, such as I_{xy} and I_{xz}, represent the products of inertia. These terms account for the mass distribution in the planes intersecting the axes, influencing how the object behaves under combined rotational and translational motion. Note that in the equations defined below, the terms x', y', and z' define the distances from the CoG to specific points in the object's frame of reference.

$$I = \begin{bmatrix} I_{xx} & -I_{xy} & -I_{xz} \\ -I_{xy} & I_{yy} & -I_{yz} \\ -I_{xz} & -I_{yz} & I_{zz} \end{bmatrix} \tag{6.57}$$

$$I_{xx} = \sum_i m_i({y'_i}^2 + {z'_i}^2) \tag{6.58}$$

$$I_{yy} = \sum_i m_i({x'_i}^2 + {z'_i}^2) \tag{6.59}$$

$$I_{zz} = \sum_i m_i({x'_i}^2 + {y'_i}^2) \tag{6.60}$$

$$I_{xy} = \sum_i m_i x'_i y'_i \tag{6.61}$$

$$I_{xz} = \sum_i m_i x'_i z'_i \tag{6.62}$$

$$I_{yz} = \sum_i m_i y'_i z'_i \tag{6.63}$$

6.6.3. Equations of motions

An analytical model of the multicopter can be derived from the equations of motion for a rigid body, as derived by Nelson in his book "*Flight Stasbility and Automatic Control*" [68], which establish the relationship between internal and external forces and moments using Newton's second law. In the force equations, the familiar $F = ma$ term is supplemented by additional components that arise due to the rotational motion of the aircraft body relative to the inertial space as described by Equation 6.64, Equation 6.65 and Equation 6.66 [68]. Similarly, the moment equations (Equation 6.79, Equation 6.80, Equation 6.81) [68] include additional terms that account for the rotational dynamics of the multicopter, which are influenced by the inertial matrix I, as described in Equation 6.57.

Translational Dynamics

$$F_x = m(\dot{u} + qw - rv) \tag{6.64}$$

$$F_y = m(\dot{v} + ru - pw) \tag{6.65}$$

$$F_z = m(\dot{w} + pv - qu) \tag{6.66}$$

Rotational Dynamics

$$L = I_x\dot{p} - I_{xy}\dot{q} - I_{xz}\dot{r} - I_{xz}pq - I_{yz}q^2 + (I_z - I_y)qr + I_{xy}pr + I_{yz}r^2 \tag{6.67}$$

$$M = -I_{xy}\dot{p} + I_y\dot{q} - I_{yz}\dot{r} + (I_x - I_z)pr - I_{xy}qr + I_{xz}(p^2 - r^2) - I_{yz}pq \tag{6.68}$$

$$N = -I_{xz}\dot{p} - I_{yz}\dot{q} + I_z\dot{r} - I_{xy}p^2 + (I_y - I_x)pq - I_{yz}pr + I_{xy}q^2 + I_{xz}qr \tag{6.69}$$

The symmetrical design of the multicopter about the x-z plane can be leveraged to simplify the moment equations. Due to this symmetry, the products of inertia I_{yz} and I_{xy} can be considered negligible. This simplification results in a reduced form of the equations of motion, similar to those commonly used for airplanes, which also typically possess a single plane of symmetry resulting in the following reduced form:

$$L = I_x\dot{p} - I_{xz}\dot{r} - I_{xz}pq + (I_z - I_y)qr \tag{6.70}$$

$$M = I_y\dot{q} + (I_x - I_z)pr + I_{xz}(p^2 - r^2) \tag{6.71}$$

$$N = -I_{xz}\dot{p} + I_z\dot{r} + (I_y - I_x)pq + I_{xz}qr \tag{6.72}$$

6.6.4. Gyroscopic Moments

In the previous section, the moment equations excluded the rotational effects of the motors. However, as noted by Stepaniak [66], the gyroscopic effects of the spinning motors can become significant, particularly because multirotors operate at relatively low speeds. These effects are so pronounced that the torque generated by the motors serves as the primary mechanism for yaw control. Due to their importance, the gyroscopic moments are incorporated into the moment equations as defined below, where H denotes the total angular momentum of the motors for x, y, and z in accordance to Equation 6.76, Equation 6.77 and Equation 6.78.

$$L = I_x\dot{p} - I_{xz}\dot{r} - I_{xz}pq + (I_z - I_y)qr + \dot{H}_x + H_zq - H_yr \tag{6.73}$$

$$M = I_y\dot{q} + (I_x - I_z)pr + I_{xz}(p^2 - r^2) + \dot{H}_y + H_xr - H_zp \tag{6.74}$$

$$N = -I_{xz}\dot{p} + I_z\dot{r} + (I_y - I_x)pq + I_{xz}qr + \dot{H}_z + H_yp - H_xq \tag{6.75}$$

$$H_x = \sum_{i=1} I_x^i\omega_x^i + I_{xy}^i\omega_y^i + I_{xz}^i\omega_z^i \tag{6.76}$$

$$H_y = \sum_{i=1} I_y^i\omega_y^i + I_{xy}^i\omega_x^i + I_{yz}^i\omega_z^i \tag{6.77}$$

$$H_x = \sum_{i=1} I_z^i\omega_z^i + I_{zy}^i\omega_y^i + I_{xz}^i\omega_x^i \tag{6.78}$$

Considering the angular momentum of the motors, which are symmetric about the x-z and y-z planes, the products of inertia of the motors are negligible, such that $I_{xy} = I_{yz} = I_{xz} = 0$. Here, I^i and ω^i represent the moment of inertia and angular velocity of the i^{th} motor, respectively. Additionally, since the motor shafts are parallel to the z-axis, the angular momentum of each motor is limited to the z-axis, resulting in $\omega_x = 0$ and $\omega_y = 0$. Consequently, the components of angular momentum along the x- and y-axes vanish, i.e., $H_x = 0$ and $H_y = 0$, while H_z is described by Equation 6.83.

The time rate of change of angular momentum is defined as torque, expressed as $\dot{H} = Q$. This relationship modifies the equations of motion to include gyroscopic moments, which are simplified to Equation 6.79, Equation 6.80, and Equation 6.81. In these equations, Q is determined for each i^{th} rotor, as described by Equation 6.84. The resulting torque about the z-axis arises due to action-reaction forces: as the rotors rotate, they exert a torque on the airframe, with the reaction torque Q^i defined with Equation 6.82.

$$L = I_x\dot{p} - I_{xz}\dot{r} - I_{xz}pq + (I_z - I_y)qr + H_z q \tag{6.79}$$

$$M = I_y\dot{q} + (I_x - I_z)pr + I_{xz}(p^2 - r^2) - H_z p \tag{6.80}$$

$$N = -I_{xz}\dot{p} + I_z\dot{r} + (I_y - I_x)pq + I_{xz}qr + Q \tag{6.81}$$

$$C_Q = \frac{Q_i}{\rho A V_{tip}^2 R} = \frac{Q_i}{\rho A \Omega^2 R^3} \tag{6.82}$$

$$H_z = \sum_{i=1} I_z^i \omega_z^i \tag{6.83}$$

$$Q = \sum_{i=1} Q^i \tag{6.84}$$

6.6.5. External Forces

Three primary external forces influence the multicopter: gravity, thrust, and aerodynamic forces. These forces are fundamental in shaping the equations of motion and are incorporated into the previously developed dynamic model. Figure 6.19 schematically illustrates the force conventions for an example multirotor, including rotor thrust, rotor torque in the direction of rotation, and weight. Meanwhile, Figure 6.20 depicts the resultant thrust, moments, torque, and aerodynamic forces.

It should be noted however that for modeling purposes, distributed forces such as thrust and drag are represented as point forces. This assumption simplifies the computational framework, making it more efficient for the preliminary design phase.

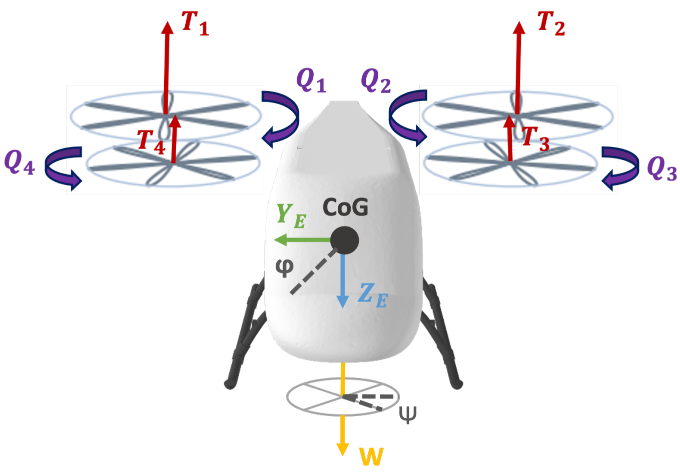

Figure 6.19: Rotor forces and torques of a multirotor schematic with 4 rotors together with yaw and roll angle convention

Gravity

In the context of multirotor dynamics, most forces, torques, and other factors exist in the body-fixed frame, while gravity is the only force naturally defined in the earth inertial frame [69]. In the inertial frame, the z-axis aligns with the local gravity vector, resulting in a positive gravitational force as expressed in Equation 6.85. When transformed into the body frame with using Equation 6.53, the gravitational force is represented by Equation 6.86.

It should be noted that since gravity acts uniformly across the entire mass of the multirotor, it can be treated as a single force passing through the center of gravity (CoG). As a result, gravity does not generate any associated moment terms, simplifying its integration into the equations of motion. Furthermore note that it is assumed that the gravity field is constant at $9.81[m/s^2]$

$$F_g = \begin{bmatrix} 0 \\ 0 \\ mg \end{bmatrix} \tag{6.85}$$

$$F_g^b = mg \begin{bmatrix} -\sin\theta \\ \sin\phi\cos\theta \\ \cos\phi\cos\theta \end{bmatrix} \tag{6.86}$$

Thrust

Thrust is the dominant external force acting on a multicopter, generated by the rotors. Unlike gravity, thrust is applied at the center of each rotor disk and is aligned with the motor shaft in the body-fixed frame as displayed in Figure 6.19. Since the motor shafts are oriented along the z-axis, the x and y components of thrust are zero, as is the moment about the z-axis due to thrust. This is mathematically expressed as $T_x = 0$, $T_y = 0$, $N_T = 0$, and $T_z = T$. The total thrust along the z-axis,Equation 6.90, is the sum of the thrust produced by all i rotors, individually expressed with Equation 6.87.

Thrust also contributes to moments when the rotor disk is not aligned with the CoG. In such cases, the offset creates a moment arm, generating moments about the CoG. These moments are proportional to the distances x' and y' from the rotor disk to the x- and y-axes in the x-y plane. The moments about the x- and y-axes are expressed in Equation 6.88 and Equation 6.89, respectively as displayed in Figure 6.20.

$$C_{T_i} = \frac{T_i}{\rho A_i V_{tip_i}^2} = \frac{T_i}{\rho A_i \Omega_i^2 R_i^2} \tag{6.87}$$

$$L_T = \sum_{i=1} x_i' T_i \tag{6.88}$$

$$M_T = \sum_{i=1} y_i' T_i \tag{6.89}$$

$$T = \sum_{i=1} T_i \tag{6.90}$$

Aerodynamic Forces

The total drag acting on a multicopter is composed of several components, each arising from different aerodynamic phenomena as enumerated below. These include parasitic drag, which increases with the square of the flight velocity; induced drag, or drag due to lift, which decreases inversely with velocity, and profile drag, which results from the rotor blades moving through the air [46]. While induced and profile drag are associated with rotor dynamics, parasitic drag arises from the shape and surface characteristics of the aircraft. It should be noted that no drag force from the side of the fuselage in yaw is assumed.

1. **Parasitic Drag:** Drag arising from the multicopter's non-lifting surfaces, such as the fuselage, arms, landing gear, and other structural components.
2. **Induced Drag:** Drag generated as a byproduct of lift production by the rotors.
3. **Profile Drag:** Drag due to the aerodynamic resistance of the rotor blades themselves.

In accordance with the "*Guidelines for a First Dimensioning of Helicopter Rotors* [46], the profile drag force on rotor blades is excluded from the multicopter dynamics analysis of forces acting on the vehicle in forward flight. This exclusion simplifies the force modeling for system dynamics but may introduce slight inaccuracies in predicting aerodynamic forces, especially at higher forward velocities where profile drag contributes significantly to the total force balance. Such underestimation could affect the predicted acceleration and deceleration characteristics during dynamic maneuvers. Additionally, profile drag plays a role in damping forces on the rotors, and its omission may lead to underestimating damping effects, potentially resulting in overpredictions of oscillatory or unstable behavior in the dynamic response. While this simplification is considered acceptable at this stage, incorporating profile drag in future refinements could enhance the accuracy of the dynamic behavior analysis. Furthermore, it is important to note that profile drag is included in the power requirements model, ensuring its impact on performance predictions, particularly in terms of power consumption, is captured.

Similarly, the induced drag is assumed to have a negligible contribution to the aerodynamic forces in the Multicopter Dynamics model and is therefore excluded from the external force calculations. This assumption is based on the observation that induced drag decreases significantly with increasing advance ratio in forward flight, making its contribution relatively minor under such conditions. Nevertheless, this is a strong assumption whose validity depends on the specific flight regime. While the induced drag term is included in the power requirements model to ensure accurate power predictions, its exclusion from the Multicopter Dynamics analysis may affect the fidelity of the dynamic model, particularly during hover or low-speed forward flight. Induced drag contributes to resistance against changes in motion, particularly during vertical or axial movements. Omitting this term might lead to overly optimistic predictions of the vehicle's responsiveness to control inputs. Future iterations of the model could incorporate induced drag into the dynamic analysis to provide a more comprehensive representation of the forces acting on the multicopter.

It is important to acknowledge that this approach simplifies the drag estimation, as real-world rotor interactions can significantly influence overall drag, especially in varying flight regimes. For instance, in forward flight, the tilt of the multicopter and varying relative airspeeds across the vehicle's surfaces can alter the effective drag. Furthermore rotor wake interactions, body interference effects, and non-uniform flow patterns can significantly affect drag in real-world scenarios but for simplification reasons this is ignored for the preliminary design phase.

Given the absence of wings or a lifting body, and to simplify the aerodynamic forces acting on the multicopter as mentioned above, this study assumes that the aerodynamic effects are limited to the parasitic drag of the fuselage. This drag is modeled using Equation 6.91, with the drag force assumed to act through the center of gravity. The area terms influencing parasitic drag are derived in Section 6.2. Under this assumption, no aerodynamic moments are generated, and the net drag forces acting on the multicopter in the equations of motion (EOM) are described by the parasitic aerodynamic force components C_x, C_y, and C_z.

$$D_p = \frac{1}{2}\rho V^2 C_D A \tag{6.91}$$

Parasitic Drag in Hover In hover, the multicopter remains stationary relative to the ground with no translational motion. However, the downwash from the rotors induces airflow around the fuselage, creating some parasitic drag where for conventional rotorcraft this effect is accounted for using the so-called "Download Factor." In contrast, for multicopters, where the fuselage is not fully within the rotor wake, this term is ignored for the preliminary analysis. Consequently, the parasitic drag force components are assumed to be $C_x = C_y = C_z = 0$ during hover.

Parasitic Drag in Axial Flight In axial flight (ascending or descending), the multicopter experiences a vertical velocity component that increases the relative airflow over the fuselage and other structural elements. Since the fuselage has the largest surface area and contributes the most to parasitic drag, the effects of other non-lifting surfaces are neglected in this analysis. As a result, the drag components are simplified to $C_z = D_{p_{axial}}$, where $D_{p_{axial}}$ represents the parasitic drag acting in the axial direction. The corresponding drag coefficient and area terms are derived in Section 6.2.

$$D_{p_{axial}} = \frac{1}{2}\rho w^2 C_{D_{top/bottom}} A_{top/bottom} \tag{6.92}$$

Parasitic Drag in Cruise During cruise flight, the multicopter tilts its airframe forward to generate horizontal motion. This tilt redirects a portion of the rotor thrust to counteract drag and sustain forward flight. As a result, in the cruise phase, parasitic drag is modeled as acting along the vehicle's forward axis and is balanced by the horizontal thrust component to maintain steady flight, as schematically illustrated in Figure 6.20, represented by C_x. The term $C_{D_{front}}$ in Equation 6.93 denotes the drag coefficient associated with the front of the fuselage, derived in Section 6.2 alongside the estimated frontal area A_{front}.

$$D_{p_{cruise}} = \frac{1}{2}\rho u^2 C_{D_{front}} A_{front} \tag{6.93}$$

6.6.6. Full Non-linear Equations of Motion

The derivation of the full nonlinear equations of motion is based on several key assumptions to simplify the modeling of the multicopter's kinematics and dynamics. It is assumed that the multicopter behaves as a rigid body with a symmetrical structure along the x-z plane. Furthermore, the Earth's rotation is neglected, and the atmosphere is considered stationary. These assumptions help isolate the vehicle's dynamics from external environmental complexities, ensuring a more tractable model.

A critical design consideration is the use of counter-rotating rotors, as also illustrated in Figure 6.19, with a layout mirrored across the z-x plane. The symmetric arrangement of rotor rotational directions ensures that the moments of inertia remain constant, and as a result, the total angular momentum about the z-axis, H_z, is zero under trim conditions. Similarly, the total torque about the z-axis is also zero, which further simplifies the analysis.

Incorporating the effects of gravity (in the form of weight), along with the total thrust, torque, and parasitic drag forces, the complete equations of motion are derived. These are shown schematically in Figure 6.20, where the total thrust force (T), total torque (Q), weight (W), and parasitic fuselage drag components (C_X, C_Y, and C_Z) are included as described by Equation 6.94, Equation 6.95, and Equation 6.96. Additionally, moments due to thrust imbalances between rotors, ΔL_T (roll moment) and ΔM_T (pitch moment), are accounted for in the body frame.

These simplifications provide the basis for analyzing the dynamics and stability of the multicopter under various flight conditions. The analysis considers both translational and rotational dynamics, expressed in terms of aerodynamic force coefficients, total thrust, total torque, and coefficients related to moments caused by thrust imbalances, as described below.

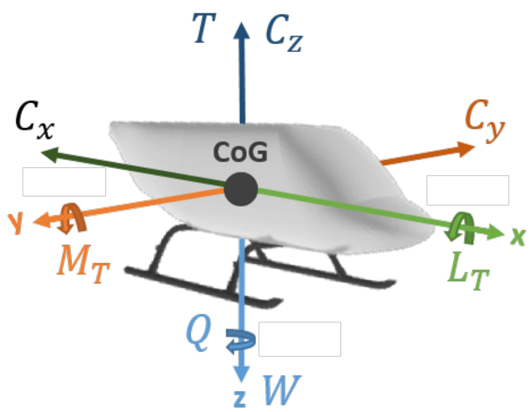

Figure 6.20: External forces and moments of the multirotor schematic in body frame

$$C_x = \frac{1}{2}\rho u^2 C_{D_{front}} A_{front} \tag{6.94}$$

$$C_y = \frac{1}{2}\rho v^2 C_{D_{side}} A_{side} \tag{6.95}$$

$$C_z = \frac{1}{2}\rho w^2 C_{D_{top/bottom}} A_{top/bottom} \tag{6.96}$$

Translational Dynamics expressed in terms of accelerations

$$\dot{u} = -g\sin\theta - \frac{C_x}{m} - qw + rv \tag{6.97}$$

$$\dot{v} = g\sin\phi\cos\theta - \frac{C_y}{m} - ru + pw \tag{6.98}$$

$$\dot{w} = g\cos\phi\cos\theta - \frac{T}{m} - \frac{C_z}{m} - pv + qu \tag{6.99}$$

Rotational Dynamics expressed in terms of angular accelerations

$$\dot{p} = \frac{I_z}{I_x I_z - I_{xz}^2} L_T + \frac{I_y I_z - I_z^2 - I_{xz}^2}{I_x I_z - I_{xz}^2} rq + \frac{I_{xz}(I_x - I_y + I_z)}{I_x I_z - I_{xz}^2} pq - \frac{H_z}{I_x} q \tag{6.100}$$

$$\dot{q} = \frac{M_T}{I_y} + \frac{(I_z - I_x)pr}{I_y} + \frac{I_{xz}}{I_y}(r^2 - p^2) + \frac{H_z}{I_y} p \tag{6.101}$$

$$\dot{r} = \frac{I_{xz}}{I_x I_z - I_{xz}^2} L_T + \frac{I_x^2 - I_x I_y + I_{xy}^2}{I_x I_z - I_{xz}^2} pq - \frac{I_{xz}(I_x - I_y + I_z)}{I_x I_z - I_{xz}^2} rq - \frac{Q}{I_z} \tag{6.102}$$

6.6.7. Linearized Equations of Motion

Linearization is a fundamental technique in flight dynamics that simplifies the mathematical representation of a system, allowing the application of well-established linear control theories and analysis tools such as root locus and state-space methods. By linearizing the equations of motion around a hover condition or any equilibrium point, a valid approximation can be achieved for small perturbations about the operating point. This process is particularly useful during the preliminary design phase to assess system stability, control effectiveness, and disturbance rejection capabilities. While the linearized model provides valuable insights, it is important to note that its validity is limited to small deviations from the equilibrium point. Consequently, the full dynamics of the system under larger disturbances are not captured.

The linearization itself is performed by applying a first-order Taylor series expansion to the nonlinear equations of motion (EOM), as derived below, while eliminating higher-order terms. As discussed earlier in Section 6.6.6, the total angular momentum about the z-axis, H_z, and the total torque under trim conditions are zero, i.e., $Q = H_z = 0$. Each equation is expanded around the trim condition, with small perturbations from the equilibrium point denoted by Δ, resulting in the following perturbation variables:

1. $u = u_0 + \Delta u$
2. $v = v_0 + \Delta v$
3. $w = w_0 + \Delta w$
4. $\phi = \phi_0 + \Delta\phi$
5. $\theta = \theta_0 + \Delta\theta$
6. $\psi = \psi_0 + \Delta\psi$
7. $p = p_0 + \Delta p$
8. $q = q_0 + \Delta q$
9. $r = r_0 + \Delta r$
10. $T = T_0 + \Delta T$
11. $Q = Q_0 + \Delta Q$
12. $L_T = L_{T_0} + \Delta L_T$
13. $M_T = M_{T_0} + \Delta M_T$

The linearized EOM around the nominal values, described by Equation 6.107, Equation 6.108, Equation 6.109, Equation 6.110, Equation 6.112, and Equation 6.111, are obtained through a Taylor series expansion. Perturbation variables are substituted, and higher-order terms are neglected. For instance, the Taylor expansion of $\sin(\theta_0 + \Delta\theta)$ is performed as shown in Equation 6.103. The aerodynamic terms contributing to the linearized model are provided by Equation 6.104, Equation 6.105, and Equation 6.106.

$$f(a + \Delta x) \approx f(a) + f'(a)\Delta x \tag{6.103}$$

$$C_x = \frac{1}{2}\rho\left(u_0^2 + 2u_0\Delta u\right) C_{D_{front}} A_{front} \tag{6.104}$$

$$C_y = \frac{1}{2}\rho\left(v_0^2 + 2v_0\Delta v\right) C_{D_{side}} A_{side} \tag{6.105}$$

$$C_z = \frac{1}{2}\rho\left(w_0^2 + 2w_0\Delta w\right) C_{D_{top/bottom}} A_{top/bottom} \tag{6.106}$$

Linearized Translational Dynamics expressed in terms of accelerations

$$\dot{u} = -g\left(\sin(\theta_0) + \cos(\theta_0)\Delta\theta\right) - \frac{C_x}{m} - \left(q_0 w_0 + q_0\Delta w + w_0\Delta q\right) + \left(r_0 v_0 + r_0\Delta v + v_0\Delta r\right) \tag{6.107}$$

$$\begin{aligned}\dot{v} =& g\Big(\sin(\phi_0)\cos(\theta_0) + \cos(\phi_0)\cos(\theta_0)\Delta\phi - \sin(\phi_0)\sin(\theta_0)\Delta\theta\Big) \\ &- \frac{C_y}{m} - \big(r_0 u_0 + r_0\Delta u + u_0\Delta r\big) + \big(p_0 w_0 + p_0\Delta w + w_0\Delta p\big)\end{aligned} \tag{6.108}$$

$$\begin{aligned}\dot{w} =& g\Big(\cos(\phi_0)\cos(\theta_0) - \cos(\phi_0)\sin(\theta_0)\Delta\theta - \sin(\phi_0)\cos(\theta_0)\Delta\phi\Big) \\ &- \frac{T_0 + \Delta T}{m} - \frac{C_z}{m} - \big(p_0 v_0 + p_0\Delta v + v_0\Delta p\big) + \big(q_0 u_0 + q_0\Delta u + u_0\Delta q\big)\end{aligned} \tag{6.109}$$

Linearized Rotational Dynamics expressed in terms of angular accelerations

$$\begin{aligned}\dot{p} =& \frac{I_z}{I_x I_z - I_{xz}^2}(L_{T_0} + \Delta L_T) + \frac{I_y I_z - I_z^2 - I_{xz}^2}{I_x I_z - I_{xz}^2} r_0 q_0 + \frac{I_{xz}(I_x - I_y + I_z)}{I_x I_z - I_{xz}^2} p_0 q_0 \\ &+ \frac{I_y I_z - I_z^2 - I_{xz}^2}{I_x I_z - I_{xz}^2}(r_0\Delta q + q_0\Delta r) + \frac{I_{xz}(I_x - I_y + I_z)}{I_x I_z - I_{xz}^2}(p_0\Delta q + q_0\Delta p)\end{aligned} \tag{6.110}$$

$$\begin{aligned}\dot{q} =& \frac{(M_{T_0} + \Delta M_T)}{I_y} + \frac{(I_z - I_x)}{I_y} p_0 r_0 + \frac{I_{xz}}{I_y}(r_0^2 - p_0^2) \\ &+ \frac{(I_z - I_x)}{I_y}(r_0\Delta p + p_0\Delta r) + \frac{I_{xz}}{I_y}(2r_0\Delta r - 2p_0\Delta p)\end{aligned} \tag{6.111}$$

$$\begin{aligned}\dot{r} =& \frac{I_{xz}}{I_x I_z - I_{xz}^2}(L_{T_0} + \Delta L_T) + \frac{I_x^2 - I_x I_y + I_{xz}^2}{I_x I_z - I_{xz}^2} p_0 q_0 - \frac{I_{xz}(I_x - I_y + I_z)}{I_x I_z - I_{xz}^2} r_0 q_0 \\ &+ \frac{I_x^2 - I_x I_y + I_{xz}^2}{I_x I_z - I_{xz}^2}(p_0\Delta q + q_0\Delta p) - \frac{I_{xz}(I_x - I_y + I_z)}{I_x I_z - I_{xz}^2}(r_0\Delta q + q_0\Delta r) - \frac{Q_0 + \Delta Q}{I_z}\end{aligned} \tag{6.112}$$

6.6.8. Hover Trim Condition

The hover trim condition, schematically illustrated in Figure 6.21, represents a state of equilibrium where the multicopter remains stationary in hover. In this condition, the initial roll and pitch angles are both zero, as are all moments about the x, y, and z axes. The earth reference frame is defined by the axes X_E, Y_E, and Z_E. Additionally, the initial linear velocities u_0, v_0, and w_0, as well as the angular rates p_0, q_0, and r_0, are all zero. The absence of torques from thrust ensures that L_{T_0}, M_{T_0}, and Q_0 are also zero. Consequently, all initial states are assumed to be zero except for the initial thrust T_0, which equals the weight of the multicopter during hover. This assumption significantly simplifies the system dynamics. Under these conditions, the aerodynamic force coefficients reduce to $C_x = 0$, $C_y = 0$, and $C_z = 0$, indicating no net aerodynamic forces acting along the body-fixed axes. These simplifications lead to the following reduced equations of motion, which govern the translational and rotational dynamics:

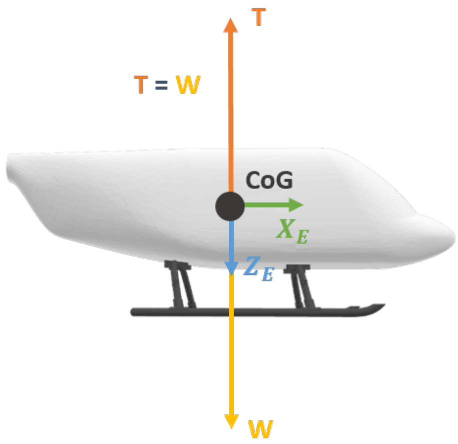

Figure 6.21: Hover trim condition forces and moments on multirotor schematics

Hover Trim Translational Dynamics expressed in terms of accelerations

$$\dot{u} = -g\Delta\theta \tag{6.113}$$

$$\dot{v} = g\Delta\phi \tag{6.114}$$

$$\dot{w} = -\frac{\Delta T}{m} \tag{6.115}$$

Hover Trim Rotational Dynamics expressed in terms of angular accelerations

$$\dot{p} = \frac{I_z}{I_x I_z - I_{xz}^2}\Delta L_T \tag{6.116}$$

$$\dot{q} = \frac{\Delta M_T}{I_y} \tag{6.117}$$

$$\dot{r} = \frac{I_{xz}}{I_x I_z - I_{xz}^2}\Delta L_T - \frac{\Delta Q}{I_z} \tag{6.118}$$

6.6.9. Longitudinal trim condition

In the steady cruise trim condition, the initial yaw angle is assumed to be zero to eliminate sideslip during forward flight. Similarly, the initial roll angle is set to zero to maintain a longitudinal trim condition, ensuring no initial velocities concerned with v_0 and w_0. However, unlike in hover, the initial pitch angle θ_0, equal to the angle of the rotor disk α_d with the free stream velocity, and forward velocity u_0 are nonzero. The horizontal thrust component required to sustain forward flight is achieved through the pitch angle relative to the earth reference frame, defined by the axes X_E, Y_E, and Z_E, as shown schematically in Figure 6.22, which illustrates the cruise trim condition along with the relevant velocity components, forces, and angles.

While the pitch angle and forward velocity in the x-direction are nonzero, the initial torques L_{T_0}, M_{T_0}, and Q_0, as well as the initial angular rates p_0, q_0, and r_0 , remain zero. Consequently, the thrust T_0 no longer equals the weight of the multirotor but must account for both lift and the horizontal force required for steady cruise. The expression for the horizontal thrust component in cruise can be derived from Equation 6.50 as further detailed in Section 6.5.4. This horizontal thrust component is then the balance force to counteract the parasitic drag term, C_x, due to the initial forward velocity, as described by Equation 6.119, while the aerodynamic force coefficients C_y and C_z remain zero. As a result, the equations of motion (EOM) for the longitudinal trim condition simplify to the following translational and rotational dynamics:

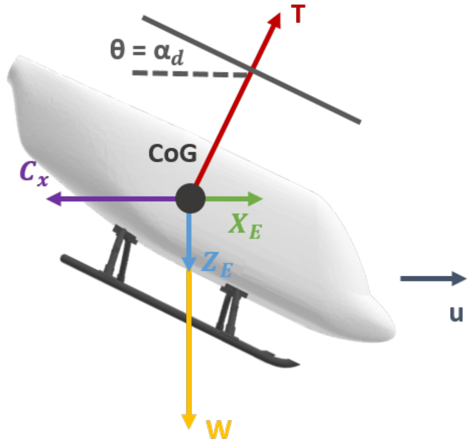

Figure 6.22: Cruise trim condition forces, moments and pitch angle on multirotor schematic

$$C_x = \frac{1}{2}\rho\left(u_0^2 + 2u_0\Delta u\right) C_{D_{front}} A_{front} \tag{6.119}$$

$$C_y = 0 \tag{6.120}$$

$$C_z = 0 \tag{6.121}$$

Linearized Translational Dynamics expressed in terms of accelerations

$$\dot{u} = -g\left(\sin(\theta_0) + \cos(\theta_0)\Delta\theta\right) - \frac{\frac{1}{2}\rho\left(u_0^2 + 2u_0\Delta u\right) C_{D_{front}} A_{front}}{m} \tag{6.122}$$

$$\dot{v} = g\cos(\theta_0)\Delta\phi - u_0\Delta r \tag{6.123}$$

$$\dot{w} = g\Big(\cos(\theta_0) - \sin(\theta_0)\Delta\theta\Big) - \frac{T_0 + \Delta T}{m} + u_0\Delta q \tag{6.124}$$

Linearized Rotational Dynamics expressed in terms of angular accelerations

$$\dot{p} = \frac{I_z}{I_x I_z - I_{xz}^2}\Delta L_T \tag{6.125}$$

$$\dot{q} = \frac{\Delta M_T}{I_y} \tag{6.126}$$

$$\dot{r} = \frac{I_{xz}}{I_x I_z - I_{xz}^2}\Delta L_T - \frac{\Delta Q}{I_z} \tag{6.127}$$

6.7. State-Space System

To assess the stability of the multicopter, a state-space representation is utilized. This approach provides a concise mathematical framework for modeling the physical system, capturing the relationship between inputs and outputs through first-order differential equations. The state-space model describes the system's dynamics as a vector of states evolving over time within a defined state space.

The state-space representation is defined by the state vector **x** (Equation 6.129), the input or control vector **u** (Equation 6.130), the system matrix **A**, and the input matrix **B** [70]. The state vector **x** comprises the key dynamic variables of the multicopter, while the control vector **u** encapsulates the control inputs. Specifically, the control vector includes the following components:

1. The change in total upward force due to total thrust, ΔT.
2. The change in roll moment around the x-axis caused by thrust imbalances, ΔL_T.
3. The change in pitch moment around the y-axis caused by thrust imbalances, ΔM_T.
4. The change in yaw moment around the z-axis due to net torque, ΔQ.

$$\dot{x} = Ax + Bu \tag{6.128}$$

$$x^T = \begin{bmatrix} \Delta x & \Delta y & \Delta z & \Delta u & \Delta v & \Delta w & \Delta \phi & \Delta \theta & \Delta \psi & \Delta p & \Delta q & \Delta r \end{bmatrix} \tag{6.129}$$

$$u^T = \begin{bmatrix} \Delta T & \Delta L_T & \Delta M_T & \Delta Q \end{bmatrix} \tag{6.130}$$

To compute the A and B matrices, the partial derivatives of the equations of motion (EOM) with respect to each state and input variable are evaluated at the trim conditions for both hover and longitudinal trim cases, as described below. The state matrix, A, is obtained as the Jacobian of the system dynamics with respect to the state vector, while the input matrix, B, is derived as the Jacobian of the system dynamics with respect to the input vector. Each element of these matrices corresponds to $\frac{\partial f_i}{\partial x_j}$ and $\frac{\partial f_i}{\partial u_j}$, respectively.

This process results in the A and B matrices, which are defined in Equation 6.131 and Equation 6.132 for the hover trim condition, and in Equation 6.133 and Equation 6.134 for the longitudinal trim condition. These matrices provide a linearized representation of the system dynamics around the respective trim points, facilitating stability and control analysis.

Hover system

$$A = \begin{bmatrix}
0 & 0 & 0 & 1 & 0 & 0 & 0 & 0 & 0 & 0 & 0 & 0 \\
0 & 0 & 0 & 0 & 1 & 0 & 0 & 0 & 0 & 0 & 0 & 0 \\
0 & 0 & 0 & 0 & 0 & 1 & 0 & 0 & 0 & 0 & 0 & 0 \\
0 & 0 & 0 & 0 & 0 & 0 & 0 & -g & 0 & 0 & 0 & 0 \\
0 & 0 & 0 & 0 & 0 & 0 & g & 0 & 0 & 0 & 0 & 0 \\
0 & 0 & 0 & 0 & 0 & 0 & 0 & 0 & 0 & 0 & 0 & 0 \\
0 & 0 & 0 & 0 & 0 & 0 & 0 & 0 & 0 & 1 & 0 & 0 \\
0 & 0 & 0 & 0 & 0 & 0 & 0 & 0 & 0 & 0 & 1 & 0 \\
0 & 0 & 0 & 0 & 0 & 0 & 0 & 0 & 0 & 0 & 0 & 1 \\
0 & 0 & 0 & 0 & 0 & 0 & 0 & 0 & 0 & 0 & 0 & 0 \\
0 & 0 & 0 & 0 & 0 & 0 & 0 & 0 & 0 & 0 & 0 & 0 \\
0 & 0 & 0 & 0 & 0 & 0 & 0 & 0 & 0 & 0 & 0 & 0
\end{bmatrix} \tag{6.131}$$

$$B = \begin{bmatrix}
0 & 0 & 0 & 0 \\
0 & 0 & 0 & 0 \\
0 & 0 & 0 & 0 \\
0 & 0 & 0 & 0 \\
0 & 0 & 0 & 0 \\
-\frac{1}{m} & 0 & 0 & 0 \\
0 & 0 & 0 & 0 \\
0 & 0 & 0 & 0 \\
0 & 0 & 0 & 0 \\
0 & \frac{I_z}{I_x I_z - I_{xz}^2} & 0 & 0 \\
0 & 0 & \frac{1}{I_y} & 0 \\
0 & \frac{I_{xz}}{I_x I_z - I_{xz}^2} & 0 & -\frac{1}{I_z}
\end{bmatrix} \tag{6.132}$$

Longitudinal system

$$A = \begin{bmatrix} 0 & 0 & 0 & 1 & 0 & 0 & 0 & 0 & 0 & 0 & 0 & 0 \\ 0 & 0 & 0 & 0 & 1 & 0 & 0 & 0 & 0 & 0 & 0 & 0 \\ 0 & 0 & 0 & 0 & 0 & 1 & 0 & 0 & 0 & 0 & 0 & 0 \\ 0 & 0 & 0 & -\frac{\rho u_0 C_{D_{front}} A_{front}}{m} & 0 & 0 & 0 & -g\cos\theta_0 & 0 & 0 & 0 & 0 \\ 0 & 0 & 0 & 0 & 0 & 0 & g\cos\theta_0 & 0 & 0 & 0 & 0 & -u_0 \\ 0 & 0 & 0 & 0 & 0 & 0 & 0 & -g\sin\theta_0 & 0 & 0 & u_0 & 0 \\ 0 & 0 & 0 & 0 & 0 & 0 & 0 & 0 & 0 & 1 & 0 & 0 \\ 0 & 0 & 0 & 0 & 0 & 0 & 0 & 0 & 0 & 0 & 1 & 0 \\ 0 & 0 & 0 & 0 & 0 & 0 & 0 & 0 & 0 & 0 & 0 & 1 \\ 0 & 0 & 0 & 0 & 0 & 0 & 0 & 0 & 0 & 0 & 0 & 0 \\ 0 & 0 & 0 & 0 & 0 & 0 & 0 & 0 & 0 & 0 & 0 & 0 \\ 0 & 0 & 0 & 0 & 0 & 0 & 0 & 0 & 0 & 0 & 0 & 0 \end{bmatrix} \tag{6.133}$$

$$B = \begin{bmatrix} 0 & 0 & 0 & 0 \\ 0 & 0 & 0 & 0 \\ 0 & 0 & 0 & 0 \\ 0 & 0 & 0 & 0 \\ 0 & 0 & 0 & 0 \\ -\frac{1}{m} & 0 & 0 & 0 \\ 0 & 0 & 0 & 0 \\ 0 & 0 & 0 & 0 \\ 0 & 0 & 0 & 0 \\ 0 & \frac{I_z}{I_x I_z - I_{xz}^2} & 0 & 0 \\ 0 & 0 & \frac{1}{I_y} & 0 \\ 0 & \frac{I_{xz}}{I_x I_z - I_{xz}^2} & 0 & -\frac{1}{I_z} \end{bmatrix} \tag{6.134}$$

6.7.1. State-Space Eigenvalues

This analysis of eigenvalues and eigenvectors is crucial for characterizing the stability, oscillatory properties, and state interactions of the system, forming the foundation for further control design and dynamic analysis. To evaluate the stability and dynamic characteristics of the system, the eigenvalues and eigenvectors of the state-space model are computed. The eigenvalues λ of the system matrix **A** are determined from the characteristic equation, as shown in Equation 6.135, where **I** is the identity matrix. These eigenvalues provide critical insights into the system's stability and dynamic response.

$$\det(\mathbf{A} - \lambda \mathbf{I}) = 0 \tag{6.135}$$

The real part of each eigenvalue indicates the stability of the corresponding mode where a stable Mode has a negative real part signifies that the mode is stable and decays exponentially over time. An Unstable Mode on the other hand has positive real part indicates instability, with the mode growing exponentially over time. At last, Neutral Stability entails a real part equal to zero corresponds to marginal stability, where the mode neither grows nor decays.

The imaginary part of an eigenvalue, if present, represents oscillatory behavior in the system where the magnitude of the imaginary component corresponds to the oscillation frequency of the mode. As a result, a purely real eigenvalue implies no oscillatory motion, while a complex eigenvalue indicates the presence of oscillations.

Each eigenvalue is associated with an eigenvector, which describes the contribution of each state variable to the corresponding mode. The magnitude and direction of each component in the eigenvector determine the influence of the state variable on the dynamics associated with the eigenvalue where larger components of an eigenvector indicate a greater contribution of the corresponding state variable to the mode's dynamics. The eigenvectors also provide insight into the modal structure of the system, aiding in understanding how states interact dynamically.

7 Optimization

In order for the VTOL to fulfill its mission as efficiently and effectively as possible, the flyer must be optimized in accordance with the mission parameters as further elaborated in Section 7.1. The design of an eVTOL is highly multidisciplinary, and therefore, to obtain the preliminary optimal design parameters as a solution to the GoAERO competition, a Multi-Disciplinary Optimization (MDO) approach is employed. MDO helps to integrate various constraints and objectives from different disciplines, resulting in an optimal and feasible solution. The disciplines incorporated for this optimization include a Dynamics model, Rotor model, Power & Energy model and Structure model.

It should be noted however, as the optimization focuses on minimizing the flyer's mass, the inherent nonlinearity in the mass estimation, as outlined in Chapter 6, classifies the optimization scheme as nonlinear. This nonlinearity is further reinforced by the constraints, which also exhibit nonlinear behavior, as discussed in Section 7.4. Following this, the chosen optimization technique to deal with the non-linear optimization scheme is elaborated upon in Section 7.7.

7.1. Optimisation Case

As outlined in Chapter 2, the productivity mission represents the most demanding scenario in terms of endurance and mass. This is due to its emphasis on the Payload-to-System Mass ratio ranking and the overall power requirements, making it critical for sizing the eVTOL's propulsion system and configuration. The mission entails ferrying a maximum payload of 144.6 kg (**REQ-OPS-01**) over a total horizontal distance of 2412 m, followed by a landing, and repeating this process until a cumulative payload of 567 kg is transported.

To satisfy these requirements, the eVTOL must complete the mission in multiple cycles, encompassing four flights with payload and four return flights without payload, amounting to a total mission distance of 19.3 km in accordance with **REQ-PERF-01**. This demanding operational profile necessitates a robust optimization framework that accounts for the interplay between payload capacity, energy efficiency, and propulsion system performance.

The flight profile for this mission includes distinct phases of steady-level climb, steady cruise, and hover, as illustrated in Figure 7.1. These phases impose specific performance requirements on the eVTOL's design, with the cruise altitude defined as detailed in Chapter 5 and in accordance with **REQ-PERF-02**. It should be noted that the cruise phase is the most energy-intensive phase for the productivity mission and thus plays a pivotal role in determining the overall system efficiency and impact of the optimization process.

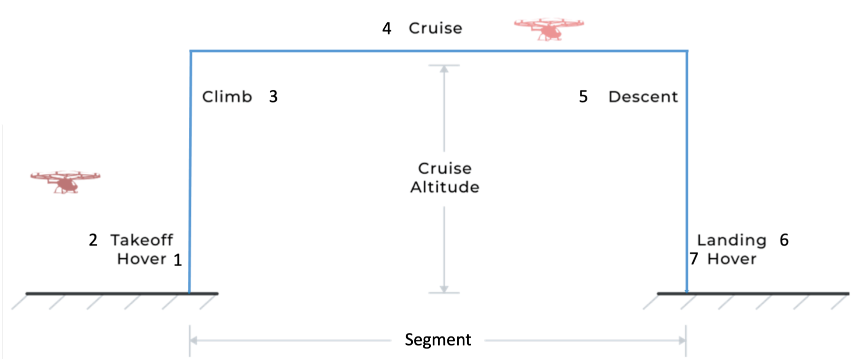

Figure 7.1: Optimisation mission profile

7.2. Objective Function

The main objective is to optimize the propulsion system configuration to minimize the Maximum Take-Off Mass (MTOM) as described in Equation 7.1. The MTOM primarily consists of the operating empty mass and useful mass, as previously discussed in Section 6.3 and formulated in Equation 6.2. It should be noted that in this optimization process, the battery mass, propulsion system mass, airframe mass, and fuel mass are treated as functions of the objective as can aslo be seen in Equation 7.1.

$$f(\bar{x}) = MTOM(\bar{x}) = M_{battery}(\bar{x}) + M_{airframe}(\bar{x}) + M_{propulsion}(\bar{x}) + M_{crew} + M_{payload} + M_{fuel}(\bar{x}) \quad (7.1)$$

7.3. Design Vector

The design variables central to the optimization process are encapsulated within the design vector, as defined in Equation 7.2, where i denotes the ith rotor. These variables serve as the foundation for the optimization, directly influencing the objective function and ultimately guiding the design towards achieving the minimum Maximum Takeoff Mass (MTOM). The design variables are carefully selected to align with the principles of momentum theory, as detailed in Section 6.5. These variables include key rotor-specific parameters that influence aerodynamic performance, power requirements, and overall system efficiency.

It should be noted, however, while the momentum theory provides valuable insights, it is an idealized model that does not account for real-world factors such as blade shape or blade twist. Notably, the assumption of no twist in the propeller design simplifies the analysis but introduces limitations, as blade twist impacts aerodynamic efficiency and overall aerodynamic performance by optimizing the angle of attack along the blade span. To address this, the design vector incorporates the thrust coefficient as a parameter for each rotor, allowing the optimization process to approximate an optimal required rotor design without explicitly modeling blade twist or shape.

Additionally, the design vector incorporates parameters related to the propulsion support structure, as detailed in Section 6.4.4. These parameters are critical for maintaining the structural integrity and weight efficiency of the multirotor configuration, ensuring it can withstand operational loads while minimizing unnecessary mass. Configuration-specific variables are also included in the design vector, significantly influencing the multirotor's dynamic behavior, as highlighted in Section 6.6, particularly through their impact on overall inertia effects and moment arms. Furthermore, the inclusion of structural and geometric parameters provides a comprehensive approach to the optimization process. This holistic integration ensures that the resulting configuration not only achieves the required performance objectives but also complies with the design constraints imposed by the GoAERO competition.

$$\bar{x} = \begin{bmatrix} c_i \\ x_{rotor_i} \\ y_{rotor_i} \\ z_{rotor_i} \\ N_{blades_i} \\ \Omega_{hover_i} \\ \Omega_{climb_i} \\ \Omega_{cruise_i} \\ \Omega_{descent_i} \\ M\hat{T}OM \\ C_{T_i} \\ r_i \\ r_o \end{bmatrix} \tag{7.2}$$

7.4. Constraints

To ensure a final optimum design that is also feasible, constraints are implemented. These constraints guarantee that the optimization process remains within the feasible design space. For this optimization problem, equality, inequality, and consistency constraints are applied, where the latter ensures the consistency of parameters between disciplines. These constraints are crucial for maintaining data integrity and avoiding inconsistencies that could result in errors or unfeasible designs.

7.4.1. Inequality Constraints

Rotor Dimensional Bound Constraint

As defined by the dimensional requirements of the GoAERO competition, the placement of rotors and their radii must remain within the dimensional bounds, as detailed in Section 5.1.4 and required by **REQ-OPS-02**. To implement this constraint, the following mathematical relations are used to ensure that the rotor centers are at least a distance R from the design space borders.

$$x_{rot} - (x_{min} + R_{rot}) = 0 \tag{7.3}$$

$$(x_{max} - R_{rot}) - x_{rot} = 0 \tag{7.4}$$

$$y_{rot} - (y_{min} + R_{rot}) = 0 \tag{7.5}$$

$$(y_{max} - R_{rot}) - y_{rot} = 0 \tag{7.6}$$

Rotor Overlapping Constraint

To prevent rotors from overlapping and to maintain the assumption of no rotor interaction effects, a constraint is introduced to ensure that the rotors' positions and radii do not overlap. The mathematical representation of this constraint is as follows.

$$\left((x_{rot_1} - x_{rot_2})^2 + (y_{rot_1} - y_{rot_2})^2 - (R_1 + R_2)^2\right) = 0 \tag{7.7}$$

Rotor Solidity

Rotor solidity, a function of the inverse aspect ratio of the propellers and the number of blades, defines the ratio of the blade area to the total disk area, as provided in Equation 6.27. The maximum solidity ratio theoretically equals 1, which implies a fully solid disk where no airflow passes through. Therefore, the solidity factor is constrained to be less than 1.

$$1 - \sigma_{rotor} = 0 \tag{7.8}$$

Achieved Velocity Constraints
To adhere to the TLARs described in Chapter 5, the minimum velocities for each flight phase must be respected. This constraint is implemented as an inequality, ensuring that the optimizer does not limit performance but meets the minimum requirements in accordance with **REQ-PERF-04**. Additionally, during descent, the absolute velocity is limited by an upper bound to avoid a scenario where the optimizer minimizes power by reducing rotor speeds to zero, leading to an unsafe descent. The descent speed is bounded between 6 m/s and 8 m/s [71] (**REQ-PERF-03**).

$$v_{climb} - v_{climb_{min}} = 0 \tag{7.9}$$

$$v_{cruise} - v_{cruise_{min}} = 0 \tag{7.10}$$

$$v_{descent} - v_{descent_{min}} = 0 \tag{7.11}$$

$$v_{descent_{max}} - v_{descent} = 0 \tag{7.12}$$

Motor Power Constraint
To ensure that the optimized design remains within feasible bounds and is technologically achievable, the maximum motor power is constrained to $640,000$ W, as specified in Table 6.4.

$$640000 - P_{rotor_{max}} = 0 \tag{7.13}$$

Rotor Support Structure Deflection Constraint
As discussed in Section 6.4.4, the rotor support structure influences the mass and rotor positions. The deflection of the structure must be limited to 0.001 m to ensure a rigid support system in accordance with **REQ-STRCT-01**. This deflection depends on the length of the support structure and the inner and outer radii of the hollow circular beams.

$$0.001 - \delta_{max} \tag{7.14}$$

Aspect Ratio Constraint
As stated by Diessen [72], the nominal aspect ratio (AR) for manned rotorcraft typically ranges between 14 and 20. The AR, defined in Equation 7.15, is a critical parameter influencing both the structural integrity and aerodynamic performance of the rotor blades. A lower AR increases induced drag, compromising aerodynamic efficiency, while a higher AR poses structural challenges, particularly in maintaining adequate torsional stiffness [46].

$$AR = \frac{R}{c} \tag{7.15}$$

$$AR - 14 = 0 \tag{7.16}$$

$$20 - AR = 0 \tag{7.17}$$

Tip Speed Constraint
The tip speed is a critical design parameter for rotor performance. As explained by Leishman [59], the tip speed of the advancing blade can enter supercritical and supersonic flow regimes, resulting in wave drag and shock-induced separation, leading to increased power requirements and limiting operational speed. To avoid advancing blade compressibility effects, a linear function, as described in Equation 7.19, represents the limit beyond which the advancing blade tip Mach number $M_{T_{adv}}$ causes a significant increase in profile drag [72]. The tip Mach number is defined by Equation 7.20, where the tip speed $V_T = \Omega \cdot R + V$, Ω represents the rotor angular velocity, R the rotor radius, and V the free-stream velocity, while c represents the speed of sound.

It should be noted, however, that the tip speed depends on the relative direction of the incoming flow to the blade rotation. For a propeller perpendicular to the airflow, the combined tip speed is described by Equation 7.18, which accounts for both rotational velocity and translational velocity. This combined speed, referred to as the helical tip speed, is typically considered during climb [73]. During cruise, the tip speed depends on the angle of the rotor disk α_{disk} relative to the airflow, as described in Equation 6.45.

$$V_{T_{helical}} = \sqrt{V_{rot}^2 + V_\infty^2} \tag{7.18}$$

$$M_{T_{adv}} = 0.85 - 0.52\frac{C_T}{\sigma} \tag{7.19}$$

$$M_{T_{adv}} = \frac{V_T}{c} \tag{7.20}$$

On the retreating side, the blade moves away from the free-stream airflow, resulting in potential blade stall due to the required increase in the angle of attack to maintain the same thrust coefficient and disk loading, as explained in Section 6.5.1. To avoid retreating blade stall, Diessen [72] suggests using Equation 7.21 to express the limit of blade loading C_T/σ, in relation to the advance ratio μ. This equation, based on wind tunnel coefficients from Talbot et al. [74], expresses the maximum allowable C_T/σ, which is also the maximum thrust-to-power ratio. The advance ratio μ is defined by Equation 6.49, representing the rotor's forward speed relative to the tip speed.

$$\frac{C_T}{\sigma} = 0.128 - 0.125\mu \tag{7.21}$$

Mathematical Constraints

Additional mathematical constraints are applied to prevent errors related to square roots and trigonometric functions. For example, during climb, the thrust produced must exceed the MTOM, as described in Equation 7.23, while during descent, the thrust must be less than the MTOM, as provided by Equation 7.22. Additionally, for calculations involving $\cos^{-1}(\alpha)$, α must be between -1 and 1 for the result to be real, and the calculated angle must be greater than zero for cruise resulting in the constraints defined by Equation 7.24, Equation 7.25 and Equation 7.26.

$$MTOM \cdot g - T_{descent} = 0 \tag{7.22}$$

$$T_{climb} - MTOM \cdot g = 0 \tag{7.23}$$

$$1 - \frac{MTOM \cdot g}{T_{cruise}} = 0 \tag{7.24}$$

$$\frac{MTOM \cdot g}{T_{cruise}} + 1 = 0 \tag{7.25}$$

$$\alpha - 0 = 0 \tag{7.26}$$

7.4.2. Equality Constraints

Thrust in Hover Constraint

To ensure that the VTOL remains stationary during hover, the thrust produced must be equal to the weight of the eVTOL. This results in the following relation.

$$T_{hover} - (MTOW * g) = 0 \tag{7.27}$$

Moment Constraint

Since steady flight is assumed during all flight phases, all moments around the center of gravity (CoG) must be zero, ensuring that angular rates are also zero. As the system is symmetrical around the x-axis, and with the use of counter-rotating rotors, the yawing moments are assumed to be zero regardless in all flight phases. The pitch moment is provided by the thrust produced by each rotor multiplied by the distance from the CoG, given by $M_y = \bar{x} \cdot T_{rotor}$, where $\bar{x}$ is the distance from the rotor to the CoG.

$$\sum M_{y_{hover}} - 0 = 0 \tag{7.28}$$

$$\sum M_{y_{climb}} - 0 = 0 \tag{7.29}$$

$$\sum M_{y_{cruise}} - 0 = 0 \tag{7.30}$$

$$\sum M_{y_{descent}} - 0 = 0 \tag{7.31}$$

7.4.3. Consistency Constraint

Consistency constraints are essential for maintaining coherence across the various disciplines and subsystems within the Multidisciplinary Design Optimization (MDO) framework. These constraints ensure compatibility by aligning the outputs of one discipline with the inputs required by another. For example, if a parameter is computed within one subsystem, the consistency constraint guarantees that this value is accurately propagated and utilized in subsequent calculations. This alignment prevents conflicts or mismatches, enabling seamless interactions between interconnected disciplines and preserving the integrity of the design process.

In this context, the $MT\hat{O}M$ serves as the consistency variable that bridges the interdependence between disciplines. Determined by the optimizer, $MT\hat{O}M$ is used for calculations across different disciplines while consistency with the objective function is enforced through an equality constraint. This approach ensures alignment between the objective function and the disciplines, maintaining the integrity and effectiveness of the optimization process.

7.5. Bounds

To narrow the design space and facilitate optimization convergence, bounds are introduced. These bounds define the feasible design space and are selected based on what is realistic for a VTOL aircraft and conventional within the aerospace industry, as summarized in Table 7.1.

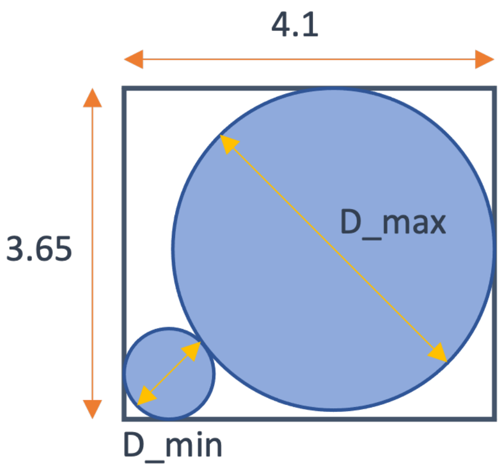

Figure 7.2: Rotor diameter design space

Table 7.1: Design vector bounds

Variable	Lower Bound	Upper Bound
c_i	0.05	0.4
R_{rotor_i} [m]	0.5	1.8
x_{rotor_i} [m]	0	4.1
y_{rotor_i} [m]	0	3.65
z_{rotor_i} [m]	1.9	4.1
N_{blades_i}	2	6
Ω_{hover_i} [rad/s]	0.1	367
Ω_{climb_i} [rad/s]	0.1	367
Ω_{cruise_i} [rad/s]	0.1	367
$\Omega_{\text{descent}_i}$ [rad/s]	0	367
MT$\hat{\text{O}}$M [kg]	400	3000
C_{T_i}	0.01	0.15
r_i [m]	0	0.25
r_o [m]	0.025	0.25

Rotor Radius

The lower bound for the rotor radius is informed by small-sized personal eVTOLs, which typically feature rotor radii ranging from 0.7 m to 0.8 m, as observed in the A³ Vahana [20] and EHang [75]. The upper bound is constrained geometrically by dimensional requirements. For the quadrotor configuration, combined with a minimum rotor radius of 0.5 m (as illustrated in Figure 7.2), the maximum rotor radius is set to 1.8 m.

Rotor Position

The bounds for rotor positions are determined by the design space defined in the TLARs (Section 5.1.4). Dimensional bounds include a length of 4.1 m and a width of 3.65 m. Rotor height is bounded by the fuselage height (1.9 m) and the GoAERO competition's maximum height requirement of 4.1 m. Furthermore the lower bound is defined by the fuselage, ensuring that propulsion support structures do not obstruct access to critical aircraft areas as per **REQ-STRCT-03** and **REQ-PROP-04**.

Number of Blades

The lower bound for the number of blades is set at two, ensuring a balanced rotor configuration. For the upper bound, the five-blade configuration of the Joby S4 serves as a reference [76].

Blade Chord

Bounds for the propeller blade chord length are informed by studies on blade shape optimization [77]. These studies suggest a range between 0.075 m and 0.2 m, consistent with findings from research on rapid blade shape optimization for eVTOL aircraft, which extends the upper limit to 0.35 m [78].

Rotor Rotational Speed

The maximum rotor rotational speed is defined as 3300 rpm, also based on the blade shape optimization work of Xia et al. [77]. The lower bound is 0 rpm, enabling the optimizer to deactivate engines during descent. During climb, hover, and cruise, the lower bound is set to 1 rpm to ensure all rotors remain active.

Rotor Thrust Coefficient

The range for the rotor thrust coefficient is derived from the previously mentioned blade optimization research [77], with the maximum value set at 0.15. This is further supported by NASA's propeller design and performance studies [79].

MTOM

The MTOM bounds are based on existing aircraft. The lower bound references the Volocopter 2X, which has an MTOM of 450 kg [80], while the upper bound is based on the Joby Aviation S4, with an MTOM of 2404 kg [76].

Support Structure Size

As detailed in Section 6.4.4, the rotor support structure is modeled as circular beams with optimizable inner and outer radii. The inner radius ranges from 0 m (allowing solid beams) to the outer radius. The outer radius is constrained between 0.025 m and 0.25 m, ensuring feasible and practical support structure designs based on engineering judgment.

7.6. Extended Design Structure Matrix

With the optimization objective, constraints, and bounds defined, the next step involves structuring the logic of the optimization framework. This framework integrates various disciplines, encapsulated in a Dynamics model, Rotor model, Power & Energy model and Structure model, by programming and interconnecting them to form a cohesive multidisciplinary optimization (MDO) system.

The overall optimization problem is represented using an eXtended Design Structure Matrix (XDSM). The XDSM is a visual tool designed to map MDO processes, highlighting the interactions and interfaces among the components of a complex system. The diagram employs a numbering system, process flow lines, and block connections to illustrate the sequence in which computational steps are executed. This comprehensive depiction enables a clear understanding of data and process flows within the architecture [81].

For this study, a simultaneous optimization approach is employed and implemented in the computational environment. Discipline analyses are simulations that model the behavior of individual aspects of the multidisciplinary system. These analyses involve solving a system of equations and returning specific response variables. Within this approach, the optimizer explicitly enforces consistency constraints while satisfying objectives and other problem constraints. The XDSM effectively captures the direct connections between the optimizer and each discipline, as illustrated in Figure 7.3, offering a clear visualization of the optimization architecture.

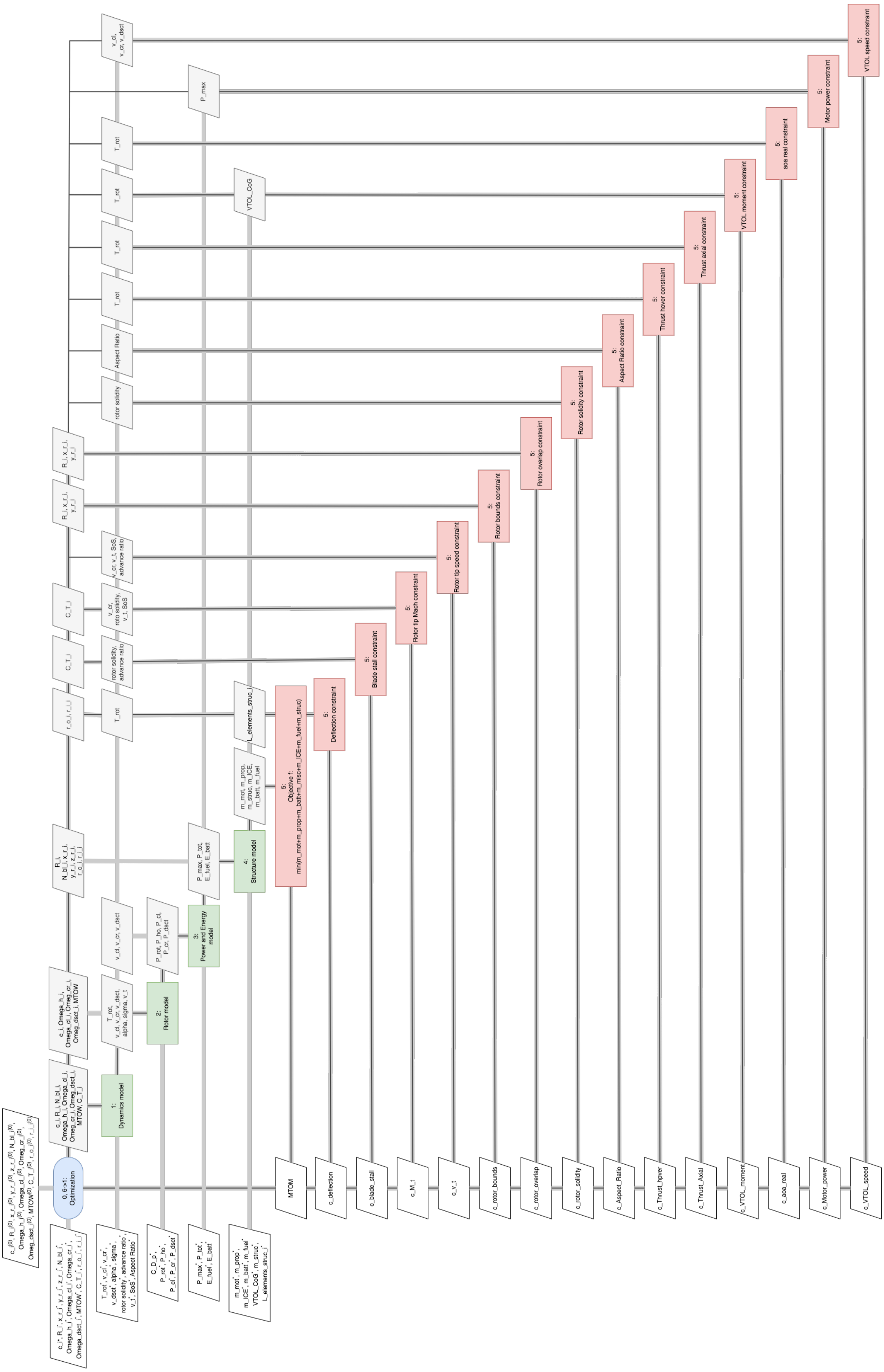

Figure 7.3: XDSM

7.7. Optimizer

7.7.1. Optimizer Characteristics

The optimization process is implemented using the `scipy.optimize.minimize` module, a versatile tool capable of handling scalar functions of one or more variables, where it has various optimization algorithms making it versatile for different types of optimization problems [82]. Among its various optimization algorithms, the Sequential Least Squares Programming (SLSQP) method is selected for this study. The Sequential Least Squares Programming (SLSQP) method is particularly well-suited for solving constrained optimization problems, as it can effectively handle a combination of bounds, equality constraints, and inequality constraints. Moreover, SLSQP is specifically advantageous for addressing nonlinear optimization problems, making it an appropriate choice for the described optimization scheme.

As a gradient-based optimizer, the SLSQP method leverages the gradients (Jacobian) of both the objective function and the constraints to iteratively refine the design variables. This approach enables efficient exploration of the design space, especially for large-scale problems where computational resources are a concern. The reliance on gradient-based techniques ensures that the optimizer can converge to a solution with a high degree of precision while maintaining computational efficiency.

7.7.2. Optimizer Settings

The optimization framework is configured to achieve a balance between convergence accuracy and acceptable runtime with the termination criteria and tolerances are summarized in Table 7.2. The tolerance for the optimization process is set to $1e-8$, striking a balance between high accuracy and manageable convergence times. Additionally, the maximum number of iterations is capped at 25,000 to prevent excessively long runtimes. The `eps` parameter, which defines the step size used for numerical gradient approximation, is left at its default value of $1.4901161193847656e-8$, as specified in the `scipy` documentation [82]. Similarly, the `finite_diff_rel_step` parameter remains unchanged, allowing the relative step size for finite difference approximations to be selected automatically.

Table 7.2: `scipy.optimize.minimize` settings

Option	Setting	Description
`method`	SLSQP	Specifies the method used.
`ftol`	1×10^{-8}	Specifies the precision goal for the value of the objective function in the stopping criterion [82].
`eps`	1.49×10^{-8}	Specifies the step size used for numerical approximation of the Jacobian [82].
`maxiter`	25000	Specifies the maximum number of iterations [82].
`finite_diff_rel_step`	None	Specifies the relative step size used for numerical approximation of the gradient [82].

7.7.3. System Setup

The eVTOL system is developed based on reference eVTOL designs with limited data and different mission requirments, meaning the optimization process does not begin with a feasible design vector. To address this, the optimization framework includes a Multidisciplinary Analysis (MDA) coordinator that configures the system prior to optimization.

The MDA coordinator accepts an initial design vector as input, evaluates all constraints, and determines whether they are satisfied or violated. In cases of constraint violations, it quantifies the severity and provides feedback to the user. This ensures that the starting point of the optimization corresponds to a feasible or near-feasible design vector. To increase the likelihood of achieving a valid global optimum, the process begins with multiple initial design guesses. Among these, the configuration yielding the lowest Maximum Takeoff Mass ($MTOM$) is selected for further analysis.

Normalization of the objective function and constraints is another critical component of the system setup. Normalization addresses challenges arising from variables or constraints with significantly different magnitudes, which can lead to numerical instability, slower convergence, or inaccurate results. By scaling all variables to a similar range, normalization enhances the efficiency of the optimization process, enabling the algorithm to explore the design space more effectively. It also ensures that no single variable disproportionately influences the objective function due to its larger absolute value, thereby preventing bias in the optimization process.

These preparatory measures, being constraint verification and normalization, and the use of multiple initial guesses, are integral to the robustness and reliability of the optimization framework. Together, they ensure the identification of feasible, accurate, and optimal design solutions, providing a solid foundation for the optimization process.

7.7.4. Initial Design Vector

The optimization process begins with an initial set of design variables, as outlined in Table 8.2, Table 8.3, and Table 8.4. These variables establish the baseline parameters for the quadrotor, hexarotor, and octorotor configurations, respectively, based on the reasoning detailed below and the coordinator as outlined in Section 7.7.3.

It should be noted, however, that given the limited availability of multirotor eVTOL data and the highly specific design requirements of the GoAERO competition, the initial design vector is constructed based on predefined bounds and constraints rather than being adapted from an existing configuration. As a result, to ensure the initial design meets thrust requirements while remaining feasible across all rotor configurations, key parameters such as the initial chord length, rotor radius, thrust coefficient, and blade count are deliberately set near their upper bounds.

Furthermore, the initial rotor positions are determined to fit within the dimensional design space without overlap, as shown in Figure 7.4, Figure 7.5, and Figure 7.6. To minimize support structure length, the rotors are positioned on top of the fuselage. Additionally, the parameters defining the rotor support structure were deliberately over-dimensioned within the set bounds to ensure compliance with the deflection constraint at the initial design point.

The resultant corresponding physical design spaces are visually represented in Figure 7.4, Figure 7.5, and Figure 7.6, illustrating the rotor layout in the x and y directions, as well as rotor dimensions and blade counts for each configuration. These representations provide a clear understanding of the initial geometry and constraints within the design space prior to optimization.

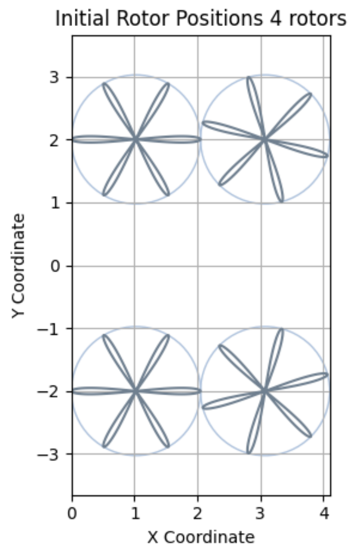

Figure 7.4: Initial quadrotor layout

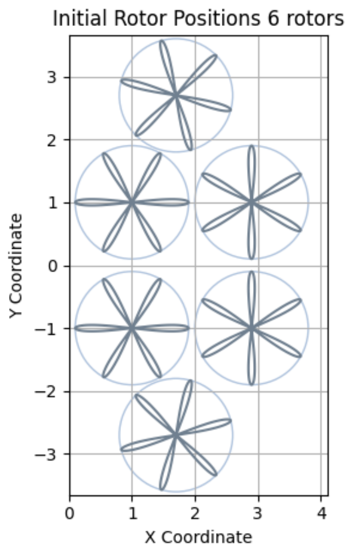

Figure 7.5: Initial hexarotor layout

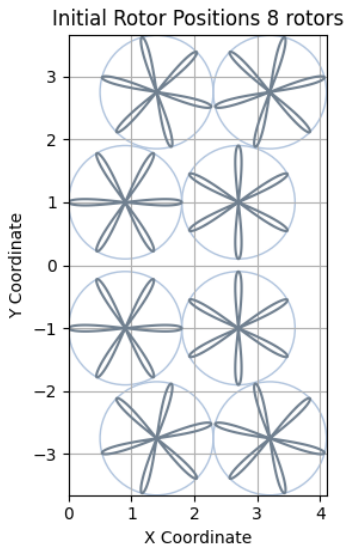

Figure 7.6: Initial octorotor layout

8

Results

8.1. Optimization Characteristics

The optimization process concluded successfully, as indicated by the termination message: ”*Optimization terminated successfully (Exit mode 0).*” This message confirms that the algorithm met the convergence criteria and provides essential information, including the exit mode, number of iterations, and counts of function and gradient evaluations, as summarized in Table 8.1.

The iteration count represents the number of times the algorithm completed its main loop. Each iteration typically involves evaluating the objective function, verifying constraints, updating design variables, and adjusting parameters to progress toward an optimal solution. The total number of iterations provides insight into the algorithm's convergence behavior and efficiency.

The number of function evaluations corresponds to how many times the objective function was computed during the optimization process. Each evaluation represents a single computation of the objective function, and a higher count may indicate either a more complex problem or reduced algorithmic efficiency.

Table 8.1: Optimization characteristics at HF = 0.1

Metric	Quad Rotor	Hexa Rotor	Octo Rotor
Time to converge [min]	252.32	185.67	263.07
Number of iterations	2596	1229	1789
Average time per iteration [min]	0.0972	0.15	0.1471
Number of function evaluations	134150	64451	98715
Average time per evaluation [min]	0.0019	0.0029	0.0027

8.2. Convergence History

To evaluate whether the optimization algorithm successfully converged to the normalized objective function while satisfying the normalized constraints, convergence plots are generated. These plots, provide insights into the trajectory of the optimization and validate the adherence to the imposed constraints.

It should be noted that, for the sake of clarity and focus, this section presents the optimization results specifically for the hexa-rotor configuration with a HF set to 0.1. Although optimizations were also performed for other configurations and HF values, these results are omitted here for conciseness but are provided in Appendix B.

8.2.1. Objective convergence

The convergence history of the normalized objective function over the total number of iterations is shown in Figure 8.1, Figure 8.2 and Figure 8.3. It should be noted that to enhance visibility of the overall progression, the y-axis has been scaled to limit displayed peaks and provide greater resolution for observing the convergence trend.

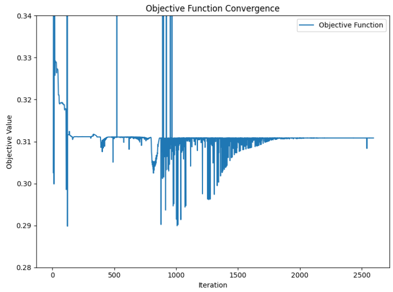

Figure 8.1: Objective convergence of quadrotor at HF = 0.1

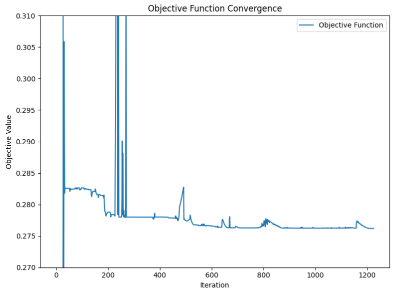

Figure 8.2: Objective convergence of hexarotor at HF = 0.1

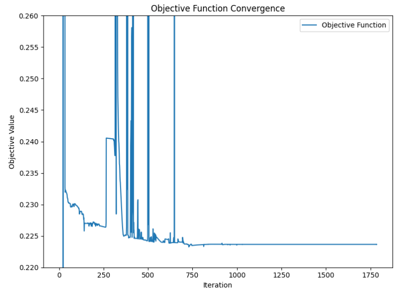

Figure 8.3: Objective convergence of octoroto at HF = 0.1

8.2.2. Constraint convergence

In Figure 8.4 and Figure 8.5, the convergence of the aspect ratio constraint and the maximum takeoff mass constraint are presented. The aspect ratio constraint comprises upper and lower bounds for each rotor blade, as described in Section 7.4.1. For the hexa-rotor configuration, constraints 1 and 2 correspond to rotor 1, constraints 3 and 4 to rotor 2, and constraints 5 and 6 to rotor 3. The MTOM constraint ensures consistency between the disciplines within the multidisciplinary design optimization (MDO) framework.

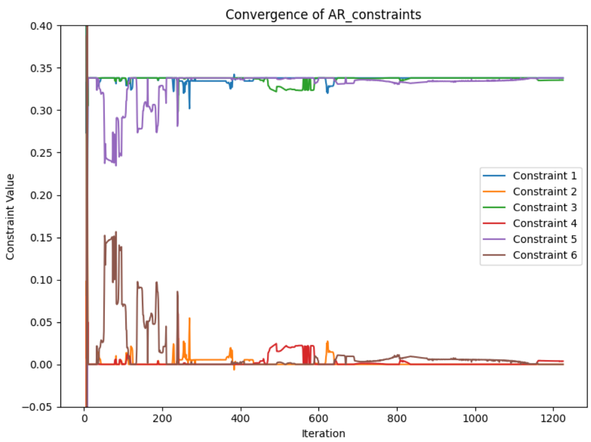

Figure 8.4: Aspect Ratio constraint convergence of hexarotor HF = 0.1

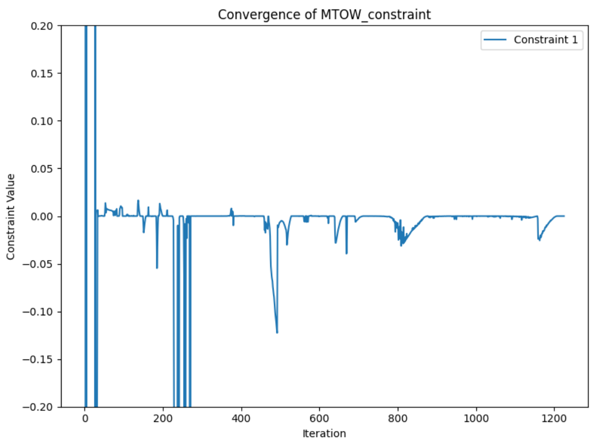

Figure 8.5: MTOM Consistency constraint convergence hexarotor HF = 0.1

The deflection constraint, shown in Figure 8.6, imposes inequality constraints on the maximum deflection of the support structures for each rotor, resulting in three constraints (one per rotor). Conversely, the moment constraint, depicted in Figure 8.7, consists of four constraints, one for each flight phase, to ensure stability regarding attitude rates during different flight conditions, as outlined in Section 7.4.2.

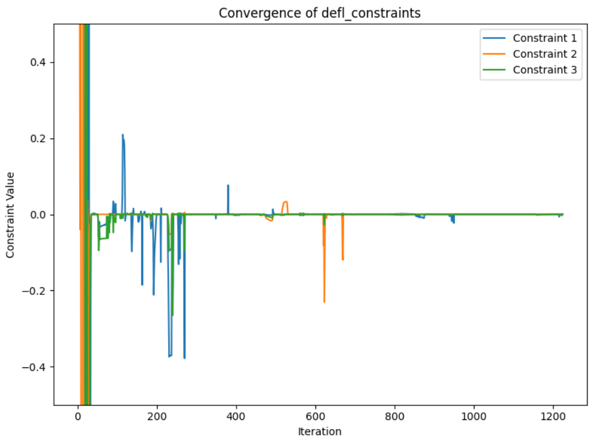

Figure 8.6: Deflection constraint convergence hexarotor HF = 0.1

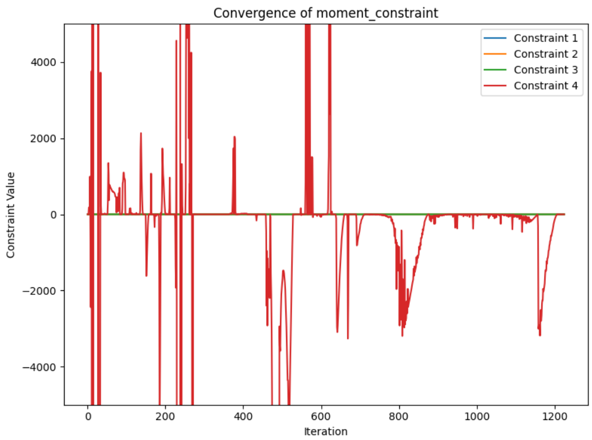

Figure 8.7: Moment constraint convergence hexarotor HF = 0.1

The convergence of the velocity constraints, for each flight phase, is illustrated in Figure 8.8. For the descent phase, constraints 3 and 4 ensure adherence to performance benchmarks, as explained in Section 7.4.1. The angle of attack constraint, depicted in Figure 8.9, includes three sub-constraints: constraints 1 and 2 ensure the argument of the arccos function remains within $[-1, 1]$, while constraint 3 ensures the angle of attack is realistic (greater than $0°$) for cruise conditions.

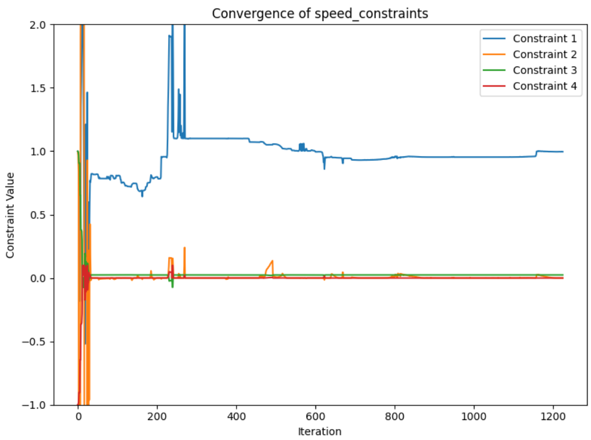

Figure 8.8: Velocity constraint convergence hexarotor HF = 0.1

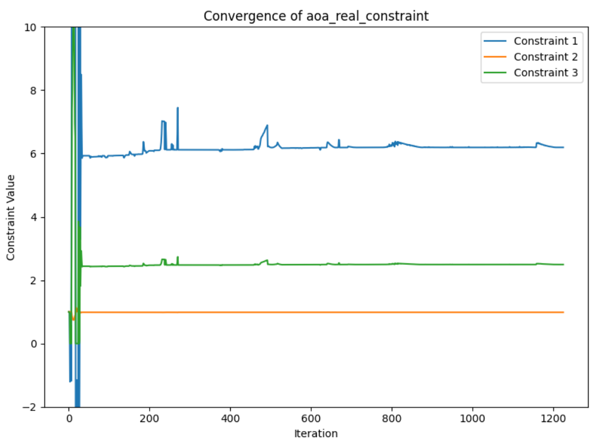

Figure 8.9: Angle of Attack constraint convergence hexarotor HF = 0.1

The tip Mach number constraint, shown in Figure 8.10, is an inequality constraint applied to each rotor to ensure the tip Mach number does not exceed its maximum allowable value. For the blade stall constraint, Figure 8.11 illustrates two inequality constraints per rotor, as described in Section 7.4.1. Constraints 1, 2, and 3 correspond to Equation 7.21 and 4, 5 and 6 correspond to the blade loading needing to be larger than 0.

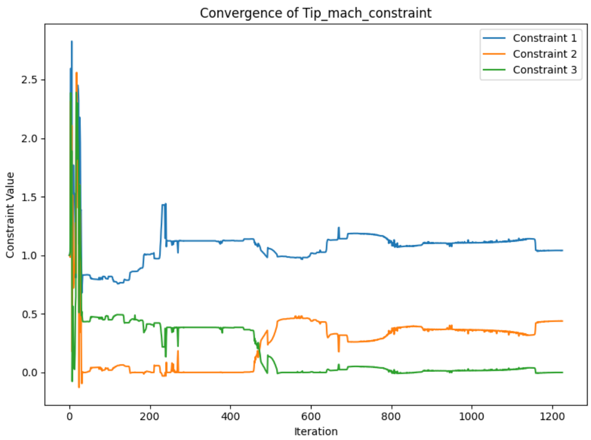

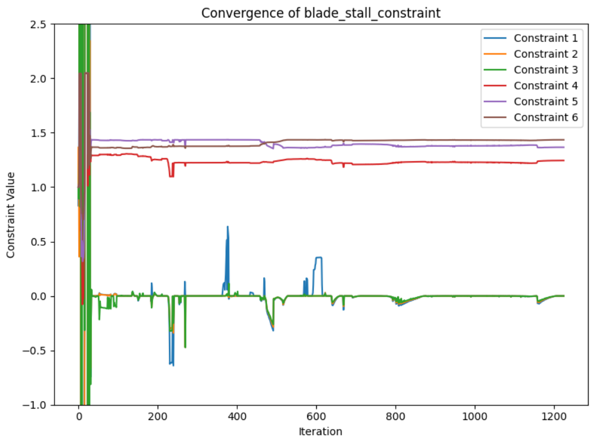

Figure 8.10: Tip Mach constraint convergence hexarotor HF = 0.1 **Figure 8.11:** Blade Stall constraint convergence hexarotor HF = 0.1

The motor power constraint, presented in Figure 8.12, ensures the maximum available power for off-the-shelf electric motors is not exceeded. Meanwhile, the rotor bound constraint (Figure 8.13) consists of 12 sub-constraints,4 per rotor, to ensure the physical design space is not violated. Specifically, constraints 1–4 correspond to rotor 1, constraints 5–8 to rotor 2, and constraints 9–12 to rotor 3, as described in Section 7.4.1.

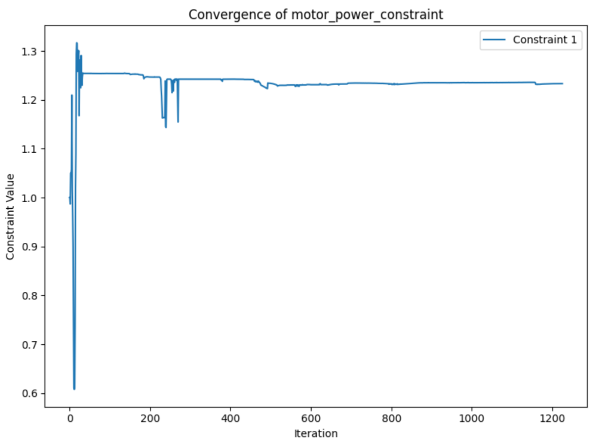

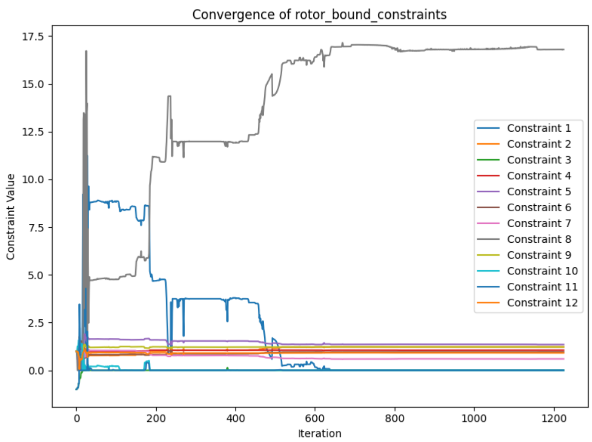

Figure 8.12: Motor Power constraint convergence hexarotor HF = 0.1 **Figure 8.13:** Rotor bound constraint convergence hexarotor HF = 0.1

The rotor solidity constraint, illustrated in Figure 8.14, imposes an inequality constraint on each rotor to maintain a solidity below 1. The axial thrust constraint, shown in Figure 8.15, includes two inequality constraints: constraint 1 ensures the produced thrust during climb exceeds the MTOM, while constraint 2 ensures the thrust during descent is less than the MTOM to avoid mathematical errors in square root calculations.

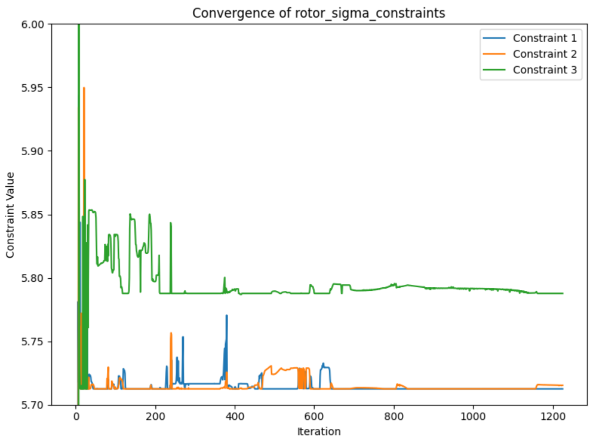

Figure 8.14: Rotor solidity constraint convergence hexarotor HF = 0.1

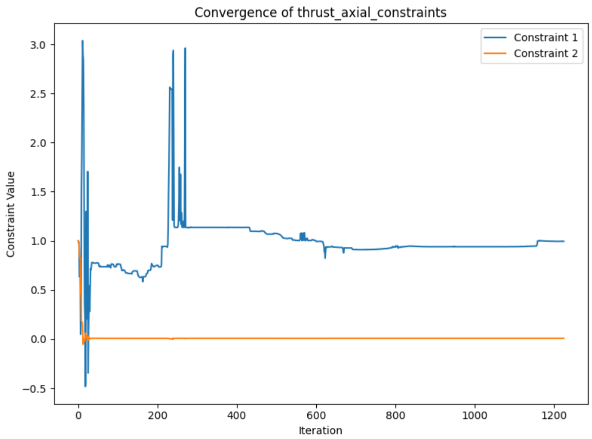

Figure 8.15: Axial thrust constraint convergence hexarotor HF = 0.1

Thrust during hover is governed by an equality constraint, visualized in Figure 8.16, which ensures the produced thrust matches the MTOW. Finally, the rotor overlap constraint, presented in Figure 8.17, includes three inequality constraints, one per rotor, to ensure no physical overlap occurs between the rotors.

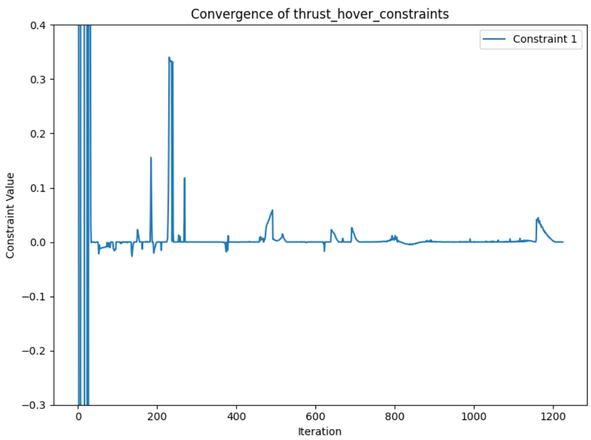

Figure 8.16: Hover thrust constraint convergence hexarotor HF = 0.1

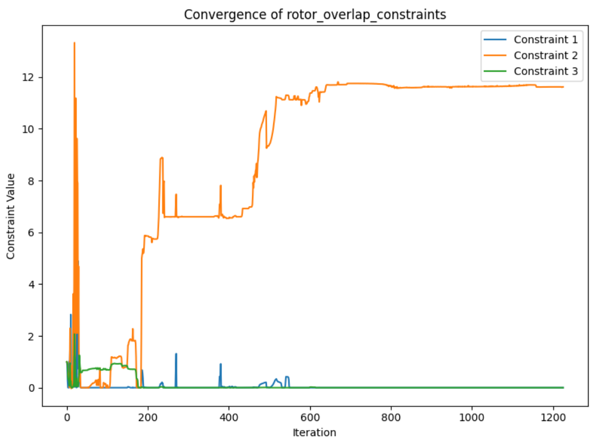

Figure 8.17: Rotor overlap constraint convergence hexarotor HF = 0.1

8.3. Design Parameter Results

For each configuration, with a hybridization factor (HF) of 0.1, the design parameters corresponding to the optimized objective function are summarized in Table 8.2, Table 8.3, and Table 8.4. These tables provide a detailed comparison of the initial and optimized values of each design parameter across the various configurations.

An analysis of these results reveals valuable insights into the impact of the optimization process on the design. The variations in parameter values demonstrate how the optimization algorithm adjusted the design to achieve the optimal solution, reflecting the necessary trade-offs to satisfy the imposed constraints while minimizing the objective function. These results also shed light on the interactions between design variables within the multidisciplinary design optimization framework, offering a deeper understanding of the complex relationships that drive the overall design objectives of this study.

Table 8.2: Optimized design parameters quadrotor

Parameter	Initial	Optimized
Objective function		
$MTOM$ [kg]	1873.48	582.28
Design vector		
c_1 [m]	0.4	0.050000
c_2 [m]	0.4	0.08480
R_{rotor_1} [m]	1.025	0.6999
R_{rotor_2} [m]	1.025	1.187
x_{rotor_1} [m]	1.025	0.9796
x_{rotor_2} [m]	3.075	2.802
y_{rotor_1} [m]	2	1.099
y_{rotor_2} [m]	2	1.587
z_{rotor_1} [m]	1.90	1.90
z_{rotor_2} [m]	1.90	1.90
N_{blades_1}	6	6
N_{blades_2}	6	6
Ω_{hover_1} [rad/s]	150	267.24
Ω_{hover_2} [rad/s]	150	152.95
Ω_{climb_1} [rad/s]	155	291.82
Ω_{climb_2} [rad/s]	155	167.02
Ω_{cruise_1} [rad/s]	150	271.98
Ω_{cruise_2} [rad/s]	150	155.66
$\Omega_{descent_1}$ [rad/s]	0.1	263.06
$\Omega_{descent_2}$ [rad/s]	0.1	150.56
$M\hat{T}OM$ [kg]	1920	582.28
C_{T_1} [-]	0.05	0.01178
C_{T_2} [-]	0.05	0.01161
r_{i_1} [m]	0.17	0.2498
r_{i_2} [m]	0.17	0.2499
r_{o_1} [m]	0.10	0.2499
r_{o_2} [m]	0.10	0.2495

Table 8.3: Optimized design parameters hexarotor

Parameter	Initial	Optimized
Objective function		
$MTOM$ [kg]	2120.57	585.49
Design vector		
c_1 [m]	0.4	0.05000
c_2 [m]	0.4	0.05605
c_3 [m]	0.4	0.05913
R_{rotor_1} [m]	0.9	0.6999
R_{rotor_2} [m]	0.9	0.7872
R_{rotor_3} [m]	0.9	0.8278
x_{rotor_1} [m]	1	0.6999
x_{rotor_2} [m]	1.7	1.866
x_{rotor_3} [m]	2.9	3.272
y_{rotor_1} [m]	1	1.100
y_{rotor_2} [m]	2.7	2.022
y_{rotor_3} [m]	1	1.227
z_{rotor_1} [m]	1.90	1.90
z_{rotor_2} [m]	1.90	1.90
z_{rotor_3} [m]	1.90	1.90
N_{blades_1}	6	6
N_{blades_2}	6	6
N_{blades_3}	6	5
Ω_{hover_1} [rad/s]	178	233.56
Ω_{hover_2} [rad/s]	178	236.52
Ω_{hover_3} [rad/s]	178	255.90
Ω_{climb_1} [rad/s]	185	223.86
Ω_{climb_2} [rad/s]	185	288.81
Ω_{climb_3} [rad/s]	185	269.15
Ω_{cruise_1} [rad/s]	178	233.56
Ω_{cruise_2} [rad/s]	178	244.84
Ω_{cruise_3} [rad/s]	178	258.88
$\Omega_{descent_1}$ [rad/s]	0.1	158.59
$\Omega_{descent_2}$ [rad/s]	0.1	288.65
$\Omega_{descent_3}$ [rad/s]	0.1	228.61
$M\hat{T}OM$ [kg]	2440	585.49
C_{T_1} [-]	0.05	0.01081
C_{T_2} [-]	0.05	0.01181
C_{T_3} [-]	0.05	0.0113
r_{i_1} [m]	0.17	0.2498
r_{i_2} [m]	0.17	0.2495
r_{i_3} [m]	0.17	0.2497
r_{o_1} [m]	0.10	0.25
r_{o_2} [m]	0.10	0.2499
r_{o_3} [m]	0.10	0.25

Table 8.4: Optimized design parameters octorotor

Parameter	Initial	Optimized
Objective function		
$MTOM$ [kg]	2642.03	590.76
Design vector		
c_1 [m]	0.4	0.05000
c_2 [m]	0.4	0.05472
c_3 [m]	0.4	0.05000
c_4 [m]	0.4	0.05001
R_{rotor_1} [m]	0.9	0.7000
R_{rotor_2} [m]	0.9	0.7996
R_{rotor_3} [m]	0.9	0.7000
R_{rotor_4} [m]	0.9	0.7168
x_{rotor_1} [m]	0.9	0.7000
x_{rotor_2} [m]	1.4	1.9130
x_{rotor_3} [m]	2.7	3.1270
x_{rotor_4} [m]	3.2	3.3570
y_{rotor_1} [m]	1.0	1.1000
y_{rotor_2} [m]	2.75	1.9800
y_{rotor_3} [m]	1.0	1.1000
y_{rotor_4} [m]	2.75	2.4980
z_{rotor_1} [m]	1.90	1.90
z_{rotor_2} [m]	1.90	1.90
z_{rotor_3} [m]	1.90	1.90
z_{rotor_4} [m]	1.90	1.90
N_{blades_1}	6	6
N_{blades_2}	6	5
N_{blades_3}	6	6
N_{blades_4}	6	6
Ω_{hover_1} [rad/s]	156	231.45
Ω_{hover_2} [rad/s]	156	240.39
Ω_{hover_3} [rad/s]	156	255.88
Ω_{hover_4} [rad/s]	156	249.68
Ω_{climb_1} [rad/s]	157	177.86
Ω_{climb_2} [rad/s]	157	320.57
Ω_{climb_3} [rad/s]	157	302.66
Ω_{climb_4} [rad/s]	157	201.46
Ω_{cruise_1} [rad/s]	156	229.61
Ω_{cruise_2} [rad/s]	156	251.40
Ω_{cruise_3} [rad/s]	156	251.48
Ω_{cruise_4} [rad/s]	156	256.88
$\Omega_{descent_1}$ [rad/s]	0.1	16.32
$\Omega_{descent_2}$ [rad/s]	0.1	330.97
$\Omega_{descent_3}$ [rad/s]	0.1	305.40
$\Omega_{descent_4}$ [rad/s]	0.1	13.56
$M\hat{T}OM$ [kg]	2500	590.76
C_{T_1}	0.05	0.01072
C_{T_2}	0.05	0.01060
C_{T_3}	0.05	0.01131
C_{T_4}	0.05	0.01131
r_{i_1} [m]	0.17	0.2499
r_{i_2} [m]	0.17	0.2494
r_{i_3} [m]	0.17	0.2499
r_{i_4} [m]	0.17	0.2494
r_{o_1} [m]	0.10	0.2498
r_{o_2} [m]	0.10	0.2500
r_{o_3} [m]	0.10	0.2499
r_{o_4} [m]	0.10	0.2500

8.4. Processed Results

To assess the impact of design variables and their interactions, a series of plots and tables are generated to illustrate how individual parameters influence the overall design. Additionally, comparative plots are created to provide insights into the differences between the various configurations.

To provide a comprehensive understanding of the physical implications of the optimized parameters, such as layout, dimensions, and distribution, Figure 8.18, Figure 8.19, and Figure 8.20 present detailed visual representations of the configurations. These figures showcase the arrangement of key components, including rotor blade count, chord length, radius, and their spatial positioning relative to the fuselage. Such visualizations clarify how the optimized parameters translate into structural and geometric changes within the design.

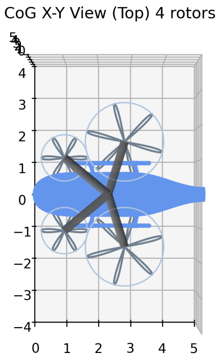

Figure 8.18: Optimised quadrotor design

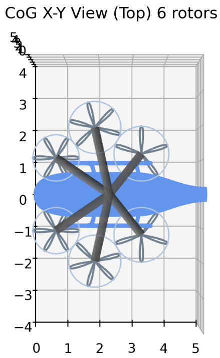

Figure 8.19: Optimised hexarotor design

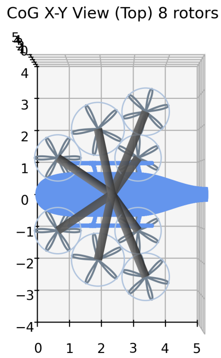

Figure 8.20: Optimised octorotor design

Further, to evaluate the effect of rotor positioning on the balance of the system, the locations of the center of gravity (COG) and center of mass (COM) for key subsystems are depicted in Figure 8.21, Figure 8.22, and Figure 8.23. These figures offer valuable insights into the balance of various configurations by highlighting the relative positions of the COG. It is important to note that the COG shown represents the combined center of gravity for all subsystems, including the turbine generator, fuel, battery, and propulsion system, while excluding the payload and crew.

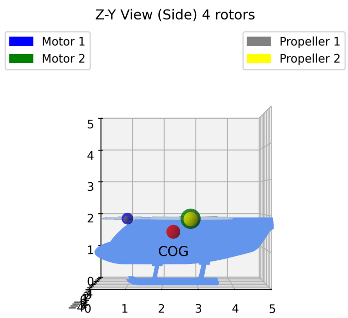

Figure 8.21: Quadrotor COG overview (Rotors, motors and total)

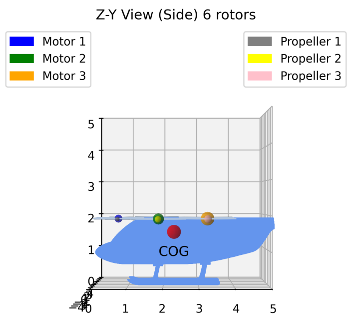

Figure 8.22: Hexarotor COG overview (Rotors, motors and total)

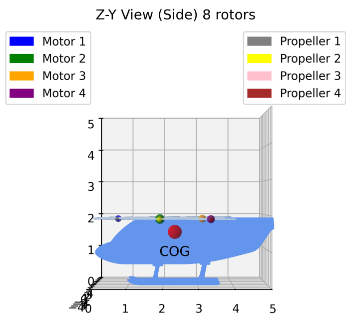

Figure 8.23: Octorotor COG overview (Rotors, motors and total)

8.4.1. Overall Characteristics

The optimized design parameters represent only the characteristics of the individual components. These parameters are integrated into various subsystems, collectively influencing the overall characteristics of each configuration.

To comprehensively evaluate the differences between configurations, a range of physical and performance metrics has been calculated. These metrics, summarized in Table 8.5, provide a detailed comparison of performance across different hybridization factors for each configuration. Analyzing these characteristics offers valuable insights into how specific design choices impact the overall system performance. This, in turn, enables a clearer understanding of the trade-offs and synergies that emerge between different configurations, helping to inform the selection of the most balanced and efficient design.

Table 8.5: Characteristics of the optimized configurations against different HF

Aircraft	Quadcopter			Hexacopter			Octacopter		
HF	0.1	0.5	0.9	0.1	0.5	0.9	0.1	0.5	0.9
OEW [kg]	241.17	344.89	490.24	242.87	359.52	506.67	249.38	364.10	526.27
Motor mass [kg]	45.45	48.00	52.84	46.02	47.68	50.36	45.56	47.31	52.22
Propeller mass [kg]	29.03	29.23	34.22	26.31	29.78	33.20	26.62	30.19	31.87
Supp-struc mass [kg]	5.15	5.20	8.17	8.30	19.31	37.12	15.56	31.61	46.10
Fuel mass [kg]	13.04	8.72	2.03	13.49	8.74	1.95	13.10	8.18	2.03
Battery mass [kg]	20.11	121.03	253.57	20.81	121.31	244.54	20.20	113.54	254.64
Battery capacity [kWh]	5.17	31.15	65.26	5.35	31.22	62.94	5.20	29.95	65.54
ICE mass [kg]	83.47	88.17	91.81	84.51	87.57	90.53	83.67	86.89	91.91
ICE power [kW]	250.40	264.50	275.44	253.55	262.73	271.61	251.02	261.63	275.75
Climb speed [m/s]	19.91	19.24	16.48	20.43	15.03	16.30	20.04	17.24	15.90
Cruise speed [m/s]	65.67	65.66	65.66	65.67	65.67	65.67	65.67	65.67	65.68
Descent speed [m/s]	8.00	8.00	8.00	8.00	8.00	7.86	8.00	8.00	7.98
Disk area [m^2]	11.93	10.99	13.40	11.27	13.91	17.05	13.40	16.40	16.19
Max Motor Power [kW]	79.28	71.18	91.07	53.34	66.82	57.21	37.63	45.87	45.18
I_{xx} [kg m^2]	187.59	171.41	219.67	199.87	258.95	380.82	269.03	351.48	408.15
I_{yy} [kg m^2]	93.79	103.68	124.49	115.04	104.08	107.52	109.29	103.67	94.91
I_{zz} [kg m^2]	214.94	209.77	276.51	249.28	297.67	422.03	312.82	389.74	436.58

8.4.2. Mass Results

The primary objective, the Maximum Takeoff Mass (MTOM), is analyzed for various hybridization factors (HF) across each configuration. HF is a key parameter that highlights the influence of hybrid propulsion systems on MTOM, revealing how different levels of hybridization affect the total system mass. Figure 8.24 illustrates the relationship between HF and MTOM for the different configurations, facilitating a direct comparison of their responses to varying levels of hybridization and the corresponding impact on MTOM. Additionally, the relative increase in MTOM between configurations is presented in Table 8.6, using the quadrotor configuration as the baseline. The analysis also quantifies the increase in MTOM for different HF values within the same configuration, with HF = 0.1 serving as the baseline for each configuration.

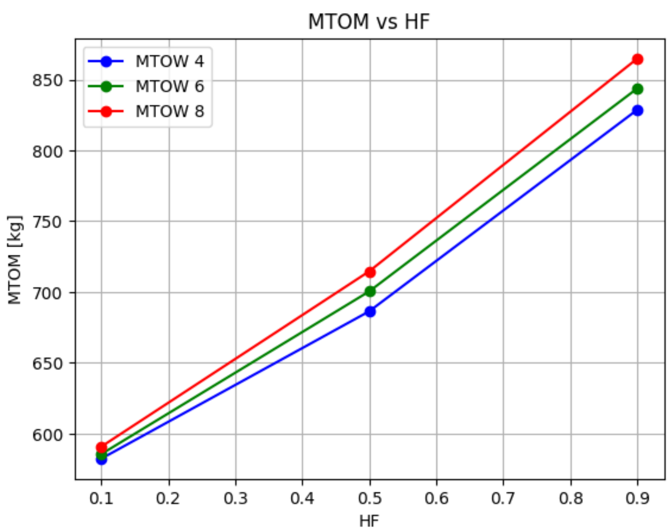

Figure 8.24: MTOM verus HF

Table 8.6: Increase in MTOM for each configuration compared to the quadrotor as baseline and Increase in MTOM for different HF to the same configuration at HF = 0.1 as the baseline

Aircraft	Quadcopter			Hexacopter			Octacopter		
HF	0.1	0.5	0.9	0.1	0.5	0.9	0.1	0.5	0.9
MTOM Increase, Configuration [%]	Baseline	Baseline	Baseline	0.53	2.05	1.82	1.19	2.58	3.23
MTOM Increase, HF [%]	Baseline	17.88	20.73	Baseline	19.66	20.46	Baseline	19.50	21.50

The displayed MTOM is the aggregate sum of multiple subsystems, each contributing a specific fraction to the total mass. The mass contributions of these subsystems are highly sensitive to the hybridization factor, reflecting how the choice of HF influences the overall mass distribution. To provide a clearer understanding of the mass distribution across subsystems within each configuration, pie charts are presented in Figure 8.25, Figure 8.26, and Figure 8.27. These visualizations break down the contributions of key subsystems to the overall MTOM, highlighting changes in subsystem contributions as HF varies. Furthermore, they allow for a comparative analysis of how the relative mass distribution differs between configurations, offering valuable insights into the trade-offs inherent in hybrid system design.

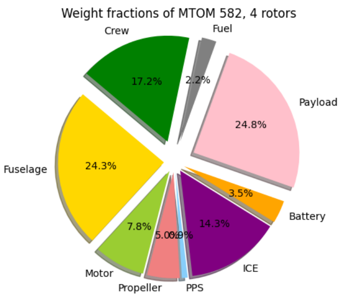

Figure 8.25: Subsystem weight fractions quadrotor at HF = 0.1

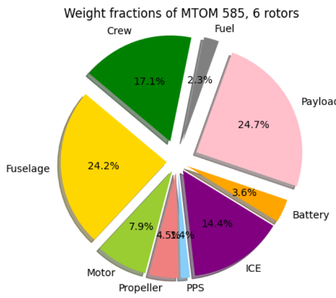

Figure 8.26: Subsystem weight fractions hexarotor at HF = 0.1

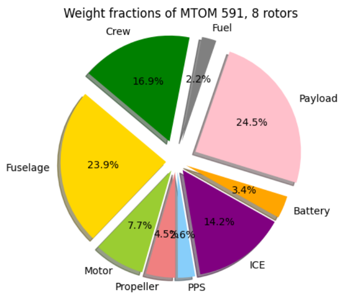

Figure 8.27: Subsystem weight fractions octorotor at HF = 0.1

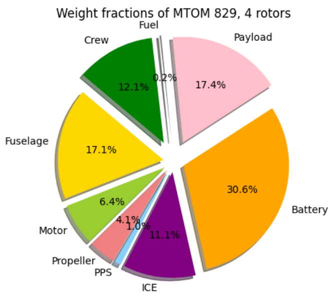

Figure 8.28: Subsystem weight fractions quadrotor at HF = 0.9

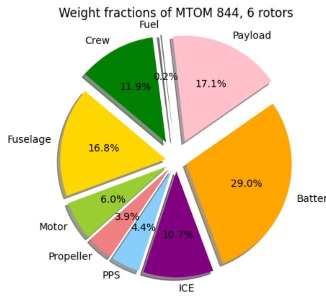

Figure 8.29: Subsystem weight fractions hexarotor at HF = 0.9

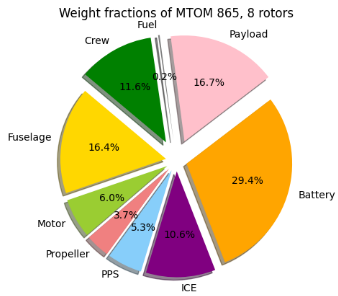

Figure 8.30: Subsystem weight fractions octorotor at HF = 0.9

8.4.3. Rotational Speeds

The thrust generated by each rotor is influenced by a combination of multiple design parameters. Together with the rotational speeds, these parameters determine the produced thrust for each configuration. Since rotational speeds are a key means of controlling the multirotor, and they vary depending on the thrust requirements for each flight phase, each phase has an optimal rotational speed distribution between the rotors. This distribution ensures that the total required thrust is generated while maintaining stability throughout the flight.

To present the results, Figure 8.31, Figure 8.32, Figure 8.33, and Figure 8.34 show the individual rotor speeds for each configuration across the different flight phases. These figures provide insight into how the rotational speeds vary for each configuration and flight phase, highlighting the relationship between the thrust requirements and the necessary adjustments in rotor speed to achieve optimal performance and a steady flight phase.

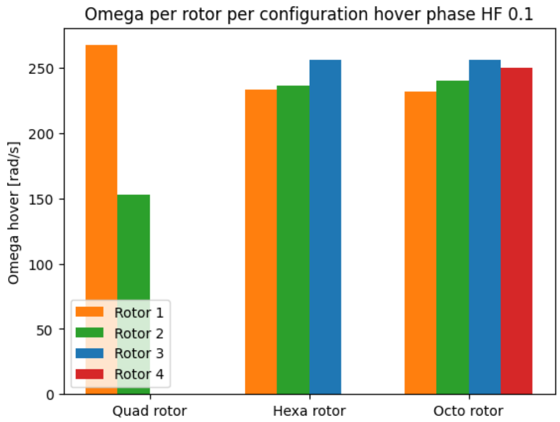

Figure 8.31: Individual rotor speed at hover for each configuration HF = 0.1

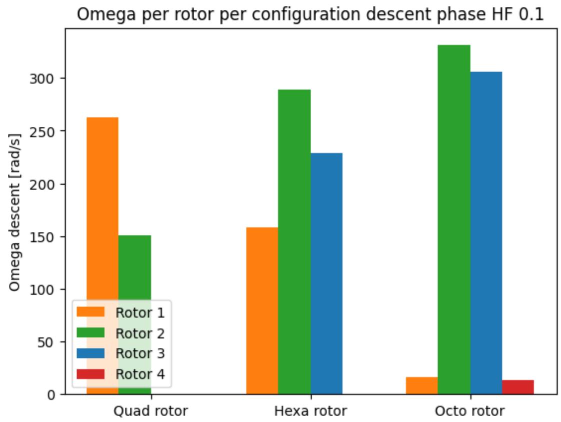

Figure 8.32: Individual rotor speed at descent for each configuration HF = 0.1

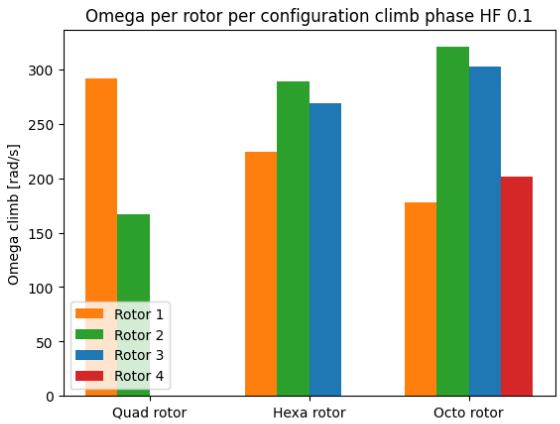

Figure 8.33: Individual rotor speed at climb for each configuration HF = 0.1

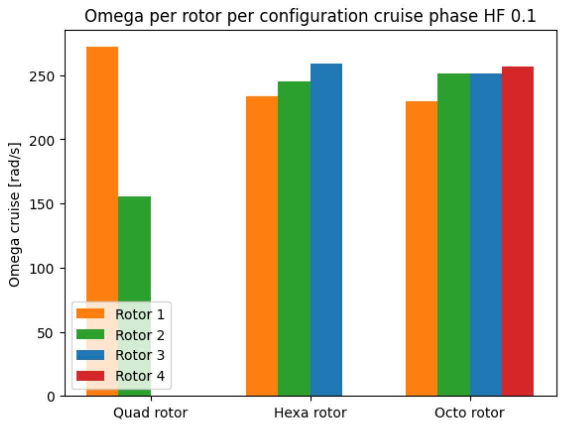

Figure 8.34: Individual rotor speed at cruise for each configuration HF = 0.1

8.4.4. Power Requirements

The objective Maximum Takeoff Mass (MTOM) is directly related to the overall power required for the system, with both factors influencing each other. To understand the differences between the configurations, Figure 8.35 presents the total installed power for each configuration at a specific hybridization factor (HF), which is sized to meet the peak power requirements of the individual rotors. To further explore the power requirements, Figure 8.36 illustrate how total power varies with increasing cruise speed. This plot offers insights into how the induced, profile, parasitic, and total power components respond to changes in cruise speed, shedding light on the contribution of each power type to the overall system performance at different speeds.

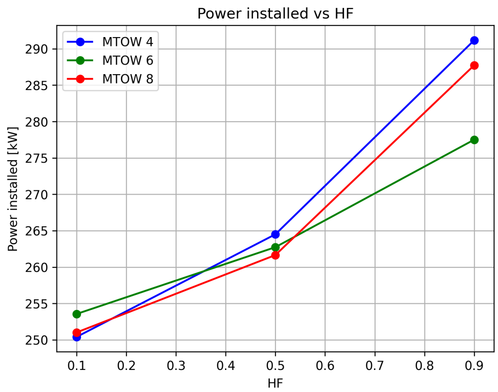

Figure 8.35: Installed power on each configuration for different HF

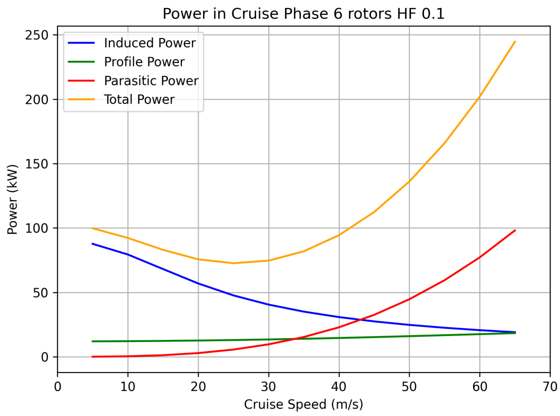

Figure 8.36: Power curves for different hexarotor cruise velocities at HF = 0.1

While the installed power provides insight into the overall power sizing of the configurations, a deeper understanding of the individual power requirements for each flight phase is essential. To achieve this, the power requirements for each steady flight phase were calculated and are shown in Figure 8.37, Figure 8.38, and Figure 8.39. These figures present the profile power, parasitic power, induced power, and total power across different flight phases.

It is important to note that, since the optimizer minimizes overall mass as part of the power optimization, the overall power characteristics of the configurations are closely aligned within a similar range. To highlight the differences in power content across the configurations, the power result of the quadrotor and octorotor are normalised with respect to the hexa-rotor configuration as displayed in Figure 8.38. This provides a clearer visualization of how each configuration differs in power consumption relative to the baseline as visualised in Figure 8.37 and Figure 8.39.

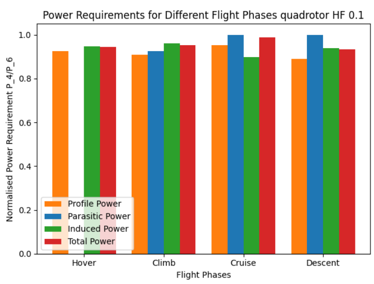

Figure 8.37: Normalised power contributions quadrotor for each flight phase at HF = 0.1

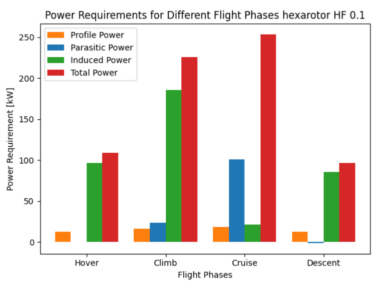

Figure 8.38: Power contributions hexarotor for each flight phase at HF = 0.1

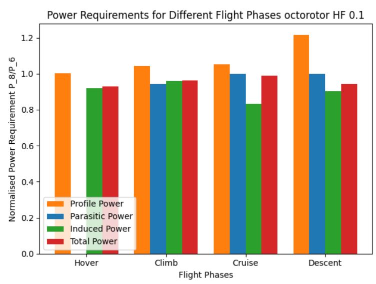

Figure 8.39: Normalised power contributions octorotor for each flight phase at HF = 0.1

8.4.5. Disk Loading and Blade Loading

As discussed in Section 3.5, disk loading and blade loading are critical performance metrics for VTOL configurations, as they provide valuable insights into hover efficiency and rotor performance. Disk loading represents the amount of mass supported by the rotor system per unit area of the rotor disk. In simpler terms, it is the ratio of the aircraft's mass to the area swept by the rotor blades. This parameter is essential for understanding the efficiency and performance of the rotor system, as it influences the required power for hover and the overall aerodynamic characteristics of the rotorcraft.

Figure 8.40 provides a comparison of disk loading and hover efficiency for each rotor across the various configurations. This figure offers a detailed examination of how blade loading varies with respect to hybridization factors, helping to assess the impact of different design choices on rotor performance.

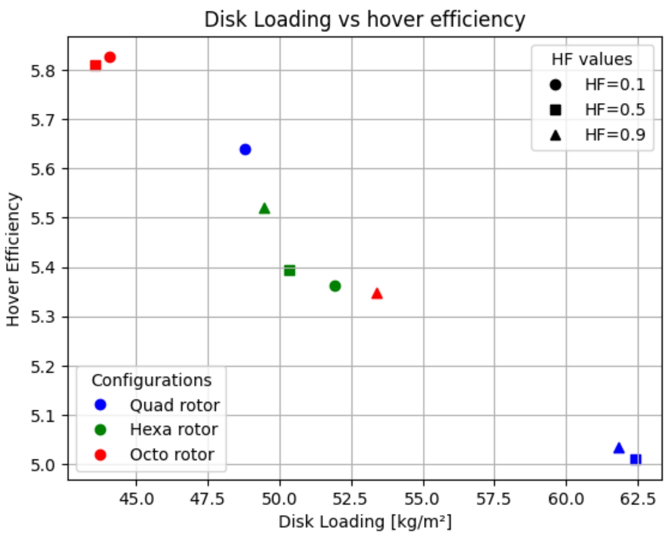

Figure 8.40: Disk loading vs hover efficiency

Blade loading is another critical parameter in rotary-wing aircraft performance, representing the amount of lift force generated by each rotor blade relative to its surface area. It quantifies the load (or force) carried per unit area of the rotor blade, directly influencing aerodynamic efficiency and overall rotor system performance. However, since the blade shape is not explicitly defined by the evaluated parameters, the indicative measure C_T/c is used to assess blade loading as displayed in Figure 8.41, Figure 8.42, and Figure 8.43 for each configuration across different hybridization factors.

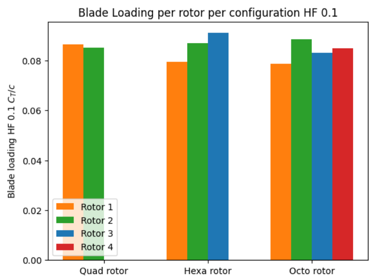

Figure 8.41: Blade loading for each configuration at HF = 0.1

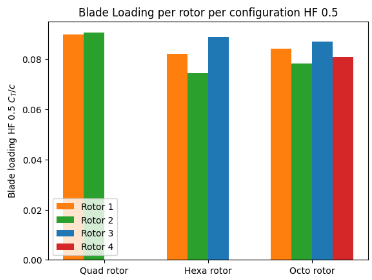

Figure 8.42: Blade loading for each configuration at HF = 0.5

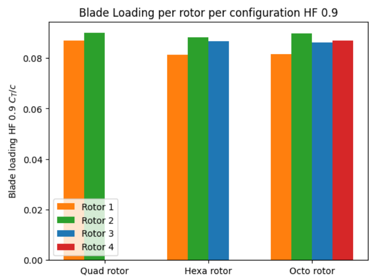

Figure 8.43: Blade loading for each configuration at HF = 0.9

8.4.6. Thrust and Attitude

The performance of the eVTOL in cruise flight is influenced by both the total thrust generated and the angle of attack required to maintain forward flight. To analyze the relationship between thrust and attitude at varying cruise speeds, Figure 8.44 presents the total thrust produced across a range of cruise velocities for each configuration. This figure provides insight into how the thrust requirements change as the cruise speed increases, highlighting the impact of different configurations on thrust generation during forward flight.

In addition to thrust, the required pitch angles to maintain steady cruise speeds are a crucial aspect of the eVTOL's flight behavior. The corresponding pitch angles for each configuration are shown in Figure 8.44. These plots allow for a comparison of how the attitude of the eVTOL adjusts with increasing cruise speed. By examining these figures, a better understanding is gained of each configuration on how thrust and attitude interact to maintain stability and performance during cruise flight.

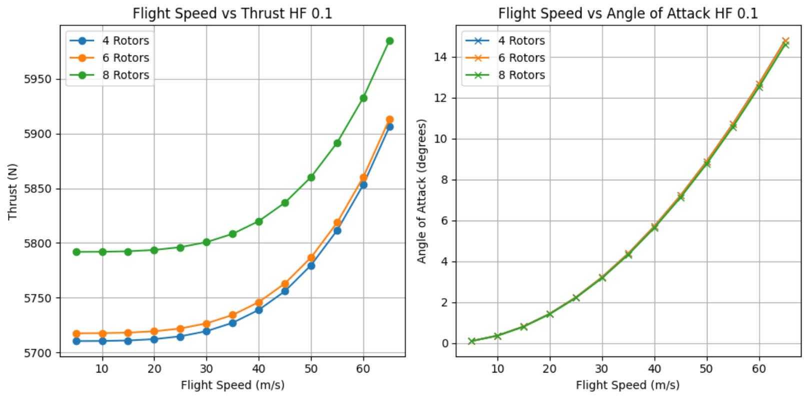

Figure 8.44: Thrust and angle of attack versus flight speed of all configurations at HF = 0.1

8.4.7. Solidity

Solidity is defined as the ratio of the total rotor blade area to the area of the rotor disk. In simpler terms, it measures how much of the rotor disk is covered by the rotor blades. Rotor solidity plays a crucial role in determining the aerodynamic efficiency and performance of the rotor system, as it influences both the lift and drag characteristics of the rotor.

Since both the rotor radius and chord length are optimization parameters in this study, the resulting optimized configurations lead to specific blade solidities for each design. To better understand the effects of solidity on rotor performance, Figure 8.46, Figure 8.45, and Figure 8.47 display the individual rotor solidities for each configuration across different hybridization factors (HF). These figures provide insights into how the optimized solidity values vary with the hybridization factor and help assess the impact of solidity on the overall aerodynamic performance of each configuration.

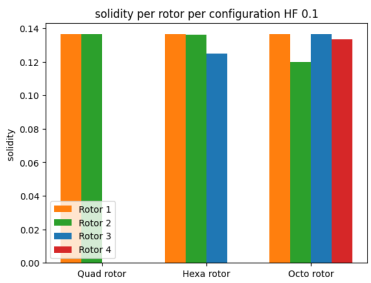

Figure 8.45: Individual rotor solidity for each configuration at HF = 0.1

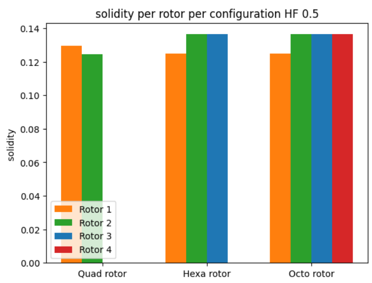

Figure 8.46: Individual rotor solidity for each configuration at HF = 0.5

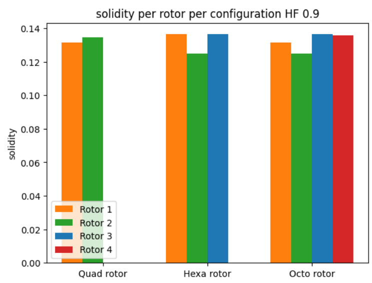

Figure 8.47: Individual rotor solidity for each configuration at HF = 0.9

8.4.8. Stability

In the context of systems of differential equations, eigenvalues play a critical role in determining the stability of trim points. Specifically, the eigenvalues of the system's state-space matrix, derived from the A matrix, reveal the system's inherent stability characteristics. To evaluate stability across different configurations, eigenvalues around the hover and cruise conditions are plotted for each configuration. These plots, presented in Figure 8.48, Figure 8.50, and Figure 8.52, provide insights into the stability of each configuration, highlighting how eigenvalues shift between hover and cruise conditions.

To complement the eigenvalue analysis, a series of plots illustrates the variation of the stability derivative X_u, which is associated with the fully real eigenvalue, as cruise velocity u changes. These plots, shown in Figure 8.49, Figure 8.51, and Figure 8.53, reveal how changes in cruise velocity influence the stability derivative. Together, these results offer an evaluation of the system's dynamic stability around the trim points and demonstrate the relationship between the stability derivative and increasing velocity.

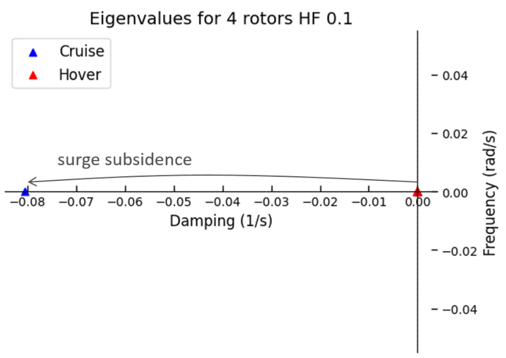

Figure 8.48: Eigenvalues around hover and cruise of quadrotor at HF = 0.1

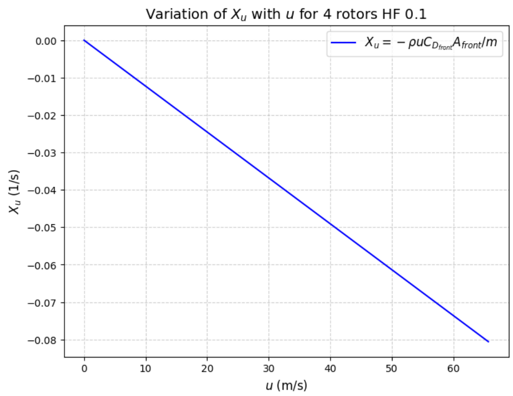

Figure 8.49: Variation of X_u quadrotor at HF = 0.1

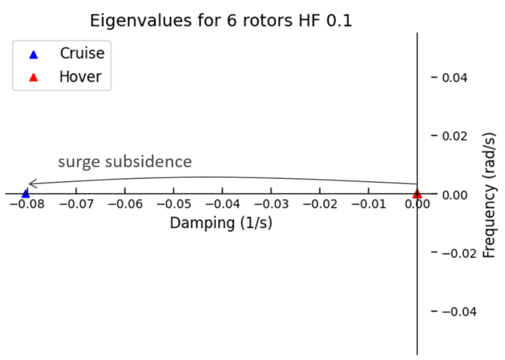

Figure 8.50: Eigenvalues around hover and cruise of hexarotor at HF = 0.1

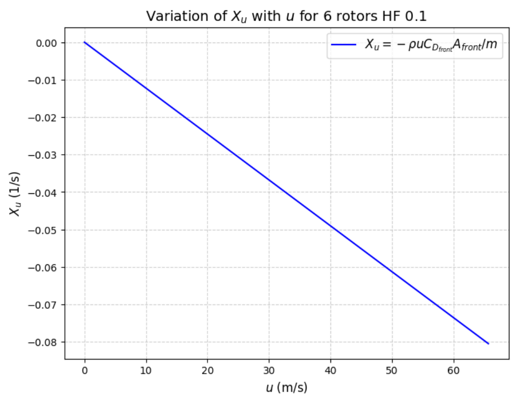

Figure 8.51: Variation of X_u hexarotor at HF = 0.1

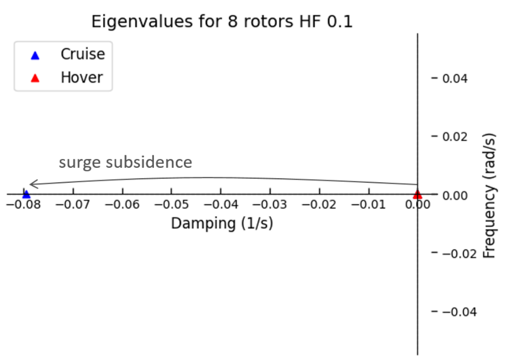

Figure 8.52: Eigenvalues around hover and cruise of octorotor at HF = 0.1

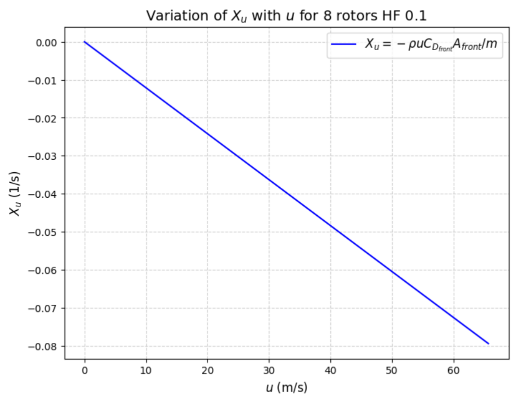

Figure 8.53: Variation of X_u octorotor at HF = 0.1

9

Discussions

9.1. Optimisation evaluation

9.1.1. Optimization Characteristics Evaluation

The optimization process for the quadrotor, hexarotor, and octorotor configurations is evaluated based on convergence behavior, computational efficiency, and the relationship between design complexity and performance. As illustrated in Figure 8.1, Figure 8.2 and Figure 8.3 the objective functions for all configurations converged successfully to a minimum, with subsequent design vectors differing by less than the assigned tolerance of 10^{-8}. This convergence is further corroborated by the exit message as discussed in Section 8.1, confirming that the optimizer met both the convergence criteria and the set constraints.

Convergence times, summarized in Table 8.1 exhibit notable differences among the configurations. The hexarotor converged the fastest, followed by the quadrotor, with the octorotor taking the longest. This trend aligns with expectations, given the varying complexities of their respective design spaces. The hexarotor's intermediate design complexity likely strikes an optimal balance, enabling efficient exploration and convergence. In contrast, the octorotor, with its increased number of rotors and associated design variables, demands additional computational effort to explore and refine its larger, more intricate design space effectively.

The number of iterations required for convergence further underscores the distinctions among the configurations. Interestingly, the quadrotor required the highest number of iterations, significantly more than both the hexarotor and the octorotor. Despite this, the average time per iteration was lowest for the quadrotor, followed by the octorotor, while the hexarotor had the highest average time per iteration.

The quadrotor's shorter iteration time can be attributed to its simpler aerodynamic and structural constraints, requiring fewer computational resources per iteration. However, its higher iteration count and increased number of function evaluations indicate that the optimizer engaged in a more extensive exploration of its design space. This behavior could stem from the increased sensitivity of the quadrotor's design to small changes in variables, making it more challenging to achieve an optimal solution while adhering to all constraints.

On the other hand, the hexarotor and octorotor configurations involve more complex interdependencies among design variables, leading to slightly higher average iteration times. However, the hexarotor's intermediate complexity facilitated a balance between exploration and exploitation of the design space, contributing to its faster overall convergence compared to the octorotor.

9.1.2. Convergence History Evaluation

The convergence plots (Figure 8.1, Figure 8.2, and Figure 8.3) reveal several key insights into the optimization process. A prominent observation is the high variability and pronounced peaks during the initial iterations. This behavior is typical of optimization algorithms, particularly during the early exploratory phase, as they navigate the design space. However, this variability can also be attributed to the initial design vector, which is based on a hypothetical multirotor configuration rather than a proven baseline. Unlike conventional optimization processes, that refine realistic designs derived from robust reference data, this study faced unique challenges as a result. The nascent state of eVTOL technology and the stringent requirements of the GoAERO competition limited the availability of reliable reference data. Consequently, the initial objective function exhibited a significant overestimation, as evidenced by its value being reduced by more than half in the early iterations before achieving more stable convergence.

A comparison of the convergence behavior across the three configurations, quadcopter, hexacopter, and octocopter, reveals several interesting trends. All three configurations exhibit a sharp decline from the initial objective value, followed by a phase of more gradual convergence. However, while the hexacopter and octocopter generally show a monotonic decrease in objective value, the quadcopter demonstrates a distinctive behavior. Around 800 iterations, the quadcopter's objective value increases from a minimum temporarily before ultimately converging to the final minimum. This suggests a local exploration phase, potentially triggered by a shift in the balance between competing constraints. Additionally, the octocopter exhibits relatively higher peak variability compared to the other configurations. This can likely be attributed to the increased number of design variables introduced by the additional rotors, amplifying the complexity of the design space and the sensitivity of the optimization process.

The interdependence of the Maximum Take-Off Mass (MTOM) constraint with other constraints is another notable observation. Peaks in the MTOM constraint are mirrored in constraints such as the axial thrust (Figure 8.15), motor power (Figure 8.12), speed (Figure 8.8), and moment constraints (Figure 8.7), as well as the overall objective convergence Figure 8.2. This correlation highlights the critical role of MTOM in determining the feasibility of the design. Conversely, constraints related to rotor characteristics, such as tip speed, exhibit comparatively weaker correlations with MTOM, indicating a more decoupled relationship. This decoupling suggests that rotor-specific design parameters are less sensitive to the overall mass and more influenced by localized aerodynamic considerations.

MTOM Constraint
The consistency constraint exhibits a similar trend to the objective function, with noticeable peaks during the optimization process as visualised in Figure 8.5. This correlation is expected due to the direct dependency of the overall design feasibility on the Maximum Take-Off Mass. Despite these occasional peaks, the optimizer demonstrates a robust ability to satisfy the consistency constraint effectively. After initial deviations, the constraint consistently converges back to zero, indicating that the optimization process successfully resolves conflicts between the MTOM and other constraints as iterations progress. Additionally, the observed adherence to the MTOM constraint suggests that the initial formulation of the constraint and its inclusion in the optimization framework were effective to use for the disciplines and result in an optimized objective.

Aspect Ratio Constraint
The convergence history of the aspect ratio constraint (Figure 8.4) shows a clear separation between the upper and lower bounds, consistent with the imposed constraints. During the optimization process, the aspect ratio value adjusts within these bounds, with opposing trends observed for the two constraints.

Significant variability is evident during the first 300 iterations, particularly in the early stages, where pronounced peaks dominate the convergence history. This variability gradually subsides as the optimization progresses and the aspect ratio stabilizes. In the initial phase, the constraint exhibits violations, as indicated by negative peaks, but the optimizer quickly adjusts the values to bring the constraint back within the feasible region. Over subsequent iterations, these violations diminish, and the constraint values converge smoothly within the allowable bounds.

Structural Deflection Constraint
The deflection constraint exhibits significant peaks during the early stages of optimization, as shown in Figure 8.6. During this phase, the constraint is violated multiple times, as indicated by the negative values in the convergence history, before eventually stabilizing. This behavior is strongly influenced by variations in mass, which affect thrust production and, consequently, the forces acting on the support structure. As the optimization progresses, the variability diminishes, and the constraint converges to a stable value, reflecting the resolution of mass-induced perturbations.

Moment Constraint
The moment constraint, depicted in Figure 8.7, demonstrates significant variability during the descent phase, with pronounced peaks in both the positive and negative regions throughout the optimization process. This indicates that the moment constraint posed a considerable challenge for the optimizer to converge.

This behavior can be attributed to the adjustments made by the optimizer to the rotational speeds of certain rotors during descent. These adjustments cause substantial variations in the generated moments, which must be balanced to satisfy the constraint. Consequently, the observed fluctuations reflect the optimizer's iterative efforts to achieve convergence.

Speed Constraint
The convergence of the speed constraint reveals significant peaks during the initial iterations across all flight phases, as shown in Figure 8.8. Among these, the cruise speed constraint exhibits the highest initial variability, followed by a rapid reduction and stabilization. The descent speed constraint also stabilizes quickly, whereas the climb speed constraint displays prolonged variability and converges to a higher value compared to the other flight phases. This extended variability in the climb speed constraint may result from the optimal climb speed being higher than the minimum allowed value, most likely to balance parasitic and induced power, whereas the other constraints align more closely with their respective minima. This behavior reflects the optimizer's efforts to balance the competing requirements for each flight phase.

Angle of Attack Constraint
The angle of attack constraint (Figure 8.9) stabilizes rapidly after the initial iterations. The early peaks reflect the optimizer's efforts to ensure that the arguments of the arccos function remain within the valid range of $[-1, 1]$ and that the angle of attack stays physically realistic (i.e., greater than 0°). This rapid stabilization demonstrates the robustness of the optimizer in addressing this constraint with minimal violations.

Tip Mach and Blade Stall Constraints
The tip Mach constraint (Figure 8.10) shows significant peaks during the initial iterations, followed by a gradual stabilization as the optimization progresses. Similarly, the blade stall constraint, represented by two inequality conditions, transitions from a phase of high variability to more refined adjustments before ultimately converging. Although both constraints exhibit pronounced peaks in the early stages, the optimizer quickly adapts, minimizing violations and guiding the constraints toward convergence with increasing precision.

Motor Power Constraint
The motor power constraint stabilizes rapidly near its final value, requiring minimal adjustments during the later stages of optimization, as shown in Figure 8.12. This behavior indicates that the constraint has a relatively limited influence on the overall design variability, particularly since no violations are observed throughout the optimization process.

Rotor Bound and Overlap Constraints
The rotor bound constraint (Figure 8.13) exhibits significant peaks and variability, particularly associated with rotor placement. Similarly, the overlap constraint (Figure 8.17) shows high variability during the early stages of optimization. Both constraints play a critical role in ensuring the physical feasibility of the rotor configuration and gradually converge as the optimization progresses.

Although the convergence process involves minimal constraint violations overall, the constraints undergo significant changes as the rotor positions are optimized. The overlap constraint displays similar characteristics, with substantial adjustments observed as the optimization refines the rotor placement, eventually achieving stable and feasible values.

Solidity Constraint
The solidity constraint (Figure 8.14) exhibits a rapid reduction in variability, quickly converging to its final value. This behavior reflects the straightforward nature of the constraint and the optimizer's efficiency in satisfying this requirement. As a reslt, while the solidity constraint shows significant peaks during the initial stages, it does not exhibit any violations and is not a limiting factor in the overall optimization process, similar to the motor power constraint.

Thrust Constraints
The thrust constraints exhibit distinct behaviors across different flight phases, as shown in Figure 8.15. During the climb phase, the thrust constraint demonstrates high variability due to the increased thrust requirements needed to overcome the eVTOL's weight. In contrast, the descent phase shows lower variability, reflecting the reduced thrust demands and corresponding lower rotor speeds.

The hover thrust constraint initially exhibits pronounced peaks in both directions but stabilizes quickly, ensuring that the generated thrust equals the MTOW. While some constraint violations and high variability are observed during the early iterations for the climb phase, the optimizer effectively adjusts the values, ensuring adherence to the constraint until convergence. In comparison, the descent thrust constraint is not violated and converges more rapidly than the climb constraint. As a result, after the initial strong fluctuations, the constraint quickly stabilizes around its converged value, demonstrating the optimizer's ability to handle early violations and achieve a steady solution.

9.2. Design Vector Evolution and Bounds Evaluation

For all configurations, the initial design vector served as a conceptual, unproven starting point for the optimization, as described in Section 7.7.4. Analyzing how the design parameters evolved throughout the optimization process provides valuable insights, particularly as the process aimed to minimize the mass of the multirotor system, focusing on both the propulsion system and structural components.

Furthermore, the design space in this study is constrained not only by the optimization constraints but also by the set bounds on various parameters, as discussed in Section 7.5. A comparison of the optimized design parameters, Table 8.2, Table 8.3 and Table 8.4 with their respective bounds provides valuable insight into which parameters are driving the optimization process and to what extent the bounds influence the final solution.

9.2.1. Rotor characteristics

Rotor radius and chord

Across all configurations, similar trends were observed, with the most notable being a general reduction in rotor radius. Furthermore, the rotor radius remains well within its upper and lower bounds, suggesting that this parameter is not a limiting factor in the optimization process. The reduction is likely driven by the optimizer's effort to minimize profile power during hover and axial flight, as derived from the equations in Section 6.5.2 and Section 6.5.3. A smaller rotor radius can also positively impact tip speed velocity and rotor mass, contributing to overall efficiency. However, this is a balancing act: profile power also scales with rotor rotational speed, which increases in response to reduced radius, ensuring sufficient thrust production. The thrust generated by the rotors depends directly on both the rotor radius and rotational speed.

As the rotor radius decreases, the average blade chord also decreases significantly, as observed in the optimized design vectors. This trend is likely driven by the aspect ratio constraint, which enforces a strict relationship between chord length and radius, keeping the chord within a bounded range. Since the aspect ratio directly links rotor radius to blade chord, any reduction in radius inherently results in a corresponding decrease in average chord length. Across all configurations, the rotor blade chord consistently reaches or approaches the lower bound.

Rotor Speed

The complexity of this balance between rotor parameters is further evident in cruise conditions, where profile power depends on the advance ratio. A reduced rotor radius increases the advance ratio for a constant rotor velocity, introducing additional trade-offs.

The rotational speeds of the rotors generally remain well within their bounds, with only two rotor sets in the octorotor configuration approaching the upper limit. This occurs primarily during the descent phase, where the speeds of the remaining rotor sets are significantly reduced. This compensation is necessary to maintain thrust balance and stability during the descent. The results indicate that the current bounds on rotational speeds are adequate but should be carefully evaluated for different flight phases to ensure feasibility.

Number of blades and thrust coefficient

For most rotors, the number of blades reaches the upper bound, except in the hexarotor and octorotor configurations, where one set of rotors reduces to five blades. This trend suggests that maximizing the number of blades generally enhances performance, likely due to increased rotor solidity and reduced blade loading as the profile power is further influenced by the solidity factor.

This observation aligns with the implications discussed in Section 6.5.1, where minimizing solidity must be approached with caution. A lower solidity requires a higher blade section angle of attack and a higher lift coefficient to maintain the same thrust coefficient and disk loading. This, in turn, increases blade loading and can lead to blade stall. Consequently, the minimum solidity value is constrained by the onset of blade stall, as defined by the constraints in Section 7.4.1. However, deviations in certain configurations may arise from aerodynamic or structural trade-offs that favor fewer blades. Reducing the solidity factor lowers the rotor's profile drag by minimizing the total blade area, which may provide performance benefits in specific cases.

The interplay between rotor parameters becomes even more evident when considering the blade loading constraint. Similarly, the thrust coefficient is optimized near its lower bound across all configurations. The reduction in thrust coefficient from the initial design point is likely a direct consequence of this stringent constraint, which aims to prevent blade stall on the retreating blade side, as discussed in Section 7.4.1.

Rotor aerodynamics
Additionally, the tip Mach number constraint further influences blade loading, underscoring the interaction between aerodynamic and structural considerations. The bounds on aspect ratio impose further restrictions on chord length and radius, leading to an interdependent optimization of rotor parameters. Since the thrust coefficient is directly linked to rotor radius and average chord through the blade loading parameter, which also depends on the advance ratio and rotational speed, these constraints collectively shape the final optimized design.

Additionally, blade loading is constrained by the advancing blade tip Mach number to limit increases in profile drag. This complex interplay between rotor radius, chord length, thrust coefficient, and rotational velocity leads to the observed trends: decreasing radius, thrust coefficient, and chord length, accompanied by an increase in rotational velocity.

As discussed further in Section 9.1.2, constraints such as tip Mach number, blade stall, and hover thrust were initially violated during the optimization process, highlighting the challenging trade-offs necessary to balance these rotor parameters. Ultimately, the optimizer converged on a solution that satisfied all constraints, resulting in a design that deviated significantly from the initial educated guess.

9.2.2. Rotor Positioning Parameters
Rotor positions evolved throughout the optimization process, particularly along the x- and y-axes, as dictated by constraints on rotor overlap and dimensional bounds. As expected, these positions remained within the set limits, further constrained by rotor radius and spatial positioning requirements to prevent overlap. However, significant variability in rotor positioning was observed, likely due to moment constraint violations during optimization. Changes in rotor size directly influenced support structure mass and aerodynamic performance, which, in turn, affected thrust and rotational velocity, ultimately shaping the final rotor positions.

Interestingly, the vertical (z) positioning of the rotors remains unchanged in the optimized results. This is likely due to the lack of significant benefits from altering the z position within the current model. Increasing the z position would only contribute to additional support structure mass without offering meaningful dynamic or structural advantages. This result points to the need for future investigations into the potential benefits of three-dimensional rotor positioning in improving system performance.

9.2.3. Rotor Support Structure Parameters
The parameters defining the rotor support structure underwent significant changes from their initial values. However, during optimization, variations in maximum takeoff mass (MTOM) and required thrust led to fluctuating forces that influenced deflection, often resulting in temporary constraint violations.

As noted earlier, the initial design was over-dimensioned to satisfy the deflection constraint. The optimizer subsequently refined the support structure parameters to maintain compliance with this constraint while taking advantage of the absence of penalties related to surface area or parasitic drag. This approach aligns with the benefits of thin-walled, large cross-sectional designs, which enhance the moment of inertia and reduce deflection, as discussed in Section 6.4.4.

Consequently, the support structure dimensions are nearly maximized within the specified bounds across all configurations. However, this finding underscores the need for a more detailed structural analysis to evaluate potential trade-offs between structural weight and aerodynamics, as a larger structure could increase overall drag and aerodynamic interference.

9.3. Optimised eVTOL Configuration Evaluation

9.3.1. Rotor evaluation

Starting from the initial configuration, as displayed in Figure 7.4, Figure 7.5 and Figure 7.6 the optimized configurations, shown in Figure 8.18, Figure 8.19 and Figure 8.20 reveal interesting changes in design parameters. Across all configurations, rotors are positioned as close to the fuselage and each other as possible while avoiding overlap, adhering to set constraints. This setup minimizes the support structure's mass, as shorter arms experience reduced bending moments, thus requiring less structural reinforcement. This outcome aligns with optimization expectations, as longer support structures would impose significant mass penalties due to the higher strength requirements.

The optimization results indicate a near-central placement of the overall center of gravity (CoG), which is necessary to achieve a balanced moment distribution. However, for the quadrotor configuration, an unusual asymmetry in rotor size emerges: the aft rotors are larger than the front ones to balance disk area requirements, compensating for limited flexibility in rotor placement due to fewer rotors. The hexacopter and octocopter, however, maintain similar rotor sizes, indicating that configurations with more rotors allow for greater homogeneity in disk loading. The optimization achieves an ideal average rotor radius of approximately $0.75\,\text{m}$ for HF = 0.1, with six blades, although quadrotor configurations deviate slightly to adapt disk loading.

Average thrust coefficients remain similar across configurations and hybridization factors, constrained primarily by blade loading limits, with solidity factors stabilizing around 0.13 to 0.14. These values reflect a bound allowed by the blade loading constraints as visualised in Figure 8.41, Figure 8.42 and Figure 8.43 suggesting an upperbound for the rotor solidity. Interestingly, while hexacopter and octocopter solidity factors remain relatively consistent across hybridization factors, the quadrotor experiences variations due to its restricted design space. This further highlights how rotor count influences design flexibility and disk loading adaptation.

9.3.2. Mass Evaluation

A clear trend emerges across the configurations: an increase in rotor count corresponds to a heavier overall system, and this relationship holds true across all hybridization factors (HFs). At lower HFs, the differences in Maximum Take-Off Mass (MTOM) between configurations are minimal, with only minor variations observed as quantified in Table 8.6 with the mass increase remaining within approximately 1%. However, at higher HFs, as illustrated in Figure 8.24, these differences become more pronounced, with the MTOM of the octocopter increasing by approximately 3% compared to the quadrotor at HF = 0.9. This indicates that hybridization amplifies the mass distinctions between rotor configurations, driven primarily by the growth in Operating Empty Mass (OEM) as system mass increases.

When analyzing the impact of hybridization, higher degrees of hybridization (i.e., increased reliance on batteries) result in a significant rise in MTOM. This trend is primarily driven by the relatively low energy density of batteries compared to fuel, requiring additional battery mass to meet energy demands. Consequently, battery mass becomes a dominant contributor to MTOM, as illustrated in Figure 8.28, Figure 8.29, and Figure 8.30.

As battery mass increases, the overall system mass and power requirements also rise, further amplifying MTOM. This effect persists even though the mass fractions of other subsystems remain relatively constant, except for the support structure, which adapts to accommodate the increased loads.

The increased battery mass also drives up the support structure mass due to the higher overall mass, particularly in hexacopter and octocopter configurations, as reflected in Table 8.6. Notably, during the initial HF step to 0.5, MTOM increases by approximately 19% across all configurations, being a significant rise. This increase is more pronounced in the hexacopter and octocopter due to the greater impact on rotor support structure mass. Beyond HF = 0.5, the rate of MTOM increase stabilizes, culminating in a total rise of approximately 21% for all configurations.

These observations underscore the critical need to optimize the design of support structures, as structural penalties become increasingly significant with rising MTOM. While the masses of components such as motors, propellers, batteries, and internal combustion engine (ICE) subsystems remain relatively consistent across configurations for a given HF, the support structure mass disproportionately affects MTOM at higher HFs. Configurations with more rotors experience greater structural mass penalties, exacerbating the overall MTOM.

However, it is important to recognize that the presented results reflect simplified system modeling and may deviate in real-world applications. The current analysis does not fully account for the masses of integrated subsystems, including cabling, fuel lines, and auxiliary components, which would contribute additional weight and complexity. Additionally, the simplified rotor support structure model likely underestimates the true impact of adding rotors. In practical scenarios, the support structure not only increases total mass but also contributes to greater parasitic drag. This added drag further elevates the overall power requirements, compounding the MTOM increase beyond the structural mass alone. These limitations highlight the importance of incorporating more detailed modeling to account for aerodynamic penalties and structural intricacies associated with multirotor configurations.

9.3.3. Inertia Evaluation

The placement of rotors significantly influences the moment of inertia around various axes. This trend is particularly evident for configurations with a larger number of rotors, such as hexacopters and octocopters. As shown in Table 8.5, the moment of inertia about the x-axis shows a general increase with hybridization factor (HF) for hexacopters and octocopters, but not for quadcopters. This increase arises from the limited design space, which necessitates placing rotors farther from the centerline to accommodate the larger disk area. Consequently, the placement amplifies the rotational inertia.

A similar pattern is observed for the moment of inertia about the z-axis. Here too, I_z increases consistently with HF across all configurations, as shown in Table 8.5. The increased total disk area, necessitated by the higher mass, pushes rotors further from the CoG, amplifying the rotational inertia about the z-axis. For both the x- and z-axes, the rise in rotor count exacerbates this trend, as the need to position rotors farther from the CoG becomes more pronounced due to spatial constraints.

In contrast, the moment of inertia about the y-axis demonstrates a different relationship. For the quadcopter configuration, I_y increases with HF, likely driven by the added weight of the rotors and motors and the increase in disk area. However, for hexacopters and octocopters, a different trend emerges: I_y decreases with an increase in the hybridization factor (HF). This decrease is likely due to the limited design space, which forces rotors to extend more outward along the y-axis and less so along the x-axis as the total rotor area increases. Notably, for higher HF values, the octocopter exhibits the lowest I_y, even lower than the quadcopter's I_y.

For the product of inertia, I_{xz}, the first observation is its overall significantly lower magnitude compared to the moments of inertia about the principal axes. This is likely due to the inherent symmetry in rotor placements, which minimizes cross-coupling between the x- and z-axes. No distinct or consistent relationship is observed between I_{xz} and HF across different configurations. While the hexacopter shows the lowest I_{xz} for HF = 0.9, its values vary at lower HF levels, suggesting no clear pattern of dominance across all hybridization factors.

9.3.4. Performance Evaluation

Diskloading and Hover efficiency

Performance metrics critical to rotorcraft design, such as disk loading and hover efficiency, are evaluated and are visualized in Figure 8.40. At lower hybridization factor (HF) values, the configurations exhibit clustering in terms of disk loading and hover efficiency. However, as HF increases and the associated maximum takeoff mass (MTOM) rises, greater deviations become evident among rotor configurations, reflecting the influence of rotor count and configuration-specific design trade-offs.

Configurations with higher rotor counts generally achieve lower disk loading due to an increase in the total rotor disk area, leading to improved hover efficiency. In contrast, the quadrotor configuration exhibits a noticeable decline in hover efficiency at higher HFs, attributed to the limitations in disk area and the resultant increase in blade loading. When compared to established eVTOL designs such as eHang and Vahana, as shown in Figure 3.10, the optimized configurations demonstrate competitive hover efficiency and disk loading values. This positions them as effective intermediaries between traditional rotorcraft and modern multirotor designs.

Bladeloading

Blade loading analysis indicates consistent average loading across configurations, although quadrotors experience higher per-blade loading due to their reduced rotor count. This increased loading results from the higher thrust required per rotor, as constrained by the overall thrust coefficient and solidity. Interestingly, HF variations do not significantly affect blade loading trends, with maximum blade loading remaining constant across configurations, reflecting a maintained balance in aerodynamic design parameters.

Thrust and angle of attack
The analysis of angle of attack for each configuration, as visualized in Figure 8.44, reveals a non-linear trend. Angle of attack initially increases exponentially before transitioning to linear growth at higher velocities. This behavior parallels the thrust curve; however, the exponential rise in thrust initiates at a higher cruise velocity compared to the angle of attack, which exhibits exponential growth from the onset of the velocity regime. The gradient of thrust increase with flight velocity decreases slightly as rotor count rises, suggesting that additional rotors distribute the aerodynamic load more evenly. At maximum speeds, configurations with more rotors, such as hexacopters and octocopters, exhibit marginally lower angles of attack, likely due to their higher mass and the associated reduction in thrust gradient.

Rotor speed
Rotational velocities across different flight phases further elucidate configuration-specific behaviors. Larger rotors operate at lower speeds due to tip-speed constraints, as demonstrated in Figure 8.31, Figure 8.32, Figure 8.33, and Figure 8.34. As expected, the lowest rotational speeds are observed during hover, while slightly higher speeds are required during cruise to overcome parasitic drag. In both cases, all rotors are effectively utilized. However, in axial flight modes, the optimizer exploits the flexibility of additional rotors in hexacopters and octocopters by selectively reducing rotational speeds for specific rotors, likely to enhance efficiency. This effect is particularly pronounced during the descent phase, as shown in Figure 8.32, where the rotational speeds of certain rotors (e.g., rotors 1 and 4 in the octorotor) are significantly reduced. This adaptability underscores the potential efficiency gains achieved with additional rotors in axial flight.

Velocities
The optimized configurations met cruise and descent speed requirements near the minimum set thresholds as shown in Table 8.5. The optimized cruise speed demonstrate a significant advantage over existing multirotor designs such as the VC2X and eHang, achieving nearly twice their cruise speed. This highlights the substantial performance gains in the cruise phase, making the design competitive with conventional rotorcraft.

Climb speeds, on the other hand, exceeded the minimum requirement of 7 m/s, likely due to induced power savings achieved through higher speeds at balance with the parasitic power. As HF and mass increase, climb speeds decrease across all configurations, while cruise and descent speeds remain closely aligned with their respective minima due to their direct dependence on parasitic drag and descent-limited power.

9.3.5. Power Evaluation

The evaluation of overall installed power, as shown in Figure 8.35, reveals distinct trends across the different configurations and hybridization factors (HF). At a low HF of 0.1, the quadrotor configuration demonstrates the lowest overall installed power. However, this advantage diminishes rapidly as HF increases, with the quadrotor exhibiting a steeper gradient in installed power compared to the hexarotor and octorotor. This behavior indicates that while the quadrotor may be advantageous for lower payloads, its performance is less robust under increased mass and power demands. Conversely, the hexarotor demonstrates a flatter gradient in installed power, suggesting enhanced power stability across varying HFs. The octorotor, despite its higher initial power requirements, exhibits a steeper gradient at elevated HFs, implying that the power efficiency gains achieved by adding rotors are offset by the accompanying weight increase.

Analyzing the power contributions across flight phases for the three configurations, normalized with respect to the hexarotor, provides further insight. For the hexarotor, the induced power shows a significant reduction, consistent with the power curve visualized in Figure 8.36. However, the cruise phase emerges as the most power-intensive phase, primarily due to the considerable increase in parasitic drag and due the power required to propel the rotor forward as explained in Section 6.5.4. This trend underscores the sensitivity of cruise performance to drag effects, which scale with velocity. Across the configurations, profile power exhibits minimal variation during hover and climb phases, with slightly elevated values during climb due to increased tip velocities. Induced power peaks during the climb phase, while hover and descent phases exhibit similar induced power requirements. Notably, during descent, the induced power benefits from the windmilling effect, reducing the overall power requirement. The descent phase also displays favorable parasitic power, which becomes negative due to the drag contributing to lift, resulting in the most power-efficient phase overall.

When comparing configurations during various flight phases, parasitic power during cruise remains consistent across configurations due to the simplified drag model employed, which does not penalize configurations for increased parasitic drag from additional support structures. For the quadrotor, hover, climb, and descent phases exhibit lower overall power requirements, likely due to reduced profile power resulting from the smaller number of rotors. Conversely, the octorotor demonstrates higher profile power during these phases, attributable to its increased rotor count. However, this is counterbalanced by a reduction in induced power, which lowers the total required power, particularly during hover. This improved load distribution among the rotors enhances efficiency in hover, where the octorotor outperforms both the quadrotor and hexarotor in terms of total power requirements.

The descent phase of the octorotor reveals an interesting dynamic; while its higher profile power may stem from its increased rotor count, its induced power advantage persists across all flight phases, further affirming the benefits of load distribution. These observations underscore the trade-offs inherent in rotor configuration design. The quadrotor offers simplicity and efficiency at lower payloads, while the octorotor excels in induced power efficiency and robustness during hover. The hexarotor, positioned between these configurations, balances power stability and efficiency across varying flight conditions, making it a strong contender for operational scenarios requiring consistent performance.

9.3.6. Cost Evaluation

As part of the GoAERO competition requirements, both reduced acquisition costs and operational costs compared to traditional rotorcraft are critical evaluation metrics. As outlined in Section 3.4, the purchase cost of an aircraft is primarily driven by its empty mass, installed power, structural and mechanical complexity, and the cost of electronic systems. For electric propulsion systems, the cost of batteries must also be explicitly included in the purchase cost estimation. On the operational side, a significant portion of costs arises from fuel or energy consumption, which tends to be lower for all-electric propulsion configurations despite their typically higher overall mass.

Acquisition Costs

Addressing acquisition costs, configurations with lower hybridization factors (HFs) generally would exhibit reduced empty mass and installed power. These factors contribute to lower presumed purchase costs, in addition to the cost of batteries being significant expense in electric propulsion. However, the hybrid system's increased mechanical and structural complexity partially offsets these savings, as hybrid architectures introduce additional components, such as turbine generators, power management systems, and control interfaces. These additions inherently increase production and integration costs.

Moreover, rotor count plays a pivotal role in acquisition costs. While increasing the number of rotors can reduce the installed power per rotor and thereby potentially decrease component-level costs, it also raises the empty mass and overall system complexity. This added complexity, particularly in terms of manufacturing, assembly, and system integration, is likely to lead to higher acquisition costs.

Operational Costs

Operational costs include energy or fuel costs, maintenance, and system longevity. At lower HFs, fuel dependency increases, resulting in higher energy costs over the aircraft's operational life. Additionally, turbine generators in hybrid systems are expected to incur higher maintenance costs due to the mechanical wear and tear associated with their moving parts. In contrast, electric propulsion systems generally demand less maintenance due to the relative simplicity and durability of electric motors and their associated components.

When comparing configurations, the increased rotor count further complicates the operational cost landscape. While more rotors can improve redundancy and system reliability, they may also require more frequent inspections and maintenance due to the higher number of components subject to wear and failure. Conversely, configurations dominated by electric systems may experience lower maintenance costs overall, aligning with the GoAERO competition's emphasis on cost efficiency.

9.3.7. Stability Evaluation

The equations of motion (EOM) provide insights into the flight mechanics of the eVTOL, as outlined in Section 6.6. Linearizing the EOM around the hover and the longitudinal trim point reveals information about the multirotor's stability and dynamics during hover and cruise. However, the accuracy of these stability evaluations depends heavily on the fidelity and granularity of the underlying mathematical model. Analyzing the external forces and moments acting on the multirotor, as presented in Section 6.6.5, shows that these forces primarily originate from rotor thrust, rotor torque, gravity, and parasitic drag.

Examining the system matrices for hover and cruise (Equation 6.131 and Equation 6.133), reveals that the external forces generated by the rotors are not part of the state matrix but are instead captured in the control matrices (Equation 6.132 and Equation 6.134). These control matrices describe variations in total thrust, roll torque, pitch torque, and yaw torque. This separation occurs because the current mathematical model contains stability derivatives related to external forces and moments that are independent of the system states. Instead, these forces are directly influenced by rotor thrust and are reflected in the control matrices, which depend on the multirotor's mass and moments of inertia.

For the hover trim point, the system matrix is influenced by gravitational components associated with perturbations in the pitch and roll angles, as well as translational and rotational rates. Since all initial states are zero, aerodynamic terms vanish from the A matrix at the hover trim point. For the longitudinal trim point, the A matrix is similar in its treatment of gravitational components and perturbations in translational and rotational rates but now includes terms associated with the multirotor's initial pitch angle, total mass, and initial velocity in the x-direction. The initial velocity in the x-direction is coupled with perturbations in the q and r states, while the mass contributes to the linearized drag term C_x. Despite these changes, the control matrix remains unchanged from the hover trim point.

Influence of rotor placement
The natural stability of the multirotor, as determined by the eigenvalues of the system matrix, is invariant to rotor configuration for a given total mass. Rotor placement, thrust characteristics, and other configuration-specific parameters do not directly appear in the system matrix. Instead, they influence the control dynamics through the control matrix. This indicates that the inherent stability characteristics are unaffected by rotor configuration under the current model, except through overall mass. Consequently, these factors become critical in control design, where inertia and moment arms significantly impact control behavior.

Rotor placement and symmetry further shape the dynamic characteristics of the system. In the derived mathematical model, the stability along the principal axes is governed by the collective effects of all rotors and any thrust imbalances. However, asymmetry around the y-z plane affects the control matrix, particularly in the change in roll torque (ΔL_T). This is primarily linked to the coupling of roll and yaw accelerations through the off-diagonal inertia tensor term I_{xz}, as detailed in Section 6.6.3.

9.3.8. Eigenvalue Analysis

The eigenvalue analysis of the linearized system matrix provides valuable insights into the system stability. Eigenvalues represent the natural modes of the system, with their real components indicating stability and their imaginary components representing oscillatory behavior, as explained in Section 6.7.1.

At the hover trim point, zero eigenvalues are observed across the different configurations, as shown in Figure 8.48, Figure 8.50, and Figure 8.52. These zero eigenvalues indicate that the corresponding mode of the system is neutrally stable. This means the system neither grows unbounded nor decays but remains constant or evolves linearly over time, depending on the initial conditions. A zero eigenvalue corresponds to a state that does not naturally return to equilibrium or diverge. For a multirotor, this behavior aligns with the fact that certain movements, in the absence of control inputs, lack restoring forces. This is because the primary external force acting on a multirotor, thrust generated by the rotors, is represented in the control matrix of the derived mathematical model rather than the system matrix.

At the cruise trim point, a fully real, negative eigenvalue is observed, as shown in Figure 8.48, Figure 8.50, and Figure 8.52. A negative real eigenvalue indicates stability in the direction associated with the corresponding eigenvector, with the system states along this mode decaying exponentially to zero over time. This behavior is desirable for stable flight. The absence of an imaginary component confirms the lack of oscillatory behavior, suggesting purely damping effects. The observed fully real eigenvalue is tied to the stability derivative X_u, which is associated with the parasitic drag term derived from the system matrix and the mass of the configuration. However it should be noted that the absence of any imaginary component in the eigenvalues may result from modeling simplifications or specific parameter choices which reduce the observed eigenvalues to be fully real.

The mode associated with the fully real eigenvalue in cruise is entirely dependent on the motion in the x-direction and is therefore characterized by the surge motion of the multirotor. Due to this exclusive x-direction dependence and the non-oscillatory nature of the mode, it can be identified as the surge subsidence mode. In this context, "surge" refers to the motion along the longitudinal x-axis, while the term "subsidence" denotes the absence of oscillatory behavior and the gradual decay of perturbations in the x-direction.

Further analysis of the stability derivative X_u, as shown in Figure 8.49, Figure 8.51, and Figure 8.53, reveals a linear decrease in X_u (becoming more negative) with increasing cruise velocity. This trend is attributed to the parasitic drag term, which contributes to the stable convergence of changes in velocity (Δu) in the absence of external control inputs means that the system naturally resists disturbances in the corresponding state (e.g., forward velocity). When X_u becomes more negative as cruise speed increases, it indicates that the damping effect due to parasitic drag grows stronger, enhancing the system its ability to resist and damp perturbations in forward velocity. The fact that X_u decreases linearly implies a consistent, proportional increase in the stabilizing force (drag) with speed.

Additionally, the analysis shows that the real eigenvalue is influenced by the overall mass of the configuration through the stability derivative X_u. As displayed in Figure 8.49, Figure 8.51, and Figure 8.53, a higher mass reduces the gradient of the stability derivative with increasing cruise velocity, thereby decreasing the magnitude of the eigenvalue in the cruise condition indicating indicates slower exponential decay resulting in a more gradual stabilization with slower damping. This demonstrates the impact of mass on the system's dynamic response and stability where an increase in mass reduces the system response.

9.4. Validating eigenvalue Results

The results obtained from this study align well with expectations derived from the mathematical model, particularly concerning the inherent controller dependence of multirotors. However, it is worth noting that research on the natural dynamics of multirotors is limited, as the majority of studies focus on closed-loop control systems rather than open-loop behavior. This gap in the literature highlights the importance of analyzing multirotor natural dynamics in the context of design optimization.

In a study by Venkatesh et al. [83], a linear model for open-loop quadcopter dynamics was developed for planar motion and PD controller design. Their analysis of the open-loop transfer function matrix identified poles at the origin when linearized around the hover trim point, indicating neutral stability. This observation aligns with the findings of this thesis, where eigenvalue analysis similarly reveals poles at the origin for the hover trim point, confirming neutral stability in that mode. However, the study by Venkatesh et al. is limited to the hover trim point and does not extend its analysis to additional trim points, such as cruise, which are explored in this thesis, providing a broader perspective on system stability across different flight conditions.

However, a comparison with the work of Niemiec and Gandhi [84] adds further context to the validation process. Their study compared quadcopters operating in ”plus” and ”cross” configurations through eigenvalue analysis, identifying two oscillatory modes in hover: a longitudinal phugoid mode (coupling longitudinal translation and pitch) and a lateral phugoid mode (coupling lateral translation and roll). Both modes are stable, with poles positioned relatively close to the origin. This differs from the findings of this study, which do not show the presence of such stable oscillatory modes.

Upon closer examination of the derived system matrix, it is evident that additional stability derivatives, such as L_p, M_q, and N_r, are not present in the mathematical model used in this paper. These derivatives account for damping effects in roll, pitch, and yaw, respectively, and their absence may explain why oscillatory modes are not observed. It is worth noting however that Gandhi's study does not explicitly detail the origin of these stability derivatives, leaving open questions about the underlying assumptions and dynamics contributing to the observed modes. The lack of detailed stability derivative data in Gandhi's work limits the ability to fully align the findings.

9.5. eVTOL Configuration HQ implications

Handling qualities (HQ) are a critical design parameter for rotorcraft, particularly for eVTOL configurations tailored to emergency response scenarios, as emphasized by the mission tasks outlined in Chapter 2. HQ significantly impacts the vehicle's ability to perform precise and controlled movements in confined or adverse environments. However, the results presented in this study provide limited insights into the HQ potential of the three configurations beyond the stability analysis and overall dependence on controller design for stability.

9.5.1. Controllability

As highlighted in the literature review (Section 3.6), determining the optimal number of rotors for multirotors is non-trivial due to the trade-offs between static and dynamic performance. While an increased number of rotors generally improves static performance, the added weight and complexity can diminish the dynamic performance advantages.

Configurations with more rotors tend to exhibit smaller individual rotor inertias due to their reduced size. This reduction in inertia theoretically requires less power per motor to achieve adequate rise times, improving responsiveness in pitch, roll, and heave control axes [85]. Research findings consistently show that configurations with higher rotor counts require lower current margins to regulate these axes, primarily because smaller rotors overcome their inertia more efficiently during thrust changes [86].

The findings of Ieter [85] further confirm this trend, demonstrating that both the hexacopter and octocopter achieve significantly lower rise times compared to the quadcopter while requiring less power per motor. Among the evaluated configurations, the octocopter achieved the shortest rise times with the least power, suggesting an advantage in responsiveness and agility for higher rotor counts.

Yaw control presents unique challenges for multirotors. Unlike roll and pitch, yawing moments are generated by the net torque differential between rotors, resulting in smaller available moments to execute yaw commands. Larger yaw commands are more likely to push rotors to their operational limits, especially for configurations with higher moments of inertia, such as the octocopter.

Studies on yaw performance during equivalent maneuvers show that the quadcopter and hexacopter remained within input limits throughout the maneuvers, while the octocopter experienced dynamic discontinuities due to input saturation. This is attributed to the higher moment of inertia of the octocopter, which requires greater yawing moments, even with more rotors available to generate torque [29].

Furthermore in this paper the difference in innertias is mapped for the different configurations themselves. While the individual rotorational innertias of the rotors decrease for the increase in rotors due to the smaller rotor size, the overall innertia generally increases of the eVTOL due to the spreading of the rotors except for the I_y due to the more evenly distributed masses within the design space compared to the other configurations. As a result the notion is to be made that while individual controll of rotors generally increases for an increase in rotor count, dynamic performance around the z-axis and x-axis degrade due to the increased innertias while around the y-axis the performance is improved at the cost of overall increase in mass.

9.5.2. Disk Loading

Disk loading plays a critical role in hover efficiency, control authority, and overall energy consumption. Lower disk loading reduces the induced power required for lift, improving both hover performance and maneuverability. Configurations with higher rotor counts, such as hexacopters and octocopters, achieve reduced disk loading by distributing lift across a larger total disk area. This reduction in per-unit thrust potentially improves stability, particularly during low-speed maneuvers, where fine control over thrust is essential for navigating confined spaces or performing precise landings.

Additionally, reduced disk loading facilitates smoother transitions between hover and forward flight, critical in emergency response scenarios where adaptability is key. Reduced disk loading, a result of spreading thrust across larger rotor areas or more rotors, decreases the amount of lift each rotor must generate. This potentially allows smoother aerodynamic transitions between hover and forward flight, as the rotor system experiences less abrupt changes in induced velocity and thrust. Lower induced power demand enhances overall energy efficiency, particularly in hover-intensive missions, making such configurations advantageous for tasks requiring prolonged hover operations, such as search-and-rescue or payload delivery in tight urban environments.

9.5.3. Center of Gravity (CoG)

A centrally located CoG is crucial for balanced moment distribution and predictable flight dynamics. Deviations in CoG placement can increase control effort and compromise stability, particularly during rapid maneuvers or high-speed transitions. This study's optimized configurations maintain a near-central CoG, which enhances both static and dynamic stability.

The centralized CoG minimizes unwanted pitch, roll, and yaw moments, simplifying control algorithms and enabling smoother transitions between flight phases. This balance not only reduces the computational burden on stabilization systems but also decreases the energy required for control corrections. Furthermore, maintaining a centralized CoG improves maneuverability by ensuring that thrust adjustments across rotors yield predictable responses, which is especially critical in emergency scenarios involving rapid repositioning or tight-space navigation.

9.5.4. Power Distribution and Stability

Higher rotor counts allow for more uniform power distribution, reducing individual rotor stresses during high-thrust maneuvers. Spreading thrust demand across multiple rotors potentially lowers mechanical strain and thermal loads on individual motors, enabling smoother thrust modulation and improved operational stability. This capability is particularly advantageous in dynamic operations where precise and rapid adjustments to thrust are required, such as during obstacle avoidance or hover-to-cruise transitions.

Even power distribution also reduces power gradients, enabling configurations with higher rotor counts to adapt quickly to control inputs without overloading individual motors as previously discussed. This adaptability enhances responsiveness and ensures reliable performance during demanding maneuvers, such as high-speed turns or rapid altitude changes. However, the added mass from extra rotors and structural components introduces a trade-off, as it increases the system's inertia, slightly reducing agility compared to lower-rotor-count configurations.

9.6. GoAERO eVTOL Evaluation

The GoAERO competition focuses on developing and operating a single-occupant, affordable, robust, and effective emergency response aircraft designed around three primary missions. These missions aim to advance eVTOL technology through three key objectives: productivity, adversity, and maneuvering. Each mission emphasizes unique performance aspects, such as payload efficiency, endurance, operational robustness in challenging conditions, and precise maneuverability. Additionally, the designs must achieve lower acquisition and maintenance costs compared to conventional rotorcraft.

Formulating the configurations in accordance with the competition's requirements, including the payload capacity to accommodate a caregiver and pilot, and optimizing the design parameters within the permissible design space enabled the evaluation of three viable configurations. These configurations adhered to the GoAERO competition guidelines and are optimized for minimum MTOM during the Productivity Mission. While all configurations complied with the competition requirements, their performance varied, making them unequal contenders.

The Productivity Mission aims to demonstrate the flyer's ability to deploy quickly and continuously while efficiently transporting payloads. This mission is identified as the most critical for sizing the overall propulsion system, as it directly influences power requirements, performance, and system mass while the performance ranking is based on the ratio of total payload weight ferried to the total weight of the system. Consequently, the configurations are optimized for MTOM in accordance with the mission's payload and range requirements.

In contrast, the Adversity Mission and Maneuvering Mission act as constraints for overall sizing and guide configuration assessments based on performance and handling qualities. The Adversity Mission focuses on robustness and operational reliability in challenging conditions, while the Maneuvering Mission evaluates the flyer's ability to navigate tight spaces, avoid obstacles, and maintain stability during critical operations such as takeoff, landing, and hovering.

9.6.1. Trade-off

When comparing the optimized configurations to existing eVTOL designs such as eHang and Vahana, it becomes evident that these configurations exhibit competitive hover efficiency and disk loading values. They effectively bridge the gap between conventional rotorcraft and modern multirotor systems. Furthermore, their cruise speeds demonstrate a significant advantage over existing multirotor designs like the VC2X and eHang while maintaining competitiveness with conventional HEMS rotorcraft, such as the Bell 505 Jet Ranger X. These findings underscore the promising potential of the configurations developed in this research.

A comparative evaluation of the configurations reveals notable distinctions. From a purely mass-oriented perspective, the quadrotor demonstrates the lowest Maximum Take-Off Mass (MTOM). This characteristic suggests it would score the highest in terms of payload-to-system ratio, aligning with the scoring criteria for the Productivity Mission. Additionally, its simpler design implies lower acquisition and maintenance costs, as fewer components typically translate to reduced maintenance demands. However, the mass evaluation also highlights that the primary difference in mass stems from the increased structural mass in higher-rotor-count configurations. Notably, the simplified structural model used in this research could understate the impact of structural optimizations, which a more detailed structural analysis might reveal.

This is the result of the clear trend emerged from the optimization results: configurations with higher rotor counts consistently exhibit greater MTOM across all hybridization factors (HFs). At lower HFs, these differences in MTOM are less pronounced, indicating that hybridization amplifies mass disparities between configurations. This phenomenon is primarily driven by the exponential rise in Operating Empty Mass (OEM) as system mass increases. Consequently, at an HF of 0.1, the quadrotor would achieve the highest productivity mission score, as all configurations are optimized to meet the same performance requirements for this mission.

When considering the Adversity and Maneuvering Missions, however, a different perspective emerges. Configurations with higher rotor counts benefit from reduced disk loading due to a larger total rotor disk area, enhancing hover efficiency. Notably, hexacopter and octocopter designs achieve more uniform disk loading across rotors, promoting control authority, stability, and energy efficiency during hover-intensive operations. This characteristic is particularly advantageous for precise maneuvers, such as navigating confined spaces or landing in challenging environments, as required by these missions. Reduced disk loading also improves the aerodynamic transitions between hover and forward flight, critical in dynamic emergency response scenarios. While increased rotor counts enhance static performance, the added weight and complexity can slightly offset these benefits in dynamic performance. However, the mass differences observed in this study are not substantial enough to significantly affect this trade-off.

Another key advantage of higher rotor counts is the ability to distribute power demands more evenly across rotors. This uniform power distribution reduces mechanical stresses on individual rotors during high-thrust maneuvers, enhancing system stability and reliability. Configurations like the hexacopter and octocopter would theoretically achieve smoother thrust modulation and improved responsiveness during demanding maneuvers, such as obstacle avoidance or rapid altitude changes. This characteristic could directly contributes to better handling qualities (HQ), particularly in dynamic operational environments.

On the other hand, increased rotor counts introduce challenges in yaw control. Configurations with higher moments of inertia, such as the octocopter, require greater yawing moments, which can push rotors closer to their operational limits during large yaw commands. For instance, the octocopter exhibited dynamic discontinuities in yaw performance due to input saturation, a limitation not observed in the quadcopter or hexacopter. Furthermore, while the octocopter's inertial properties improved pitch and roll responsiveness, its yaw dynamics are negatively affected by the higher moment of inertia.

The hybridization factor (HF) also plays a pivotal role in the trade-off analysis. Lower HFs generally result in reduced MTOM and better performance in the Productivity Mission due to lower fuel dependency and overall system mass. However, hybrid systems with higher HFs provide operational advantages, such as reduced fuel consumption and lower energy costs over the aircraft's lifecycle. The increased reliance on electric propulsion systems also lowers maintenance demands, as electric motors are inherently more durable and simpler to maintain than turbine generators.

Despite these advantages, the increased structural complexity and higher acquisition costs of hybrid systems must be considered. Configurations with higher rotor counts or more electrified systems inherently demand more intricate manufacturing and integration processes, driving up costs. Additionally, the added weight from extra rotors and structural components in higher-rotor-count configurations increases the system's inertia, slightly reducing agility compared to quadrotor designs.

Ultimately, the trade-off between rotor count, hybridization factor, and mission requirements highlights the need for a balanced approach. While the quadrotor excels in terms of productivity and cost-effectiveness, configurations with higher rotor counts offer superior performance in hover efficiency, handling qualities, and adaptability, making them more suited to the Adversity and Maneuvering Missions. These findings underscore the importance of aligning configuration selection with specific mission priorities to optimize overall performance in the GoAERO competition.

9.6.2. Proposed Configuration

Concerned with lower HF, the reliance on the turbine generator increases, potentially driving up acquisition costs due to increased system complexity. Moreover, lower HFs generally result in higher operational costs, primarily due to increased fuel consumption and maintenance requirements associated with turbine generators. To comprehensively evaluate the trade-offs, further analysis is necessary to assess the overall performance and mass benefits relative to the additional costs incurred at lower HFs to be able to propose a viable value.

Depending on the desired trait, different configurations excel in various aspects of the GoAERO competition.

For missions prioritizing general mass constraints, the quadrotor at a low Hybridization Factor (HF) emerges as the optimal choice. Its lower Maximum Take-Off Mass (MTOM) leads to a higher payload-to-system mass ratio, aligning well with the productivity mission. Additionally, the simpler architecture of the quadrotor suggests reduced acquisition and maintenance costs due to fewer components.

Despite this, configurations with higher rotor counts demonstrate significant handling quality (HQ) and hover performance advantages, including enhanced hover efficiency and control authority. From a controllability perspective, the addition of rotors generally results in reduced power gradients, faster rise times, and improved responsiveness. These benefits argue in favor of the octocopter concerned with the maneuvering and adversity mission.

However, the octocopter presents challenges that cannot be overlooked. Larger yaw commands required to counteract its higher moments of inertia, combined with the inherent dependence of multirotors on controllers for stability, may limit its responsiveness and dynamic performance around the z-axis and x-axis. While increased damping due to higher inertia enhances stability, it simultaneously reduces agility. Furthermore, the octocopter's greater structural mass and complexity, coupled with potential interaction effects between closely spaced rotors, diminish its viability, especially at higher HFs where the performance gains do not outweigh the mass penalties.

Balancing these considerations, the hexacopter is proposed as the most viable configuration for further development in the GoAERO competition. While its MTOM is higher than that of the quadrotor, the hexacopter achieves a favorable balance between mass, controllability, and overall HQ. The additional rotors provide greater design flexibility, enabling optimization of rotor placement, size, and redundancy, while maintaining manageable complexity compared to the octocopter. The hexacopter also benefits from improved handling qualities and hover performance, which are critical for the adversity and maneuvering missions. Moreover, it mitigates the drawbacks of increased inertia and yaw response challenges inherent in the octocopter, ensuring robust performance across the varied mission profiles of the competition.

9.7. Limitations

This thesis faces several limitations stemming from modeling assumptions, simplifications, and the defined scope of the study. These limitations, while necessary to make the problem manageable within the preliminary design phase, affect the fidelity and potential applicability of the results to real-world scenarios. By acknowledging these constraints, this research seeks to provide a clear context for interpreting its findings and to outline areas for future investigation.

9.7.1. Aerodynamics

Key simplifications in the aerodynamic modeling include the use of idealized methods, such as momentum theory, to calculate rotor thrust. This approach assumes inviscid, incompressible, and steady flow, which, while suitable for preliminary analyses, fails to fully capture real-world phenomena such as blade-tip effects and rotor wake dynamics. These discrepancies are partially mitigated by incorporating a figure of merit (FoM), but the resultant predictions still diverge from actual performance. Additionally, the actuator disk model assumes an infinite number of blades operating within a uniform streamtube, oversimplifying the complexities of real-world rotor dynamics.

It is important to note that this study excludes rotor wake interaction effects and rotor-airframe interaction effects, as outlined in the initial assumptions. A relevant study investigating the aeromechanics and wake of a quadcopter in forward flight [87] using large-eddy simulations and a Vortex Particle–Mesh method highlights the significant impact of rotor-rotor aerodynamic interactions. These interactions are shown to notably affect the performance of rear rotors, altering the aircraft's overall trim conditions. Consequently, the performance differences observed among quadcopter, hexacopter, and octocopter configurations in this thesis may not fully capture the influence of such effects, nor do they account for potential mitigation strategies such as staggered rotor placements.

However, the same study concludes that the contributions of rotors to the overall lift and drag of the airframe are negligible. This finding supports the exclusion of airframe interaction effects in this study, validating the assumption of a simplified model for rotor forces. Furthermore, the authors indicate that while their research focused on a small-scale drone, the scalability of rotor-airframe interaction effects to larger Urban Air Mobility (UAM) vehicles ensures the broader applicability of these results. Thus, the findings of this study remain robust within the scope of the chosen assumptions and design framework.

The aerodynamic modeling also assumes constant air density and neglects environmental effects, such as crosswinds, rain, and gusts, which could significantly influence real-world performance. Furthermore simplified geometric shapes (e.g. ellipsoids) are used to estimate drag coefficients, excluding the effects of complex shapes, surface irregularities, and detailed aerodynamic interactions.

9.7.2. Modeling Scope

The computational simulations in this study rely on idealized assumptions, including perfect initial conditions and steady-state operations, while excluding the effects of operational wear-and-tear and transient dynamics. Key external disturbances, such as wind gusts, electromagnetic interference, and extreme weather conditions, are omitted from the model, even though they are critical considerations for disaster response scenarios. Additionally, variations in gravitational acceleration due to altitude or geographic location are neglected.

The model assumes constant payload, crew, and fuel masses, disregarding dynamic variations during missions such as fuel consumption or payload redistribution, which could impact stability, performance, and handling qualities (HQ). Furhtermore parasitic drag is assumed to dominate for the dynamic model, with induced and profile drag forces excluded due to their relatively smaller contributions. While this simplification streamlines the calculations, it introduces inaccuracies in stability predictions compared to real-world conditions.

The hybrid-electric propulsion system is modeled with fixed energy density and efficiency values, ignoring the potential effects of temperature, aging, and operational stresses on system performance. Furthermore, the fuel mass is conservatively overestimated, potentially leading to inaccuracies in optimal fuel consumption predictions for specific mission profiles. These simplifications limit the applicability of the results to real-world conditions and suggest the need for further refinement in future studies.

9.7.3. Stability and Nonlinear Dynamics

The evaluation of stability in this study is based on linearized state-space models. While effective for initial analysis, these models fail to capture the nonlinear dynamics, unsteady aerodynamic effects, and pilot interaction influences that arise during complex or aggressive maneuvers. This limitation may result in an incomplete understanding of the vehicle's dynamic behavior under real-world operating conditions.

Stability assessments rely heavily on the control matrix, emphasizing stability achieved through active control rather than the inherent natural stability of the airframe. Consequently, HQ is to be approached predominantly as a control design challenge, potentially overlooking opportunities for airframe-level design improvements that could enhance stability and reduce reliance on active control systems.

Additionally, gyroscopic effects, which can significantly influence handling during rapid yaw or roll maneuvers, are not explicitly evaluated. These effects could play a critical role in determining dynamic stability and maneuverability. Addressing these limitations would require incorporating nonlinear dynamics, pilot-in-the-loop simulations, and more comprehensive modeling of gyroscopic interactions and unsteady aerodynamic phenomena.

9.7.4. Structural Limitations

The structural analysis in this study is based on statistical mass estimation methods derived from historical data. While useful for preliminary design, these methods may not fully account for advancements in materials science or innovative structural configurations, potentially leading to inaccuracies in weight predictions and load distribution. This limitation could result in conservative or overly optimistic performance estimates.

The rotor system is modeled with rigid blades, neglecting flexibility and aeroelastic effects that significantly influence stability, dynamic response, and overall performance. Similarly, the fuselage, support structures, and rotors are treated as rigid bodies, ignoring vibrational modes and structural deformation under operational loads. These simplifications overlook critical aeroelastic interactions that could affect handling qualities, stability, and structural integrity during real-world operations.

Additionally, vibrational modes and aeroelastic phenomena, which play a significant role in multirotor performance, are not explicitly analyzed. The absence of these considerations impacts the fidelity of the results, particularly for configurations operating under high loads or in dynamic environments. Addressing these limitations would require advanced computational techniques, such as finite element analysis (FEA) or coupled aeroelastic simulations, to better predict structural performance and interactions.

10
Conclusions and Recommendations

This thesis presents a comprehensive optimization framework for multirotor eVTOL designs tailored to emergency response missions, aligning with the objectives of the GoAERO competition. By focusing on three primary mission profiles, i.e. Productivity, Adversity, and Maneuvering, this research developed a robust and efficient emergency response aircraft capable of excelling across diverse performance metrics. The optimization process prioritized minimizing the Maximum Take-Off Mass (MTOM) while meeting payload, range, and operational requirements mandated by the competition.

This study examined the optimization of various multirotor configurations, quadrotor, hexarotor, and octorotor, focusing on design trade-offs, constraint adherence, and performance metrics. The analysis explored the interplay between rotor count, hybridization factors, and overall system performance, providing key insights into the implications of configuration-specific parameters.

Additionally, by deriving and linearizing the equations of motion (EOM) around the hover and longitudinal trim points, and formulating the dynamic system, the inherent stability characteristics of multirotor systems are evaluated. These findings enhance the understanding of multirotor eVTOL design and serve as a foundation for the future development of emergency response aircraft capable of excelling in real-world applications.

These critical design trade-offs, including energy efficiency, payload capacity, and stability, are systematically addressed, resulting in optimized configurations suitable for demanding operational scenarios. This research provides a proof of concept for multirotor eVTOL configurations that meet stringent performance requirements while leveraging innovative hybrid-electric propulsion systems and advanced optimization techniques with the central research question being:

> *What are the optimal design parameters that drive handling qualities for a hybrid multirotor emergency response eVTOL in the GoAERO competition?*

Optimisation

The optimization process demonstrated successful convergence across all configurations, with the algorithms effectively meeting convergence criteria and constraints. The results validate the use of momentum theory for power requirements and the framework's ability to explore and refine the design space.

Distinct behaviors among configurations were revealed during convergence histories. Early peaks in the objective function and constraints reflected the exploratory phase of the optimization, shaped by the nascent state of eVTOL technology and limited reference data. These challenges were successfully resolved by the optimizer, demonstrating its capability to navigate constraint-driven design challenges.

The evaluation of the design bounds highlighted the importance of rotor blade parameters, number of blades, and rotor positioning in shaping the final design. While rotor radius and positioning were not limiting factors, rotor blade chord length and thrust coefficient were consistently optimized near their lower bounds, indicating aerodynamic and structural constraints that governed the design choices. Furthermore, the analysis of support structure dimensions revealed a tendency to maximize the structure's size within the given bounds, suggesting that future investigations could benefit from exploring trade-offs between structural mass and aerodynamic penalties.

Overall, the optimization study successfully demonstrated the intricate interplay between design complexity, computational efficiency, and constraint satisfaction for multirotor eVTOL configurations. The findings highlight the effectiveness of the optimization framework in navigating complex design spaces and provide valuable insights for future research on eVTOL aircraft design, particularly in refining rotor configurations, structural components, and computational strategies for enhanced performance and feasibility.

Configuration

Optimized configurations highlight trends in rotor placement and size, emphasizing efforts to minimize support structure mass while maintaining a near-central center of gravity (CoG) to balance moments. The findings underscore the impact of rotor count on design flexibility, with hexacopters and octocopters achieving greater homogeneity in disk loading and and overall rotor parameters compared to quadrotors, which faced constrained design spaces when it comes to rotor parameters.

Mass evaluation reveals the substantial influence of hybridization and rotor count on Maximum Takeoff Mass. Battery mass emerges as a critical contributor to MTOM, driving up support structure requirements and emphasizing the importance of optimizing structural design. While configurations with fewer rotors demonstrate lower MTOW at higher HFs, the simplified model employed in this study suggests potential underestimations of structural and aerodynamic penalties associated with increased rotor counts. Future work should incorporate more detailed subsystem modeling to refine these estimates.

Inertia analysis revealed that higher rotor counts increase moments of inertia, which can significantly impact control. A greater moment of inertia results in slower system dynamics, reducing agility and responsiveness. These findings emphasize the importance of carefully considering inertia properties in the early design stages to achieve a balance between stability and responsiveness.

Performance evaluation guided to the benefits of increased rotor count for hover efficiency and control authority. Quadrotor configurations faced challenges in maintaining efficiency due to elevated blade loading, while hexacopter and octorotor designs demonstrated robust power performance and energy efficiency. Despite these challenges, the optimized configurations exhibit competitive performance metrics, positioning them favorably against existing eVTOL designs in terms of hover efficiency compared to other eVTOLS and cruise speed compared to HEMS rotorcraft.

The findings highlight the inherent trade-offs between rotor count, hybridization factor (HF), and mission-specific priorities. Configurations with lower rotor counts, such as the quadrotor, excelled in terms of payload-to-system mass ratio and simplicity, making them ideal for the Productivity Mission. Their reduced MTOM and lower acquisition and maintenance costs reinforce their suitability for applications prioritizing mass efficiency and cost-effectiveness. However, these designs faced limitations in hover efficiency, control authority, and handling qualities, which are critical for the Adversity and Maneuvering Missions showing the importance of considering HQ in an early stage.

Stability and Handling Qualities

Stability

The eigenvalue analysis provides valuable insights into the stability characteristics of the multirotor system at both hover and cruise trim points. At the hover trim point, the presence of zero eigenvalues indicates neutral stability, reflecting the absence of inherent restoring forces in the natural dynamics of the system. This behavior aligns with expectations, as multirotor motions remain unconstrained without control inputs. Namely, an examination of the system matrices for hover and cruise reveals that the external forces generated by the rotors are not included in the state matrix but are instead captured within the control matrices. This distinction underscores the multirotor's reliance on active control for stability.

The cruise trim point on the other hand reveals a fully real, negative eigenvalue corresponding to the surge subsidence mode, which signifies stable, non-oscillatory decay of disturbances in the longitudinal direction. The stability derivative X_u plays a key role in this behavior, with its dependence on parasitic drag and system mass highlighting the proportional relationship between cruise velocity and stability.

Furthermore, the linear decrease in X_u with increasing cruise speed demonstrates how aerodynamic drag contributes to stability at higher velocities. However, the effect of system mass slows the stabilization process, assuming the drag force acts through the center of gravity (CoG). These findings highlight the critical role of system mass and aerodynamic properties in shaping the dynamic response and stability of multirotors across different flight conditions.

This analysis not only corroborates findings from prior studies, such as those by Venkatesh et al. [83] regarding neutral stability in hover but also shows the dynamics concerned with cruise conditions. However, the absence of oscillatory modes observed in other studies, such as those by Niemiec and Gandhi [84], underscores a possible limitations of the current mathematical model, where the stability derivatives like L_p, M_q, and N_r are not seen in the system matrix. These omissions highlight the need for further refinement of the model to possibly capture additional dynamic behavior. Overall, this study contributes to the broader understanding of multirotor natural dynamics for the derived mathematical mode, providing a valuable foundation for future work on open-loop stability and control system design.

Configuration specific Handling Qualities
From literature it follows that configurations with higher rotor counts achieved better power distribution, reducing mechanical strain on individual motors during high-thrust maneuvers. However, the resulting increase in mass and inertia introduced challenges for agility. While higher rotor counts enhance control responsiveness, due to smaller rotors and improved rise times, they also increase moments of inertia, which degrade agility. The octocopter's dynamic discontinuities during yaw maneuvers further illustrate the stability and control challenges associated with higher moments of inertia.

Lower disk loading in configurations with higher rotor counts improves hover efficiency and control authority, making these configurations well-suited for precision operations. The reduced per-unit thrust demand and induced power requirements facilitate smoother transitions between hover and forward flight, a critical attribute in emergency response scenarios. These configurations also enhance energy efficiency, particularly for hover-intensive missions, by distributing lift across a larger total disk area.

GoAERO Implications

The findings highlight the inherent trade-offs between rotor count, hybridization factor (HF), and mission-specific priorities. Configurations with lowest rotor count, i.e. the quadrotor, excelled in terms of payload-to-system mass ratio and simplicity, making them ideal for the Productivity Mission. Their reduced MTOM and lower acquisition and maintenance costs reinforce their suitability for applications prioritizing mass efficiency and cost-effectiveness. However, this design faced limitations in hover efficiency, control authority, and handling qualities, which are critical for the Adversity and Maneuvering Missions.

Among the evaluated configurations, the hexacopter emerged as the most viable option for the GoAERO competition, striking an optimal balance between mass, handling qualities, and overall mission performance. Its additional rotors provide greater design flexibility and redundancy, enhancing robustness and adaptability across diverse mission profiles. While its MTOM is only marginally higher than that of the quadrotor, the hexacopter effectively mitigates the agility and yaw control limitations observed in the octocopter, making it a compelling choice for further development.

Final Remarks

This thesis makes a valuable contribution to the advancement of eVTOL technology for emergency response applications. By addressing critical gaps in early-stage HQ assessments on the basis of other literature and configuration optimization, it provides actionable insights for designing high-performance aircraft tailored to the stringent requirements of the GoAERO competition. The integration of a hybrid propulsion system, multidisciplinary optimization frameworks, and HQ principles highlights the potential for eVTOL systems to bridge the gap between conceptual design and practical implementation.

10.1. Recommendations

The findings from this study provide actionable recommendations for advancing future research and development in eVTOL systems. Several limitations identified in this study underscore areas requiring further investigation as outlined below.

Hybrid Propulsion Systems and Subsystems Modeling

The analysis highlights the significant mass and possible cost advantages of hybrid propulsion systems, impacting both acquisition and operational expenses. However, the current model does not comprehensively evaluate an integrated propulsion system with all its subsystems. Future research should develop a more detailed propulsion system model, encompassing subsystems such as energy storage, power electronics, and thermal management. Once a refined propulsion model is established, a more accurate cost and mass estimation framework can be developed. This would facilitate optimized eVTOL sizing based on HF requirements and operational scenarios while improving the understanding of the trade-offs between cost and performance.

Exploring advanced hybrid power systems, including regenerative energy recovery and adaptive power distribution, could further enhance mission endurance and efficiency. For example, sizing the hybrid system to include regenerative capabilities could reduce overall battery requirements, particularly for missions with higher hybridization factors (HF). This could lead to lighter designs and improved performance.

Structural Model Refinements

The structural analysis in this study used a simplified rotor support model. Future work should implement detailed structural modeling, focusing on innovative support designs that minimize the structural mass penalty associated with increased rotor counts. Integrating advanced materials and topology optimization techniques could further enhance the structural efficiency of multirotor systems. Furhtermore combining the structural and aerodynamic analyses would allow for holistic optimization, balancing mass savings with aerodynamic performance to maximize system efficiency.

Rotor Optimization and Aerodynamic Refinements

The first step for advancing the proposed configuration is implementing a detailed rotor design, including blade profile and twist to refine aerodynamic models. This enhanced understanding of rotor aerodynamics can inform better design decisions, creating a more realistic and robust model for overall system simulations.

Subsequent research should include rotor interaction effects, modeled using Computational Fluid Dynamics (CFD). CFD analyses could determine the optimal vertical (z-axis) positioning of rotors while also providing insights into wake interactions and induced drag. Combining these results with structural analyses of the rotor support system would enable realistic rotor-support co-design, ensuring aerodynamic and structural efficiency. Additionally, using CFD outputs, center-of-pressure locations and detailed drag coefficients can be derived for the overall system. This would enable simulations of configuration-level aerodynamic moments and stability under various attitudes.

Control System Development and Mission Simulations

Multirotors are inherently unstable and thus need a controller to operate. An inportant next step thus revolves around developping a controller capable to be used in simulations. Furthermore, integrating rotor dynamics and stability derivatives into advanced control strategies could significantly improve lateral and longitudinal stability during high-performance maneuvers. A simulation-ready eVTOL model provides the foundation for developing and testing control systems. The following steps are recommended:

1. Design and implement a controller to make the system adhere to ADS-33 Handling Qualities (HQ) criteria. The controller should align with system frequency response requirements and ensure compliance with Level 1 HQ standards during maneuvering and adverse conditions.
2. Use the controller to simulate three distinct missions: productivity, adversity, and maneuvering. Quantify performance metrics and analyze the results to identify configuration improvements.
3. Investigate how feedback control strategies influence the eigenvalue spectrum, system stability, and robustness against disturbances. This analysis will provide insights into coupled dynamics and the interaction between the control system and the vehicle's structural and aerodynamic behavior.

Environmental and Operational Considerations

Finally, research should evaluate the impact of environmental factors such as wind, turbulence, and operational variability on stability and control. Including these factors in simulations would enhance the reliability and robustness of eVTOL systems in real-world operations. Additionally, modeling ground effects during hover and transitions would refine aerodynamic efficiency predictions and improve stability assessments, particularly for urban environments with confined operational spaces.

References

[1] HeroX. "Goaero design competition." Accessed on Mar 4, 2024. (2024), [Online]. Available: https://www.herox.com/goaero.

[2] Skypod Aerospace. "Vtol 101: The ultimate guide to vertical take off and landing." Accessed on Apr 20, 2024. (2018), [Online]. Available: https://medium.com/skypod/vtol-101-the-ultimate-guide-to-vertical-take-off-and-landing-561c5ec68fad.

[3] TU Delft. "Aerospace students revive leonardo da vinci's aerial screw." Accessed on October 21, 2024. (2020), [Online]. Available: https://www.tudelft.nl/en/stories/articles/aerospace-students-revive-leonardo-da-vincis-aerial-screw-and-turn-it-into-an-electric-personal-aerial-vehicle-for-today.

[4] Flightline Weekly. "Vtol: A brief history." Accessed on October 22, 2024. (2021), [Online]. Available: https://www.flightlineweekly.com/post/vtol-a-brief-history.

[5] M. Filipenko. "Back to the future: A rough comparison of 70s vtol concepts to current evtol designs." Accessed on Jul 24, 2024. (2020), [Online]. Available: https://medium.com/@mykhaylo.filipenko/back-to-the-future-a-rough-comparison-of-70s-vtol-concepts-to-current-evtol-designs-c34b87ab480f.

[6] S. B. Anderson, "Historical overview of v/stol aircraft technology," Ames Research Center, 19810010574, Mar. 1981.

[7] M. Hirschberg. "Electric vtol wheel of fortune." Accessed on Jan 19, 2025. (2017), [Online]. Available: https://evtol.news/news/commentary-electric-vtol-wheel-of-fortune.

[8] EASA. "Vertical take-off and landing (vtol)." Accessed on Jun 23, 2024. (), [Online]. Available: https://www.easa.europa.eu/en/light/topics/vertical-take-and-landing-vtol.

[9] Lilium. "What it takes to design an aircraft from scratch." Accessed on May 21, 2024. (2020), [Online]. Available: https://lilium.com/newsroom-detail/lilium-architecture-design-principles.

[10] O. Ugwueze, T. Statheros, N. Horri, M. A. Bromfield, and J. Simo, "An efficient and robust sizing method for evtol aircraft configurations in conceptual design," *Aerospace*, vol. 10, no. 3, p. 311, 2023.

[11] M. D. Pavel and G. D. Padfield, "Progress in the development of complementary handling and loading metrics for ads-33 manoeuvres," Presented at the American Helicopter Society 59th Annual Forum, American Helicopter Society, 2003.

[12] Bell. "Bell 505." Accessed on Oct 23, 2024. (), [Online]. Available: https://www.bellflight.com/products/bell-505.

[13] G. Palaia, K. A. S. amd V. Cipolla, V. Binante, and D. Zanetti, "A conceptual design methodology for e-vtol aircraft for urban air mobility," *Applied Sciences*, vol. 11, no. 22, 2021.

[14] D. F. Finger, C. Braun, and C. Bil, "A review of configuration design for distributed propulsion transitioning vtol aircraft," Presented at the Asia-Pacific International Symposium on Aerospace Technology 2017, Asia-Pacific International Symposium on Aerospace Technology, Oct. 2017.

[15] OpenAI. "Chatgpt 3.0." Accessed on Mar 20, 2024. (2024), [Online]. Available: https://chat.openai.com/chat.

[16] eVTOL.news. "Acubed vahana alpha two (defunct)." Accessed on Apr 24, 2024. (), [Online]. Available: https://evtol.news/acubed-vahana-alpha-two-defunct.

[17] Vertical Magazine. "The pivotal year in electric vtol progress." Accessed on Aug 25, 2024. (2024), [Online]. Available: https://verticalmag.com/features/pivotal-year-electric-vtol-progress/.

[18] Free3D. "Kittyhawk self-flying taxi." Accessed on May 30, 2024. (2024), [Online]. Available: https://free3d.com/3d-model/kittyhawk-self-flying-taxi-red-rigged-8536.html.

[19] eVTOL News. "Vertical aerospace va-x2." Accessed on Jun 28, 2024. (2024), [Online]. Available: https://evtol.news/vertical-aerospace-seraph/.

[20] EHang. "Media coverage." Accessed on Sep 26, 2024. (2020), [Online]. Available: https://www.ehang.com/news/p/9.html.

[21] M. Shamiyeh, R. Rothfeld, and M. Hornung, "A performance benchmark of recent personal air vehicle concepts for urban air mobility," Presented at the Congres of the International Council of the Aeronautical Sciences, ICAS, 2018.

[22] F. Barra, P. Capone, and G. Guglieri, "A methodology for preliminary performance estimation of a hybrid-electric tilt-wing aircraft for emergency medical services," Presented at the International Conference on Unmanned Aircraft Systems, ICUAS, Sep. 2020.

[23] M. Hepperle, "Electric flight – potential and limitations," German Aerospace Center, DLR Technical Report, 2012.

[24] W. Johnson and C. Silva, "Nasa concept vehicles and the engineering of advanced air mobility aircraft," *The Aeronautical Journal*, vol. 126, pp. 59–91, 2021.

[25] U. Cakin, Z. Kaçan, Z. A. Aydogan, and I. Kuvvetli, "Initial sizing of hybrid electric vtol aircraft for intercity urban air mobility," Presented at the AIAA AVIATION 2020 FORUM, AIAA AVIATION, Jun. 2020.

[26] Y. Mihara, P. Pawnlada, A. Nakamoto, T. Nakamura, and M. Nakano, "Cost analysis of evtol configuration design for an air ambulances system in japan," Presented at the CESUN Conference, CESUN, 2020.

[27] D. Yilmaz, M. D. Pavel, and I. Yavrucuk, "Helicopter design for handling qualities enhancements," Presented at the 35th European Rotorcraft Forum, European Rotorcraft Forum, 2009.

[28] D. Kotarski, P. Piljek, and J. K. D. Majetić, "Performance analysis of fully actuated multirotor unmanned aerial vehicle configurations with passively tilted rotors," *Applied Sciences*, vol. 11, p. 8786, 2021.

[29] M. L. Ireland, A. Vargas, and D. Anderson, "A comparison of closed-loop performance of multirotor configurations using non-linear dynamic inversion control," *Aerospace*, vol. 2, no. 3, pp. 325–352, 2015.

[30] J. Goerres, "Framework for comparing and optimizing of fully actuated multirotor uavs," M.S. thesis, Twente University, Feb. 2019.

[31] G. E. Cooper and R. P. Harper, "The use of pilot rating in the evaluation of aircraft handling qualities," NASA, Washington, D.C., Technical Report NASA-TN-D-5153, 1969, NASA Technical Note.

[32] J. Verbeke, "Elicopter design for handling qualities," M.S. thesis, Delft University of Technology, Nov. 2009.

[33] B. Lawrence, C. R. Theodore, W. Johnson, and T. Berger, "A handling qualities analysis tool for rotorcraft conceptual designs," *The Aeronautical Journal*, vol. 122, no. 1252, pp. 960–987, 2018.

[34] C. Malpica, S. Withrow-Maser, J. Aires, *et al.*, "Handling qualities of multirotor rpm-controlled electric-vertical take-off and landing (evtol) aircraft for urban air mobility (uam)," Presented at the Vertical Flight Society 79th Annual Forum Technology Display, Vertical Flight Society, Publisher Name, May 2023.

[35] J. C. Gibson, "Development of a design methodology for handling qualities excellence in fly by wire aircraft," Ph.D. dissertation, Delft University of Technology, Feb. 1999.

[36] K. Perry. "Ambulance deserts the struggle for timely cardiac arrest intervention." Accessed on Jun 10, 2024. (2023), [Online]. Available: https://avive.life/blog/ambulance-desert/.

[37] North West Air Ambulance Charity. "Our fleet." Accessed on Apr 14, 2024. (), [Online]. Available: https://www.nwairambulance.org.uk/what-we-do/our-fleet/#:~:text=We%20normally%20cruise%20at%20around,conflict%20with%20commercial%20air%20traffic..

[38] M. Kerler and W. Erhard, "Evaluation of helicopter flight missions with intended single engine operation," Institute for Flight Propulsion, Technische Universität München, 2014.

[39] Conklin de Decker. "Aircraft operating cost and performance guide bell 505 jet ranger x." Accessed on Jun 12, 2024. (), [Online]. Available: https://conklindedecker.jetsupport.com/details/Bell%20505%20Jet%20Ranger%20X.

[40] Harris Supply Solutions. "5 reinforcing bar." Accessed on May 11, 2024. (), [Online]. Available: http://m.harrissupplysolutions.com/5-rebar.html.

[41] Rothesay. “Sandbag wall construction guide.” Accessed on Sep 9, 2024. (2019), [Online]. Available: https://www.rothesay.ca/wp-content/uploads/2019/04/SANDBAG-WALL-CONSTRUCTION.pdf.

[42] W. Stickney. “Bell 505 jet ranger x price and operating costs.” Accessed on Mar 13, 2024. (2024), [Online]. Available: https://boltflight.com/bell-505-jet-ranger-x-price-and-operating-costs/.

[43] Helis Database. “Med-pac stretcher for bell 505 air ambulance.” Accessed on Jul 27, 2024. (2019), [Online]. Available: https://www.helis.com/database/news/med-pac-stretcher-bell-505/.

[44] Bell Textron. “Bell-505-product-specifications.” Accessed on October 28, 2024. (2024), [Online]. Available: https://www.bellflight.com/-/media/site-specific/bell-flight/documents/products/505/bell-505-product-specifications.pdf.

[45] D. Perry. “Analysis: Bell 505 jet ranger x technical description.” Accessed on Mar 29, 2024. (2015), [Online]. Available: https://www.flightglobal.com/analysis-bell-505-jet-ranger-x-technical-description/117128.article.

[46] M. D. Pavel, *Helicopter master course*, Power Point slides, 2022.

[47] A. Richter and P. A. Nikrityuk, “Drag forces and heat transfer coefficients for spherical, cuboidal and ellipsoidal particles in cross flow at sub-critical reynolds numbers,” *International Journal of Heat and Mass Transfer*, vol. 55, no. 4, pp. 1343–1354, 2012.

[48] CourseHero. “B-747 weight and balance manual.” Accessed on Jun 22, 2024. (2021), [Online]. Available: https://www.coursehero.com/file/p4kqhng6/Aircraft-Operational-Empty-Weight-OEW-The-same-as-Basic-Operating-Weight-BOW/.

[49] D. B. Schwinn, P. Weiand, M. Buchwald, and M. Schmid, “Rotorcraft fuselage weight assessment in early design stages,” Presented at the Deutscher Luft- und Raumfahrtkongress, DLRK, Sep. 2018.

[50] J. Roskam, *Airplane Design Part VI: Preliminary Design of Aircraft Systems*, 8th ed. Warrendale, PA, USA: SAE International, 2018.

[51] R. de Vries, M. Hoogreef, and R. Vos, “Range equation for hybrid-electric aircraft with constant power split,” *Journal of Aircraft*, vol. 57, pp. 1–6, 2020, Presented at the 35th European Rotorcraft Forum.

[52] A. Batra, R. Raute, and R. Camilleri, “On the range equation for hybrid-electric aircraft,” *Aerospace*, vol. 10, no. 8, p. 687, 2023.

[53] J. Zong, B. Zhu, Z. Hou, X. Yang, and J. Zhai, “Sizing and mission profile analysis of the hybrid-electric propulsion system for retrofitting a fixed wing vtol aircraft,” *International Journal of Aerospace Engineering*, vol. 2022, p. 9 384 931, 2022.

[54] E. Torenbeek, *Synthesis of Subsonic Airplane Design*, 1st ed. Dordrecht, The Netherlands: Delft University Press, 1982.

[55] K. Alambra and N. Swanson. “Beam deflection calculator.” Accessed on Aug 17, 2024. (2024), [Online]. Available: https://www.omnicalculator.com/construction/beam-deflection.

[56] Chegg. “Question: P2: For the shaded shapes shown in the figure below: (a) determine the moment of inertia about the x-axis for each case shown.” Accessed on Jul 16, 2024. (), [Online]. Available: https://www.chegg.com/homework-help/questions-and-answers/p2-shaded-shapes-shown-figure-determine-moment-inertia-x-axis-case-shown-b-calculate-perce-q58972371.

[57] University of Cambridge. “Young´s modulus - density selection map.” Accessed on Jun 18, 2024. (), [Online]. Available: https://www.doitpoms.ac.uk/tlplib/optimisation-biomaterials/modulus_density.php.

[58] grantadesign. “Ashbycharts.” Accessed on Jun 15, 2024. (), [Online]. Available: https://www.grantadesign.com/education/students/charts/.

[59] D. Leishman, *Principles of Helicopter Aerodynamics*, 2nd ed. Cambridge, UK: Cambridge University Press, 2006.

[60] MIT. “Performance of propellers.” Accessed on Jul 3, 2024. (), [Online]. Available: https://web.mit.edu/16.unified/www/FALL/thermodynamics/notes/node86.html.

[61] Y. Fukumine and Z. Lei, “Estimation of evtol flight performance using rotorcraft theory,” Presented at the Congres of the International Council of the Aeronautical Science, ICAS, Sep. 2022.

[62] G. M. Hoffmann, H. Huang, S. L. Waslander, and C. J. Tomlin, “Quadrotor helicopter flight dynamics and control: Theory and experiment,” American Institute of Aeronautics and Astronautics, Aug. 2007.

[63] E. Gopalakrishnan, “Quadcopter flight mechanics model and control algorithms,” M.S. thesis, Czech Technical University, May 2017.

[64] C. W. Chan and T. Y. Kam, “A procedure for power consumption estimation of multi-rotor unmanned aerial vehicle,” *Journal of Physics: Conference Series*, vol. 1509, 2020.

[65] M. E. Balli, “Evtol aircraft conceptual design and optimization,” M.S. thesis, POLITECNICO DI MILANO, 2020.

[66] M. J. Stepaniak, “A quadrotor sensor platform,” Ph.D. dissertation, The Russ College of Engineering and Technology of Ohio University, Nov. 2008.

[67] T. Saleh and K. Aboukassem, “Study the equations of motion for a hexacopter aerial vehicle based on the newton-euler method,” *International Journal of Computer Science Trends and Technology (*, vol. 6, no. 4, 2018.

[68] R. C. Nelson, *Flight Stability and Automatic Control*, 2nd ed. Boston, Massachusetts: McGraw-Hill Book Co, 1998.

[69] S. M. WALLE, “Dynamic modeling and trajectory tracking control of hexacopter using sliding mode controller,” M.S. thesis, ADDIS ABABA SCIENCE and TECHNOLOGY UNIVERSITY, Jan. 2019.

[70] Z. Tahir, W. Tahir, and S. A. Liaqat, “State space system modeling of a quad copter uav,” *Indian Journal of Science and Technology*, vol. 9, no. 27, 2019.

[71] J. Barbagello, *Instrument procedures handbook*, FEDERAL AVIATION ADMINISTRATION, Sep. 2017.

[72] T. van Diessen, “Development of an integrated approach to an initial design of a multi rotor unmanned aerial vehicle,” M.S. thesis, Delft University of Technology, 2012.

[73] A. Wood. “Aircraft propeller theory.” Accessed on October 25, 2024. (2022), [Online]. Available: `https://aerotoolbox.com/propeller/`.

[74] P. D. Talbot, J. V. Bowles, and H. C. Lee, “Helicopter rotor and engine sizing for preliminary performance estimation,” *AIAA*, pp. 86–1756, 1986.

[75] Y. Yang, Y. Liang, S. Pröbsting, *et al.*, “Sizing of multicopter air taxis—weight, endurance, and range,” *Aerospace*, vol. 11, no. 3, p. 200, 2024.

[76] eVTOL.news. “Joby aviation s4 production prototype.” Accessed on Jun 2, 2024. (), [Online]. Available: `https://evtol.news/joby-aviation-s4-production-prototype`.

[77] X. Xia, D. Ma, L. Zhang, X. Liu, and K. Cong, “Blade shape optimization and analysis of a propeller for vtol based on an inverse method,” *Applied Sciences*, vol. 12, no. 7, p. 3694, 2022.

[78] N. Qiao, T. Ma, J. Fu, L. Zhang, X. Wang, and P. Xue, “Rapid blade shape optimization for contra-rotating propellers for evtol aircraft considering the aerodynamic interference,” *Aerospace*, vol. 10, no. 1, p. 54, 2023.

[79] L. D. KOCH, “Design and performance calculations of a propeller for very high altitude flight,” M.S. thesis, CASE WESTERN RESERVE UNIVERSITY, Feb. 1998.

[80] eVTOL News. “Volocopter 2x.” Accessed on October 29, 2024. (2024), [Online]. Available: `https://evtol.news/volocopter-2x/`.

[81] A. B. Lambe and J. R. A. Martins, “Extensions to the design structure matrix for the description of multidisciplinary design, analysis, and optimization processes,” Presented at the World Congress on Structural and Multidisciplinary Optimization, Congress on Structural and Multidisciplinary Optimization, 2021.

[82] SciPy. “Scipy.optimize.minimize.” Accessed on Aug 26, 2024. (), [Online]. Available: `https://docs.scipy.org/doc/scipy/reference/generated/scipy.optimize.minimize.html`.

[83] P. Venkatesh, S. Vadhvana, and V. Jain, “Analysis and control of a planar quadrotor,” Indian Institute of Technology, Jun. 2021.

[84] R. Niemiec and F. Gandhi, “A comparison between quadrotor flight configurations,” Presented at the 42nd European Rotorcraft Forum, European Rotorcraft Forum, 2016.

[85] S. Withrow-Maser, C. Malpica, and K. Nagami, “Multirotor configuration trades informed by handling qualities for urban air mobility application,” Presented at the Vertical Flight Society 76th Annual Forum, Vertical Flight Society, 2020.

[86] M. Bahr, M. McKay, R. Niemiec, and F. Gandhi, “Handling qualities of fixed-pitch, variable-speed multicopters for urban air mobility,” *The Aeronautical Journal*, vol. 126, no. 1300, pp. 952–972, 2021.

[87] D. Caprace, A. Ning, P. Chatelain, and G. Winckelmans, "Effects of rotor-airframe interaction on the aeromechanics and wake of a quadcopter in forward flight," *Aerospace Science and Technology*, vol. 130, 2022.

A

Optimisation constants as defined in the code

Table A.1: Constants as used for the optimisation code

Parameter	Description	Value/Unit
	Constants	
ρ	Air density	$1.225\,\mathrm{kg/m^3}$
g	Gravitational acceleration	$9.80665\,\mathrm{m/s^2}$
k	Inverse of figure of merit (FoM)	1.15 (dimensionless)
	Top Area Drag Parameters	
A_{top}	Top surface area	$4.73\,\mathrm{m^2}$
$C_{D,\text{top}}$	Drag coefficient (top area)	0.956 (dimensionless)
	Bottom Area Drag Parameters	
A_{bottom}	Bottom surface area	$4.73\,\mathrm{m^2}$
$C_{D,\text{bottom}}$	Drag coefficient (bottom area)	0.956 (dimensionless)
	Front Area Drag Parameters	
A_{front}	Frontal surface area	$2.16\,\mathrm{m^2}$
$C_{D,\text{front}}$	Drag coefficient (front area)	0.27 (dimensionless)
	Gas Properties	
γ	Ratio of specific heats	1.4 (dimensionless)
R_g	Specific gas constant for air	$287\,\mathrm{J/(kg\cdot K)}$
μ	Dynamic viscosity of air	1.7894×10^{-5} Pa · s
	Defined Weights (kg)	
W_{fuselage}	Fuselage weight	$141.427\,\mathrm{kg}$
W_{payload}	Payload weight	$144.6\,\mathrm{kg}$
	Support Structure Properties	
E	Young's modulus of CFRP	181×10^9 Pa
ρ_{CFRP}	Density of CFRP	$1600\,\mathrm{kg/m^3}$
	Velocities (m/s)	
$v_{\text{climb,min}}$	Minimum climb velocity	$7\,\mathrm{m/s}$
$v_{\text{descent,max}}$	Maximum descent velocity	$-6\,\mathrm{m/s}$
$v_{\text{descent,min}}$	Minimum descent velocity	$-8\,\mathrm{m/s}$
$v_{\text{cruise,min}}$	Minimum cruise velocity	$65.67\,\mathrm{m/s}$
	Battery SOC	
$\text{SOC}_{\text{initial}}$	Initial state of charge	0.8 (80%)
$\text{SOC}_{\text{final}}$	Final state of charge	0.2 (20%)

Parameter	Description	Value/Unit
	Cruise Parameters	
h_{cruise}	Cruise altitude	600 m
d_{cruise}	Cruise distance	2375 m
	Power Margin	
PM	Power margin	0.1 (10%)
	Center of Gravity Locations (m)	
$\text{CoG}_{\text{ICE},x}$	ICE CoG in x direction	2.19 m
$\text{CoG}_{\text{ICE},z}$	ICE CoG in z direction	$\max_z$ m
$\text{CoG}_{\text{EC},x}$	Electric CoG in x direction	2.19 m
$\text{CoG}_{\text{EC},z}$	Electric CoG in z direction	1.40 m
	Payload and Crew Masses (kg)	
m_{pilot}	Pilot mass	80 kg
m_{medic}	Medic mass	80 kg
m_{patient}	Patient mass	80 kg
m_{rebar}	Rebar mass	33.6 kg
m_{sandbags}	Sandbag mass	36 kg
	Hover Time	
t_{hover}	Hover time	10 s
	Efficiencies	
η_{battery}	Battery efficiency	0.99
η_{em}	Electric motor efficiency	0.95
η_{eg}	Electric generator efficiency	0.98
η_{gt}	Gas turbine efficiency	0.35
	Energy Densities	
e_{bat}	Battery energy density	260 Wh/kg
e_f	Fuel energy density	$11,900$ Wh/kg
	Power Density	
pd_{ICE}	ICE power density	3000 W/kg
	BSFC	
BSFC	Brake-specific fuel consumption	280×10^{-6} kg/Wh
	Segments and Rotors	
N_{hover}	Number of hover segments	8
N_{climb}	Number of climb segments	8
N_{cruise}	Number of cruise segments	8
N_{descent}	Number of descent segments	8

B

Convergence history and characteristics remaining optimisations

B.1. Optimisation characteristics HF = 0.5

Table B.1: Optimization characteristics at HF = 0.5

Metric	Quad Rotor	Hexa Rotor	Octo Rotor
Time to converge [min]	119.25	111.87	120.059
Number of iterations	1251	647	848
Average time per iteration [min]	0.0953	0.1729	0.1416
Number of function evaluations	68738	35527	44514
Average time per evaluation [min]	0.0017	0.0031	0.0027

B.2. Optimisation characteristics HF = 0.9

Table B.2: Optimization characteristics at HF = 0.9

Metric	Quad Rotor	Hexa Rotor	Octo Rotor
Time to converge [min]	509.99	246.35	737.40
Number of iterations	5407	2054	5160
Average time per iteration [min]	0.0943	0.1199	0.1429
Number of function evaluations	323027	108491	279470
Average time per evaluation [min]	0.0016	0.0023	0.0026

B.3. Convergence History HF = 0.1

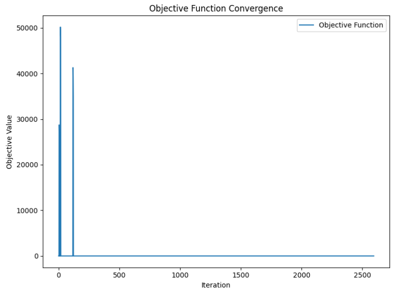

Figure B.1: Objective convergence quadrotor HF = 0.1

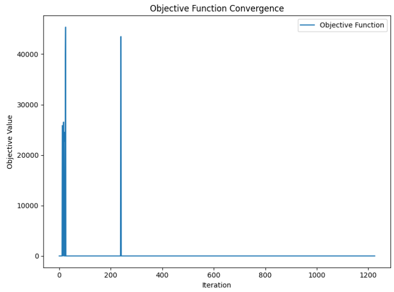

Figure B.2: Objective convergence hexarotor HF = 0.1

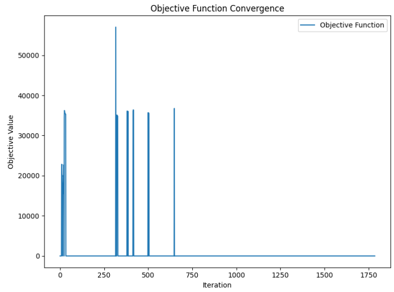

Figure B.3: Objective convergence octorotor HF = 0.1

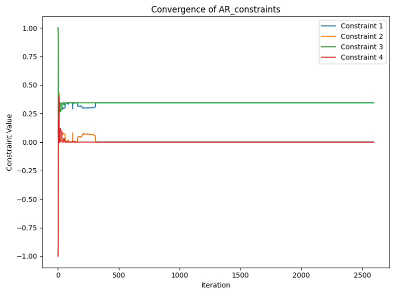

Figure B.4: Aspect Ratio constraint convergence quadrotor HF = 0.1

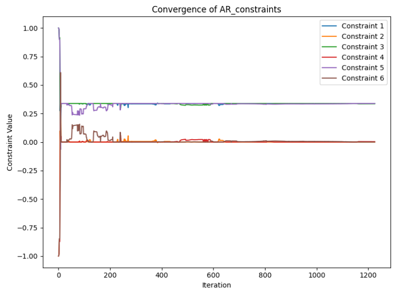

Figure B.5: Aspect Ratio constraint convergence hexarotor HF = 0.1

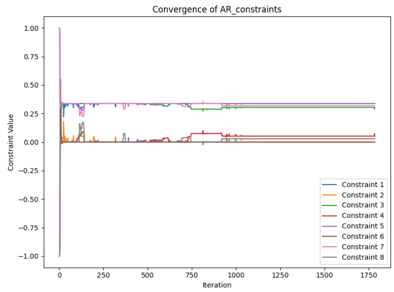

Figure B.6: Aspect Ratio constraint convergence octorotor HF = 0.1

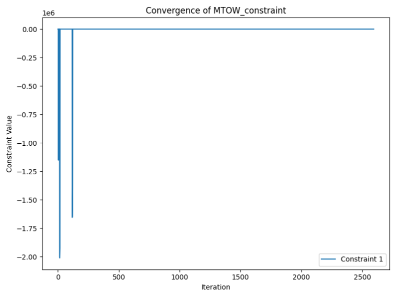

Figure B.7: MTOM Consistency constraint convergence quadrotor HF = 0.1

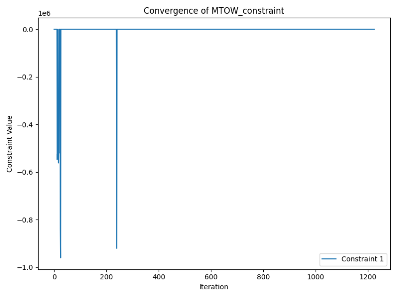

Figure B.8: MTOM Consistency constraint convergence

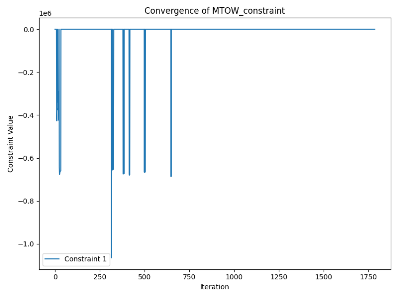

Figure B.9: MTOM Consistency constraint convergence

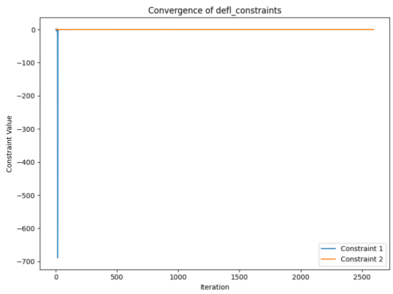

Figure B.10: Deflection constraint convergence quadrotor HF = 0.1

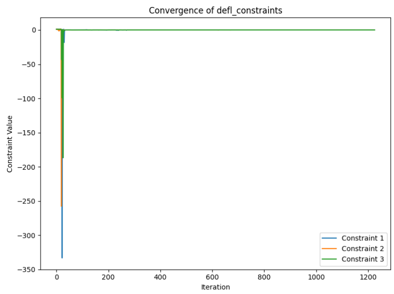

Figure B.11: Deflection constraint convergence

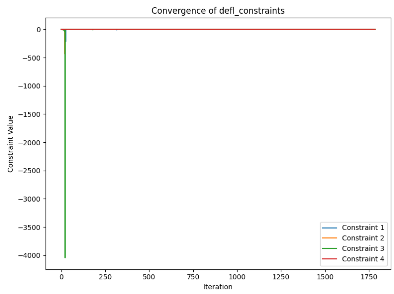

Figure B.12: Deflection constraint convergence

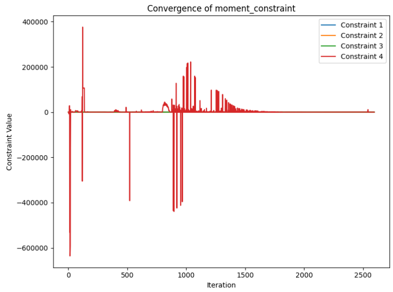

Figure B.13: Moment constraint convergence

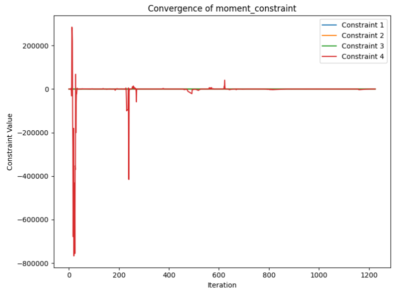

Figure B.14: Moment constraint convergence quadrotor HF = 0.1

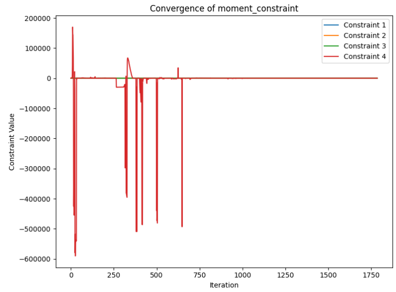

Figure B.15: Moment constraint convergence octorotor HF = 0.1

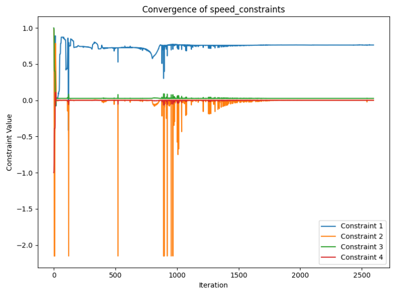

Figure B.16: Velocity constraint convergence quadrotor HF = 0.1

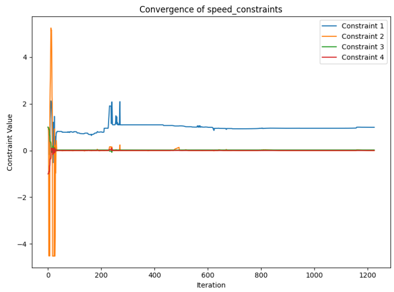

Figure B.17: Velocity constraint convergence hexarotor HF = 0.1

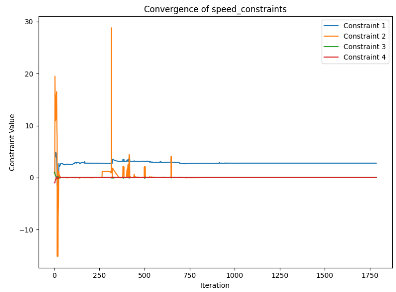

Figure B.18: Velocity constraint convergence octorotor HF = 0.1

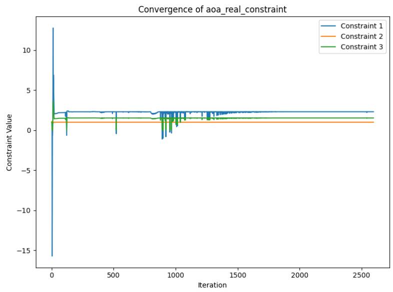

Figure B.19: Angle of Attack constraint convergence quadrotor HF = 0.1

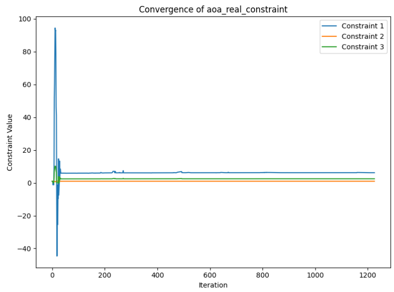

Figure B.20: Angle of Attack constraint convergence hexarotor HF = 0.1

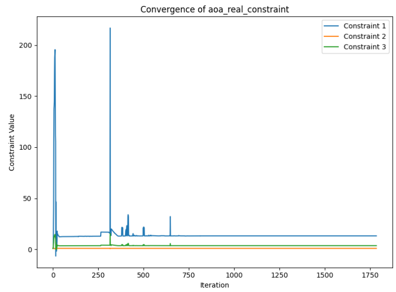

Figure B.21: Angle of Attack constraint convergence octorotor HF = 0.1

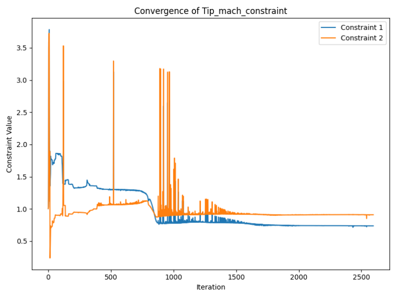

Figure B.22: Tip Mach constraint convergence quadrotor HF = 0.1

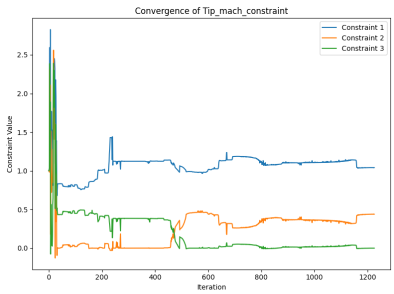

Figure B.23: Tip Mach constraint convergence hexarotor HF = 0.1

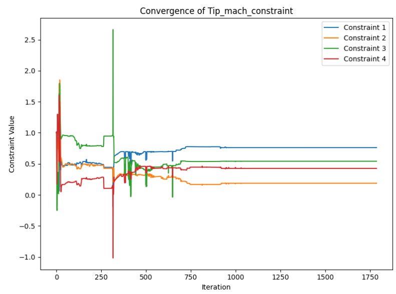

Figure B.24: Tip Mach constraint convergence octorotor HF = 0.1

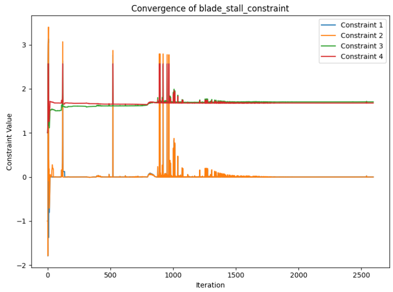

Figure B.25: Blade Stall constraint convergence quadrotor HF = 0.1

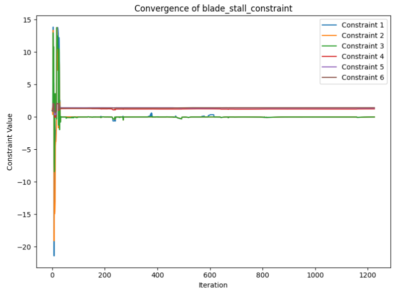

Figure B.26: Blade Stall constraint convergence hexarotor HF = 0.1

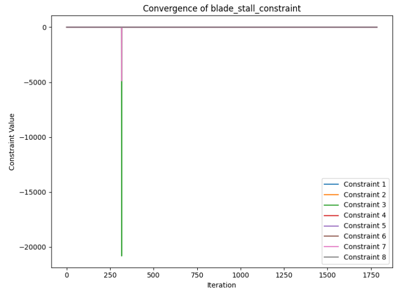

Figure B.27: Blade Stall constraint convergence octorotor HF = 0.1

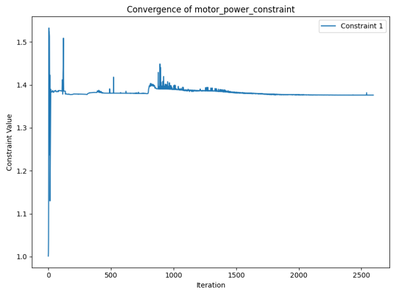

Figure B.28: Motor Power constraint convergence quadrotor HF = 0.1

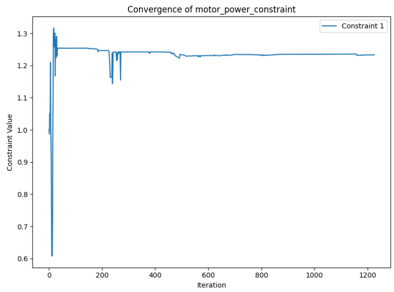

Figure B.29: Motor Power constraint convergence hexarotor HF = 0.1

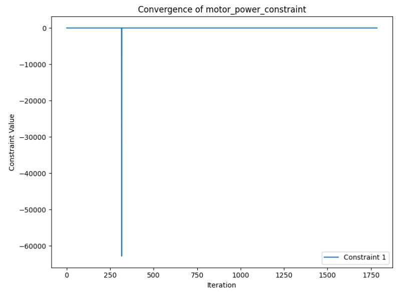

Figure B.30: Motor Power constraint convergence octorotor HF = 0.1

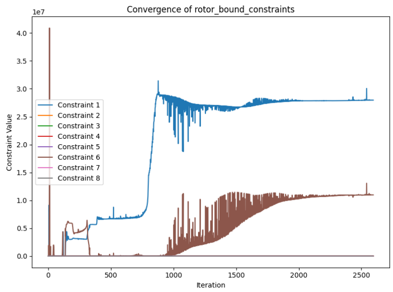

Figure B.31: Rotor bound constraint convergence quadrotor HF = 0.1

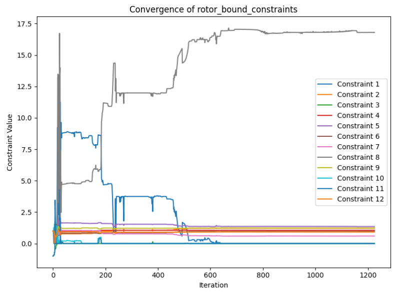

Figure B.32: Rotor bound constraint convergence hexarotor HF = 0.1

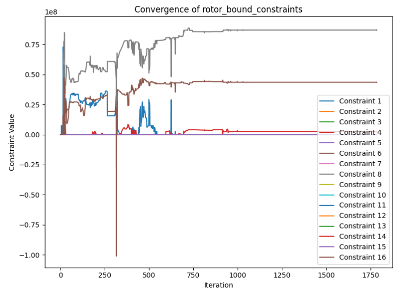

Figure B.33: Rotor bound constraint convergence octorotor HF = 0.1

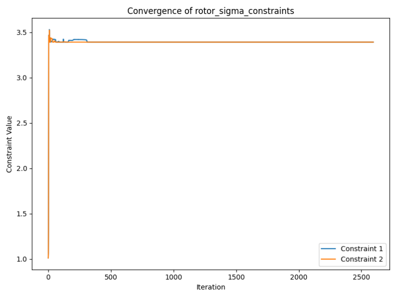

Figure B.34: Rotor solidity constraint convergence quadrotor HF = 0.1

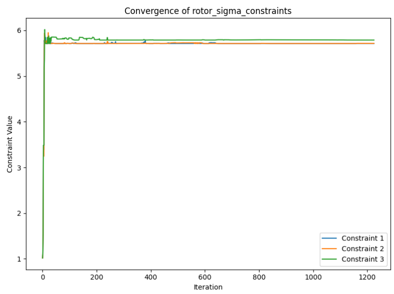

Figure B.35: Rotor solidity constraint convergence hexarotor HF = 0.1

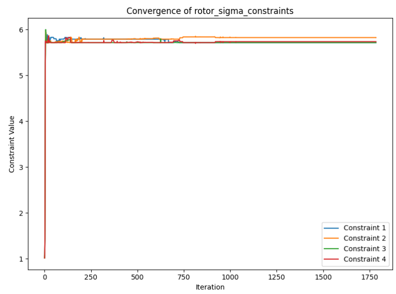

Figure B.36: Rotor solidity constraint convergence octorotor HF = 0.1

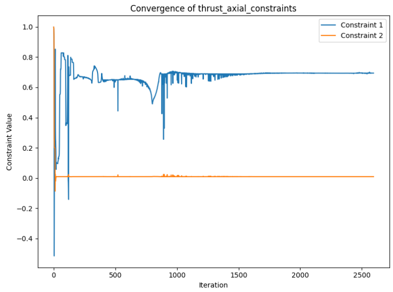

Figure B.37: Axial thrust constraint convergence quadrotor HF = 0.1

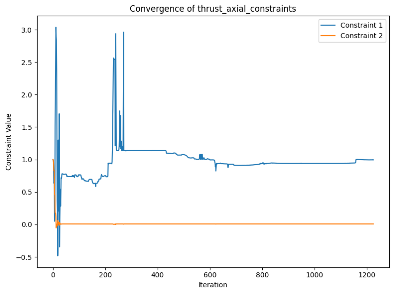

Figure B.38: Axial thrust constraint convergence hexarotor HF = 0.1

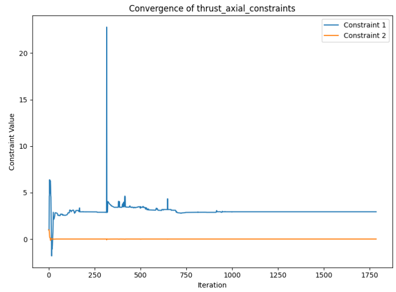

Figure B.39: Axial thrust constraint convergence octorotor HF = 0.1

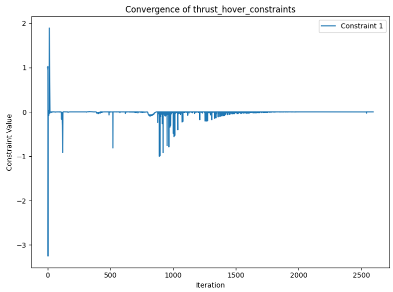

Figure B.40: Hover thrust constraint convergence quadrotor HF = 0.1

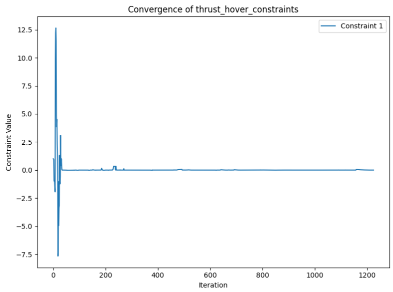

Figure B.41: Hover thrust constraint convergence hexarotor HF = 0.1

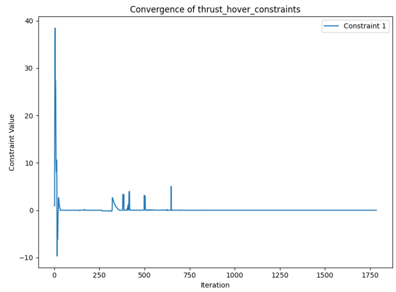

Figure B.42: Hover thrust constraint convergence octorotor HF = 0.1

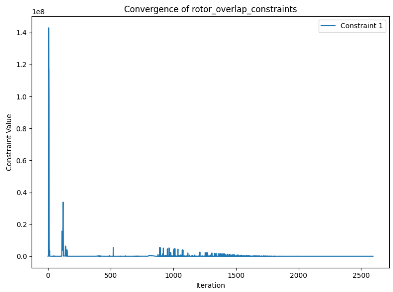

Figure B.43: Rotor overlap constraint convergence quadrotor HF = 0.1

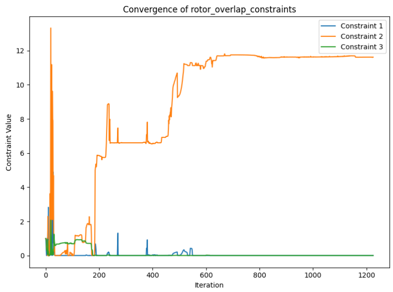

Figure B.44: Rotor overlap constraint convergence hexarotor HF = 0.1

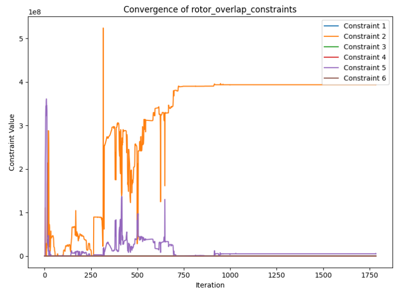

Figure B.45: Rotor overlap constraint convergence octorotor HF = 0.1

B.4. Convergence History HF = 0.5

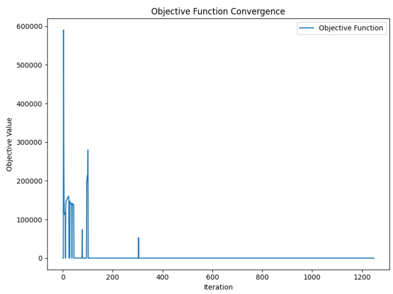

Figure B.46: Objective convergence quadrotor HF = 0.5

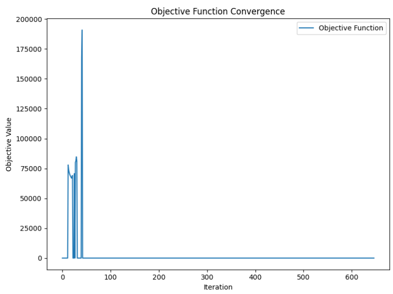

Figure B.47: Objective convergence hexarotor HF = 0.5

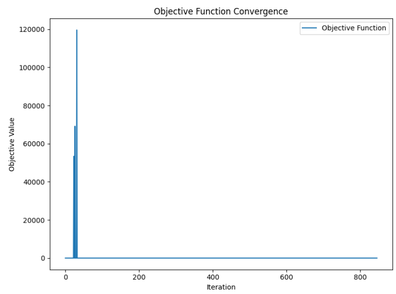

Figure B.48: Objective convergence octorotor HF = 0.5

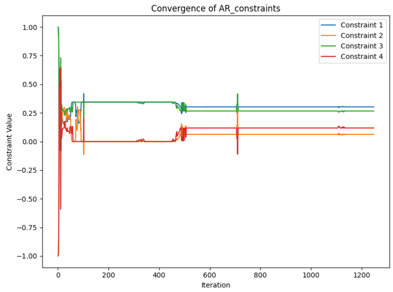

Figure B.49: Aspect Ratio constraint convergence quadrotor HF = 0.5

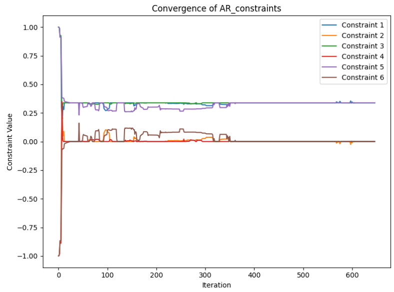

Figure B.50: Aspect Ratio constraint convergence hexarotor HF = 0.5

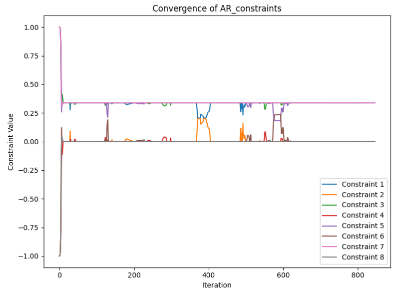

Figure B.51: Aspect Ratio constraint convergence octorotor HF = 0.5

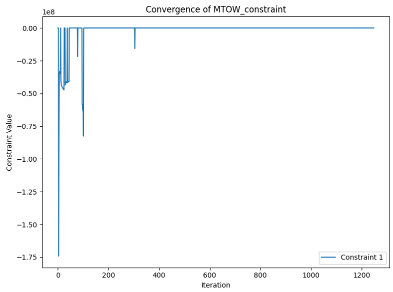

Figure B.52: MTOM Consistency constraint convergence quadrotor HF = 0.5

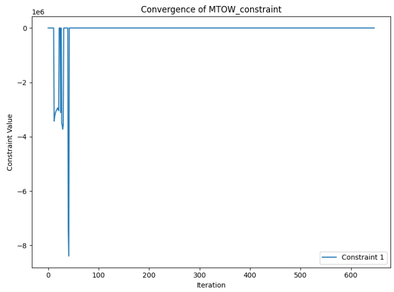

Figure B.53: MTOM Consistency constraint convergence hexarotor HF = 0.5

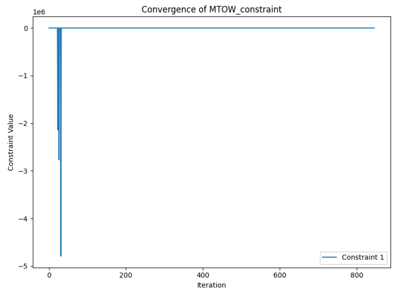

Figure B.54: MTOM Consistency constraint convergence octorotor HF = 0.5

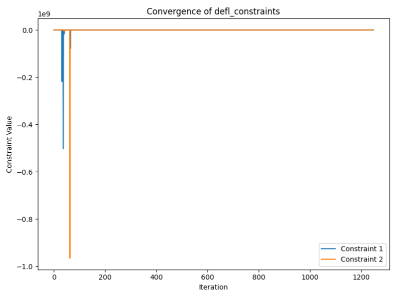

Figure B.55: Deflection constraint convergence quadrotor HF = 0.5

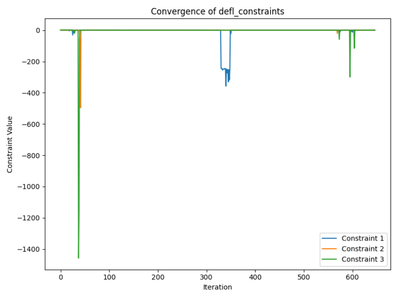

Figure B.56: Deflection constraint convergence hexarotor HF = 0.5

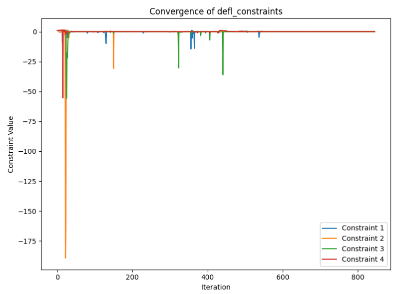

Figure B.57: Deflection constraint convergence octorotor HF = 0.5

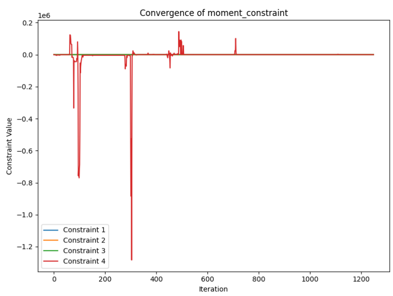

Figure B.58: Moment constraint convergence quadrotor HF = 0.5

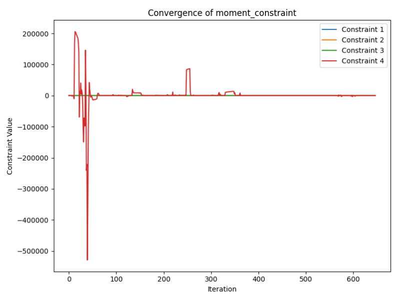

Figure B.59: Moment constraint convergence hexarotor HF = 0.5

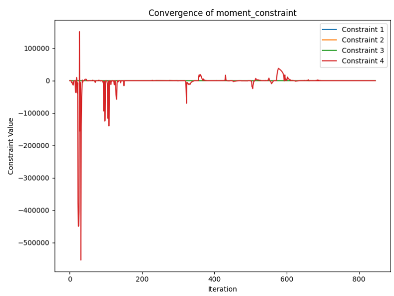

Figure B.60: Moment constraint convergence octorotor HF = 0.5

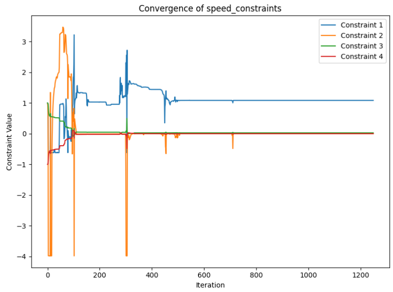

Figure B.61: Velocity constraint convergence quadrotor HF = 0.5

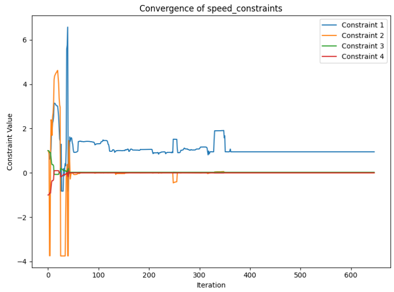

Figure B.62: Velocity constraint convergence hexarotor HF = 0.5

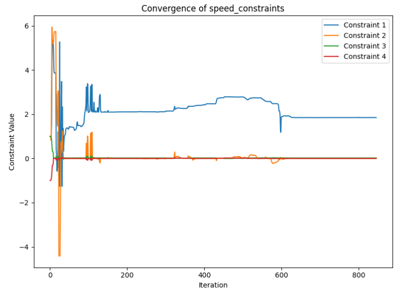

Figure B.63: Velocity constraint convergence octorotor HF = 0.5

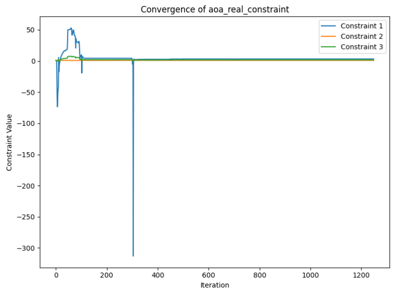

Figure B.64: Angle of Attack constraint convergence quadrotor HF = 0.5

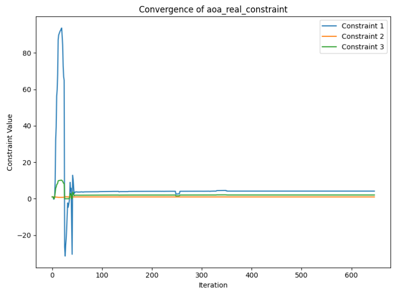

Figure B.65: Angle of Attack constraint convergence hexarotor HF = 0.5

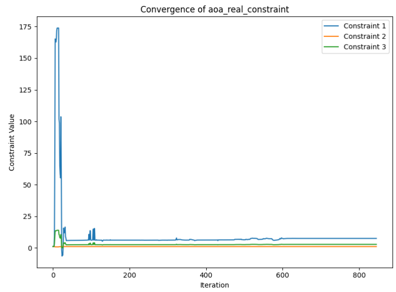

Figure B.66: Angle of Attack constraint convergence octorotor HF = 0.5

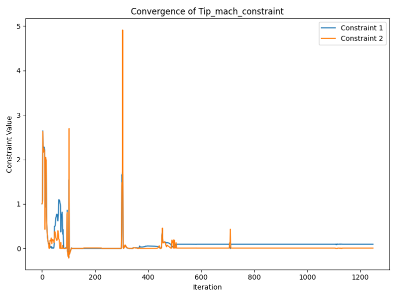

Figure B.67: Tip Mach constraint convergence quadrotor HF = 0.5

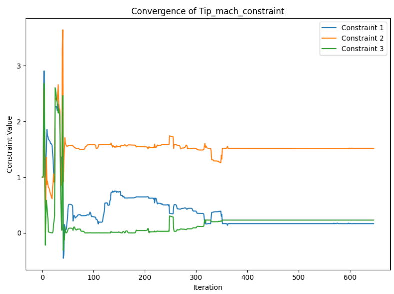

Figure B.68: Tip Mach constraint convergence hexarotor HF = 0.5

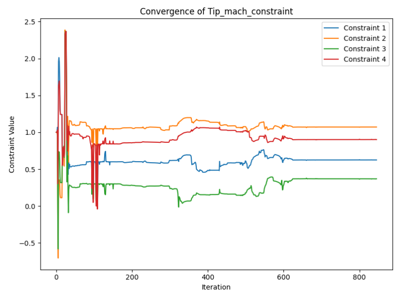

Figure B.69: Tip Mach constraint convergence octorotor HF = 0.5

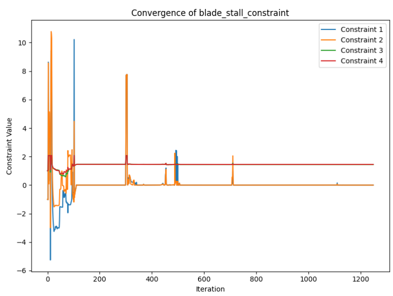

Figure B.70: Blade Stall constraint convergence quadrotor HF = 0.5

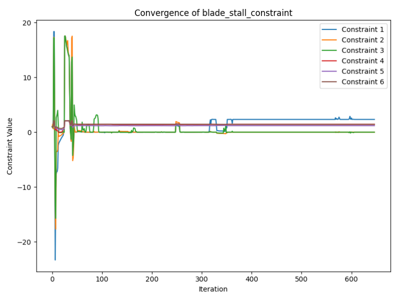

Figure B.71: Blade Stall constraint convergence hexarotor HF = 0.5

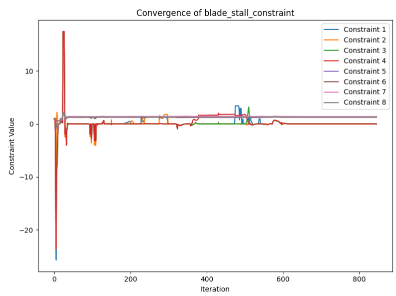

Figure B.72: Blade Stall constraint convergence octorotor HF = 0.5

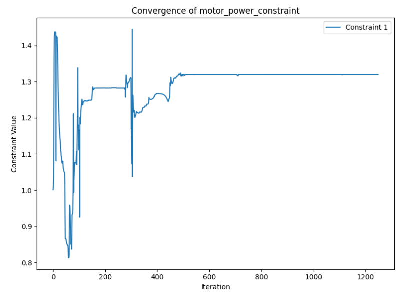

Figure B.73: Motor Power constraint convergence quadrotor HF = 0.5

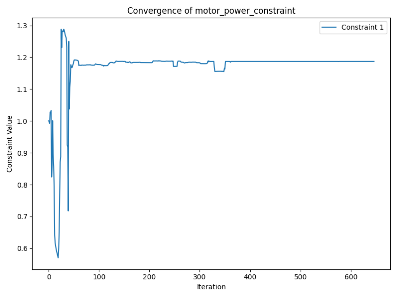

Figure B.74: Motor Power constraint convergence hexarotor HF = 0.5

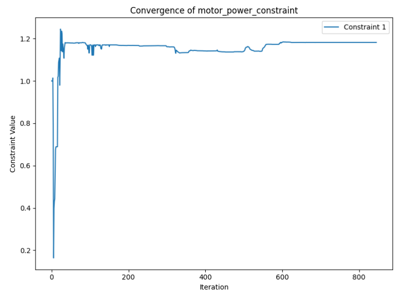

Figure B.75: Motor Power constraint convergence octorotor HF = 0.5

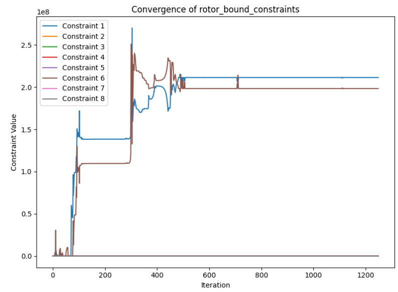

Figure B.76: Rotor bound constraint convergence quadrotor HF = 0.5

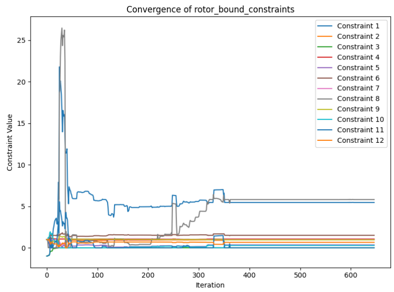

Figure B.77: Rotor bound constraint convergence hexarotor HF = 0.5

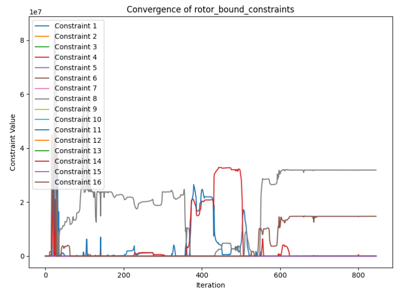

Figure B.78: Rotor bound constraint convergence octorotor HF = 0.5

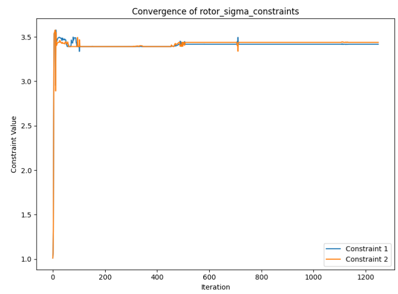

Figure B.79: Rotor solidity constraint convergence quadrotor HF = 0.5

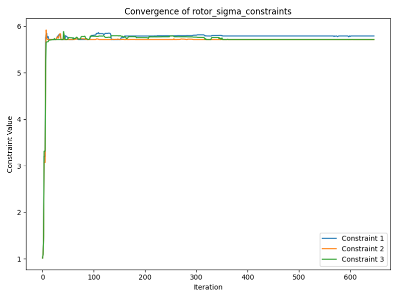

Figure B.80: Rotor solidity constraint convergence hexarotor HF = 0.5

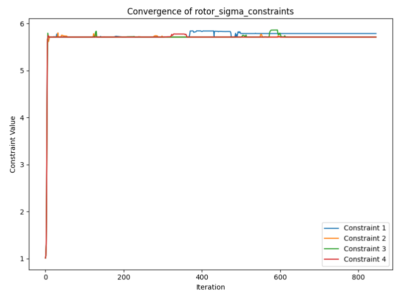

Figure B.81: Rotor solidity constraint convergence octorotor HF = 0.5

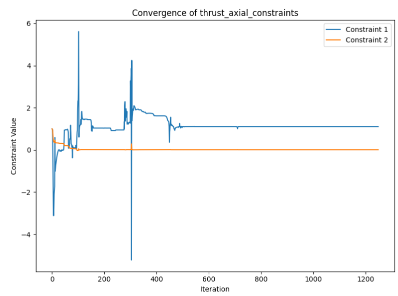

Figure B.82: Axial thrust constraint convergence quadrotor HF = 0.5

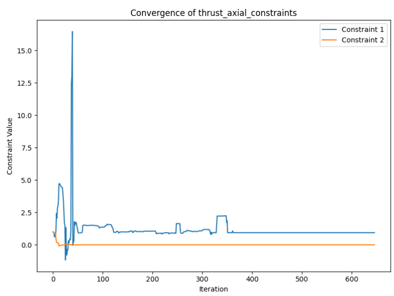

Figure B.83: Axial thrust constraint convergence hexarotor HF = 0.5

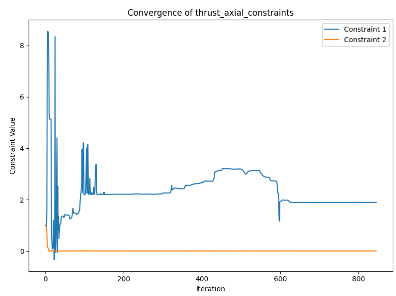

Figure B.84: Axial thrust constraint convergence octorotor HF = 0.5

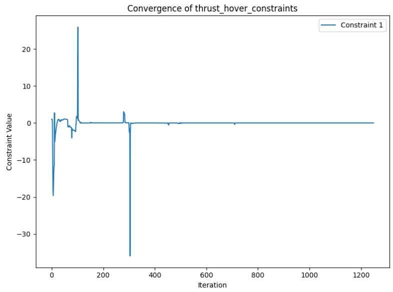

Figure B.85: Hover thrust constraint convergence quadrotor HF = 0.5

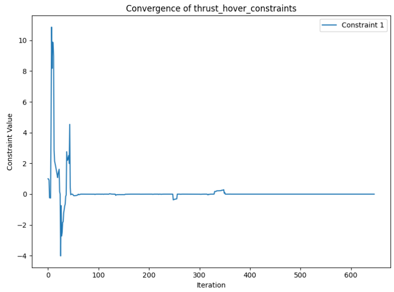

Figure B.86: Hover thrust constraint convergence hexarotor HF = 0.5

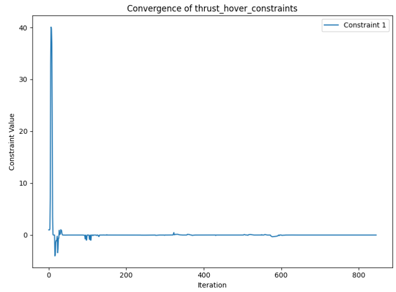

Figure B.87: Hover thrust constraint convergence octorotor HF = 0.5

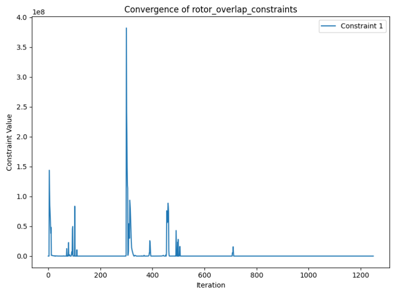

Figure B.88: Rotor overlap constraint convergence quadrotor HF = 0.5

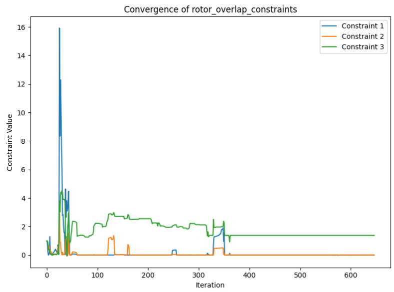

Figure B.89: Rotor overlap constraint convergence hexarotor HF = 0.5

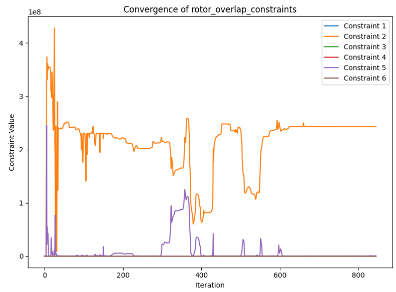

Figure B.90: Rotor overlap constraint convergence octorotor HF = 0.5

B.5. Convergence History HF = 0.9

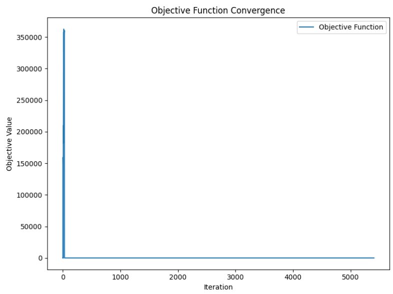

Figure B.91: Objective convergence quadrotor HF = 0.9

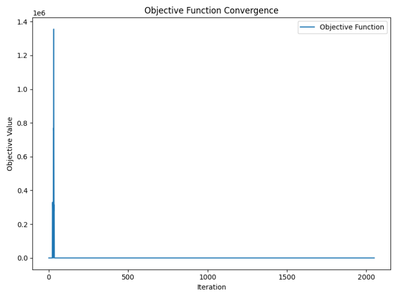

Figure B.92: Objective convergence hexarotor HF = 0.9

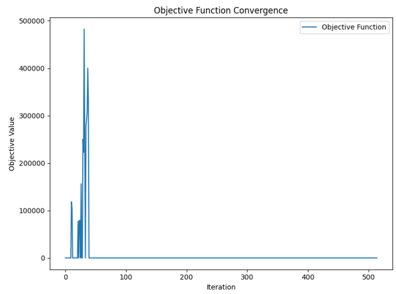

Figure B.93: Objective convergence octorotor HF = 0.9

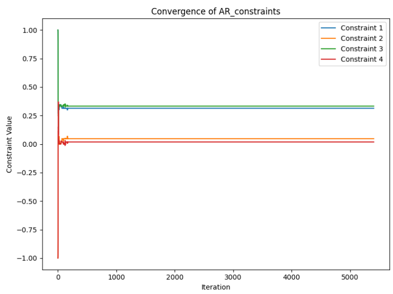

Figure B.94: Aspect Ratio constraint convergence quadrotor HF = 0.9

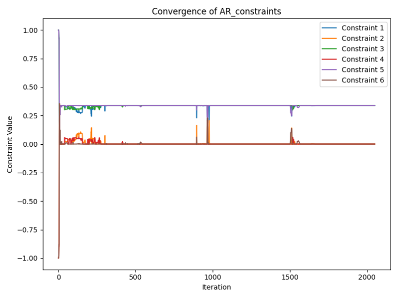

Figure B.95: Aspect Ratio constraint convergence hexarotor HF = 0.9

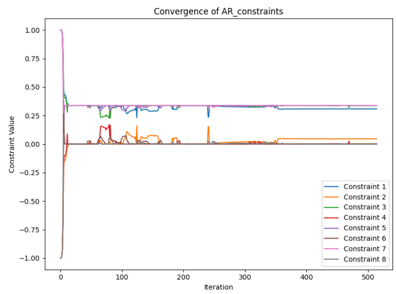

Figure B.96: Aspect Ratio constraint convergence octorotor HF = 0.9

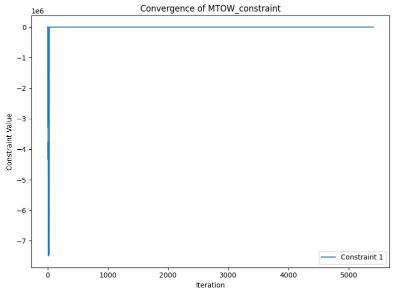

Figure B.97: MTOM Consistency constraint convergence quadrotor HF = 0.9

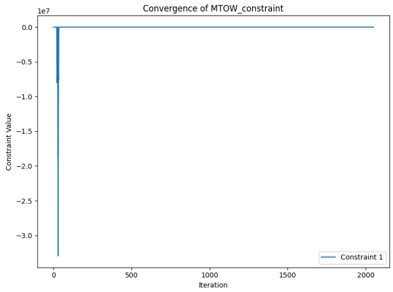

Figure B.98: MTOM Consistency constraint convergence hexarotor HF = 0.9

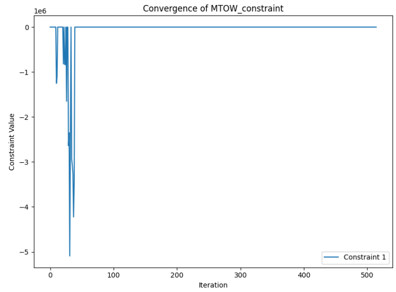

Figure B.99: MTOM Consistency constraint convergence octorotor HF = 0.9

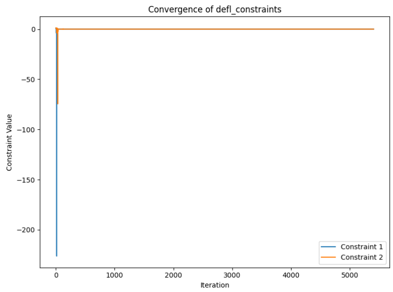

Figure B.100: Deflection constraint convergence quadrotor HF = 0.9

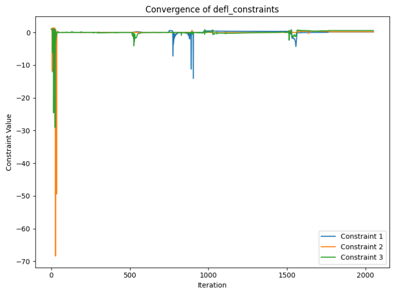

Figure B.101: Deflection constraint convergence hexarotor HF = 0.9

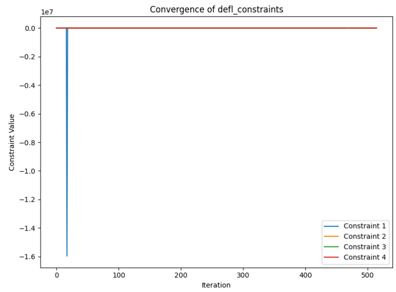

Figure B.102: Deflection constraint convergence octorotor HF = 0.9

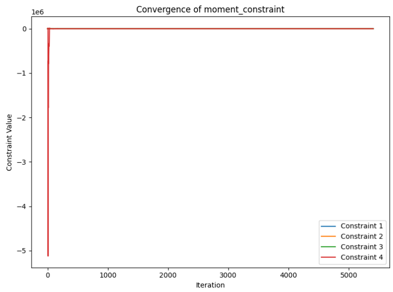

Figure B.103: Moment constraint convergence quadrotor HF = 0.9

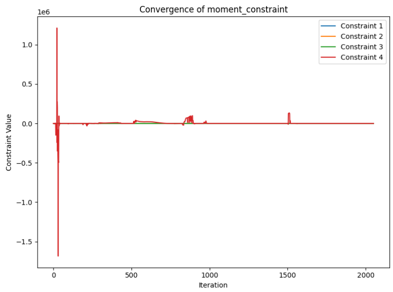

Figure B.104: Moment constraint convergence hexarotor HF = 0.9

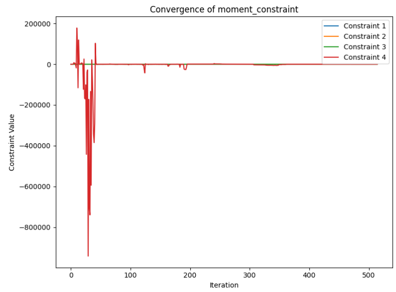

Figure B.105: Moment constraint convergence octorotor HF = 0.9

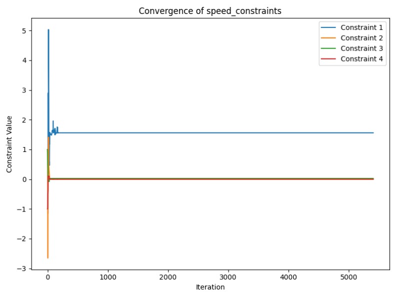

Figure B.106: Velocity constraint convergence quadrotor HF = 0.9

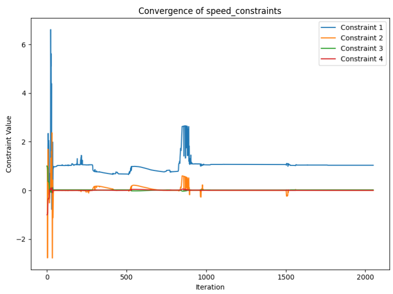

Figure B.107: Velocity constraint convergence hexarotor HF = 0.9

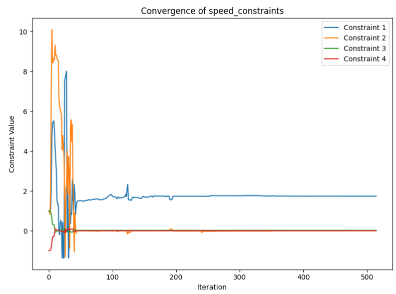

Figure B.108: Velocity constraint convergence octorotor HF = 0.9

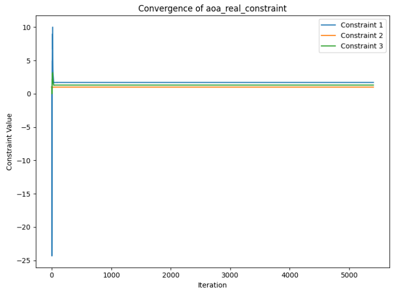

Figure B.109: Angle of Attack constraint convergence quadrotor HF = 0.9

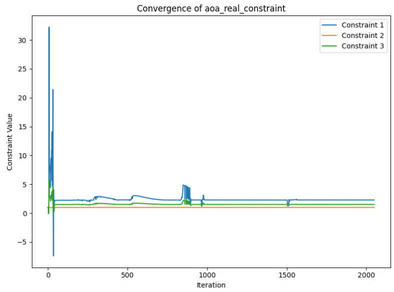

Figure B.110: Angle of Attack constraint convergence hexarotor HF = 0.9

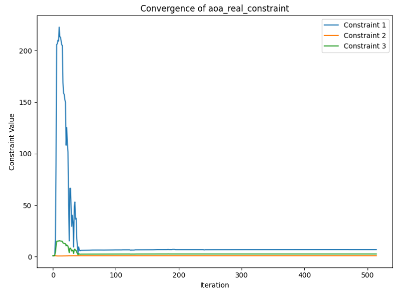

Figure B.111: Angle of Attack constraint convergence octorotor HF = 0.9

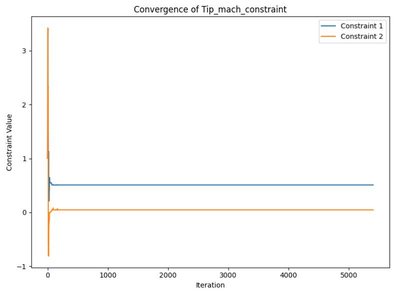

Figure B.112: Tip Mach constraint convergence quadrotor HF = 0.9

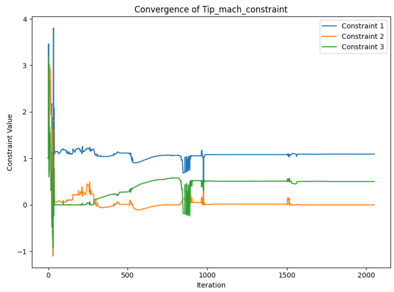

Figure B.113: Tip Mach constraint convergence hexarotor HF = 0.9

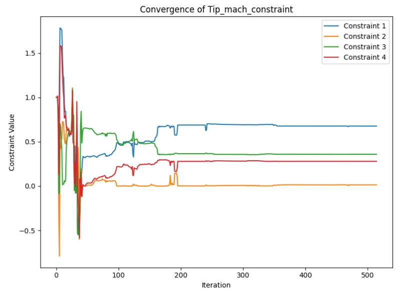

Figure B.114: Tip Mach constraint convergence octorotor HF = 0.9

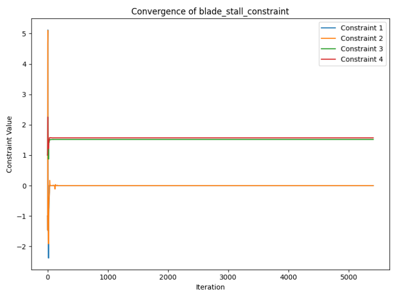

Figure B.115: Blade Stall constraint convergence quadrotor HF = 0.9

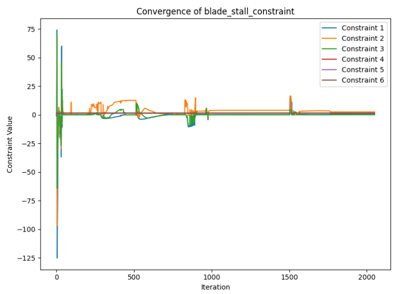

Figure B.116: Blade Stall constraint convergence hexarotor HF = 0.9

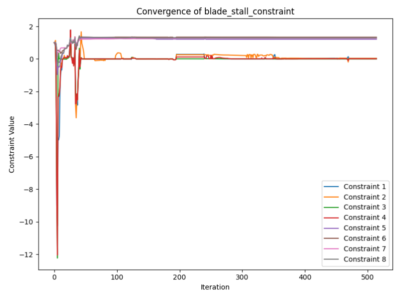

Figure B.117: Blade Stall constraint convergence octorotor HF = 0.9

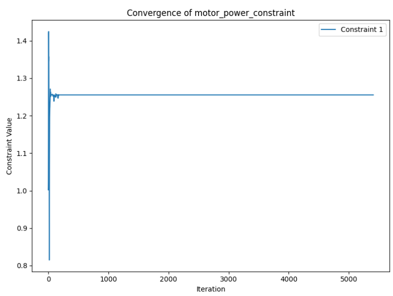

Figure B.118: Motor Power constraint convergence quadrotor HF = 0.9

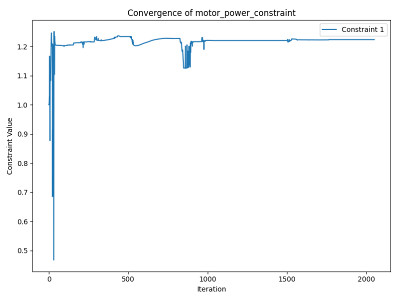

Figure B.119: Motor Power constraint convergence hexarotor HF = 0.9

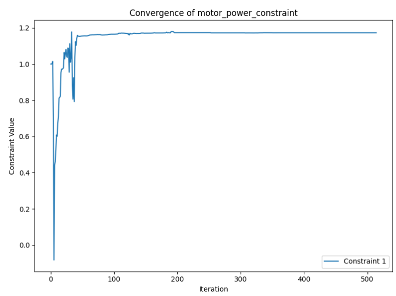

Figure B.120: Motor Power constraint convergence octorotor HF = 0.9

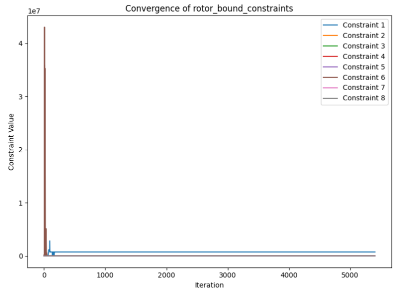

Figure B.121: Rotor bound constraint convergence quadrotor HF = 0.9

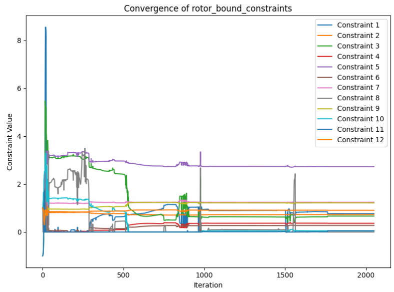

Figure B.122: Rotor bound constraint convergence hexarotor HF = 0.9

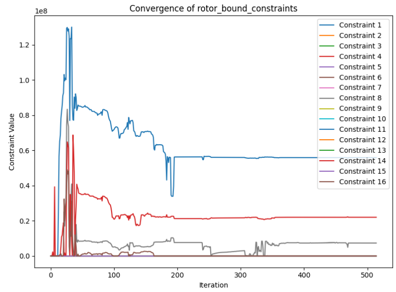

Figure B.123: Rotor bound constraint convergence octorotor HF = 0.9

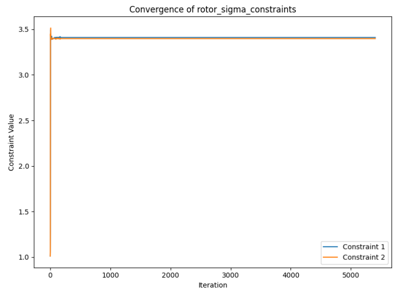

Figure B.124: Rotor solidity constraint convergence quadrotor HF = 0.9

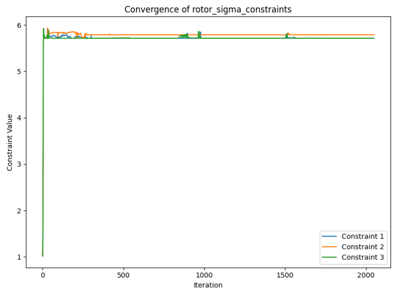

Figure B.125: Rotor solidity constraint convergence hexarotor HF = 0.9

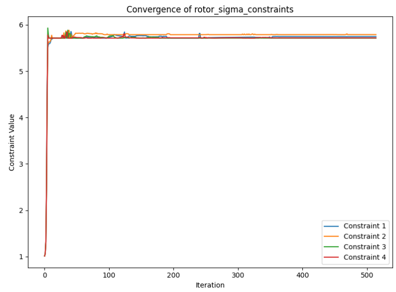

Figure B.126: Rotor solidity constraint convergence octorotor HF = 0.9

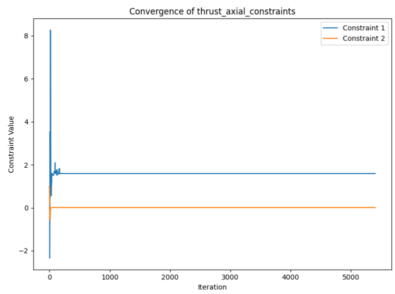

Figure B.127: Axial thrust constraint convergence quadrotor HF = 0.9

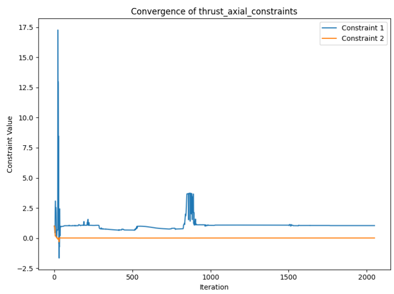

Figure B.128: Axial thrust constraint convergence hexarotor HF = 0.9

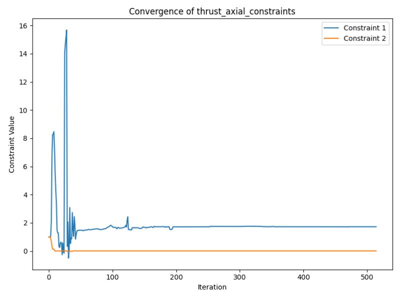

Figure B.129: Axial thrust constraint convergence octorotor HF = 0.9

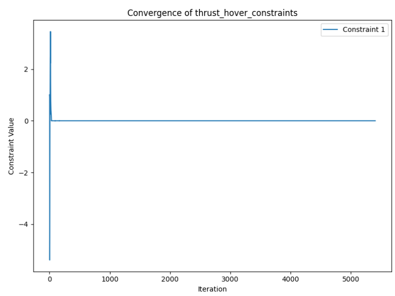

Figure B.130: Hover thrust constraint convergence quadrotor HF = 0.9

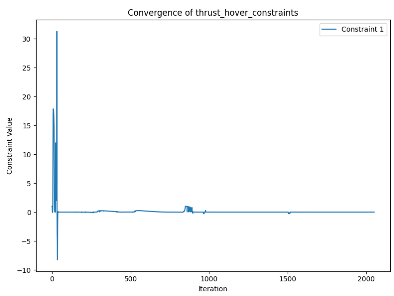

Figure B.131: Hover thrust constraint convergence hexarotor HF = 0.9

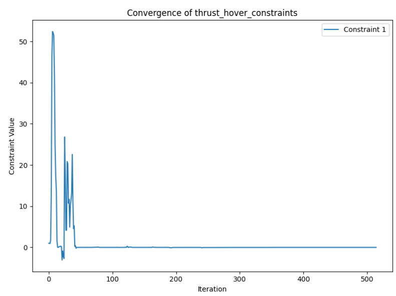

Figure B.132: Hover thrust constraint convergence octorotor HF = 0.9

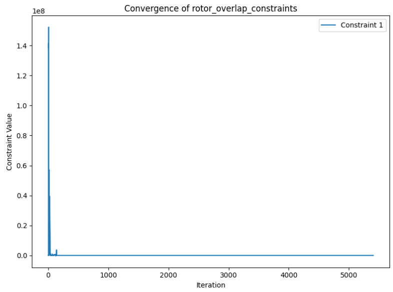

Figure B.133: Rotor overlap constraint convergence quadrotor HF = 0.9

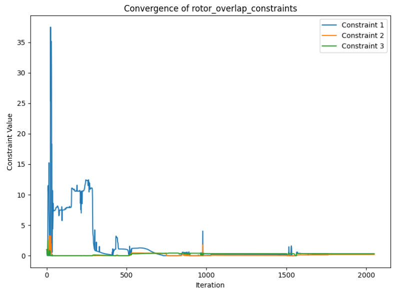

Figure B.134: Rotor overlap constraint convergence hexarotor HF = 0.9

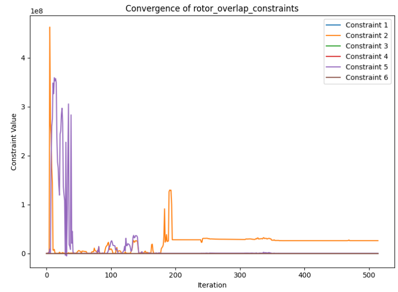

Figure B.135: Rotor overlap constraint convergence octorotor HF = 0.9

C

Optimisation results of remaining configurations

C.1. Processed Results HF = 0.5

C.1.1. Configuration Results HF = 0.5

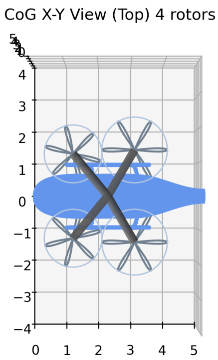

Figure C.1: Optimised quadrotor design HF = 0.5

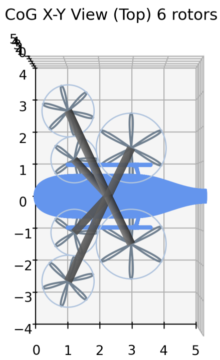

Figure C.2: Optimised hexarotor design HF = 0.5

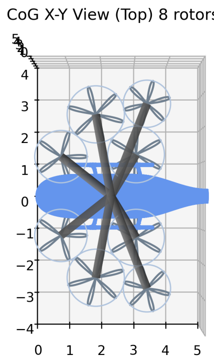

Figure C.3: Optimised octorotor design HF = 0.5

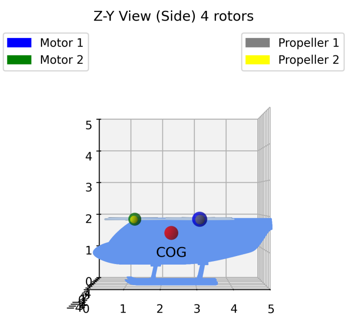

Figure C.4: Quadrotor COG overview HF = 0.5 (Rotors, motors and total)

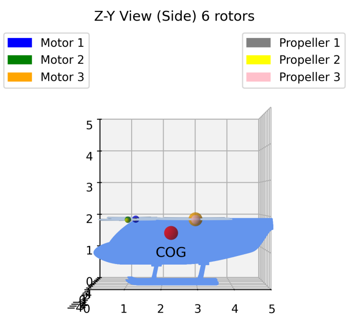

Figure C.5: Hexarotor COG overview HF = 0.5 (Rotors, motors and total)

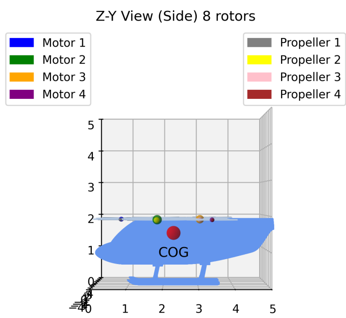

Figure C.6: Octorotor COG overview HF = 0.5 (Rotors, motors and total)

C.1.2. Mass Results HF = 0.5

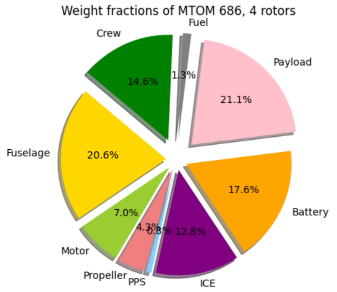

Figure C.7: Subsystem weight fractions quadrotor at HF = 0.5

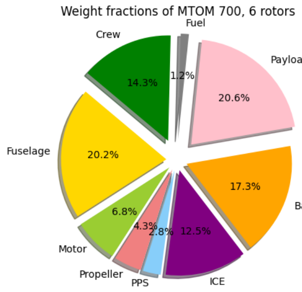

Figure C.8: Subsystem weight fractions hexarotor at HF = 0.5

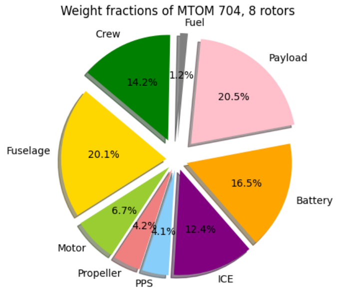

Figure C.9: Subsystem weight fractions octorotor at HF = 0.5

C.2. Processed Results HF = 0.9

C.2.1. Configuration Results HF = 0.9

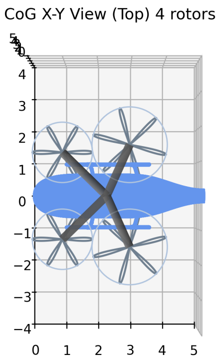

Figure C.10: Optimised quadrotor design HF = 0.9

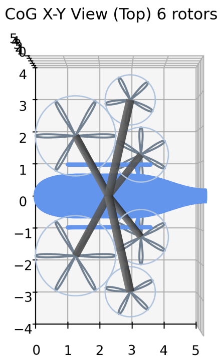

Figure C.11: Optimised hexarotor design HF = 0.9

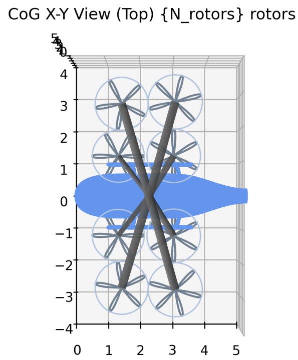

Figure C.12: Optimised octorotor design HF = 0.9

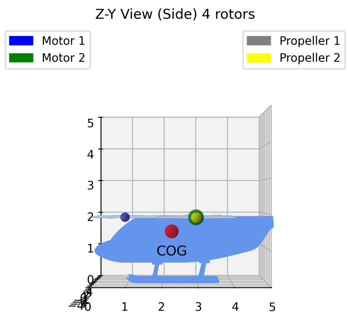

Figure C.13: Quadrotor COG overview HF = 0.9 (Rotors, motors and total)

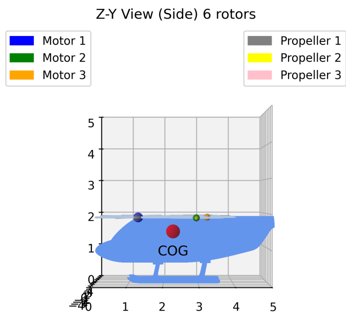

Figure C.14: Hexarotor COG overview HF = 0.9 (Rotors, motors and total)

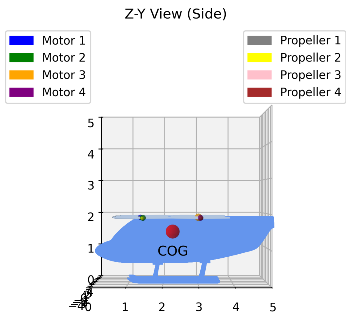

Figure C.15: Octorotor COG overview HF = 0.9 (Rotors, motors and total)

C.3. Design Parameter Results HF = 0.5

Table C.1: Optimized design parameters quadrotor

Parameter	Initial	Optimized
Objective function		
$MTOM$ [kg]	1873.48	686.38
Design vector		
c_1 [m]	0.4	0.06747
c_2 [m]	0.4	0.05693
R_{rotor_1} [m]	1.025	0.9932
R_{rotor_2} [m]	1.025	0.8740
x_{rotor_1} [m]	1.025	3.106
x_{rotor_2} [m]	3.075	1.243
y_{rotor_1} [m]	2	1.393
y_{rotor_2} [m]	2	1.274
z_{rotor_1} [m]	1.90	1.90
z_{rotor_2} [m]	1.90	1.90
N_{blades_1}	6	6
N_{blades_2}	6	6
Ω_{hover_1} [rad/s]	151	208.32
Ω_{hover_2} [rad/s]	151	241.13
Ω_{climb_1} [rad/s]	154	223.63
Ω_{climb_2} [rad/s]	154	258.84
Ω_{cruise_1} [rad/s]	151	211.00
Ω_{cruise_2} [rad/s]	151	244.22
$\Omega_{descent_1}$ [rad/s]	0.1	205.56
$\Omega_{descent_2}$ [rad/s]	0.1	237.93
$\hat{MTOM}$ [kg]	1960	686.38
C_{T_1} [-]	0.05	0.01165
C_{T_2} [-]	0.05	0.01126
r_{i_1} [m]	0.17	0.2496
r_{i_2} [m]	0.17	0.2497
r_{o_1} [m]	0.10	0.2499
r_{o_2} [m]	0.10	0.2499

Table C.2: Optimized design parameters hexarotor

Parameter	Initial	Optimized
Objective function		
$MTOM$ [kg]	2120.57	700.45
Design vector		
c_1 [m]	0.4	0.05000
c_2 [m]	0.4	0.05606
c_3 [m]	0.4	0.07516
R_{rotor_1} [m]	0.9	0.7006
R_{rotor_2} [m]	0.9	0.7849
R_{rotor_3} [m]	0.9	1.052
x_{rotor_1} [m]	1	1.246
x_{rotor_2} [m]	1.7	1.060
x_{rotor_3} [m]	2.9	2.963
y_{rotor_1} [m]	1	1.100
y_{rotor_2} [m]	2.7	2.574
y_{rotor_3} [m]	1	1.452
z_{rotor_1} [m]	1.90	1.90
z_{rotor_2} [m]	1.90	1.90
z_{rotor_3} [m]	1.90	1.90
N_{blades_1}	6	5
N_{blades_2}	6	6
N_{blades_3}	6	6
Ω_{hover_1} [rad/s]	174	281.53
Ω_{hover_2} [rad/s]	174	197.96
Ω_{hover_3} [rad/s]	174	191.69
Ω_{climb_1} [rad/s]	176	162.44
Ω_{climb_2} [rad/s]	176	278.59
Ω_{climb_3} [rad/s]	176	202.66
Ω_{cruise_1} [rad/s]	174	296.68
Ω_{cruise_2} [rad/s]	174	190.33
Ω_{cruise_3} [rad/s]	174	193.77
$\Omega_{descent_1}$ [rad/s]	0.1	46.14
$\Omega_{descent_2}$ [rad/s]	0.1	285.87
$\Omega_{descent_3}$ [rad/s]	0.1	192.40
$\hat{MTOM}$ [kg]	2325	700.45
C_{T_1} [-]	0.05	0.01027
C_{T_2} [-]	0.05	0.01014
C_{T_3} [-]	0.05	0.01210
r_{i_1} [m]	0.17	0.2325
r_{i_2} [m]	0.17	0.2489
r_{i_3} [m]	0.17	0.2496
r_{o_1} [m]	0.10	0.2326
r_{o_2} [m]	0.10	0.2499
r_{o_3} [m]	0.10	0.2499

Table C.3: Optimized design parameters octorotor

Parameter	Initial	Optimized
Objective function		
$MTOM$ [kg]	2642.03	704.07
Design vector		
c_1 [m]	0.4	0.0565
c_2 [m]	0.4	0.06163
c_3 [m]	0.4	0.06106
c_4 [m]	0.4	0.05098
R_{rotor_1} [m]	0.9	0.7910
R_{rotor_2} [m]	0.9	0.8628
R_{rotor_3} [m]	0.9	0.8549
R_{rotor_4} [m]	0.9	0.7137
x_{rotor_1} [m]	0.9	0.7910
x_{rotor_2} [m]	1.4	1.841
x_{rotor_3} [m]	2.7	3.057
x_{rotor_4} [m]	3.2	3.385
y_{rotor_1} [m]	1.0	1.191
y_{rotor_2} [m]	2.75	2.468
y_{rotor_3} [m]	1.0	1.254
y_{rotor_4} [m]	2.75	2.788
z_{rotor_1} [m]	1.90	1.90
z_{rotor_2} [m]	1.90	1.90
z_{rotor_3} [m]	1.90	1.90
z_{rotor_4} [m]	1.90	1.90
N_{blades_1}	6	5
N_{blades_2}	6	6
N_{blades_3}	6	6
N_{blades_4}	6	6
Ω_{hover_1} [rad/s]	169	182.01
Ω_{hover_2} [rad/s]	169	238.23
Ω_{hover_3} [rad/s]	169	221.53
Ω_{hover_4} [rad/s]	169	199.11
Ω_{climb_1} [rad/s]	170	185.77
Ω_{climb_2} [rad/s]	170	254.65
Ω_{climb_3} [rad/s]	170	249.62
Ω_{climb_4} [rad/s]	170	170.14
Ω_{cruise_1} [rad/s]	169	231.20
Ω_{cruise_2} [rad/s]	169	186.73
Ω_{cruise_3} [rad/s]	169	228.60
Ω_{cruise_4} [rad/s]	169	237.31
$\Omega_{descent_1}$ [rad/s]	0.1	32.57
$\Omega_{descent_2}$ [rad/s]	0.1	302.12
$\Omega_{descent_3}$ [rad/s]	0.1	224.07
$\Omega_{descent_4}$ [rad/s]	0.1	61.65
$\hat{MTOM}$ [kg]	2932	704.07
C_{T_1}	0.05	0.01052
C_{T_2}	0.05	0.01067
C_{T_3}	0.05	0.01186
C_{T_4}	0.05	0.01100
r_{i_1} [m]	0.17	0.2499
r_{i_2} [m]	0.17	0.2487
r_{i_3} [m]	0.17	0.2498
r_{i_4} [m]	0.17	0.2498
r_{o_1} [m]	0.10	0.2497
r_{o_2} [m]	0.10	0.2499
r_{o_3} [m]	0.10	0.2499
r_{o_4} [m]	0.10	0.2499

C.4. Design Parameter Results HF = 0.9

Table C.4: Optimized design parameters quadrotor

Parameter	Initial	Optimized
Objective function		
$MTOM$ [kg]	1873.48	828.68
Design vector		
c_1 [m]	0.4	0.06266
c_2 [m]	0.4	0.08036
R_{rotor_1} [m]	1.025	0.9110
R_{rotor_2} [m]	1.025	1.141
x_{rotor_1} [m]	1.025	0.9184
x_{rotor_2} [m]	3.075	2.958
y_{rotor_1} [m]	2	1.311
y_{rotor_2} [m]	2	1.541
z_{rotor_1} [m]	1.90	1.90
z_{rotor_2} [m]	1.90	1.90
N_{blades_1}	6	6
N_{blades_2}	6	6
Ω_{hover_1} [rad/s]	155	214.10
Ω_{hover_2} [rad/s]	155	183.91
Ω_{climb_1} [rad/s]	156	223.80
Ω_{climb_2} [rad/s]	156	192.24
Ω_{cruise_1} [rad/s]	155	216.00
Ω_{cruise_2} [rad/s]	155	185.54
$\Omega_{descent_1}$ [rad/s]	0.1	211.75
$\Omega_{descent_2}$ [rad/s]	0.1	181.89
$\hat{MTOM}$ [kg]	2060	828.68
C_{T_1} [-]	0.05	0.01143
C_{T_2} [-]	0.05	0.01208
r_{i_1} [m]	0.17	0.2496
r_{i_2} [m]	0.17	0.2494
r_{o_1} [m]	0.10	0.25
r_{o_2} [m]	0.10	0.25

Table C.5: Optimized design parameters hexarotor

Parameter	Initial	Optimized
Objective function		
$MTOM$ [kg]	2120.57	843.77
Design vector		
c_1 [m]	0.4	0.08630
c_2 [m]	0.4	0.05395
c_3 [m]	0.4	0.05904
R_{rotor_1} [m]	0.9	1.208
R_{rotor_2} [m]	0.9	0.7553
R_{rotor_3} [m]	0.9	0.8266
x_{rotor_1} [m]	1	1.285
x_{rotor_2} [m]	1.7	2.934
x_{rotor_3} [m]	2.9	3.258
y_{rotor_1} [m]	1	1.808
y_{rotor_2} [m]	2.7	2.894
y_{rotor_3} [m]	1	1.241
z_{rotor_1} [m]	1.90	1.90
z_{rotor_2} [m]	1.90	1.90
z_{rotor_3} [m]	1.90	1.90
N_{blades_1}	6	6
N_{blades_2}	6	5
N_{blades_3}	6	6
Ω_{hover_1} [rad/s]	176176	143.55
Ω_{hover_2} [rad/s]	176	281.16
Ω_{hover_3} [rad/s]	176	234.23
Ω_{climb_1} [rad/s]	178	154.82
Ω_{climb_2} [rad/s]	178	157.38
Ω_{climb_3} [rad/s]	178	305.04
Ω_{cruise_1} [rad/s]	176	144.81
Ω_{cruise_2} [rad/s]	176	282.90
Ω_{cruise_3} [rad/s]	176	236.67
$\Omega_{descent_1}$ [rad/s]	0.1	145.94
$\Omega_{descent_2}$ [rad/s]	0.1	180.40
$\Omega_{descent_3}$ [rad/s]	0.1	279.45
$\hat{MTOM}$ [kg]	2375	843.77
C_{T_1} [-]	0.05	0.01110
C_{T_2} [-]	0.05	0.01103
C_{T_3} [-]	0.05	0.01103
r_{i_1} [m]	0.17	0.01103
r_{i_2} [m]	0.17	0.01103
r_{i_3} [m]	0.17	0.2067
r_{o_1} [m]	0.10	0.2232
r_{o_2} [m]	0.10	0.25
r_{o_3} [m]	0.10	0.2079

Table C.6: Optimized design parameters octorotor

Parameter	Initial	Optimized
Objective function		
$MTOM$ [kg]	2642.03	855.47
Design vector		
c_1 [m]	0.4	0.0573
c_2 [m]	0.4	0.0564
c_3 [m]	0.4	0.0562
c_4 [m]	0.4	0.0510
R_{rotor_1} [m]	0.9	0.8037
R_{rotor_2} [m]	0.9	0.8055
R_{rotor_3} [m]	0.9	0.7930
R_{rotor_4} [m]	0.9	0.8319
x_{rotor_1} [m]	0.9	1.468
x_{rotor_2} [m]	1.4	1.465
x_{rotor_3} [m]	2.7	3.095
x_{rotor_4} [m]	3.2	3.103
y_{rotor_1} [m]	1.0	1.203
y_{rotor_2} [m]	2.75	2.813
y_{rotor_3} [m]	1.0	1.193
y_{rotor_4} [m]	2.75	2.818
z_{rotor_1} [m]	1.90	1.90
z_{rotor_2} [m]	1.90	1.90
z_{rotor_3} [m]	1.90	1.90
z_{rotor_4} [m]	1.90	1.90
N_{blades_1}	6	6
N_{blades_2}	6	5
N_{blades_3}	6	6
N_{blades_4}	6	6
Ω_{hover_1} [rad/s]	168	240.04
Ω_{hover_2} [rad/s]	168	244.10
Ω_{hover_3} [rad/s]	168	253.88
Ω_{hover_4} [rad/s]	168	223.35
Ω_{climb_1} [rad/s]	169	263.08
Ω_{climb_2} [rad/s]	169	240.48
Ω_{climb_3} [rad/s]	169	350.95
Ω_{climb_4} [rad/s]	169	71.50
Ω_{cruise_1} [rad/s]	168	224.11
Ω_{cruise_2} [rad/s]	168	262.91
Ω_{cruise_3} [rad/s]	168	239.01
Ω_{cruise_4} [rad/s]	168	241.88
$\Omega_{descent_1}$ [rad/s]	0.1	130.04
$\Omega_{descent_2}$ [rad/s]	0.1	313.86
$\Omega_{descent_3}$ [rad/s]	0.1	247.65
$\Omega_{descent_4}$ [rad/s]	0.1	224.77
$\hat{MTOM}$ [kg]	2900	855.47
C_{T_1}	0.05	0.01133
C_{T_2}	0.05	0.01102
C_{T_3}	0.05	0.01156
C_{T_4}	0.05	0.01027
r_{i_1} [m]	0.17	0.2498
r_{i_2} [m]	0.17	0.2499
r_{i_3} [m]	0.17	0.2499
r_{i_4} [m]	0.17	0.2499
r_{o_1} [m]	0.10	0.25
r_{o_2} [m]	0.10	0.2483
r_{o_3} [m]	0.10	0.2497
r_{o_4} [m]	0.10	0.2489